Reactive Inkjet Printing

of Silk Swimmers

By:

Yu Zhang

A dissertation submitted to the University of Sheffield in accordance with the

requirements of the degree of Doctor of Philosophy

The University of Sheffield

The Department of Biological and Chemical Engineering.

Submission Date

September 2017

Abstract

Biological Micro-motors are one of the most remarkable products of evolution; they can perform biological tasks with surprisingly high efficiency. A novel form of miniaturized man-made self-propelled micro-motors based on silk have been designed and fabricated in this thesis. These 'swimmers' were made from regenerated *Bombyx mori* silk fibroin via 3D reactive inkjet printing under ambient processing conditions. While *Bombyx mori* silk exhibits impressive mechanical properties, remarkable biocompatibility, controlled biodegradability, environmental stability, and morphologic flexibility, silk swimmers have expanded the range of potential applications even to biomedical platform and sensitive protein therapeutics.

Micro-motors are able to convert chemical or external energy into mechanical motion. Two different types of propulsion mechanisms were studied for silk swimmers: catalytically powered bubble propulsion and surface tension gradient powered. For bubble propelled swimmers the trust is created by oxygen bubbles, generated by the decomposition of hydrogen peroxide, and being released off the surface of the swimmers. Trajectory analysis of catalytic powered swimmers placed in hydrogen peroxide fuel solutions revealed long-lasting and site-specific controlled motion. In contrast, surface tension gradient (Marangoni flows) driven swimmers, via the dissolution of PEG_{400}, resulted in faster smoother motions which however was short lasting and less controllable.

Utilising 3D reactive inkjet printing as a fabrication technology to generate swimmers, allows to readily varying the structure of the swimmers by changing

Abstract

the inks, printing scripts and parameter settings. In this thesis, this process is used to customize swimmers and incorporate other functional moieties for applications including drug delivery, bio-mixing and cancer cell detection and capture.

Dedication

This thesis is dedicated to my parents, family members

and friends,

For their endless love, support and encouragement.

Acknowledgements

Publications

[1] P. Rider, Y. Zhang, C. Tse, Y. Zhang, D. Jayawardane, J. Stringer, et al., "Biocompatible silk fibroin scaffold prepared by reactive inkjet printing," Journal of Materials Science, 2016.

[2] D. A. Gregory, Y. Zhang, P. J. Smith, X. Zhao, and S. J. Ebbens, "Reactive Inkjet Printing of Biocompatible Enzyme Powered Silk Micro-Rockets," Small, vol. 12, pp. 4048-4055, 2016.

Book Chapter

[1] D. A. Gregory, Y. Zhang, S.J.Ebbens, and X.Zhao "Reactive inkjet printing-chapter 8 Reactive inkjet printing of regenerated silk fibroin as a 3D scaffold for autonomous swimming devices (micro-rockets)"

Conference Papers

[1] Y. Zhang, D. A. Gregory, P. J. Smith, X. Zhao, "Regenerated silk fibroin as an inkjet printable biomaterial", in Printing For Fabrication (NIP), Society for Imaging Science and Technology, Manchester 2016, p.406.

[2] D. A. Gregory, Y. Zhang, P. J. Smith, X. Zhao, and S. J. Ebbens, "Altering the Bubble Release of Reactive Inkjet Printed Silk Micro-rockets", in Printing For Fabrication (NIP), Society for Imaging Science and Technology, Manchester 2016, p.452.

Oral Presentations

[1] "Inkjet Printing of Silk Fibroin Scaffolds", oral presentations at University of Sheffield Engineering Symposium 2015, Sheffield UK.

Publications

[2] "Regenerated silk fibroin as an inkjet printable biomaterial", oral presentations at Printing for Fabrication (NIP) September 2016, Manchester, UK.

Table of Contents

Table of Contents

Table of Contents

Table of Contents

List of Tables

List of Figures

List of Figures

List of Figures

List of Figures

List of Figures

List of Figures

Chapter 1 Introduction and Literature Review

1.1 Introduction

This chapter firstly introduces the *Bombyx mori* Silk, an animal silk, including its typical mechanical and physical properties, different physical structures, and advanced and multifunctional applications. Secondly, self-propelled motors are introduced as silk is a desired material to make those motors. This second part introduces the classification of the self-propelled motors based on the different energy input. The catalytic bubble propulsion and concentration gradient propulsion will be highlighted. This chapter thirdly introduces the inkjet printing technology, including the classification of inkjet printing, what kinds of basic inks and additives have been used, and applications to data. I will highlight the section about critical parameters for ink printability and explain how to use silk bio-inks for an inkjet printer. Finally, a schematic overview of the self-propelled motors, made from regenerated silk fibroin (RSF) based inks by inkjet printing, will be summarized.

1.2 Silk (*Bombyx Mori*)

1.2.1 An overview of *Bombyx Mori* silk

Silk, derived from *Bombyx mori (B. mori)* silkworm (shown in **Figure 1-1**A), has been used in the textile industry and as biomedical suture material for centuries. Native *B. mori* silk fibres are approximately 10-25 μm in diameter and are composed of the core fibroin protein coated with sericin protein (shown in **Figure 1-1**B and C) [1-5]. Sericin is a family of hydrophilic proteins that count for 25%-30% of the total silkworm cocoon by weight [1, 6, 7].

Figure 1-2 shows the schematic image of the core fibroin which consists of a light chain (~26kDa) and a heavy chain (~ 390kDa); a single disulfide bond at the C-terminus links the two chains [3, 8]. The amino acid composition of silk fibroin from *B.mori* consists mainly of 43% glycine, 30% alanine and 12% serine. The heavy chain consists of crystalline regions (β-sheet structures), less crystalline regions (β-turn structure) and N,C-terminus.

(A) *Silkworm (Bombxy mori)* **(B)** **(C)**
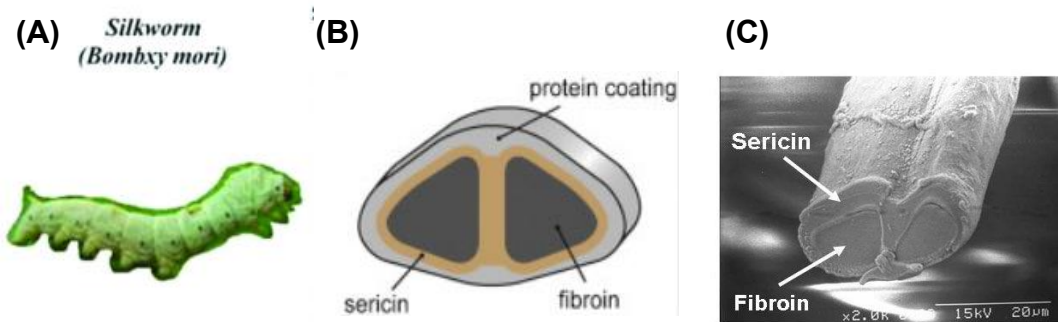
Figure 1-1 A) An image of a *Bombyx mori* silkworm [5]. B) The schematic illustration of the composite structure of a cocoon fiber [4]. C) Scanning electron microscope image of a single *B. mori* silkworm cocoon fiber [9].
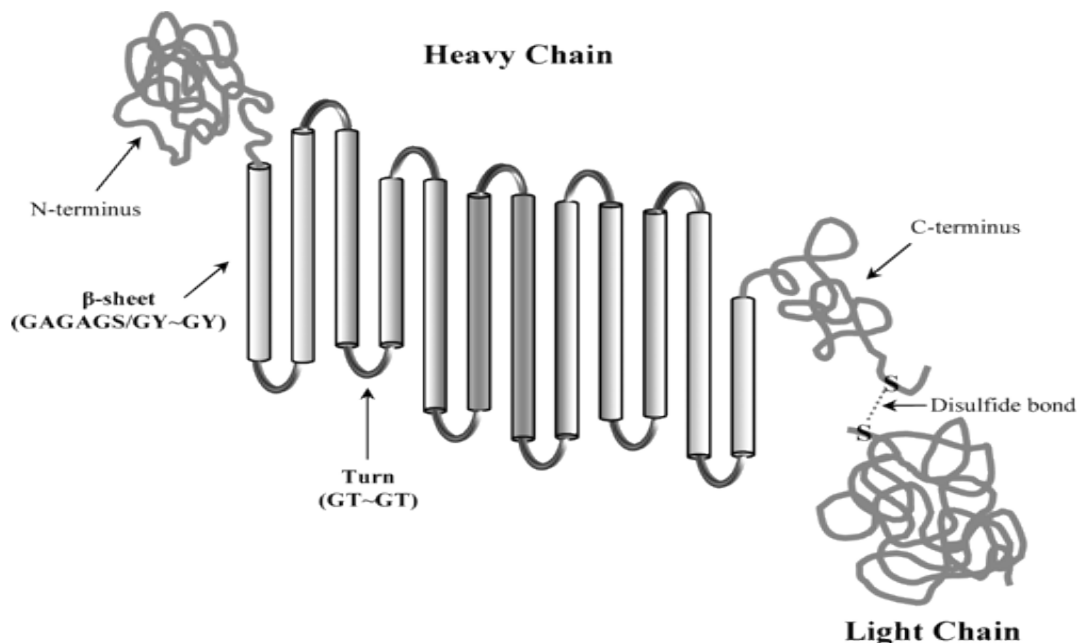
Figure 1-2 The schematic image of portable 2D structure of silk core fibroin, illustrating the heavy chain (N,C-terminus, beta-sheet and Turn secondary structure) and light chain. The two chains are linked with disulfide bond.

Silk polymorphs

Three silk polymorphs have been observed to date, they are silk Ⅰ, silk Ⅱ and silk Ⅲ [3].

In nature, silk Ⅰ is a kind of water-soluble protein found in the gland of silkworms. When silk Ⅰ is exposed to physical spinning or heat, it transforms to a stable crystalline structure called silk Ⅱ. Natural silk fibres are semi crystalline and consist of crystalline silk Ⅱ beta-sheet and highly aligned amorphous regions [3, 10]. This property not only exists in natural silk, it also has been observed in regenerated silk fibroin (RSF). Silk Ⅰ can also be induced to silk Ⅱ under the addition of organic solvents (e.g. methanol, ethanol, and acetone), salts (such as potassium chloride, calcium chloride, and so on) or physical treatment (like shear force and heat) [3, 11, 12].

Both silk Ⅰ and silk Ⅱ can be found in nature while silk Ⅲ is an assembled interfacial polymorph. Silk Ⅲ was observed in ultrathin film (Langmuir-Blodgett silk film or cast silk film) and assembled on an air/water or oil/water interface. Silk Ⅲ has a helical structure and the needle-shaped silk Ⅲ was observed in a helical conformation which pushes the alanine (hydrophobic) and serine (hydrophilic) residues to opposite sides of the interface. Thus, silk Ⅲ fibroin has potential to be used as surfactant [13]. However, Silk Ⅲ will not be described and used in this thesis due to it is an unstable structure and only can be find at the water/air interface.

1.2.2 The properties of silk fibroin as biomaterial

B. mori silks (as illustrated in **Figure 1-3**) have impressive mechanical properties, remarkable biocompatibility, controlled biodegradability, environmental stability, morphologic flexibility and the ability for amino acid side change modification to immobilize growth factors [1, 3, 6, 14-18].
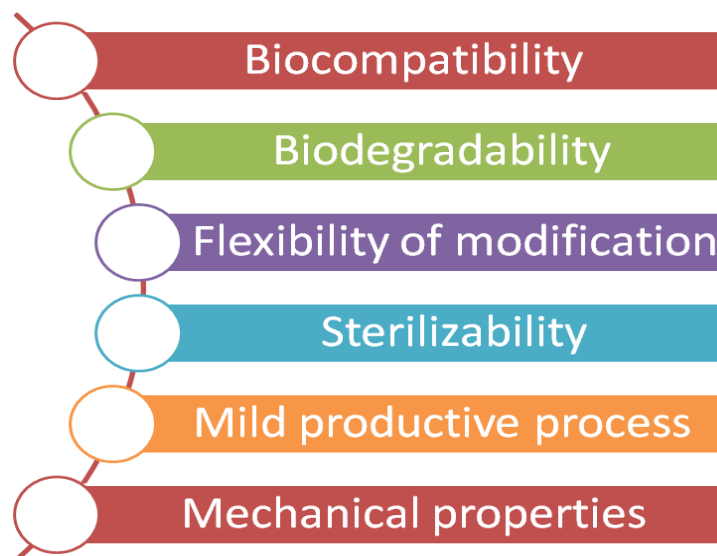
Figure 1-3 The image lists the characteristic of *B.mori* silk.

Mechanical Properties

The silk fibroin, core protein mainly with β-sheet structure, has high toughness and mechanical strength [6]. The mechanical strength is about 0.6 GPa which is better than other commonly used biomaterials, including tendon collagen (0.15 GPa), wool (0.2 GPa), and resilin (0.003 GPa) [19]. In terms of toughness, silk fibers (70 MJ m^{-3}) are greater than most synthetic materials such as Kevlar 49 fibre (50 MJ m^{-3}), carbon fibre (25 MJ m^{-3}) and high-tensile steel (6 MJ m^{-3}) [19]. The ultimate tensile strength of *B.mori* silk fibers is 740 MPa while PLA is 28-50 MPa and collagen is in the range of 0.9-7.4 MPa. Thus, silk is an excellent candidate biomaterial for biomedical applications.

Biocompatibility and immunological response

Biocompatibility is an important property of biomaterials. The international standardization organization (ISO) has the biocompatibility requirements: ISO 10993 to determine whether a new material can be transplanted *in vivo* [20]. Generally, the histocompatibility and hem-compatibility of the biomaterials are checked by immunological responses, cytotoxicity test, skin irritation test and sensitization test. Silk has been known as a biocompatible materials for a long time [6]. The applications of using silk as suture [3, 21, 22] or wound dressing [23-29] are the best examples to prove the remarkable biocompatibility of silk. Many different types of silk based suture such as virgin and black braided [6, 22, 30] have been analysed and showed low immune response.

Nowadays, the silk based biomaterials are not only used as suture also used in tissue engineering and life science. In 1999, Santin et al. reported that compared with polystyrene and poly(2-hydroxyethyl methacrylate), silk fibroin showed less adhesion of immune-competent cells [31]. In 2005, Meinel et al. showed that silk fibroin film induced a lower immunological response than polylactic acid films and collagen films [32]. In 2014, Shen et al. reported silk fibroin (SF) scaffolds have milder immunological response than acellular collagen Ⅰ/Ⅲ (AC), paper and gel-foam scaffolds when they used as substitution of subcutaneous tissue of middle ear cavity in rat models [33]. In my study, based on the biocompatibility of silk fibroin, the self-propulsion motor which is fabricated by regenerated silk fibroin has the change to be used for cell culture and other medical applications.

Biodegradability

Biodegradability is the capability of the materials to be degraded by biological

reactions. The process of the enzymatic degradation is termed as biodegradation [34]. Biodegradability of silk materials has been extensively studied both *in vitro* and *in vivo*. For *in vitro*, the degradation process has been determined by checking the weight loss, the change in morphology and the amount of intermediate degradation products. Interestingly, Wang et al. found that pre-irradiating silk based material under 30-500 kGy dose of gamma-ray promotes the rate of collagenase biodegradation [35]. For *in vivo*, the biodegradation has been tested by the integrity, morphology changing and mechanical strength of the transplants. Wang et al. studied the degradation of RSF scaffolds in rats. The results demonstrated that the scaffolds were tolerated by the host rats and the rate of degradation has a correlation with the morphology and mechanical properties of the scaffolds [36]. It is desirable that the rate of degradation of the designed structure can match the rate of new tissue growth. Li et al. showed that the higher the content of silk II structure in RSF scaffold, the lower the degradation rate observed. This observation indicates that the degradation rate can be tailored by controlling the percentage of beta-sheet structure [37, 38].

Specific enzymes have been used to analyse the biodegradation of the silk based materials (Table 1-1). For example, Numata et al. established the biodegradation model of anti-parallel beta sheet silk crystals. The biodegradation rate of using protease XIV was faster than that of alpha-chymotrypsin. The slow degradation process mimicked the natural degradation process in the human body and showed no cytotoxic products from the degradation [39]. Pritchard et al. also used protease XIV to analyse the rate of drug release on silk based devices [40]. Therefore, the enzyme protease XIV

can be used to control the biomaterial degradation rates as well. Compared to other kinds of biomaterials such as collagen, the degradation of regenerated silk is longer but tailorable. Therefore, in the future, degradation rate of silk materials can be tailored to fit broad applications in various fields.

Table 1-1 Biodegradation (enzyme based) for differernt silk forms.

Enzyme types	Function	Silk Forms	Ref.
Protease XIV	Fast biodegradation process	anti-parallel beta sheet silk crystals	**[39, 40]**
Alpha-chymotrypsin	Mimic natural environment in the human body	anti-parallel beta sheet silk crystals	**[39]**
Collagenase	--	Silk filaments	**[35]**
Collagenase IA	Bone tissue repair	Silk scaffolds	**[41]**

Flexibility of surface modification

Surface modification is an action of decorating the materials in order to add some extra properties to their surfaces. In 1984, Pierschbacher et al. had found that the integrin recognition sequence RGDS promote cell adhesion [42]. After many years of research, Galeotti et al. demonstrated the possibility of chemical modification on silk films. The azido rich surface of the silk films reacted with alkyne terminated of polyethylene glycol by click reaction. Then they used fluorescent technique to prove the success of the click reaction [43]. Dhyani and Singh could control the cell attachment characteristic of regenerated silk fibroin films by graft polymerization. They developed a technique which used plasma etching to graft pAAc, pHEMA and PEG on the silk films (Table 1-2). These chemicals modified the surface hydrophobic properties and changed the cell adhesion in the later cell culture [44].

Chemical reaction is the main ways using for surface modification. However, the limitation on chemical reaction conditions (i.e. the shortage of functional groups and using toxic reagents) requires some other convenient ways to modify the surfaces.

Table 1-2 Lists of the ways of the surface modification on silk

Silk forms	Additive	Linking ways	Results	Ref.
Films	polyethylene glycol	The azido rich surface of the silk films reacted with alkyne terminated of polyethylene glycol by click reaction		[43]
Films	pAAc, pHEMA and PEG	Plasma etching		[44]
Silk Fiber	--	Oxygen and Ar plasma-treated	controlling the silk surface roughness promoting the adsorption capacity of the silk fibres	[45]
Films	PET-SF PET-PAA-SF	plasma pretreatment followed by SF dip coating	mesenchymal stem cells (MSCs) exhibited optimum density	[46]
Scaffolds	wheat germ agglutimin		adipose-derived stromal cells adhesion enhanced	[47]
Nano-fibrous mats	dextran		promoting the wound healing	[23]

Some researchers have used plasma treatment for the modification of silk based biomaterials. For example, Boonla et al. demonstrated oxygen and argon plasma treatments are able to control the silk surface roughness. They also analysed the thermodynamics and desorption kinetics of lac dyeing (Lac dye is one of the well-known natural reddish dyestuffs) on silk and concluded plasma treatments were able to promote the adsorption capacity of the silk fibres [45]. Later, Liang et al. made poly (ethylene terephthalate)-silk fibroin films by plasma pre-treatment of PET followed by silk fibroin dip coating. They

controlled the biocompatibility of the films and found the films promote the proliferation and attachment of mesenchymal stem cells (MSCs). The simple method provided the possibility of batch production of PET-SF films [46].

Meanwhile, the plant lectin has been used to modify silk based biomaterials. Teuschl et al. compared adipose-derived stromal cells adhesion between pure native silk fibroin scaffold and wheat germ agglutinins modified silk fibroin scaffold. They demonstrated that the plant lectin modified scaffold promoted cell seeding step and did not cause *in vitro* immune response in peripheral blood mononuclear cells or adverse influence on proliferation and differentiation of adipose-derived stromal cells [47].

Surface modification has not only been used on silk films and scaffolds, but also used on other silk fibroin forms. Kim et al. examined a dextran-modified silk mat and proved the modification promoted wound healing [23].

In conclusion, surface modification helps to improve the properties of silk biomaterials. This modifiable character of silk-based biomaterials increases their value in tissue engineering applications, and also extends to various application fields such as *in vivo* drug delivery and disease diagnosis.

Sterilizability

Sterilization refers to any process that kills or devitalizes the microorganisms; this treatment is a vital pre-process for cell culture and *in vivo* implantation [3, 15, 28, 48]. Most medical applications require sterilization to retain the remarkable properties of the regenerated silk biomaterials and the regenerated silk fibroin should have diverse options for sterilization in order to satisfy the practical requirements. Compared with other fibrous proteins, such as

collagen, silk based materials have an important feature which is the versatility of options for sterilization [29].

Hofmann et al. verified that using an autoclave in a dry state is the optimal sterilization technique for regenerated silk fibroin (RSF) scaffolds [49], since this method does not change the morphology [49]. Silk fibroin scaffolds can also be sterilized using ethylene oxide [6], 70% ethanol [49, 50],or radiation [3, 51, 52].

Mild productive process of RSF solution

Adequate extraction and preparation of the core protein, i.e. fibroin, is required for medical applications [53]. Firstly, the adhesive protein, sericin which covers the surface of fibroin needs to be removed. Normally, sericin is removed by boiling in 0.02 M Na_2CO_3. Then, the extracted silk fibroin is dissolved into inorganic solvents (e.g. 9.3 M LiBr, $CaCl_2$) or an organic solvent (e.g. 1,1,1,3,3,3-hexafluoro-2-propanol, HFIP) and further generated to different material formats according to the applications [53]. The water based processing without using harmful chemicals helps the post treatment to load some sensitive drugs on RSF biomaterials. Furthermore, the mild process contributes to allow the integrating of electronic or photonic biosensors into RSF materials [20].

1.2.3   Different material formats of RSF

A variety of aqueous or organic solvent-processing methods can be used to generate different silk material formats in order to fit the various aims of applications [37, 53] The materials formats include hydrogels, spheres, films, fibres, tubes, sponges and scaffolds (shown in **Figure 1-4**) [53]. In this thesis, a new method will be explored to make a special type of silk scaffolds.
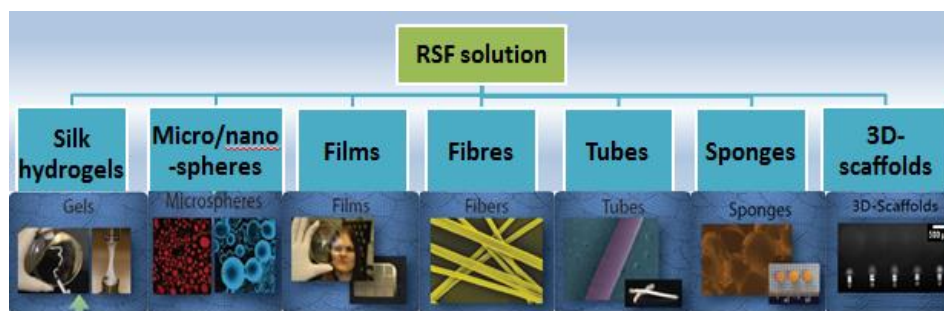
Figure 1-4 Schematic of material morphologies fabricated from regenerated silk fibroin [53].

Hydrogels

The transition from RSF solution to hydrogels is affected by pH, temperature, electric current, vortex, ion concentration such as Ca^+ and K^+ and the concentration of RSF solution [20, 54]. By varying to these parameters, researchers designed different ways to make silk hydrogels. This thesis introduces some methods which use RSF solution to produce silk hydrogels because they are well documented and widely used [53].

Sonication Method: Wang et al. reported a novel treatment-sonication method-to produce silk hydrogels. RSF solution is put into an Eppendorf tube and sonicated with a Sonifier, then incubated at 37 °C. The ultrasonic wave promoted the formation of beta-sheet in RSF solution and the sol-gel transition process was visible with the sonication treatment [55].

Vortex Method: Yucel et al. demonstrated the vortex-induced hydrogelation. According to the typical circular dichroism spectroscopy, RSF solution equilibrated at 25°C in a water bath and then mixed at 3200 rpm by a vortexer to induce protein self-assembly and silk hydrogels. The results showed that the vortex duration, the vortex temperature and the concentration of RSF solution affected the hydro gelation kinetics. This vortex technique was simple and rough, but convenient and versatile [56].

Electro-gelation Method: Leisk et al. discovered that electricity promoted the formation of adhesive gel and this process is termed as electro-gelation. The hydrogels appeared on the positive electrode under certain direct current electric fields. However, the electro gelation was a reversible process. The newly formed hydrogel dissolved when the polarity of the voltage was reversed. This process was novel, with the flexible operation promoting the electro-hydrogels to some special applications. For example, using the reversible hydrogels allowed a trigger inductor to be made [57].

The structure and properties of silk hydrogels influence their broad applications. To date, they have been used for cell encapsulation [55], cell culture matrix [58], therapeutic delivery devices [59] and tissue repair substitutes [60].

Films

In general, silk films are fabricated from casting the aqueous or organic silk solution onto substrates [3, 53, 61]. According to the substrates used, the films could be classified as patterned films [62] or non-patterned films [53]. So the cast substrates have important effects on RSF films. At present, RSF films are also produced by Langmuir-Bologett [63] and spin coating [20].

The films are usually produced by two steps. Firstly, using the RSF solutions cast or spins coating the initial films. Secondly, immersing the initial films into the methanol makes final stable films. Drying, water annealing and stretching techniques also are used to get the stable silk films [3].

The silk films not only have a convenient productive process, but also have tuneable properties. The thickness of silk is controlled by a layer-by-layer

technique. The roughness can be adjusted by the percentage of PEO in RSF solution. RSF films contain plenty of chemical and physical binding sites on the surface which promotes surface modification on the silk films such as loaded drugs on wound dressing [29] and added nutrition to promote cell culture [44].

Fine fibres

Electro-spinning technique is famous for producing ultrafine polymer fibres [26, 64-67]. To date, over 50 kinds of polymers successfully fabricate nano-fibres through this technique. Thus, electro-spinning technique is selected to make artificial silk fibres by using RSF solution. A typical electro-spinning setup contains a high voltage supplier, a capillary needle and a grounded collector [64]. Badami et al. research produced desired silk fibres by controlling substrate, solution, process and environment parameters [68]. At the same time, the electro-spinning process well mimics the productive process of natural silk fibres. Nowadays, the electro-spinning silk fibres are made for nano-fibres mats or membranes in order to satisfy the requirements of cell culture or tissue engineering [6, 64].

Besides the electro-spinning technique, Kinahan et al. invented microfluidic approach to fabricate silk fibres [69]. The main part of the microfluidic device was a cross-shaped channel which contains one outlet and three inlets. The channel completely imitated the secreting gland of the silkworm and the researchers control the productive silk fibres through adjusting the processing parameters [69].

Furthermore, Ha et al. fabricated silk fibres through wet fibre spinning [70]. The wet spinning setup consists of a mechanical pump, a syringe, a coagulation bath, a wash bath, draw rolls and a take-up roll. The post-treatments (the

coagulation bath and the wash bath) improved the mechanical properties and toughness of RSF. This innovation promoted the industrial production of silk filaments [70].

Besides the mentioned methods, thin fibres are able to fibrate by phase separation, template synthesis, drawing and self-assembly methods [71].

RSF tubes

RSF tubes are widely used in blood vessel engineering [6, 64, 71, 72]. At present, the macro vascular tubes, with diameters bigger than 6 mm are synthesized easily. However, the researchers created a new technique to synthesize nanotubes. This report introduces two kinds of RSF tubes synthetic approaches [53]. One is dipping methods; the other one is using regenerated silk spinning fibres to make tubes.

Dip Method

Lovett et al. prepared micro-tubes through dipping stainless steel wire into RSF solution [73]. First, they prepared 20-30% silk fibroin solution and dipped 0.64mm diameter stainless steel into RSF solution. Then, they immersed the coated RSF stainless steel into methanol. This step helped transform the amorphous liquid to crystalline beta-sheet conformation. They repeated the dipping and immersing step 2-4 times. Next, they left the samples to dry overnight. At last, Lovett et al. got the silk tubes by placing the samples into a surfactant solution with the dip method [73].

Spinning Method

In addition, silk tubes are made by rotating silk fibres on an axially reciprocating mandrel. The quality of fibres has significant influence on the

prepared tubes. Nowadays, the spinning fibres are prepared by electro-spinning, wet spinning or gel spinning [53, 64, 70, 72, 74]. Michael L. Lovett et al. elaborated the gel spinning fibres were most suitable for making silk tubes. The winding of silk fibres improved the mechanical strength and toughness of RSF tubes[74]. At the same time, the spinning-gel tubes were customized. The inner diameters of tubes were adjusted by the diameter of the used mandrels. The porousness of silk tubes was controlled by the percentage of PEO in RSF solution. It was convenient for the engineers to fabricate the required micro-tubes [72, 74].

Micro/nano spheres

Many methods have been used in producing micro/nano-spheres (particles). To date, it has been known that spray drying [75], emulsification-solvent evaporation [76], stir freeze-thawing [77], encapsulation [78, 79], attritor and jet milling [80, 81], phase separation [82, 83], ultra-fine particle processing system [84] and desolvation [85] methods could make micro/nanoparticles (Table 1-3).

In general, the micro/nanoparticles are used as drug or enzyme encapsulation devices [20, 85, 86]. In order to use the particles *in vivo*, nano-/micro-particles are required. The handy procedure for production of nanoparticles (rapidly adding RSF solution into excess acetone to produce transparent silk fibroin nanoparticles [83]) also shows their commercial value. Zhu et al. loaded Neutral Protease on SFNs by bio-conjugation; optimized the conditions on SFN-NP bio-conjugation. Finally, the designed nanoparticles also showed their possibilities for industrial scale production [83]. Thus, to make silk particles or RSF particles shows their various fabrication benefits and commercial values. This study is based on the idea of making the small scale particles.

Table 1-3 The methods of generating functional RSF particles

Year	Particles	Methods	Ref.
2003	Micro-	Spray-drying	[75]
2005	Micro-	Emulsification-solvent evaporation	[76]
2007	Micro-	Stir freeze-thawing	[77]
2008	Micro-	Encapsulation	[78, 79]
2009	Ultrafine powder	Attritor and jet milling	[80, 81]
2010	Micro-	Phase separation	[82]
2011	Nano-	Phase separation	[83]
2011	Micro-	Ultra-fine particle processing system	[84]
2013	SF-album Nano-	De-solvation	[85]
2013 2014	Submicron	Milling	[87] [88]
2017	Magnetic –silk Nano-	Freeze	[89]

Scaffolds

To date, scaffolds are produced by gas foaming method [90], salt leaching method [90], lyophilisation [90, 91], aqueous-induced method [53, 92], whisker-reinforced method [93], and 3D-printing method. The produced regenerated silk-based scaffolds have tuneable porosity, remarkable mechanical properties and tailorable biodegradation [36]. These characteristics of silk-based scaffolds are good for cell culture and drug release [64]. In tissue engineering, many researchers used silk-based scaffolds to repair articular cartilage [94] and bone tissue [95].

1.2.4   Applications

In this section of the review I will highlight some applications of man-made composite materials based on regenerated silk fibroin protein. These applications include four categories: textile industry, sutures and dressing for wounds, tissue engineering, and drug delivery. In this study, the applications in textile industry is not introduced due to it is not related.

Native silkworm silk has been used as biomedical sutures for decades, and in textile production for centuries [49]. Despite decades of use as medical sutures, RSF is now being rediscovered and considered as a new-type of natural biomaterial for a range of biomedical applications [3, 16, 19, 20, 96-98]. Comparing to composite biopolymers (e.g. nucleic acids and protein polysaccharides) and protein such as collagens, silk fibroin protein provides interesting mechanical properties and the low toxicity which meet almost all desirable characteristics for biomedical applications [3, 97, 99]. Among biomedical applications, the tissue engineering applications which are based on the cell culture on scaffolds has a good development in recent years.

The patients who suffered terrible traffic accidents, vicious assaults and some other kind of serious disaster require the repair of tissue or organs in a hurry. The shortage of organs and tissues from donors is a severe problem in clinical or emergency surgery. Under the circumstances, some artificial scaffolds are fabricated by using RSF biomaterials to repair the injured tissues such as bone and cartilage [45, 70, 73-79], ligament or tendon [80, 81], skin and mucosal [28, 82, 83], hepatic [84-86] and other tissues (listed in Table 1-4).

Table 1-4 Other application of silk based biomaterials in tissue engineering

Forms	Application Field	Ref.
Silk fibroin nanofibrous scaffolds	Vascular tissue regeneration	[87]
Silk conduits	Neural tissue regeneration	[88]
Porous silk scaffolds	Cardiac tissue regeneration	[89]
Wedge shaped silk scaffolds	Meniscus tissue regeneration	[90]
Gel spinning silk tubes	Bladder tissue regeneration	[91]
Silk fibroin membranes	Eardrum tissue regeneration	[92]

Besides the previous biomedical applications, silk fibroin based particles or scaffolds are widely analysed and used as the drug and gene delivery vectors [93-98]. So far, RSF drug delivery has been mainly used for wound dressings as they are continuous transferring drugs to cure and protect the wound [28, 99-101]. Other research focused on using SF coated drug delivery systems (e.g. liposomes) in cancer therapy [102-104]. Moreover, use of SF for oral drug delivery leads to some interesting applications. For example, the slow protease digestion of SF tablets avoids damaging the shape during mechanical stimulation in the gastrointestinal tract [105] which showed SF tablets as potential long lasting oral drug delivery systems. Overall, RSF drug delivery system will lead to extension application by intensified explorations in the future.

1.3 Self-propelled motors

Artificial self-propelling objects which are designed to perform selected mechanical movements (such as rotation, shutting, delivery and collective behaviour) in response to external stimuli have attracted lots of attention in the past few years. Those motors are small autonomous devices capable of achieving complex tasks while being self-propelled in fluids [100, 101]. In this study, a novel kind of self-propelled motor, called silk 'swimmers', was fabricated based on RSF (introduced in section 1.2). In this section, a review will briefly summarize the design, fabrication and applications of those self-motion devices.

1.3.1 Sources of energy for self-propelled motors

When analysing the movement of small scale particles in a solution under a microscope, normally they are seen to move around randomly. This phenomenon is called Brownian motion which is caused by the thermal energy of the surrounding fluid. In order to avoid the random movement of the self-propelled motors and achieving a directed motion, external stimuli should be provided. These stimuli are loaded into certain place of the self-motion devices and operate using some type of energy input. A number of energy inputs have been used (e.g. electric and /or magnetic fields, photonic or acoustic waves, thermal or concentration gradients, and chemical or enzymatic reactions) on the self-propelled motors.

Table 1-5 lists the self-propelled motors which are principally characterized based on the type of energy input that they use. It also lists the number, size and scale, and the advantages in specific applications for each type of motors.

Table 1-5 The classification of micro- and nano-motors based on the type of energy input

	Type name	Propulsion Mechanism	Advantages/Applications	Ref.
Biological Motors	Living organisms driven motors Microtubes (~ 50 μm long)	The flagellar propulsion of the cell	1.Demonstrated the separation of a selected sper-driven micro-motor 2.Selected sperm cells can be remotely guided to the egg cell 3.Easy to control	[102]
	DNA- or RNA-processing enzymes motors	Enzymes invest chemical energy direct the DNA or RNA movement	1. Nature	[103]
Synthetic Motors	Catalytic motors From Nano-/micro to Small scale	Self-electrophoresis Interfacial tension induced motion Bubble propulsion Diffusiophoresis	1. Mimic nature and transfer to artificial 2. Direction control 3. Shape designable 4. Multifunctional fabrication methods 5. Widely investigated	[104-107]
	Thermal motors Micro-particles (~ 3 μm in diameter)	Temperature gradient	1. Fuel-free locomotion 2. A biocompatible tool to perform bioanalytical tests	[108]
	Concentration gradient motors Micro-	Concentration gradient	1. Simple procedure	[109]
	Magnetically driven motors Mircro-	Magnetic field	1. Fine control the direction of the motors (Initial way) 2. Commercial applications 3. Contact free with the motors	[99, 110-113]
	Electrically driven motors Micro-	Electric field	1. Enable wireless control 2. obviate chemical fuel	[114, 115]
	Photodriven motors Nano-/ micro-	Light	1. Renewable energy source 2. Easy to control 3. Contact free with the motors 4. No waste products	[116-118]
	Ultrasound driven motors Nano-	Ultrasound waves	Contact free with the motors	[119-121]

Because my thesis carried out studies on catalytic powered devices, I will highlight the review on the synthetic motors, which include catalytic motors based on various chemical or biochemical fuels, and discuss respective limitations of these devices.

Catalytic motors (Bubble propulsion)

Catalase is a bio-enzyme found in cells that is able to efficiently degrade hydrogen peroxide (H_2O_2) to water (H_2O) and oxygen (O_2), and thus to translate chemical energy into mechanical energy. Catalase from bovine liver contains four porphyrin heme (iron) groups which allow the enzyme to react with the H_2O_2. While the complete molecular mechanism of catalase is not known, the reaction is found based on two stages (shown in Eq. {1.1}) [122, 123].

$$H_2O_2 + Fe(III) - E \rightarrow H_2O + O = Fe(IV) - E(.+)$$
$$H_2O_2 + O = Fe(IV) - E(.+) \rightarrow H_2O + Fe(III) - E + O_2$$
{1.1}
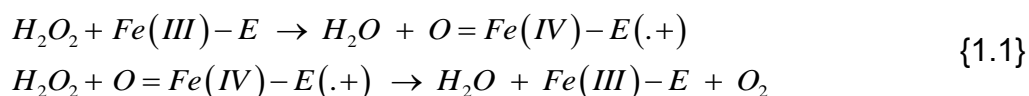
In the last two decades, bubble propelled catalytic and bio-catalytic small engines have been analysed for various applications. In 2008, Pantarotto et al. made a multi-catalytic powered nanotube from multi-walled carbon nanotubes (MWCNTs). **Figure 1-5** shows the schematic images of the bio-hybrid propulsion system. The conversion of glucose by glucose oxidase (GOx) produces di-hydrogen peroxide, which is degraded by catalase to form oxygen gas bubbles which propel the MWCNTs [124]. This autonomously moving carbon nano-tubes offer an opportunity in analysing the behaviour of complex multienzyme ensembles [124].
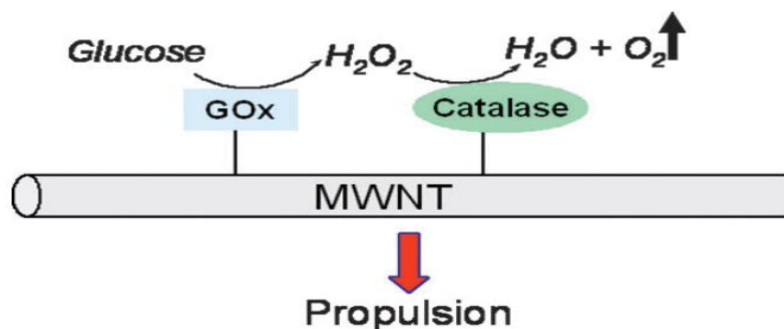
Figure 1-5 Schematic images of a biohybrid propulsion system based on the enzymes glucose oxidase and catalase, immobilized covalently to water-soluble MWCNTs bearing carboxyl functionalities [124].

Then, in 2010, Sanchez et al. rolled up thin Ti / Au films into micro-tubes and the Ti / Au micro-tube where the inner Au layer was functionalized with self-assembled monolayers of 3-mercaptopropionic acid. They reported this micro-engine was the first one which effective uses enzymes as catalysts (shown in **Figure 1-6**) [125].
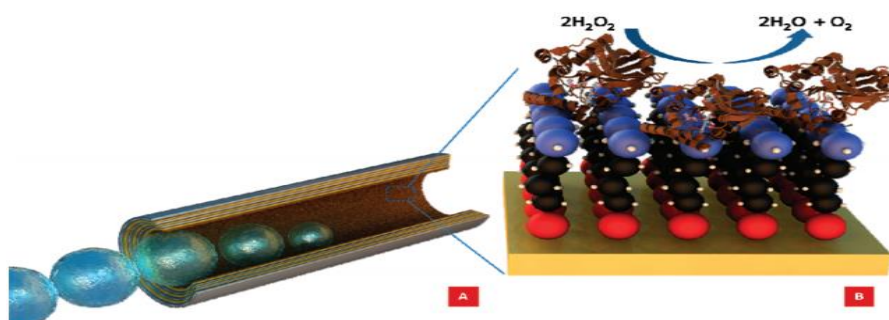
Figure 1-6 Schematic images of the over view hybrid bio-catalytic micro-engine (A); Surface modification of inner Au layer (B) [125].

In 2013, Wang et al. reported a novel micro-motor which was used for water quality testing based on the changing of the propulsion behaviour of it in the presence of pollutants [126]. Poly (3,4-ethylenedioxythiophene) / Au-catalase micro-tubes was used the scheme illustrating in **Figure 1-7**.
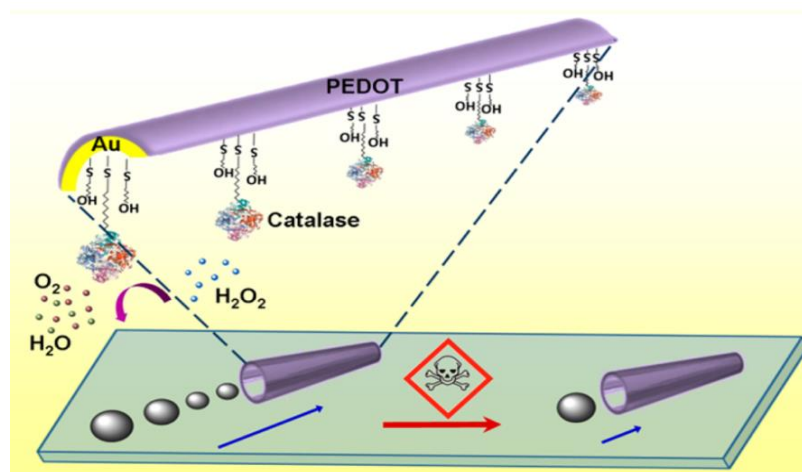
Figure 1-7 The schematic demonstrats the effect of pollutants on the micro-motor moving speed through inhibition of the catalase catalytic layer (bottom) along with the process used for fixing the enzyme at the inner gold surface of the tubular microengine via a mixed 11-mercaptoundecanoic acid / 6-mercaptohexanol self-assembled monolayer (top) [126].

In this thesis, a catalase bio-catalytic micro-engine was fabricated by inkjet printing methods by mixing the catalase into RSF based biomaterial solution. This is also a report on the effective use of enzymes as catalysts in self-propelled micro-engines.

Diffusiophoresis motors (concentration gradient)

For small scale, fluid flow appears in the presence of various externally applied gradients, such as electric, magnetic, and pressure. Each of these gradients generates a direct force on a fluid or particles and drives movement [109]. Diffusiophoresis describes a particle which is driven by gradient without the application of any outside force [127] or transfers the free energy of chemical reaction, dissolution, or precipitation into a directed motion of fluid and particles [128]. The mechanism has been observed since 1947 by Derjaguin et al. [129] and the physics of diffusiophoresis motion has been established in both theories and experiments. However, for several decades, diffusiophoresis has often been ignored or considered as an esoteric lab phenomenon [109].

Velegol et al. did a survey on various motion system where gradients may be generated spontaneously [109]. There are two general types of diffusiophoresis, non-electrolyte [130] and electrolyte [131]. The system can have diffusiophoretic transport when a system has the following situation: a) ions with different co-efficient; b) a concentration gradient resulting from any number of physical process such as dissolution, evaporation, reactions, precipitation, or condensation; c) particles or surfaces with finite zeta potentials [109]. The different salt types or surface charge are useful clues in determining whether an observed phenomenon is caused due to diffusiophoresis.

Surface Tension controlled motors (Marangoni Effect)

Marangoni effect happens when there is a gradient of surface tension at the interface between two phases, mostly appearing on liquid/gas interface [132, 133]. The surface tension gradient is typically caused by variations in the solute concentration, surfactant concentration, and temperature variations along the interface. In some multicomponent liquids or eutectics, the direction of the gradient of surface tension tangential to the interface can be changed by altering the concentration of the solutes at the surface or by adding surfactants. Depending on the fluid, a rather strong convective motion is produced [134].

In this thesis, PEG_{400} was mixed in swimmers and when put the swimmers on water solution; PEG_{400} works as surfactant and changes the surface tension at the air/water interface. This caused the Marangoni effect and resulted in strong motion of swimmers on the air/water interface. In case where the concentration drives the variation of the surface tension, the Marangoni effect is referred to as the *solutocapillary effect*.

1.3.2 Different methods and forms for self-propelled motors

Nowadays, a lot of fabrication methodologies are employed to fabricate multifunctional self-propelled objects. The methods include angled electron beam evaporation, sputter coating, template-assisted deposition, photolithography, and 3D printing [135]. The forms for the self-propelled motors: particle, rods, tubes and other specific designed structure showed in **Figure 1-8**. For the beam evaporation, sputter coating, and template-assisted deposition methods, all of them have a limitation on convenient adjusting the size, scale and material of the motors during the fabrication process. So these methods result in higher fabricating cost and inconvenient when a new type of self-propelled motors is required.
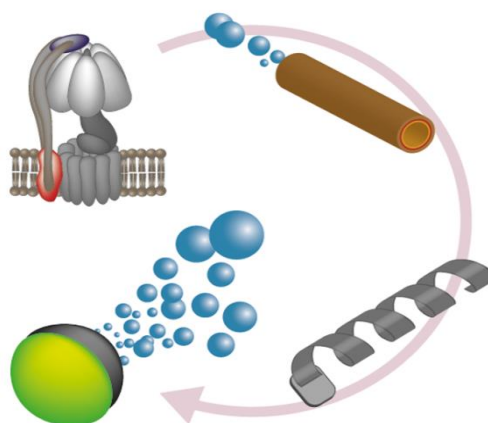
Figure 1-8 Schematic images show the different forms of self-propelled motors [135].

Thus, above all the mentioned fabrication methodologies, I am interested in using 3D printing technology to generate some functional self-propelled motors due to its a more customer friendly technique. It is convenient to custom-made particles by only changing the setting of the printing parameters on the linked computer system and changing the inks. There are a few different types of 3D printers have been used to fabricated self-propelled motors. In 2015, Chen et

al. fabricated an artificial 'micro-fish' by microscale continuous optical printing (µCOP) which was the first report in the presentation of 3D technology to produce self-propelled motors (showed in **Figure 1-9**) [136].

Based on the self-propelled motor examples in this section, I plan to use inkjet printing technique to fabricate RSF 'swimmers' (micro-rockets, stirrers and swimming letters which are described in Chapter 4, 5 and 6 in this thesis, respectively). RSF was selected due to its remarkable characterises, especially on its biocompatibility and formation transitions. Inkjet printing technique shows up because it incorporates a simple and convenient way to fabricate various kinds of self-propelled motors (e.g. the changing of the size and patterns of the particles by quickly adjusting the printing scrips) and use aqueous based solution as the printing inks (the RSF material are easy to dissolve in solutions).
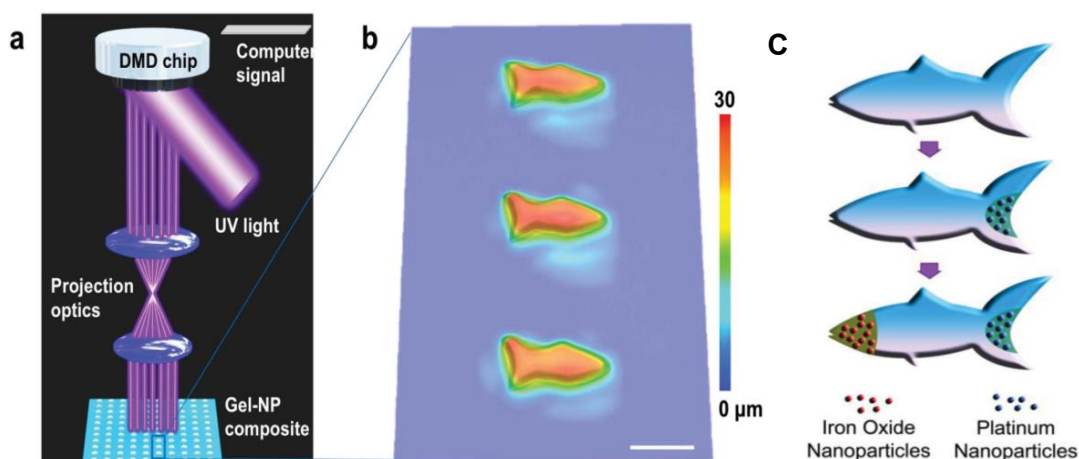
Figure 1-9 a) Schematic demonstration of the µCOP method to fabricate micro-fish. UV light illuminates the DMD mirrors, generating an optical pattern specifi ed by the control computer. The pattern is projected through optics onto the photosensitive monomer solution to fabricate the fish layer-by-layer. b) 3D microscopy image of an array of printed micro-fish. Scale bar, 100 µm. c) Schematic illustration of the procedure of functionalizing a microfish for guided catalytic propulsion. Platinum nanoparticles are first loaded into the tail of the fish for propulsion through catalytic decomposition of H_2O_2. Second, Fe_3O_4 nanoparticles are loaded into the head of the fish for magnetic control. [136].

1.4 Inkjet Printing Technique

As mentioned in section 1.3, 3D printing technology shows up among various fabrication methods of self-propelled motors. Among the 3D printing technology, Inkjet printing technology is most fit my requirements of fabricating silk 'swimmers'. In the past decades, inkjet printing has become a highly capable tool for manufacturing, especially for micro-manufacturing. Before, it is widely known by its applications in photos and graphics. Nowadays, the use of inkjet printers to print functional materials attracts more and more attention and extends its applications into the other areas such as biomedical application [137], biosensors [138], tissue engineering [139, 140] and so on.

Inkjet printing is a computer-aided technique that deposits inks (such as solutions or suspensions) in pre-determined places on the substrate with computer control [141]. This section comprehensively describes the major types of inkjet printers, the critical parameters of ink printability, the basic inks and the functional molecules which can be loaded into the basic inks.

1.4.1   Inkjet Printer

According to the formation mechanisms of ink droplets, the inkjet printers are classified into two main modes which are continuous inkjet (CIJ) printer and drop-on-demand (DOD) inkjet printer. **Figure 1-10** lists the classification of the inkjet printer based on the two main modes and their subdivisions.
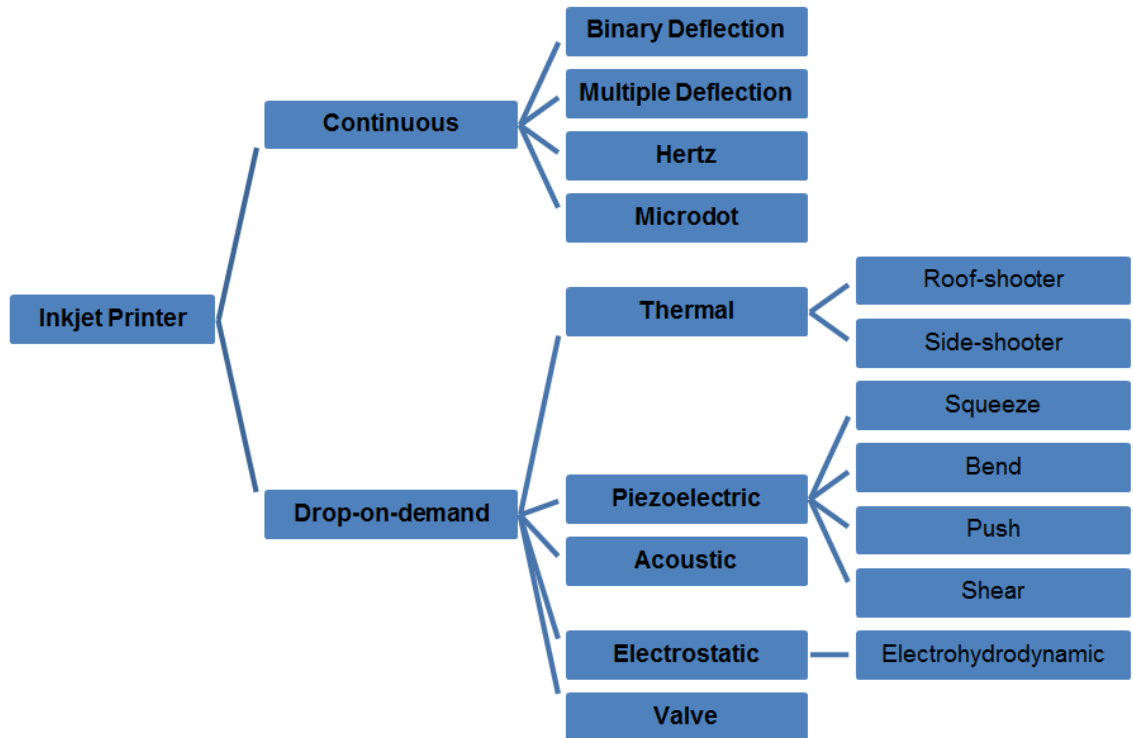
Figure 1-10 The classification of Inkjet printers based on the formation mechanisms of ink droplet [138, 141].

Continuous inkjet printer

Figure 1-11 shows the process of how CIJ printers generate droplets on the matrix [138, 140]. The continuous inkjet printer is named because its creation of ink droplets is constant. A high-pressure pump vibrating piezoelectric crystal nozzles is required to form ink droplets. Then the formed droplets are selectively charged through signals by the linked electrode. The images are formed by the uncharged droplets which are ejected onto the matrix; the gutter will collect the charged droplets for recirculation. The benefit of the CIJ printer is its high speed of printing. However, the disadvantage is the printing nozzles are easily blocked if the inks dry quickly. Hence, the inks must not dry too quickly and be chargeable.
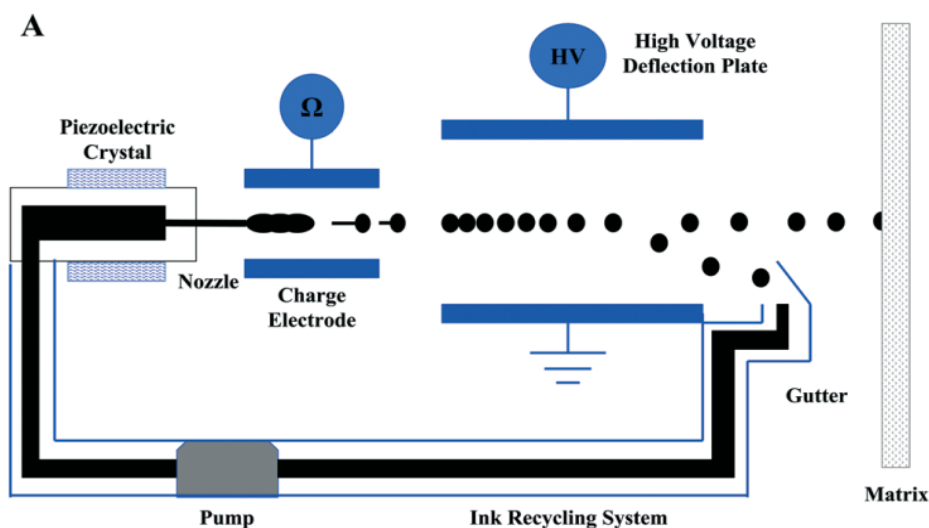
Figure 1-11 schematic images shows the typical structure of continuous inkjet printing [140].

Drop-on-demand (DOD) printer

In a DOD printer, the droplets eject only when they are required, and this is controlled by propagating a pressure pulse in an ink filled chamber. In contrast to CIJ printer, the DOD printer allows smaller droplets to be generated and higher position accuracy [142, 143]. As the formation of droplets by DOD printers relies on a pressure pulse, the subclasses of DOD printer are based on the methods about how they generate the pressure pulse (shown in **Figure 1-10**) [138, 141]. The thermal and piezoelectric methods are dominant in modern inkjet printing, electro hydrodynamic (EHD) is prominent, and the acoustic and valve are still in the development stage.

Thermal inkjet printer

The thermal inkjet printer which is also called bubble jet inkjet printer generates bubbles by heating up (high temperature 350 to 400 °C) the inks rapidly in the ink chamber to cause a pressure pulse. This pressure pulse pushes the ink droplets out through the nozzle (shown in **Figure 1-12** (a)).

When the ink droplets are ejected, the force which comes from the vapour bubble collapsing refills the ink chamber [138, 141].
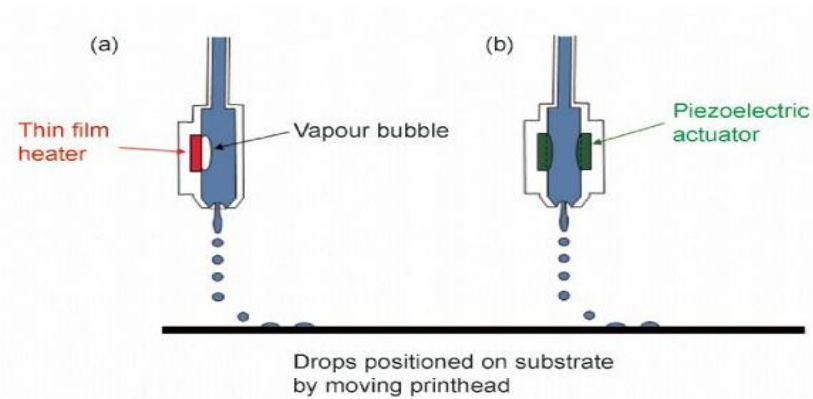
Figure 1-12 Schematic images illustrate a typical a) thermal and b) piezoelectric DOD inkjet printer [144].

Piezoelectric inkjet printer

The basic components of piezoelectric inkjet printer contain a piezo-ceramic plate, and an electric device. The DOD printers rely on the piezo-ceramic plate to create ink droplets. Normally, in order to protect the piezo-ceramic plate without being damaged by unintended reaction with inks, a thin diaphragm is bonded on it. The printing process is briefly described with the following steps: the electric device generates a pressure wave on the piezo-ceramic plate which causes the ink to be ejected from the nozzle. Then, as the droplets are ejected, the electric pulse is removed, which allows the piezo-ceramic plate to return to its normal shape and the ink is refilled (Shown in **Figure 1-12** (b)). Finally, the printing goes on by repeating the previous two steps. Based on the distortion of the piezo-ceramic plate, there are four main types of the DOD inkjet printers: squeeze, bend, push, and shear mode (**Figure 1-13**). **Figure 1-13**A shows the squeeze mode which comprises a radially polarized piezo-ceramic tube around the nozzle [138,

141]. In my research, the Jetlab IV printer was used and it belonged to the squeeze mode DOD inkjet printers.
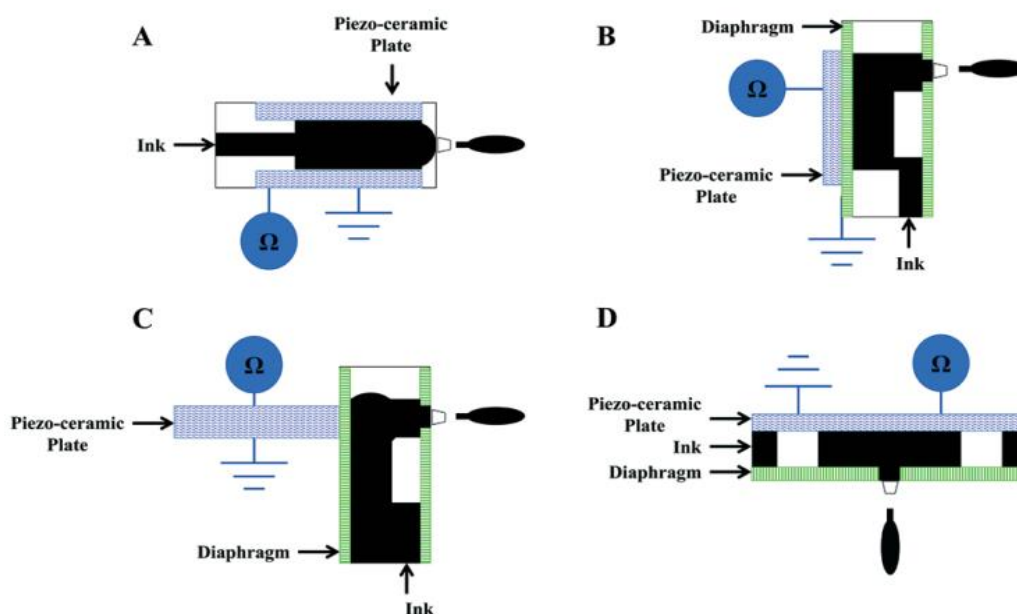
Figure 1-13 Schematic images show different types of DOD inkjet printers, A) squeeze mode, B) bend mode, C) push mode, and D) shear mode [138]. The squeeze mode contain the piezo-ceramic plate which is a tube shape. In the bend and push mode, the piezo-ceramic plate deformation and the direction of the electric field are in parallel. However, in the shear mode they are perpendicular to each other [138, 145].

1.4.2 Inkjet printing inks

The properties of Inkjet printing inks determine not only the printing quality but also what type of printing system is suitable for this ink. Normally, the inks contain two parts: base materials and additives [138, 146]. The base materials are the main components of the inks which control the characteristics of the formation of ink droplets. Normally, the base materials need to be dissolved in some solution including aqueous solutions, and non-aqueous solutions [138]. Many materials have been used in inkjet printing including synthetic materials (polymer [137, 147, 148], ceramics [144, 149, 150]), metal nanoparticle, and biomaterials (proteins, polysaccharide and algae).

The additives focus on stabilizing or adjusting the functional properties of the ink according to the requirements of different applications [151]. There are many different types of additives, such as colorants, viscosity modifiers, surfactants, humectants, chelating agents, biocides and so on. In this research, I used some surfactants (e.g. PEG_{400}), functional proteins (e.g. biotin, enzyme), and dye (e.g. ink blue).

1.4.3   Critical parameters for ink printability

In order to determine the printability of an ink, there are two main parts that should be considered: one is the rheological properties of the ink which shows the theoretical printability [151-157], another one is the type of printing system which determines the operative printability of the inks in the end. Generally, the most important physical properties to take into account are density (ρ), surface tension (γ), viscosity (η) and nozzle diameter (d) [152, 154, 155, 158]. According to the Navier-Stokes equation, these physical properties can be used to evaluate the inertial force, capillary force and viscous force for forming stable droplet by a number of dimensionless groupings of physical constants [151, 152]. The most useful constants are the Reynolds (Re), the Weber (We) and the inverse (Z) of the Ohnesorge (Oh) numbers (listed in Table 1-6).

Theoretical printability

The theoretical printability can be calculated from Reynolds number, Weber number, and Ohnesorge number (**Table 1-6**) [151-157]. Finally, the inverse of the Ohnesorge number called Z parameter is used to indicate printability. The earliest important work trying to understand the mechanisms of drop generation was reported by Fromm who identified the Oh and proposed that Z $>$ 2 for stable drop generation [158]. Then, Reis and Derby refined Z of the

printable solution to be in the range of 1 to 10 [152]. When Z is too low, viscous forces are dominant, which requires large pressure for ejection; contrary, if Z is too high a continuous column is ejected that can result in satellite droplets forming alongside the main drop. Later, Jang et al. [154] redefined the printable range as 14 ⩾ Z ⩾ 4 by considering characteristics such as position accuracy, maximum allowable jetting frequency, and single-drop formability. Jang et al. recognized that the lower limitation of Z is controlled by the dissipation of the pressure pulse by fluid viscosity, and the upper limit of Z is governed by the point at where a satellite forms instead of a single droplet.

However, several groups reported stable inkjet printing even for 4 > Z > 1 and Z < 14. Liu et al. illustrated that by adding extra negative pressure to Z > 14 inks, a single droplet with a double waveform can be produced and satellite droplets avoided [155].

Table 1-6 Typical fluidic parameters for ink drop ejection form piezoelectric inkjet print heads [159].

Dimensionless groupings of physical constants	Equations	Ref.
Reynolds number	$\mathrm{Re} = \dfrac{\rho v L}{\eta}$	[158] [152] [154] [155] [151] [160]
Weber number	$\mathrm{We} = \dfrac{v^2 \rho L}{\gamma}$	
Ohnesorge number	$\mathrm{Oh} = \dfrac{\sqrt{\mathrm{We}}}{\mathrm{Re}} = \dfrac{\eta}{\sqrt{\gamma \rho L}}$	
Z	$Z = \dfrac{1}{\mathrm{Oh}}$	
ρ= density of the fluid (kg/m-3); v = velocity (m s-1); γ = surface tension (N m-1); L = characteristic linear dimension (travelled length of the fluid) (m); η= dynamic viscosity of the fluid (Pa s or N s m-2 or kg (m s)-1)		

The printing system

In this research, a piezoelectric-based DOD inkjet printing process was utilized as the enabling method for building objects from ink droplets. The applications of these printed objects concentrated on drug delivery, tissue engineering and related biomedical area. So the ink materials should have good biocompatibility, good biodegradability, balanced remarkable mechanism properties, flexibility of modification, easy to sterilize, and mild productive process. However, most polymer materials only have some of these required properties. Thus, it is important to find a material which can meet most of the required properties. In this study, the regenerated *B. mori* fibroin solution is selected and used as the bio-ink for inkjet printer since it meets most of the requirements.

1.4.4   Applications of 3D printing RSF biomaterials

In 2014, Suntivich et al. demonstrated the use of inkjet printing method to fabricate silk 'nests' which hosted cells for prospective bio-sensing application [161]. **Figure 1-14** shows the schematic images of how they constructed silk multilayers nests by layer-by-layers inkjet printing and adjusting the pH of the silk-polylysine to pH 5.5 to form a stable structure. They printed a layer of silk-polylysine dots and then printed another layer of silk-polyglutamic acid dots on top of silk-polylysine dots at the same position to form the silk bilayer stabilized structure unit by ionic interactions. Then, they imprinted *E.coli* cells in the cell nests and cell cultured the silk nests which showed the cells were strictly confined by silk nests and successful encapsulation of *E. coli* cells without compromising cell shape or function.
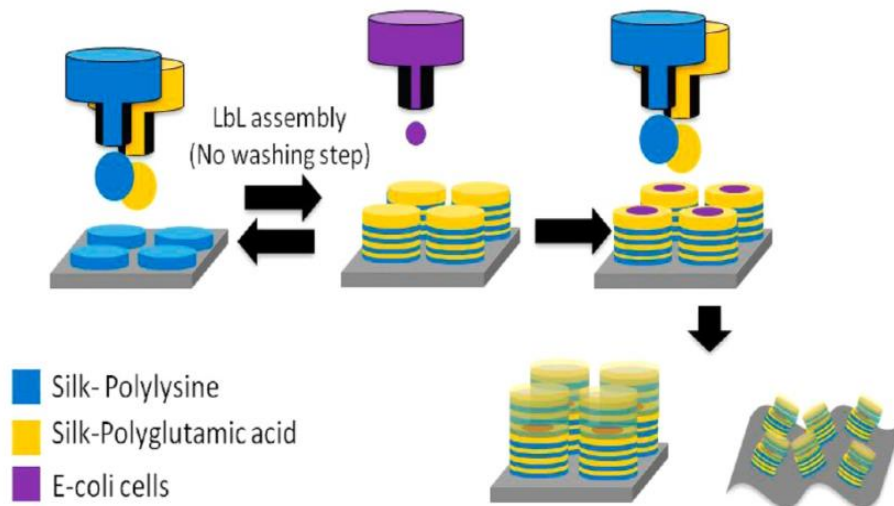
Figure 1-14 Schmeitic images of fabrication process of inkjet-assisted silk array for cell encapsulation [161].

In 2015, Tao et al. reported how to use inkjet printing technique printed regenerated silk fibroin, including printable forms and printable functions. A commercial inkjet printer (Dimatix DMP 2800, Santa Clara, CA, USA) was used in their research and focused on bio-printing functional silk inks (regenerated silk solutions by adding nanoparticles, enzymes, growth factors, antibiotics, and antibodies) to illustrate the versatility of Dimatix inkjet printing [153].

In 2016, my group published two papers, one demonstrated the preparation of regenerated silk fibroin scaffolds by reactive inkjet printing (JetLab IV) and analysed the biocompatibility of regenerated silk fibroin scaffolds by growth of fibroblast cells on their surface [38]. The other demonstrated inkjet printing micro-rockets which is described in my thesis Chapter 4 [162].

In 2017, Shi et al. demonstrated the fabrication of silk fibroin-gelatin scaffolds by using extrusion 3D printer (Einstart-S, Shining3D, China) to repair injured cartilage tissue (shown in **Figure 1-15**) [163].
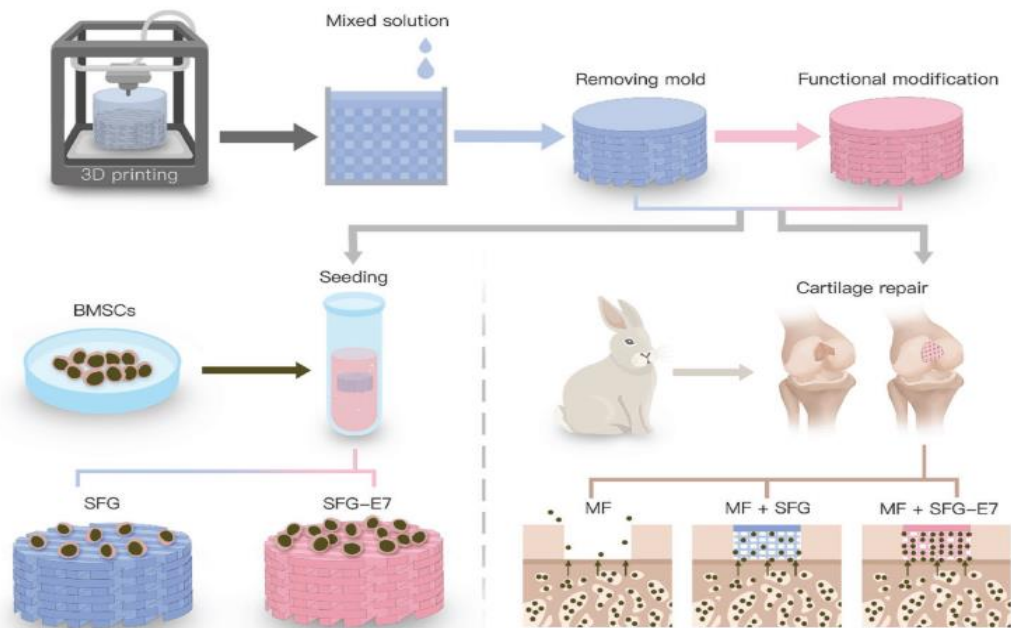
Figure 1-15 Schematic images illustrated the fabrication of functional silk fibroin-gelatin scaffolds and the growth of bone marrow mesenchymal stem cells (BMSCs) *in virto* and repair of injured cartilage tissue of rabaits *in vivo* [163].

1.5 Scope and objectives of thesis

The following schematic, **Figure 1-16**, give an overview of the swimmers that were made from the regenerated silk fibroin (RSF) material by inkjet printing via this thesis.

For the experiment chapters, Chapter 3 demonstrates the printability of RSF solution (inks) and how to design, fabricate and control the quality of the printed patterns. In Chapter 4, it firstly introduces how to generated self-propelled motors with RSF inks by inkjet printing. Secondly, this chapter discusses the characterization of RSF micro-rockets (shown in Figure 1-16A) and analyse their trajectory in fluids. Furthermore, it mentions about the optimization process of the printing process and guilds to fabricate other types of silk swimmers.

Chapter 5 mainly demonstrates how to control the trajectories of silk swimmers by controlling the movement mechanisms, the printing layers, and fuel concentration if fuels are required. ' ⌐ ' shape stirrers (shown in Figure 1-16B) were designed due to their central symmetry structure and they results in circular trajectory (the changing of the trajectory is convenient to be observed by analyse their rotation speed). One possible application of using the silk swimmers for bio-mixing is analysed in chapter as well.

The last experiment chapter, Chapter 6, demonstrates how to further control the trajectories by printing different structures of the silk 'wimmers'. The letters contains most of the different structure (axial symmetry, central symmetry and various irregular structures), so RSF letter swimmers are designed and printed in this chapter. Figure 1-15C shows the representative RSF Letters swimmers:

'NATURE' swimmers. The beads capture experiment in this chapter not only shows one possible application for silk 'swimmers', also demonstrates how to making functional swimmers by loading extra functional ingredients on them.
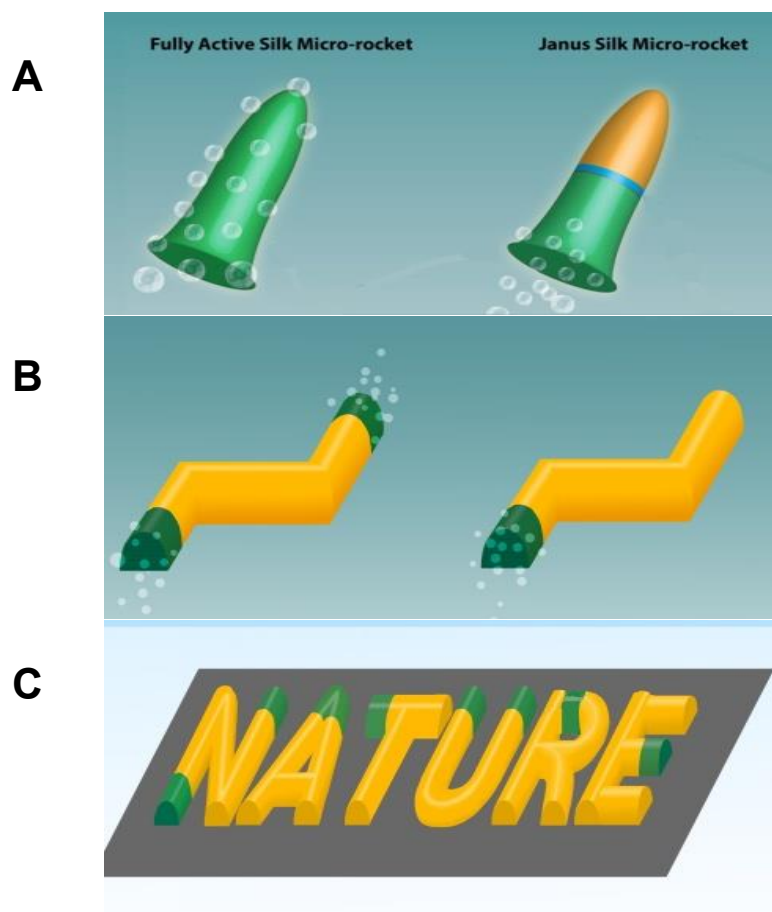
Figure 1-16 Self-propelled motors schematic overview: A) RSF micro-rockets, B) RSF stirrers, and C) RSF letters. Green represents RSF / PEG_{400} / Catalase inks and yellow reprsents RSF / PEG400 inks.

Chapter 2 Materials and Methods

2.1 Preparation Procedures of silk ink solution

Nature silk fibres are possible to be re-dissolved in some alkaline and acidic solutions. This property helps to reform the nature proteins according to different applications. The following procedures were used to make silk ink solutions (**Figure 2-1**)
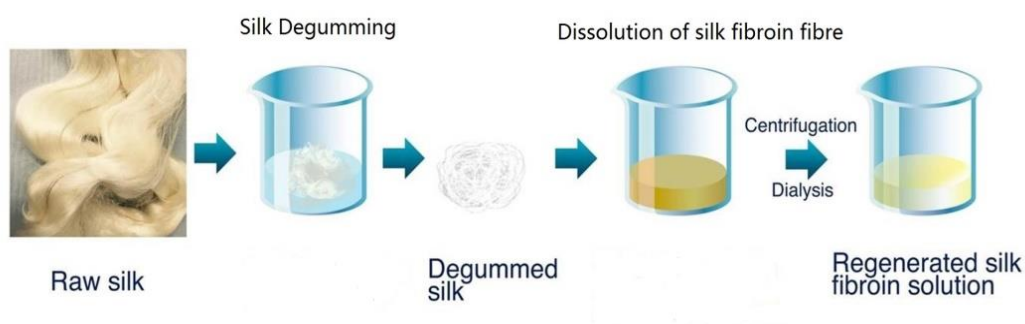
Figure 2-1 Preparation of RSF solution contains three main steps which are degumming, dissolving and dialysis.

2.1.1 Materials

Raw silk of *B. mori* was purchased from a silk reeling manufacturer in Suzhou, Jiangsu Province in China. All the experiment used the same single batch of the purchased silk. All other chemicals were obtained commercially at analytical grade. Ultrahigh quality water (Purelab UHQ, Vivendi Water System Ltd.) was used to prepare solutions.

2.1.2 Silk Degumming

Silk from bave of *B. mori* was degummed in order to remove sericin. Briefly, raw silk was added in boiling 0.02 M sodium carbonate (Na_2CO_3) solution for 30 minutes (10 mins, 60 mins, 90 mins or 120mins was selected depending on the experiment requirements). Then, the resulting silk materials were rinsed

with UHQ water until the solution was looked clear and dried in drying cabinet at 30 °C overnight.

2.1.3 Dissolution of silk fibroin fibre

The silk fibroin fibres are able to be dissolved in a few of alkaline/acid inorganic solutions such as lithium bromide (LiBr) solution, acid/$CaCl_2$ or $CaCl_2$/Ethanol/Water and organic solvent such as 1,1,1,3,3,3-hexafluoro-2-propanol (HFIP) [14, 53, 164-166]. In this thesis, Ajisawa's reagent and LiBr solution were selected due to their long lasting and green chemical process.

Dissolution of silk fibroin fibre with Ajisawa's reagent

The Ajisawa's method (this method used Ajisawa's reagent to dissolve silk fibroin (Figure **2-2**). A reagent mixed of $CaCl_2$ / Ethanol / Water = 1:2:8 molar ratios) was used to dissolve silk fibroin [167]. 1 g of the degummed fibroin was dissolved in 10 ml of the Ajisawa's reagent at 75 ^{o}C for 3 hours under mild stirring. The resulting SF solution was allowed to cool down and dialysed in UHQ water for approximately 5 days in 2 kDa molecular weight cutoff dialysis tubing at room temperature (22 ^{o}C) to remove the salts. Dialysis water was changed until the electric conductivity of the dialysis solution was in close proximity to the electric conductivity of UHQ water. Next, the dialysed SF solution was centrifuged at 10000 rpm for 15 mins. The clear solution was prepared for printing as bio-ink.

Dissolution of silk fibroin fibre with LiBr reagent

This method used 9.3 M lithium bromide (LiBr) instead of Ajisawa's reagent. 1 g of the degummed fibroin fibre was dissolved in 10 ml of 9.3 M LiBr reagent at

75 °C for 3 hours under mild stirring (Figure **2-2**). The following steps were as

the same as Ajisawa's method.
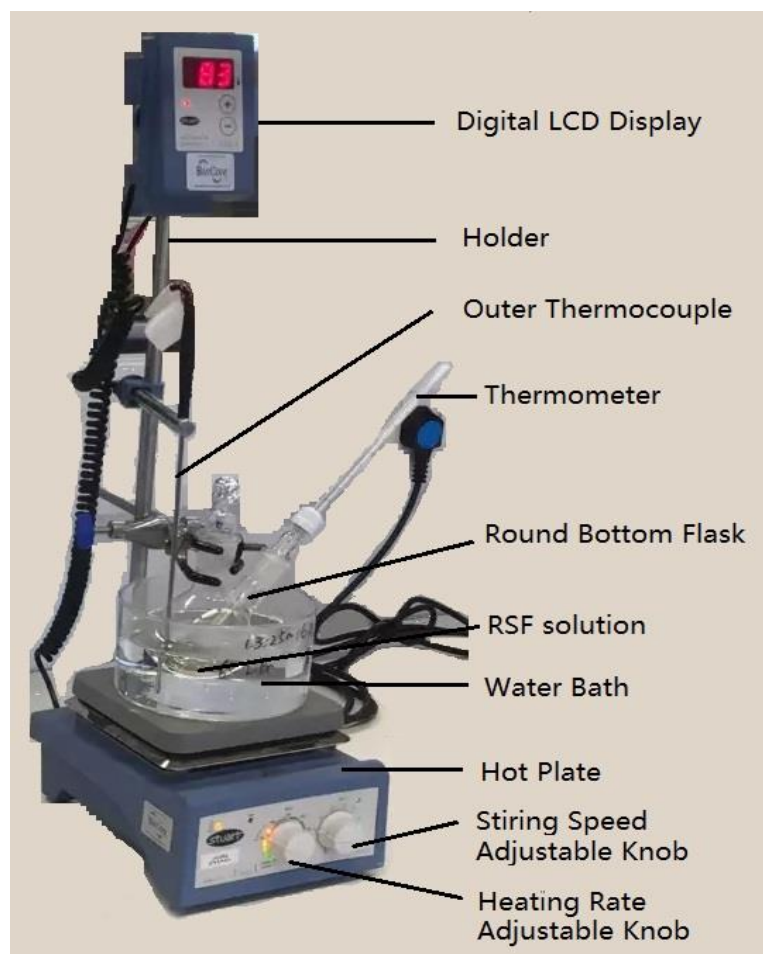
Figure 2-2 The setup of the system for silk fibroin dissolving process. The system consists of a hotplate (including temperature control system) and a water bath system.

2.2 Physical properties of ink analytical techniques

2.2.1 Viscosity

Overview

The viscosity of RSF solution was measured by Vibro Viscometer (SV-1A Vibro Viscometer, A&D Company, Limited, Japan). It adopts the sine-wave vibration technique (SV type) which provides high measurement accuracy. SV-1A was selected as it can measure a small amount of sample (2 ml), temperature and viscosity of fluid simultaneously, and very low to very high viscosity (from 0.3 mPa·s to 1000 mPa·s).

Viscosity

Viscosity, which is also called a viscosity coefficient, reflects the resistance to flow of a fluid and the resistance to the movement of an object through a fluid. It can be affected by temperature. The symbol η was used to represent viscosity. The Systeme International (SI) unit of viscosity is the Pascal-second (Pa·s).

The derivational process of the viscosity of fluid at a physics point is shown in **Figure 2-3**. Plate T is parallel to the fixed plate B and the distance between them is x_0. Plate T is moved parallel to plate B at a constant speed V_0, if the fluid between plate T and plate B is also moved parallel to plate B and has produced a steady flow, this is defined as Couette Flow.

As shown in **Figure 2-3** the velocity at a known distance x between plate B and plate T is V, they are in proportion. D is the slope of the straight line AB. It also equals to the increased quantity of the velocity per unit distance, so D is called a shear rate Eq. {2.1}.

$$D = \frac{V}{x} = \frac{dV}{dx}$$

{2.1}

The fluid layers at distance x and at distance x+dx move parallel to each other at speed V and V+ dV respectively. An internal frictional force develops between them because the velocities are different. The frictional force relied on the unit area of the plane parallel to the flow direction between plate T and plate B is termed as shear stress (τ). It is proportionate to shear stress D, where η stands for the constant,

$$\tau = \eta D$$

{2.2}

Eq. {2.2} represents Newton's law of viscosity. Proportional constant η is defined as viscosity.

$$\eta = \frac{\tau}{D}$$

{2.3}

The viscosity of the fluid at specific temperature is constant in proportion of shear stress. The fluid is called a Newtonian fluid. Otherwise, it is called non-Newtonian fluid.
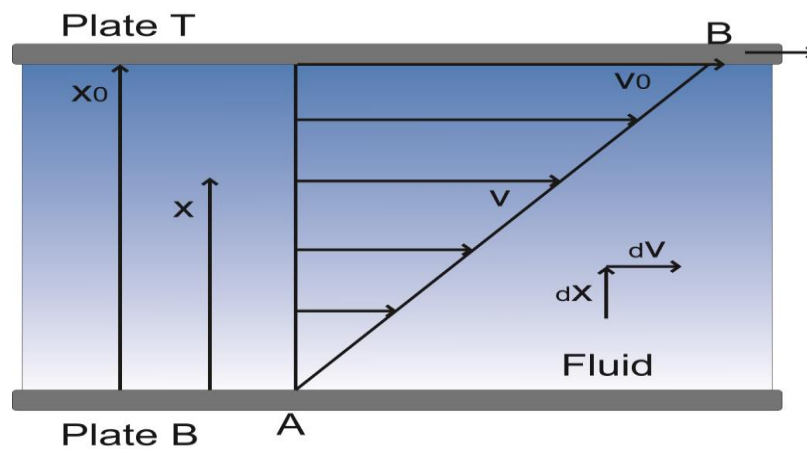
Figure 2-3 Deduce the viscosity of Newtonian Fluid (Couette flow) at a physics point.

Operating principle of viscometer

In **Figure 2-4**, two thin sensor plates in a tuning fork arrangement are driven with electromagnetic force to vibrate at their natural (resonant) frequency of 30 Hz within the sample fluid. Viscosity is then calculated based on the proportional relationship between the amount of electric current required to drive and maintain the sensor plates at constant vibration amplitude.
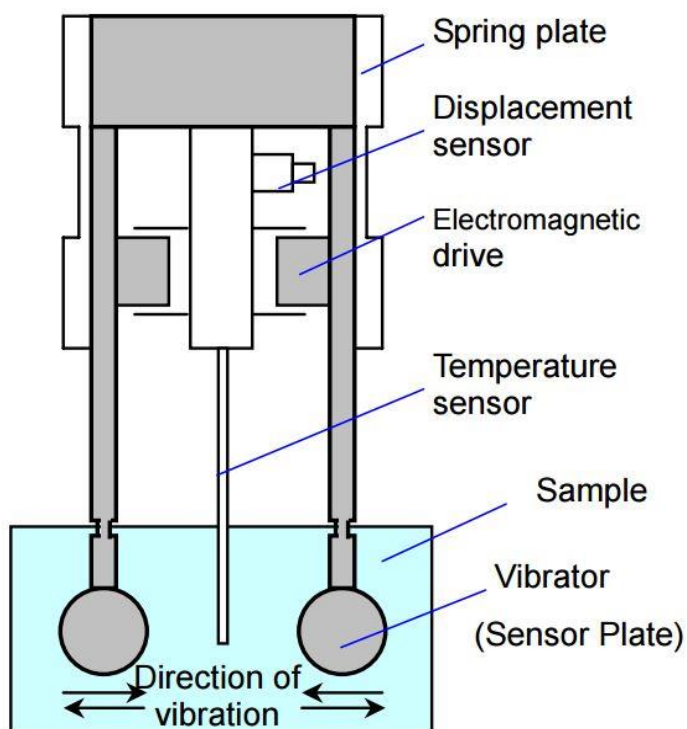
Figure 2-4 The structure of viscometer used in Vibro Viscometer (SV-1A). The method is recognized as a Japan industrial standard for viscosity measurement of liquids (JIS Z8803). The tuning fork Vibro Viscometer is also accredited as a standard device for the Japan Calibration Services System (JCSS) along with capillary and rotational viscometer.

Experimental procedures for Vibro Viscometer

The experiment procedures followed the general instruction. All the samples should be tested as same as the printing temperature, here it tested under room temperature (~20°C). 5 ml were prepared for each sample.

2.2.2 Surface tension

Surface tension

The elastic tendency of a fluid surface which is satisfied with the least and smoothest surface area is defined as surface tension. It is denoted by the symbol γ. It can be defined as Eq. {2.4}, where F_s is stretching force (N) and l is unit length (m). The SI unit is N/m.

$$\gamma = \frac{F_s}{l}$$

{2.4}

Surface tension is an advantage to organisms and nature. However, according to different applications, there exists a need to change the surface tension of fluid. For example, to remove dirt off from clothes, washing powder was used as surfactants to reduce the surface tension of water. Normally, changing temperature or adding impurities alters fluid's surface tension.

a) Temperature

The surface tension is affected by the temperature. As the temperature decreases, the surface tension increases. Water is an ideal fluid to show the relationship between surface tension and temperature (**Figure 2-5**).
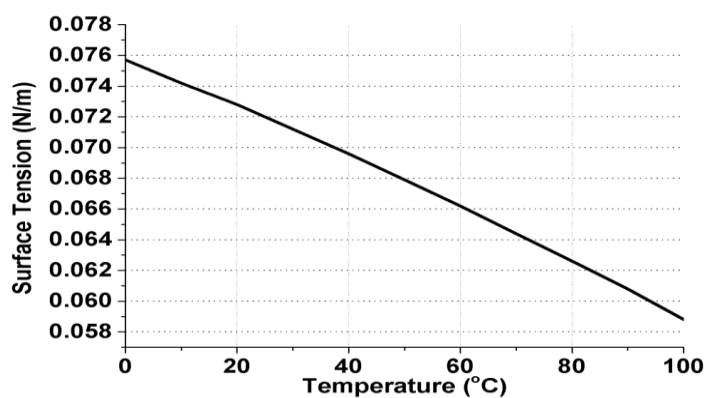
Figure 2-5 The diagram depicts the relationship between surface tension and temperature of water [168].

b) Impurities

The surface tension can be either increased or decreased by adding impurities. The higher solubility of a substance, for example, sodium chloride, will increase the surface tension, whereas a substance with low solubility, such as phenol, will decrease the surface tension [169].

Principles of surface tensiometer

The surface tension of different concentrations of RSF solution was measured by a Tensiometer (Tensiometer K11 Mk4 with Display Panel KB0803, KRÜSS GmbH, Hamburg) which shows in **Figure 2-6** Tensiometer consists of a high speed mobile sample stage and electronic balance and connected with display panel which shows the results of surface tension.
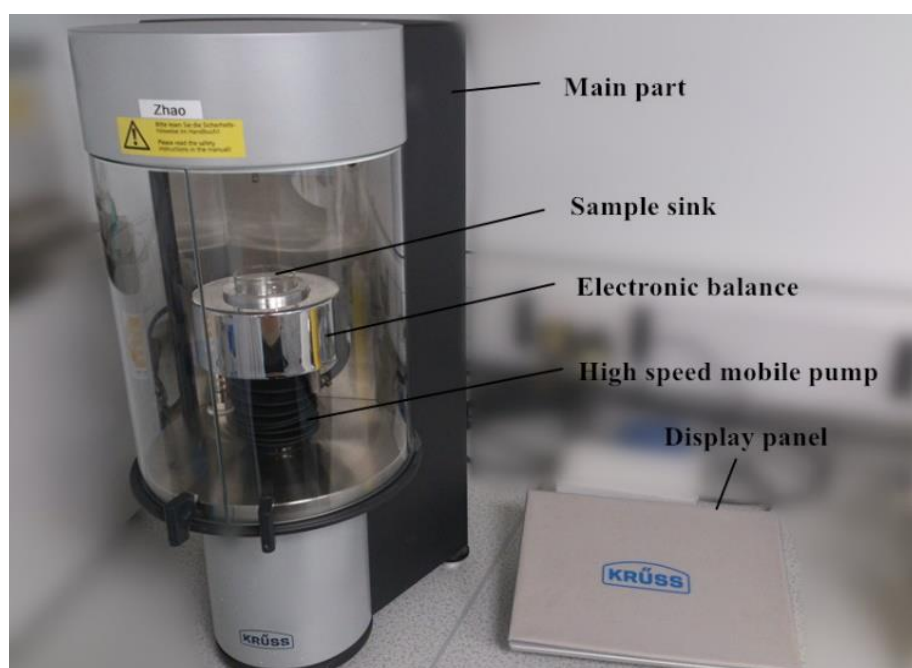
Figure 2-6 The setup of the KRUSS Force Tensiometer K11. This surface tensiometer consists of a high speed mobile sample stage and electronic balance and connected with display panel which shows the results of surface tension.

Wilhelmy plate method is used to test the surface tension of RSF solutions because no correction was required for the surface tension values. In this method, when a vertically suspended Wilhelmy platinum plate (**Table 2-1**) touches a liquid surface, then a force F (N) acts on this plate. Surface tension can be described using the following equation:

$$\gamma = \frac{F}{l \bullet cos\theta}$$

{2.5}

Where γ = Surface tension (mN/m)

F = Force, which is measured by a force sensor of the tensiometer (N)

l = Wetted length of the plate, which is equal to its perimeter (mm)

Table 2-1 Wilhelmy platinum plate (Krüss)

Probe name	Krüss Standard Plate
Width	19.9 mm
Height	10 mm
Depth	0.2 mm
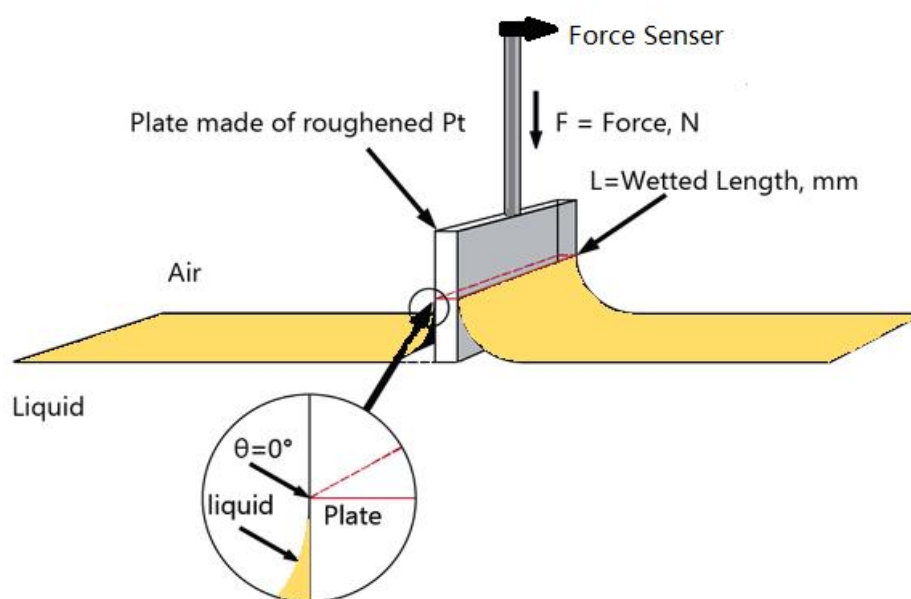
Figure 2-7 Schematic diagram of the Wilhelmy plate method.

Experimental procedures of surface tensiometer

The experiment followed the general instruction. Before the measurement, glass dish should be washed with 5% Decon90 detergent, then flushing with tap water, finally rinsing with DI water several times. The surface tension of the UHQ water was tested before testing each concentration to ensure no contamination would occur. The Wilhelmy plate should be washed and then dried using flame torch. When the sample solution was changed, the clean procedure should be repeated. 6-8 ml sample were prepared for each sample. The setting parameters of the tensiometer listed in Table 2-2 and kept constant throughout the experiment.

Table 2-2 Setting parameters for the tensiometer.

Maximum measuring time	7200 seconds
Number of Values	720
Data Acquisition mode	Linear
Values for mean	20
Standard Deviation	0.1 mN/m
Immersion Depth	2 mm
Surface Detection Speed	10 mm/min
Surface Detection Sensitivity	0.01 g
Ionization Time	0 s

2.2.3 Contact Angle

Principles

The angle which a liquid-vapor interface meets a solid surface is called contact angel (θ_c). The contact angle is calculated through Young-Laplace Equation as it plays the role of a boundary condition via the equation.

$$\gamma_{SG} - \gamma_{SL} - \gamma_{LG} \cos\theta_C = 0 \qquad \textbf{(Young's Equation)}$$

Where γ_{SG} = The solid-vapor interfacial energy

γ_{SL} = The solid-liquid interfacial energy

γ_{LG} = The liquid-vapor interfacial energy
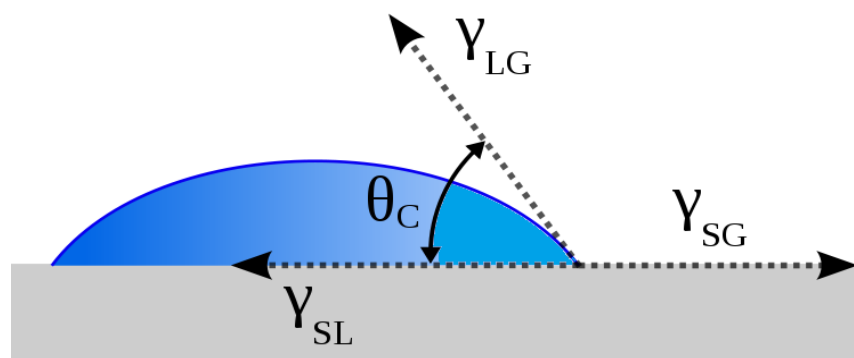
Figure 2-8 Schematic of a liquid drop showing the quantities in Young's equation.

In the case of using water as the liquid phase, measuring contact angle helps to determine the hydrophobicity / hydrophilicity of different material surfaces. The hydrophilic surfaces are those whose contact angles are below 90° and surfaces whose contact angles are above 90° are considered as hydrophobic [170]. If the contact angle is above 150°, the surface is determined as super-hydrophobic surface [171].
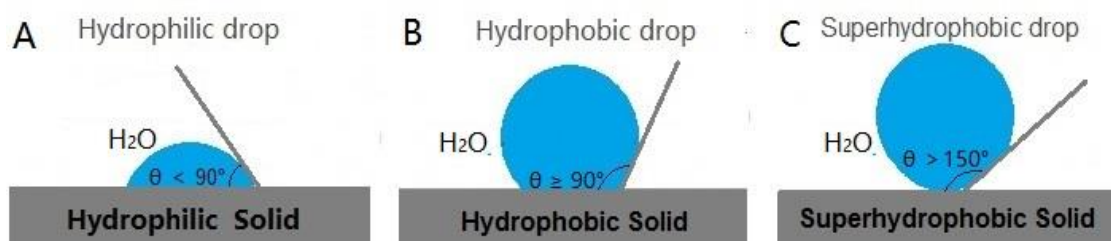
Figure 2-9 Schematic of the hydrophobicity / hydrophilicity of different solid surfaces. A) θ < 90°, hydrophilic surface; B) θ ≥ 90°, hydrophobic surfaces; C)θ > 150°, super-hydrophobic surface.

Experimental procedures

The static sessile drop method is used for the characterization of solid surface energies. The sessile drop contact angle is measured by a contact angle goniometer using an optical subsystem to capture the profile of a pure liquid on a solid substrate. The angle formed between the liquid-solid interface and the liquid-vapor interface is the contact angel. Currently, the sessile drop technique system employs high resolution cameras and software to capture and analyse the contact angle.
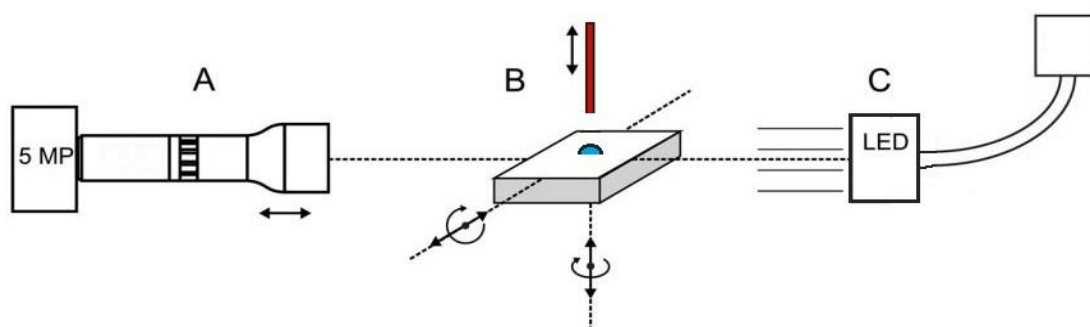
Figure 2-10 Experimental setup used for contact angle goniometry in this work [172]. Images are recorded through a high resolution telecentric objective (1.7×, adjustable aperture) fitted with a 5 MP monochrome CCD camera (A). The sample stage moves in xyz (B). The drop is suspended above the sample stage at an adjustable height. Illumination by the telecentric backlight illuminator (C) provides parallel illumination and improves image contrast and definition of object edges as compared to standard illumination.

2.3 Sample preparation techniques

2.3.1 Spin coating

Overview

Spin coating is a procedure used to deposit even, thin films or distribute substance on flat substrates. The machine which is used for spin coating is called a spin coater (or spin processor). In this experiment a spin coater (Laurell WS-400BZ-6NPP/LITE) was used.

General Theory

Spin coating involves the application of a film evenly across the surface of a substrate by coating a solution of the desired material (e.g. RSF or enzymes) in a solvent while it is rotating. When the spin coater was spinning (shown in **Figure 2-11**), the centrifugal force helped to spread the sample solution. The thickness of deposited films ranges from a few nm to a few μm.
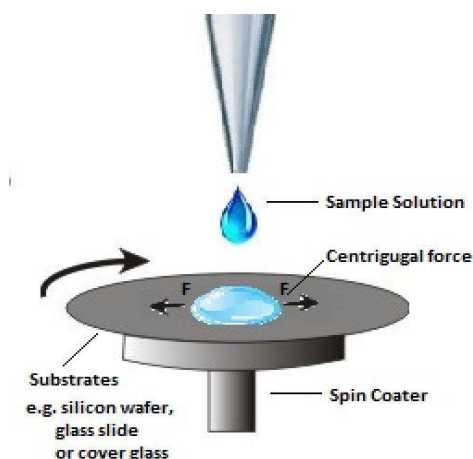
Figure 2-11 Schematic of the spin coating theory.

Figure 2-12 illustrates the general process of a spin coating. Firstly, using pipette adds a small amount of sample solutions onto the centre of the substrate at low speed or no spinning (Figure 2-12A). Then substrate is rotated at high speed and most of solution is flung off the side (Figure 2-12B). That

means the centrifugal force together with the surface tension of the solution pulls the solution coating into an even covering. The higher the speed of rotating, the thinner the film is. Figure 2-12C shows the solvent is evaporated and the desired material is left. Finally, the solvent of the solution fully dries and the thin film is formed by the leaving desired molecules on the surface (Figure 2-12D).
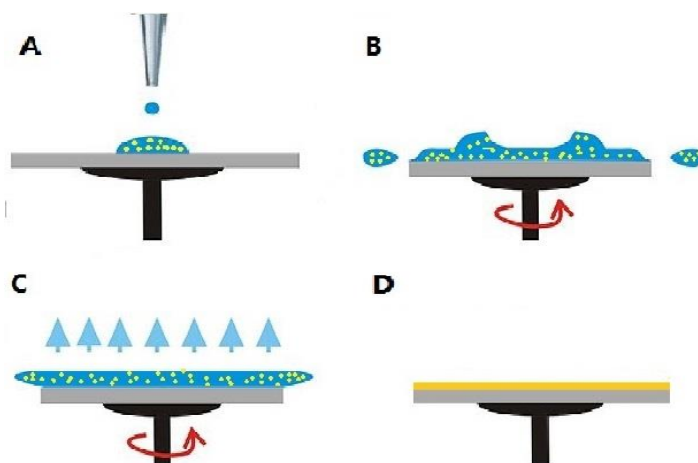
Figure 2-12 Schematic of the spin coating process. A) Add sample solution, B) rotation, c) evaporation and d) fully dry.

2.3.2 Inkjet printing

Overview

The Jetlab IV print station (**Figure 2-13**) manufactured by MicroFab Technologies, Inc. which used for drop-on-demand (DOD) laboratory application. It relies on piezoelectric method to generate pressure pulse to form ink droplets. The Jetlab II printer station is digitally controlled by the software MicroFab (TECHNOLOGIES INC. Plano, Texas, USA). The software digitally controls ejection of droplets on predetermined position when it is required [142].
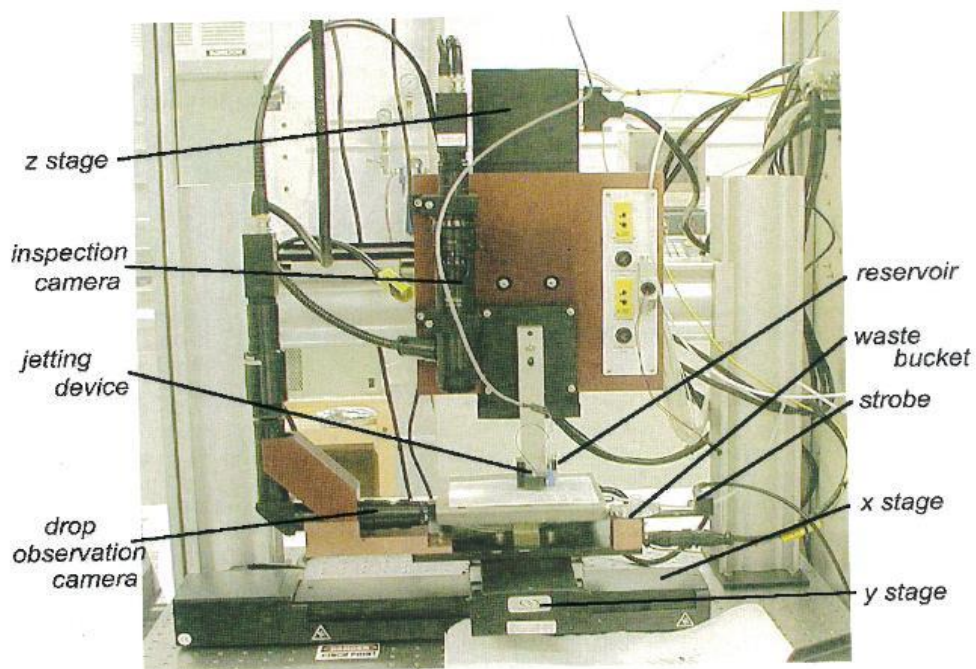
Figure 2-13 Overview of a jetlab II print station, including the x, y, and z stages, inspection and observation camera, jetting device, ink reservoirs and waste bucket.

Principles of inkjet printer

DOD piezoelectric inkjet printer provides the ability to produced three dimensional (3D) scaffolds because those scaffolds are formed by printing a liquid precursor (ink) drop on substrates layer by layer. The print station (**Figure 2-13**) mainly consists of MicroJet^{TM} jetting devices, two or more motion stages and cameras. MicroFab (TECHNOLOGIES INC. Plano, Texas, USA) was used as JetLab control program. This software digitally controls the JetLab print station especially jetting device through selecting suitable electric pulse.

Ink-jet microdispenser

The piezoelectric inkjet printer relies on piezoelectric material deforming to create droplets. The deformation is based on electric pulse which is controlled by MicroFab program. The electric pulse generates a pressure wave that

results in the ink being ejected out of the printer head. When the electric pulse is removed, the ink will be filled into the glass tube. Then, the piezoelectric material plate returns to its original shape (shown in **Figure 2-14**) [138].
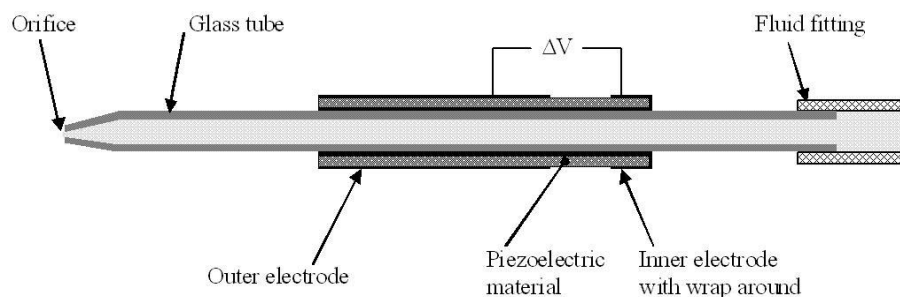
Figure 2-14 The structure of ink-jet micro-dispenser. The printer-head consists of piezoelectric devices, glass tube (orifice) and electrodes.

Effect of pressure wave on the formation of printed RSF droplets

As described in chapter 1, functional printed patterns are formed by the deposition of stable and single droplets. Apart from the physical properties of RSF inks，the formation of droplets are also affected by the mechanical actuation of the ink chamber. In a piezoelectric DOD print head, the droplets are controlled by a pressure wave to form a pulse which is used to fire jetting devices. There are five times for "Rise", "Dwell", "Fall", "Echo", and "Final rise", and three voltage levels "Idle", "Dwell" and "Echo" in adjusting the pulse shape as illustrated in **Figure 2-15**. Adjusting these parameters ultimately decides the shape of the inkjet printing droplets, and then the quality of the droplets demonstrates whether the used solution is printable inks for inkjet printer.
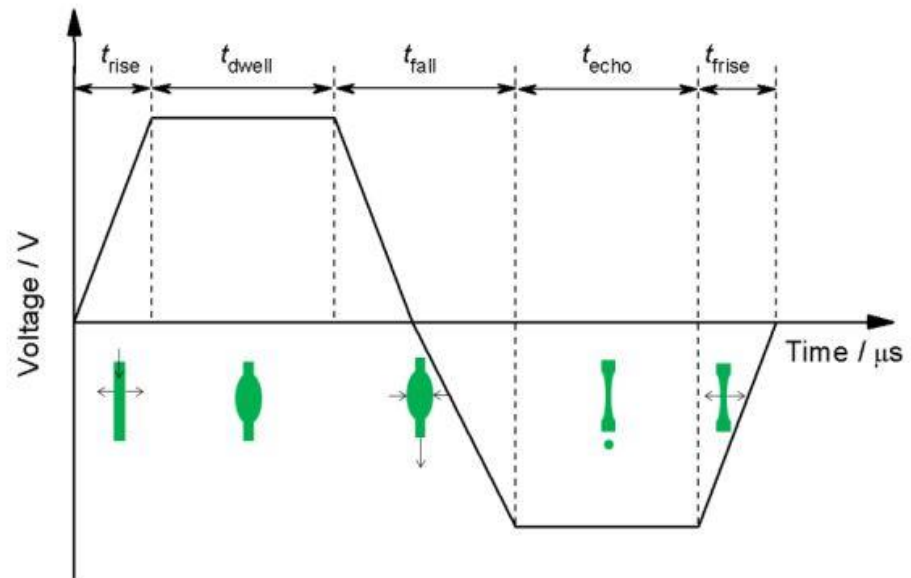
Figure 2-15 A typical pressure wave pulse generated in piezoelectric DOD print head and the droplet formation process.

Experimental procedures for inkjet printer

The experiment process followed general instruction. The printing parameters were adjusted based on the used inks. The printing patterns controlled by the scripts.

2.4 Characterizations of printed samples

2.4.1 Microscopy

Most of my experimental samples cannot be seen with naked eyes, so microscopy plays an important role in my studies. Microscopy is the technique which magnifies images of small samples. In this research, it helped to observe the morphology of inkjet printing micro-samples and record the micro-rockets routes by linking the microscopes with Charged Coupled Device (CCD) cameras.

2.4.2 Optical microscopy

Overview

The optical microscope is also called light microscope. It uses visible light and a system of lenses to magnify images of tiny substance on a stage. Microscope (Nikon ECLIPSE LV150, Japan) was used in my studies, shown in **Figure 2-16**.
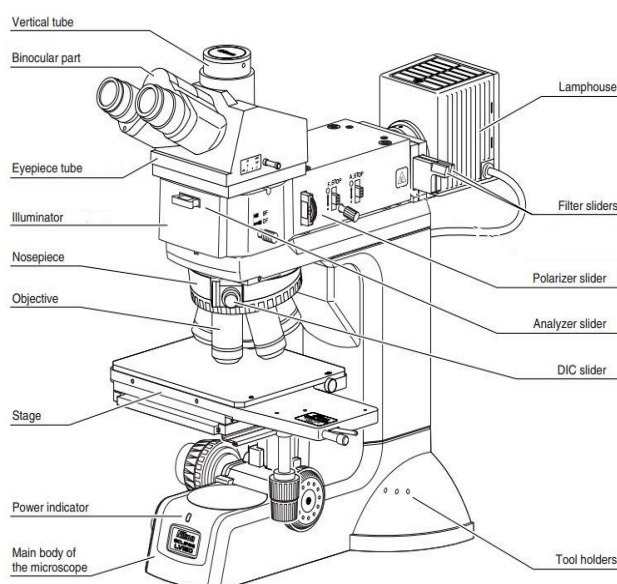
Figure 2-16 Schematic of Nikon ECLIPSE LV150A microscope with Digital Eclipse Camera system (online open right images).

Principles

There are two basic types of light microscopes which are simple microscopes and compound microscopes. The used Nikon microscope (**Figure 2-17**) is a compound microscope which consists of an objective lens, a focus lens, an ocular lens, visible lights and linked with CCD camera for capturing images. The magnified images of objects are created by an objective lens, and those images are further magnified by an ocular lens (the eyepiece) for viewing. The final magnification is calculated as the product of the magnifying power of the objective lens times the magnifying power of the eyepiece.
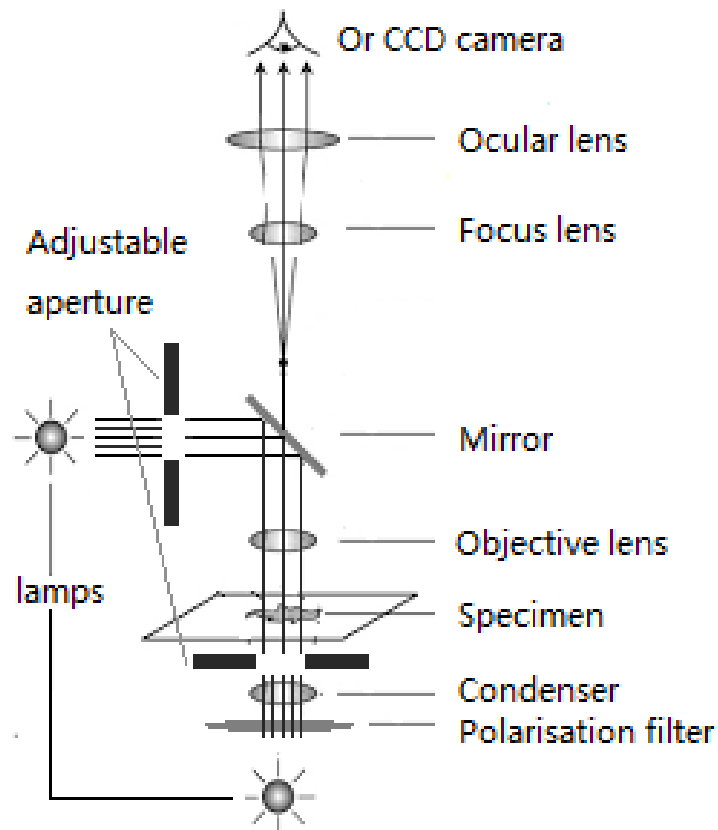
Figure 2-17 Schematic of an optical mircroscope with 2 lamps, above one for reflective lighting and below one for transmitted illumination (the image was drawn by Yu Zhang, based on the principle of optical microscope).

2.4.3 Fluorescence Microscopy

Overview

Fluorescence is a physical phenomenon which organic and inorganic specimens can absorb and subsequent re-radiate light. A fluorescence microscope is an optical microscope that uses fluorescence and phosphorescence instead of visible light to analyse the properties of fluorescence marked specimens.

Principles

The specimen is illuminated with light of a specific wavelength which is absorbed by the fluorophores, causing them to emit light of longer wavelengths. The illumination light is separated from the much weaker emitted fluorescence through the use of a spectral emission filter. Typical components of a fluorescence microscope are a light source, and the emission filter. The filters and the dichroic beam-splitter are chosen to match the spectral excitation and emission characteristics of the fluorophore used to mark the sample. In this manner, the distribution of a single fluorophore is imaged at a time. Multi-color images of several types of fluorophores must be composed by combining several single-color images.

The majority of fluorescence microscopes, especially those used in the life sciences is of the epifluorescence design shown in the **Figure 2-18**. Light of the excitation wavelength is focused on the specimen through the objective lens. The fluorescence emitted by the specimen is focused to the detector by the same objective that is used for the excitation which for greater resolution will need objective lens with higher numerical aperture. Since most of the excitation light is transmitted through the specimen, only reflected

excitatory light reaches the objective together with the emitted light and the epifluorescence method therefore gives a high signal-to-noise ratio. The dichroic beam-splitter acts as a wavelength specific filter, transmitting fluoresced light through to the eyepiece or detector, but reflecting any remaining excitation light back towards the source.
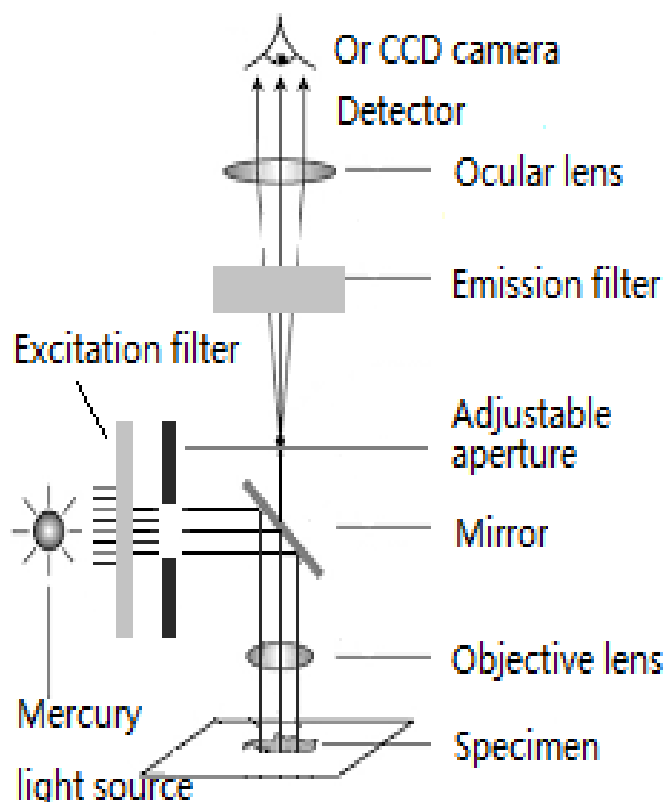
Figure 2-18 Schematic of fluorescence microscope (drawn by Yu Zhang, based on the principle of fluorescence microscope).

Experimental procedures

In my research, the fluorescence microscope was used for showing the enzyme distribution in micro-rockets. Fluorescein isothiocyanate (FITC) was used to label catalase. The excitation wavelength of FITC is range from 467-498 nm while the emission wavelength of FITC is from 513 nm to 556 nm. The related emission filter set was selected and used in Nikon ECLIPSE LA150A microscope.

2.4.4 Atomic Force Microscopy

Overview

Atomic force microscopy (AFM) is one kind of scanning probe microscopes (SPMs) which are designed to measure local properties (height, friction or magnetism) with a probe [173, 174]. AFM provides a 3D profile of the surface with a very high resolution on the order of fractions of a nanometre, more than 1000 times better than the optical diffraction limit. Thus, the AFM has the advantage of imaging almost any type of surfaces, including polymers, ceramics, composites, glass and biological samples.

Principles

The AFM relies on the forces between a sharp probe (<10 nm) and surface at very short distance (0.2~10 nm probe-sample separation)[173]. The force is not measured directly, but calculated by the stiffness of the cantilever. This force can be described using Hooke's Law:

$$F = -kz \qquad \{2.6\}$$

where F = The force,

k = the stiffness of the cantilever (spring constant of cantilever)

z = the distance the cantilever is bent

If the spring constant of cantilever (typically 0.1~1 N/m) is less than surface, the cantilever bends and the deflection is monitored.

AFM has a feedback loop using the laser deflection to control the force and probe position. **Figure 2-19** presents the typical configuration of AFM. A semiconductor diode laser is reflected off the back of a cantilever with a sharp

tip and detected by a photodiode detector. This detector measures and calculates the bending of cantilever when the probe is scanned over the sample surface and export a map of the surface topography.
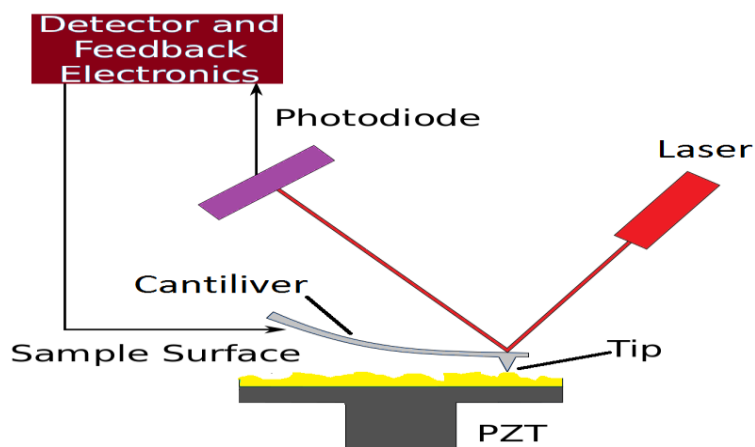
Figure 2-19 Typical configuration of an atomic force microscope (drawn by yu zhang, based on the principle of AFM).

The AFM can be operated in three modes, depending on the force-distance curve of AFM (**Figure 2-20**) and the related application.

a) Contact mode: when the stiffness of cantilever is less than surface, the cantilever bends. Tip is hard contact with the surface. The red curve in **Figure 2-20** shows the repulsive regime. By maintaining a constant cantilever deflection, the force between the probe and the sample remains constant and an image of the surface is obtained. It is fast and can be used in friction analysis. The disadvantage is that it may damage/deform soft samples. However, imaging in liquids often resolves this issue.

b) Tapping mode: The imaging is similar to contact mode. However, in this mode the cantilever is oscillated at its resonant frequency. The blue curve (**Figure 2-20**) shows the force range of this mode which is called

attractive regime. In this range the tip lightly 'taps' on the sample surface during scanning, contacting the surface at the bottom of its swing. By maintaining constant oscillation amplitude, a constant tip-sample interaction is maintained and an image of the surface is obtained. This mode allows high resolution of samples that are easily damaged (e.g. biological samples). The disadvantage is that it is slower and more challenging to image in liquids compared with contact mode.

c) Non-contact Mode: The probe is far from the sample surface and there is no deflection. The black curve (**Figure 2-20**) shows the force range of this mode. The probe does not contact the sample surface, but oscillate above the adsorbed fluid layer on the surface during scanning. The surface topography can be measured due to attractive Van Der Waals forces. The advantage is that it exerts very low force on the sample. However, it has lower resolution and pollutant on the surface can interfere with oscillation. Normally this mode needs an ultra-high vacuum environment to have best imaging
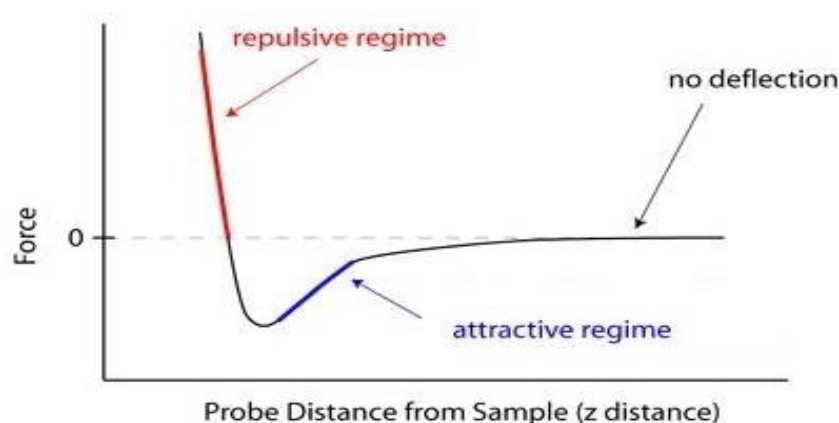
Figure 2-20 Force-distance curve for AFM. Red curve shows tip is in hard contact with the furfae; repulsive regime. Blue curve shows tip is pulled toward the surface;attractive regime. Black curve shows tip is far from the surface;no deflection.

Experiment procedures

Surface analysis of spin coating RSF films was performed in tapping mode using a Nanoscope IIIa (Digital Instruments, USA) with a oxide-sharpened Si3N4 tip mounted on a triangular cantilever with spring constant of 0.58 N/m (specified by the manufacturer). Images were taken in air and flattened and plane fitted as required. Roughness and section data were analysed using the software Nanoscope.

2.4.5 Interferometry (optical profiler)

Overview

Optical profiler is also known as a white light interferometer. It can measure surface texture and shape from nanometer-scale roughness to millimetre-scale step heights. In this project, 3D optical microscope (ContourGT-K, Brucker, USA) was used to measure the morphology and the height of inkjet printing samples. It exhibits the high speed, good accuracy, high precision and low noise. Contour GT-K installed NanoLens^{TM} module and specific Vision64^{TM} productivity software.

Principles of optical profiler

Optical interference profiling uses the wave properties of light to compare the optical path difference between a test surface and a reference surface.

A white light beam is split into two half, one half of the beam is reflected from a test material and the other half of the split beam is reflected from the reference mirror. When the distance from the beam splitter to the reference mirror is the same as the beam splitter is from the test surface and the two half beams are recombined, destructive and constructive interference occurs in the combined beam wherever the length of the light beams vary. The light and dark bands

occur on the images (**Figure 2-21**). This phenomenon is known as interference fringes. As the reference mirror is close to perfect flatness, the optical path differences are due to height variances in the test surface. Then, the interference beam is focused into a digital camera. The installed software can calculate height difference across a surface when the wavelength is known.
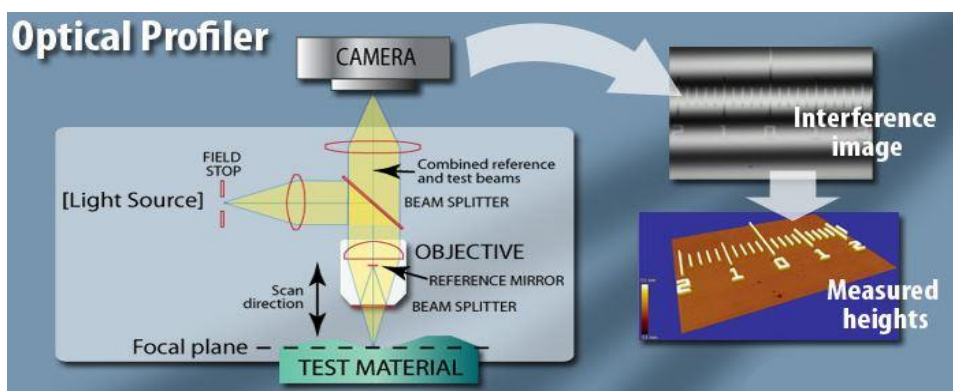
Figure 2-21 Schematic diagram of optical profiler (online open right image).

Experimental procedures for optical profiler

Experiment process followed the general instruction. In order to avoid the inverted images which were produced by protuberant printed patterns on the smooth glass slides and silicon wafers, all the printed samples were coated with gold by sputter coater.

2.4.6 Fourier transform infrared spectroscopy (FTIR)

Overview

Fourier transform infrared spectroscopy (FTIR) is a sensitive technique used to identify organic (and in some cases inorganic) chemicals. FTIR spectrometers are widely used in organic synthesis, polymer science, petrochemical engineering, pharmaceutical industry and food analysis. It also can be used to investigate the mechanism of chemical reaction and detect unstable substances due to FTIR spectrometers can be hyphenated to chromatography.

In this research, IRPrestige-21 Shimadzu FTIR Spectrophotometer was used to identify some chemical functional groups such as amide I and amide II which prove the existence of silk I and silk II structure [2].

Principle

The basic components of an FTIR spectrometer include a light source, interferometer, sample compartment, amplifier, detector, analog-to-digital (A/D) convertor, and a computer. The source radiation passes the sample by the interferometer and reaches the detector. Then the amplifier amplifies the signal (which is produced by the detector) and A/D convertor converts that signal to digital signal. Finally, the digital signal is transferred to a computer in which Fourier transform is calculated. The process shows in **Figure 2-22**.
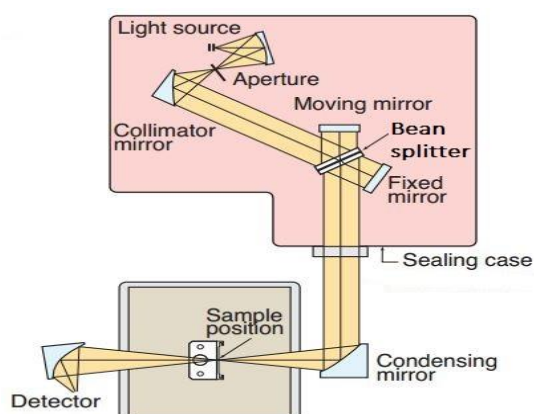
Figure 2-22 Schematic diagram of IRPrestige-21 Shimadzu FTIR Spectrophotometer

Experimental procedures

RSF solutions were used to form films by spin coater on silicon wafer. Some of the samples were immersed into ethanol for seconds. All of samples were dried in oven at 30 ℃ overnight. Then these samples were measured by FTIR Spectrophotometer (IRPrestige-21, Shimadzu, Japan). Absorption spectra in the range 1750-1400 cm^{-1} were acquired on amide I and amide II structure by an accumulation of 64 scans with a resolution of 2 cm^{-1} [175].

2.5 Mathematical techniques used to characterise propulsion systems

This thesis investigates two different types of propulsion mechanisms, namely catalytically powered bubble propulsion and surface tension gradient powered. It is important to characterize their motion using various mathematical approaches. In this section, the concepts of the mathematical methods which have been used throughout this work are explained and will be referenced accordingly.

2.5.1 Self-propelled swimmers

It is important to understand the type of motion for a particle. If the particles are moving on their own (e.g. via chemical reaction, surface tension gradient) rather than simply undergoing Brownian motion, diffusion or other flow phenomena, it is called self-propelled particles. The diffusion coefficient (D_0) of spherical particles in a liquid is given by Eq. {2.7}:

$$D_0 = \frac{k_B T}{(6\pi\eta R)} M^0$$

{2.7}

Where, k_B = the Boltzmann constant; T = the absolute temperature ; R = the radius of the particle; η = the viscosity of solution; M^0 = a unit tensor of 3 × 3 elements; this is also known as the Stokes-Einstein diffusion coefficient for the particular particle [176].

Particles rotate randomly, where the amount of rotation relies on the size of the particle. This random rotation is named as the rotational diffusion (t_R^{-1}), which is shown in Eq. {2.8}) for spherical particles.

$$t_R^{-1} = \frac{k_B T}{\left(8 \rho h R^3\right)} \qquad \{2.8\}$$

For these equations to deem it is necessary that the diffusion is not inhibited by forces closing to a solid interface, even though it is for particles that are in a bulk solution. In the case of particles that are near a wall, a corrected diffusion equation D_H has to be used [177], which is given by Eq. {2.9}, where M^0 is replaced by M^H which is the hindered diffusion tensor and is given by Eq. {2.10}, where Λ described by Eq. {2.11} and h means the distance of the particle from the wall [178].

$$D_H = \frac{k_B T}{\left(6\pi\eta R\right)} M^H \qquad \{2.9\}$$

$$M^H = \left(1 - \frac{9}{16}\Lambda + \frac{1}{8}\Lambda^3 - \frac{45}{256}\Lambda^4 - \frac{1}{16}\Lambda^5\right)^{-1} \qquad \{2.10\}$$

$$\Lambda = \frac{R}{R+h} \qquad \{2.11\}$$

2.5.2 Trajectory analysis of swimmers

In this thesis, printed RSF swimmers resembled a rod-like structure (chapter 4) and special structure ('└┐' shape in chapter 5, or different letters shape in Chapter 6), were tracked on both their extreme points (called dual point tracking) in ImageJ by using a manual tracking plugin [179].

The dual point tracking allowed determination of the direction and orientational changes of the self-propelled swimmers during their motion. The angle of travelling and the angle of orientation were calculated for every frame of the videos. A custom built LabVIEW program (written by Dr David Gregory) was used to calculate the changing of the angles. This tracking software was

initially designed and programmed by Dr J.R. Howse and Dr S. Ebbens [180].

In Chapter 4, the rockets swimmers were manually tracked and the analysing

of the changing angles shown in Figure 2-23. For swimmers in Chapter 5 and

Chapter 6, the special shaped RSF-swimmers were manually selected in a

rectangular frame and two tracked points were at the middle point of the

shorter side (dual point tracking) show in Figure 2-24.
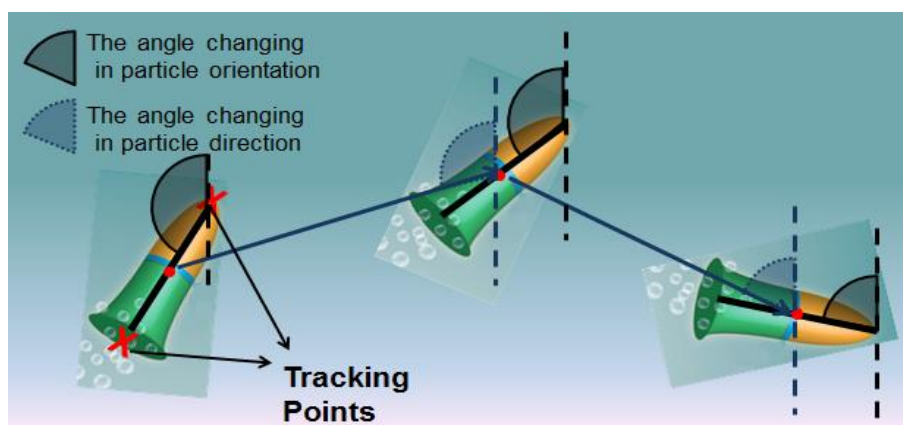
Figure 2-23 Schematic showing the angles to calculate the orientation dependence of the swimmers, manually selected the extreme two point.
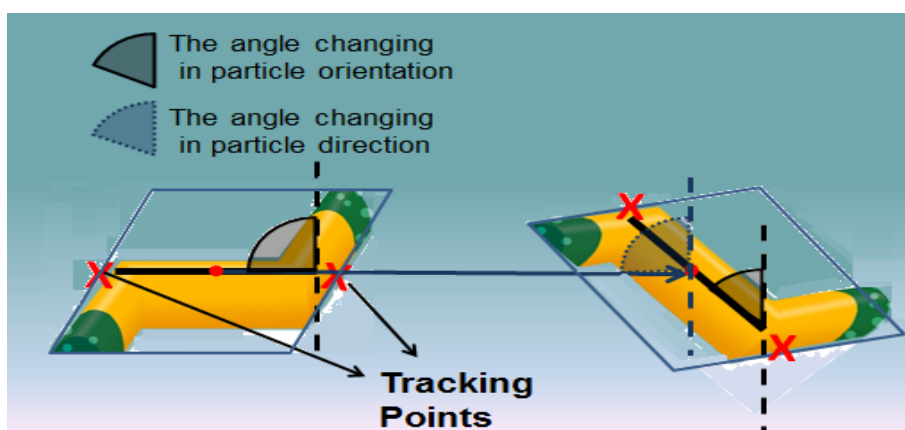
Figure 2-24 Schematic showing the angles to calculated the orientiation dependence of the swimmers, mamually selected a rectangular frame for special shape swimmers.

2.5.3 Persistence length

Persistence length is one method that used to quantitatively characterize

trajectories of the bubble-propelled swimmers[181]. Basically, persistence

length is used as a measure of the stiffness or bending properties of a polymer chain. The persistence length L_P illustrated the distance along a set of chain segments where the correlation of the angle θ between segment vectors is lost, for example, a linear set of chain segments results in a larger L_p than a set of chain segments showing loops or curves [182, 183]. Furthermore, without normalisation persistence length will reflect both directionality and velocity.

The trajectories of bubble-propelled swimmers are able to be considered a chain of vectors. Persistence length for each trajectory (between every frame) was calculated by first computing the average cosine angle ($cos\theta$) between vectors at all segment distances L along the chain.

Figure 2-25 shows that by superimposing vectors at position j on the vector at starting position i and calculating $cos\theta$ ($j \geq i$ and i represents all starting positions along the chain). Eq. {2.12} shows the 2D trajectories a plot of ($cos\theta$) against separation distance $L = \Delta L(j - i)$ [181].

$$(\cos \theta) = e^{-(L/2L_P)}$$
{2.12}
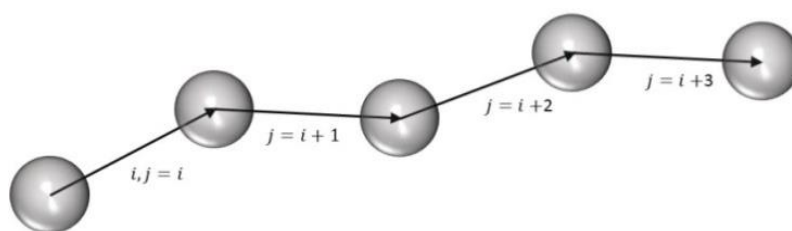
Figure 2-25 Schametic demonsting LP calculating for assuming the bubble propelled swimmer trajectories as a chain of vectors. LP is found by calculating the average $cos\,\theta$ between the starting vector at position i and the superimposed vectors at position j, for all separation distances $L = \Delta L(j - i)$ along the chain and all starting positions i. [181]

The chain conformation is related on the relationship between L (L$_c$) and L$_p$ (shown in Figure 2-26). When L$_p$ >> L$_c$, it means a linear set of chain. When L$_p$

~ L_c, the chain shows a curve or loop track. When $L_p \ll L_c$, it means the chain is flexible [184].
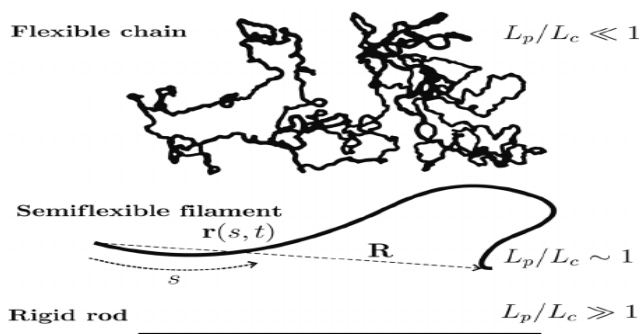
Figure 2-26 Chain conformation depends on persistence length L_p and contour length L_c [184].

2.5.4 Mean squared radius of Gyration

Mean squared radius of gyration, $R_g{}^2$ calculates the average mean squared distance of each point on a trajectory from a defined central fixed point. It reflects how compact, or spread out in space a given trajectory segment is. In this thesis, $R_g{}^2$ was calculated by using Eq. {2.13} which is similar to the definition used for polymer chain analysis.

$$R_g^2 = \frac{1}{N}\sum_{i=1}^{N}\left(r_i - r_{mean}\right)^2$$

{2.13}

2.5.5 Trimmed mean (Data analysis)

A trimmed mean is a calculation of averaging that removes a small designated percentage of the largest and smallest values before calculating the mean (a standard arithmetic averaging formula). It helps remove the influence of data point on the tails that may unfairly affect the traditional mean. The average data from the trajectories of swimmers analysed in this thesis, using trimmed mean (removing 0.05% of both largest and smallest values) to calculate the mean value.

Chapter 3 Optimizing Printing

Parameters for Silk Fibroin Inks

3.1   Introduction

The increasing morbidity and the limited supply of donors require tissue engineering (TE) as a treatment of organ failures [20, 185]. The TE method involves regenerating tissues within suitable scaffolds with the aim of transplanting the artificial structured tissues to the target site. These constructed scaffolds require high biocompatibility, tailorable biodegradability and good mechanical properties. Materials like metals, polymers, and ceramics, are widely used to fabricate these scaffolds [186]. Among these materials, a natural biomaterial, regenerated silk fibroin (RSF), is of interest because of its water-based preparation process and remarkable properties such as good biocompatibility, tailorable biodegradability and good mechanical properties [2, 3, 20, 38, 82, 159, 187-189].

With the development of novel approaches for biomaterial fabrication, TE scaffolds are more convenient to be built up than before. In the past three decades, electrospinning was used to fabricate fibrous TE scaffolds.[64] However, electrospinning has a number of fundamental problems remaining unsolved, such as the suitable viscosity of the solution for spinning process still cannot be controlled.[64] Nowadays, inkjet printing has emerged as the most attractive direct patterning technique for versatile designs. It is convenient to fabricate tissue scaffolds as it is fully digitally driven with a computer.[138]

Using *Bombyx mori* (*B. mori*) silk as the base biomaterials, an RSF aqueous solution was developed and used as an ink for inkjet printing (mentioned in section 1.4). Here, reactive inkjet printing (RIJ) was employed for the first time, which included a chemical treatment using methanol, in order to ensure a rigid

detachable silk scaffold was formed. RIJ is a method of allowing two different ink solutions to react together to generate a new compound, or alternatively to produce a change in the silk fibroin polymorphic form. The key property of the ink is its ability to form single droplets. Thus, this chapter explores the physical characterisation of a regenerated silk fibroin (RSF) solution with the purpose of controlling solution quality and investigates of the use of the RSF solutions as new bio-inks. The quality of RSF solutions was controlled by adjusting its preparation process such as controlling degummed time and dissolve time, and selecting the suitable solvent (Ajisawa's reagent or 0.02M LiBr solution), by the physical properties of the inks themselves and by adjusting the printing parameters.

Furthermore, this chapter demonstrates the printability of the RSF inks and optimizing printing conditions of RSF bio-ink through establishing the relationships between RSF peptide concentrations, number of printing layers and the total thickness of the printed patterns. Various patterns such as dot arrays, lines, films, particles and complex logos, for example 'SHEFFIELD ENGINEERING', have been fabricated. Last but not least, the printability of RSF inks is the fundamental for this thesis.

3.2   Experimental Methods

3.2.1 Materials

The details of the used materials were described in Chapter 2 Section 2.1.1.

3.2.2 Silk Degumming

The silk degumming process was described in Chapter 2 Section 2.1.2.

3.2.3 Preparation of Regenerated Silk Fibroin Solution

The preparation of RSF solution was described in Chapter 2 Section 2.1.3.

The RSF solutions prepared from silk fibres exposed to 5, 10, 30, 60, 90, and 120 min degumming times were dissolved in Ajisawa's reagent (A reagent mixture of $CaCl_2$ / Ethanol / Water = 1:2:8 molar ratios) and 9.3 M aqueous LiBr separately. The temperature was 75 °C for 3 hours. The stock RSF solution was diluted to the following concentration: 0.1 mg/ml, 1 mg/ml, 10 mg/ml, 30 mg/ml, and 50 mg/ml. For following measurements, the pH of the solution was controlled at 7.0 ± 0.5 after each dilution by using a small amount of NaOH or HCl.

3.2.4 Sodium Dodecyl Sulfate Polyacrylamide Gel Electrophoresis (SDS-PAGE)

Samples of silk prepared using varied degumming times (5, 10, 30, 60, 90 or 120 min) were analysed by SDS-PAGE using 6% Tris-acetate precast gels and

Tris-acetate running buffer. 20 micrograms of protein per well were run as denaturing, reduced samples according to the manufacturer's instructions (200 V constant for 3 h). Separated proteins were detected with Colloidal Blue staining according to the manufacturer's instructions. The molecular weight was estimated from unstained protein standard. All SDS-PAGE gel materials were prepared.

3.2.5 Surface Tension Measurements

Surface tension (mN/m) of RSF solutions were measured at 20 °C using surface tensiometer (Tensiometer K11 Mk4 with Display Panel KB0803, KRÜSS GmbH, Hamburg) according to the manufacturer's instructions. Each solution was measured triplicate (n=3). Details were described in Chapter 2 Section 2.2.2.

3.2.6 Viscosity Measurements

Dynamic viscosity (mPa·s) of RSF solutions were measured at 20 °C using Vibro Viscometer (SV-1A Vibro Viscometer, A&D Company, Limited, Japan) according to the manufacturer's instructions. For each solution, three samples were made (N=3). Details steps were described in Chapter 2 Section 2.2.1.

3.2.7 Contact Angle Measurement

The extracted form of a sessile drop was measured by a contact angle measuring system which is described in Chapter 2 Section 2.2.3.

3.2.8 Inkjet Printing process

A drop-on-demand (DOD) Inkjet printer (MicroFab IV, MicroFab Inc., USA) as shown in Chapter 2 Section 2.2.5 was used to conduct the printing work. A piezoelectric print-head with a 60 µm diameter orifice (MicroFab Inc., USA) was used for printing the RSF solutions. All methanol and RSF/deionised water (Di-water) solutions were printed using a low temperature jet and print-head. The Inkjet printing process was described in Chapter 2 Section 2.3.2.

3.2.9 FTIR analysis

Beta-sheet crystal content was measured according to FTIR ((IRPrestige-21, Shimadzu, Japan)), which is described in Chapter 2 Section 2.4.6.. Briefly, 10mg/ml RSF solutions were spin coated on silicon wafers and air dried for 18 hours. To induce beta-sheet crystallization, the RSF films were treated by spin coating a layer of methanol on top and then air dried.

3.2.10 Optical Profiler (Contour GT)

The details of the used materials were described in Chapter 2 Section 2.4.5.

3.3   Results and Discussion

3.3.1 Physical characterisation of Regenerated Silk Fibroin Solution

Normally, the printability of a ink depends on their physical characterisation (including molecular weight, viscosity, surface tension and concentration) and the setting of printing parameters. This section mainly analyse the physical characterisation of RSF solution and build up the RSF solution data base which supports the choice of the printing RSF inks for the further work.

3.3.1.1 Effect of Degumming Time on Silk Fibroin yield

As described in Chapter 1 Section 1.2.1, silk fibres are composed of the core fibroin fibres coated with a kind of glue-like protein called sericin. The core fibroin fibres contain a light chain (about 26 kDa) and heavy chain (about 390 kDa) which are present in a 1:1 ratio and linked by a single disulphide bond [2, 3, 15]. The coated sericin is a family of hydrophilic proteins which was removed by degumming in this study. **Figure 3-1** shows the effect of various degumming time (5, 10, 30, 60, 90 and 120 minutes) on the weight yield of silk fibroin by using 0.02 M Na_2CO_3 degumming solution. It is known that sericin is account for twenty-five to thirty percent of the total mass of silk fibers [3, 6]. Eq. {3-1} shows how to calculate weight yield of silk fibroin, where P_y is the mass percentage of degummed silk to raw silk; W_D is the weight of degummed silk (g); W_R is the weight of the raw silk fibers (g).

$$P_{yield} = \frac{W_D}{W_R} \times 100\%. \qquad \{3\text{-}1\}$$

Figure 3-1 shows that most of the sericin (~ 25 % of the mass of raw silk fibres) was removed within 5 minutes. Then, the results indicate that increasing degumming time from 5 to 120 minutes resulted in a decrease of

the yield weight percentage of silk fibroin. Furthermore, the decrease was not

sharp and the yield percentage of fibroin was within 70% to 75%. It also means

that boiled 0.02 M Na_2CO_3 solutions mainly removes sericin. This result is

consistent with the results which were published by Kaplan et al. [3, 6]. The

influences of different degumming time on printing experiments still need

further tests to justify (See section 3.3.2).
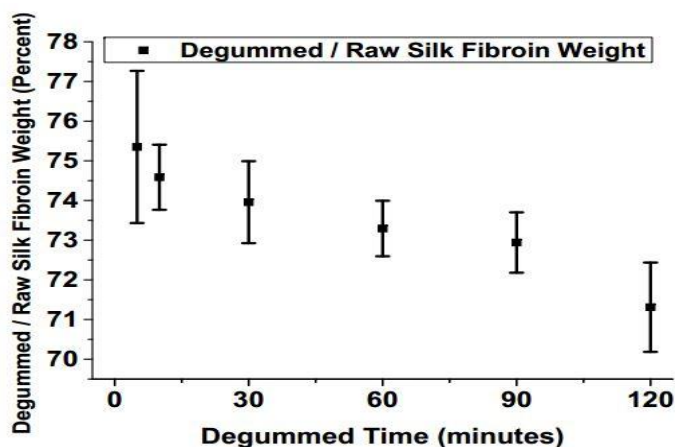
Figure 3-1 Effect of degummed time on weight change of silk fibre. The weight change showed by the ratio of the weight of degummed silk fibre to the weight of raw silk fibre. N > 10, error bars represent standard deviation.

3.3.1.2 Effect of Degumming and dissolution Methods RSF Molecular Weight (MW)

In Figure 3-2, the images show the regenerated silk fibroin (RSF) solutions

which were made from different degummed time silk fibres by Ajisawa's

method (Figure 3-2A) and 9.3 M aqueous LiBr (Figure 3-2B). All RSF solution

samples were centrifuged under the speed of 12,000 rpm by a centrifuge

(Biofuge fresco, Germany) before poured in to 5ml transparent vials. From left

to right, the vials were filled with 2 ml RSF solutions with degumming time from

10, 30, 60, 90, and 120 minutes, respectively. The macroscopic difference of

the effect of various degumming time and dissolved methods on RSF solutions

were the transparency. For Ajisawa's' method, **Figure 3-2**-A shows that the longer degumming time is, the clearer the RSF solution would be. For LiBr solution, it also shows the difference of transparency of RSF solutions on different degummed time but not as clear as those solutions which are dissolved by Ajisawa's solution. Furthermore, by comparing the same degummed time RSF solutions with different dissolved methods, RSF solutions which were dissolved in 9.3 M aqueous LiBr are more transparent than the solutions which were dissolved in Ajisawa's reagent. In general, the results indicate that both degumming time and dissolving methods influence the gelation time of RSF solutions. The gelation time directly demonstrated how long the RSF inks can be store in the fridge. However, the printing tests are required to justify which RSF solution is suitable for printing. By comparing the same printed pattern samples can guide which RSF solution is good for printing.
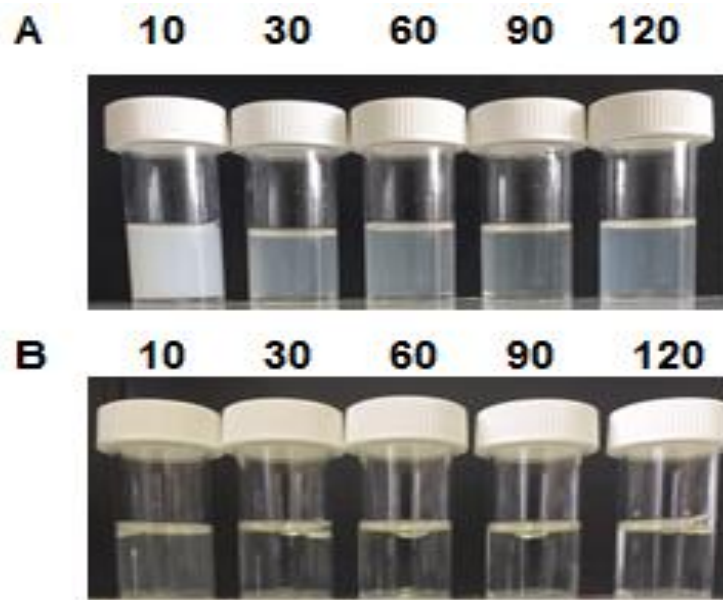
Figure 3-2 Image of regenerated silk fibroin solutions which were made from different degummed time silk fibroin fibres by A) Ajisawa's method; B) 9.3 M LiBr reagent. From left to right tubes were RSF solutions made from 10, 30, 60, 90 and 120 min degumming silk fibres.

3.3.1.3 Effect of degumming time on molecular weight of RSF solutions

This section explores how the degumming time and different dissolving reagents influence on the molecular weight of the RSF solutions. In order to determine the molecular weight (MW) of RSF, SDS-PAGE analysis was used. Figure 3-3 show the SDS-PAGE analysis of various degumming time (5,10,30,60,and 90 minutes) of RSF solution with Ajisawa's dissolved solution (A reagent mixed of $CaCl_2$ / Ethanol / Water = 1:2:8 molar ratios); **Figure 3-4** show the SDS-PAGE analysis of various degumming time (10,30,60, 90 and 120 minutes) of RSF solution with 9.3 M LiBr solution. In general, differences in degumming time in 0.02 M Na_2CO_3 resulted in the changes in electrophoretic mobility. SDS-PAGE results showed that each protein samples existed as a smear and that as degumming time increased, the smear moved down the gel.

For Ajisawa's dissolved solution (shown in **Figure 3-3**), silk degummed for 5 and 10 min had a molecular weight distribution from 100 kDa up to over 250 kDa, 30 min degumming produced silk with a broad molecular weight distribution from about 75 kDa to 260 kDa. The majority of the silk protein produced by the 60 min degumming time was less than 250kDa and the 90 min degumming time produced silk proteins that were predominantly 37 kDa to 150 kDa range. For LiBr dissolving solution, Figure 3-4 shows that silk degummed for 10 min had a molecular weight distribution predominantly in over 150 kDa range, 30 min degumming produced silk with a distribution over 100 kDa. The majority of the silk proteins produced by the 60 degumming time was over 75 kDa. Silk degummed for 90 min had a molecular weight

distribution in the 250 kDA to 50 kDa, 120 min degumming produced silk with a broad molecular weight distribution ranging all the standards. Here，no 5 min degummed results as sample solution changed to gel during the running process. Compared to the MW which has been determined by Wray et al. [190], the results shown in **Figure 3-4** are close to their data. The difference may be caused by the different SDS-PEGA system and source of silk (provided by different company). Both works confirmed that treating silk fibroin under the heated alkaline aqueous conditions encountered during degumming impacts the molecular weight [164, 190, 191]. The arrow line in Figure 3-4 help to demonstrate the trend of the changing of MW with different degumming times.
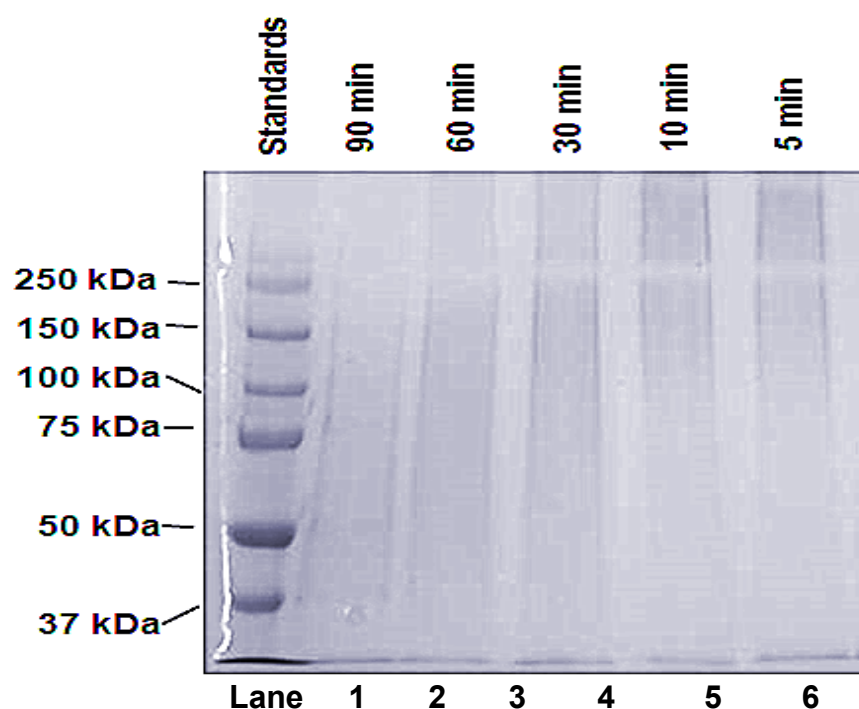
Figure 3-3 SDS-PAGE analysis of silk subjected to various degumming times and stained with colloidal blue. Each solution repeat 9 times (N=9), the representative image shows Lane 1: Mark; Lane 2: silk degummed for 90 min; Lane 3: silk degummed for 60 min; Lane 4: silk degummed for 30 min; Lane 5: degummed for 10 min; Lane 6: degummed for 5 min.
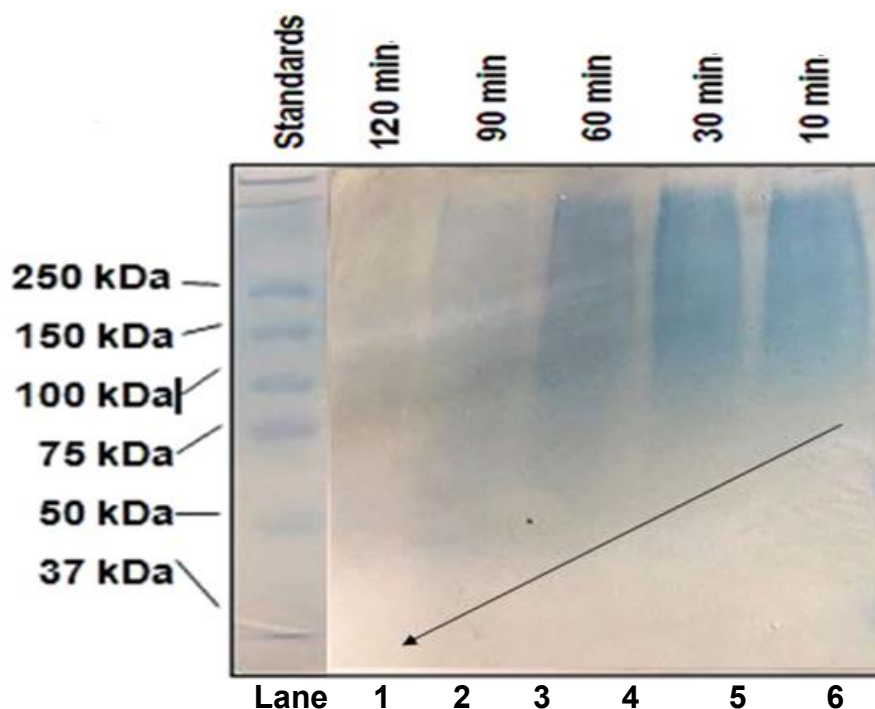
Figure 3-4 SDS-PAGE analysis of silk subjected to various degumming times and stained with colloidal blue. Each solution repeat 9 times (N=9), the representative image shows Lane 1: Mark; Lane 2: silk degummed for 10 min; Lane 3: silk degummed for 30 min; Lane 4: silk degummed for 60 min; Lane 5: degummed for 90 min; Lane 6: degummed for 120 min.

3.3.1.4 Effect of Degumming Time on the Regenerated Silk Solution Surface Tension

Surface tension for aqueous silk solution prepared from silk fibres exposed to variedly degumming times are shown in Figure 3-5 and Figure 3-6. The degumming times are 10, 30, 60, 90, and 120min and the concentration of RSF solutions are controlled as follows: 0.1, 1, 10, 30, and 50 mg/ml.

Figure 3-5 shows surface tension of RSF solutions which were dissolved in Ajisawa's reagent (CaCl$_2$-RSF solutions). With increased protein concentration, decreased surface tension appears. There was a significantly decrease in surface tension of CaCl$_2$-RSF solutions at concentration between 0.1 and 1 mg/ml. The surface tensions of CaCl$_2$-RSF solutions indistinctively decreased with increased concentration from 10 mg/ml to 50 mg/ml. However,

the relationship between surface tension of CaCl$_2$-RSF solutions and degumming times is not clear, suggesting the different degumming durations have a little influence on surface tension of RSF solution while the concentration is the main parameter affecting the surface tension.

Figure 3-6 shows surface tension of RSF solutions which were dissolved in LiBr reagent (LiBr-RSF solutions). The surface tension decreased with increased concentration. There was a dramatic decrease in surface tension of LiBr-RSF solutions at concentration between 0.1 and 1 mg/ml as well. However, for 10 min degumming time, the surface tension at 10 mg/ml is considerably higher than would be expected, the large error bar suggest it is an operation mistake.

Overall, surface tension of aqueous RSF solutions was mainly affected by concentration. For both types of dissolution methods, the surface tension decreased with increased concentration. According to the trend line, the surface tension value will remain in the range from 43 mN/m to 45 mN/m rather than slight decrease when continuously increase concentration over 20 mg/ml. The relationship between surface tension and degumming durations are not clear which means degumming time are not mainly affect parameter for surface tension of RSF solutions. Comparing surface tension values in Figure 3-5 and Figure 3-6, RSF solutions which were made from two different dissolutions (Ajisawa's reagent or 9.3 M aqueous LiBr) had similar values. It means that those two dissolutions do not effect on surface tension value of RSF solutions.
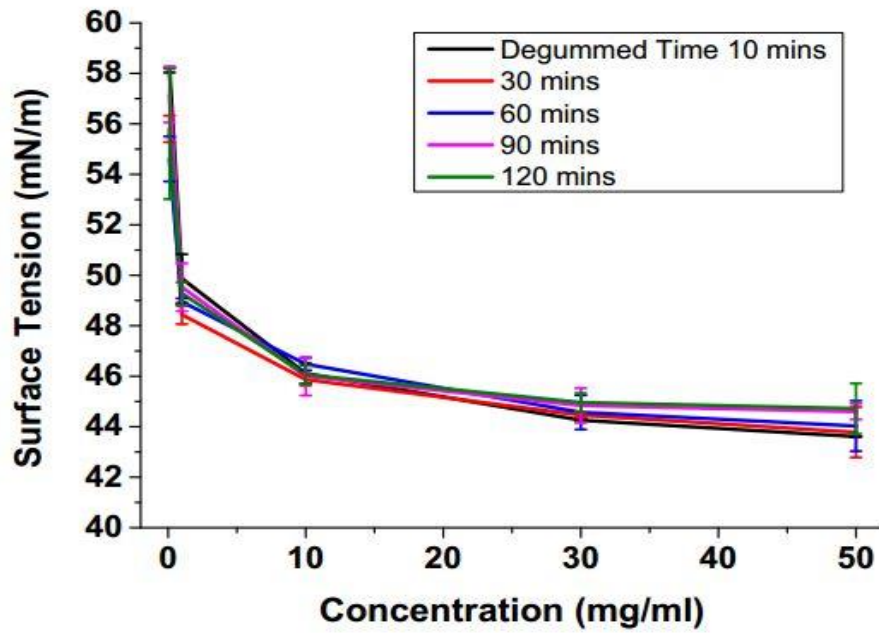
Figure 3-5 Surface tension (mN/m) vs concentration of 0.1, 1, 10, 30, and 50 mg/ml for a series of degumming times (10, 30, 60, 90, and 120 mins). RSF solutions was dissolved by Ajisawa's reagent. Each solution repeat 3 times (N=3), error bars represent standard deviation.
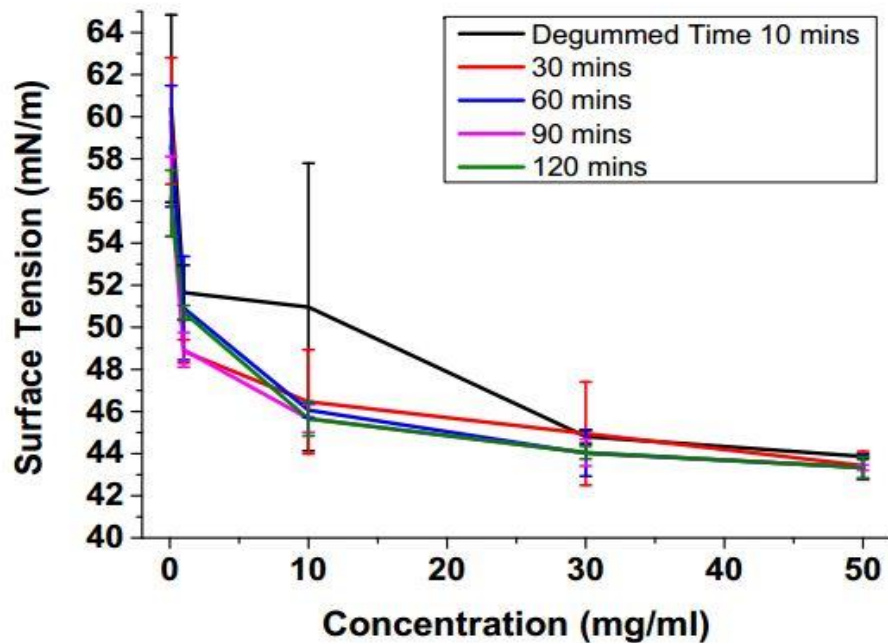
Figure 3-6 Surface tension (mN/m) vs concentration of 0.1, 1, 10, 30, and 50 mg/ml for a series of degumming times (10, 30, 60, 90, and 120 mins). RSF solutions was prepared by 9.3 M LiBr reagent. Each solution repeat 3 times (N=3), error bars represent standard deviation.

3.3.1.5 Effect of Degumming Time on the Regenerated Silk Solution Dynamic Viscosity

Viscosity values for RSF solutions prepared from Ajisawa's reagent ($CaCl_2$-RSF solutions) and 9.3 M LiBr reagent (LiBr-RSF solutions) related to varied degumming times and concentrations are shown in Figure 3-7 and Figure **3-8**, respectively.

Figure 3-7 shows that the viscosity of the $CaCl_2$-RSF solutions increased with increased concentration (0.1, 1, 10, 30, and 50 mg/ml). For degumming times from 10 to 120 mins, the viscosity increased with decreased degumming time except 30 min degumming time. However, the large error bar (represents stand deviation) in 30 min degumming time suggests that the difference may come from the accuracy of the Vibro viscometer or operation mistakes. Overall, the viscosity of $CaCl_2$-RSF solutions with low concentrations (0.1, 1, and 10 mg/ml) are similar to the viscosity of purified water.

Viscosity of the LiBr-RSF solutions increased with increased concentration as shown Figure **3-8**, for degumming times for 10 to 120 mins, the viscosities of LiBr-RSF solutions decrease with increasing degumming time. The LiBr-RSF solutions viscosity of the 10 min degumming time is higher than the $CaCl_2$-RSF solution viscosity of the 10 min degumming time, suggesting that the LiBr-RSF solution transitions from solution state to a partially crosslinked state quicker than $CaCl_2$-RSF solutions. Pritchard et al. determined the kinematic viscosities of silk solution exposed to 10, 30, 60 and 90 min degumming times by using a cSt range viscometer [164]. 10 min degummed silk solution also showed the higher viscosity than 30, 60 and 90 min degummed time silk solution which was consisted to the results in this thesis.
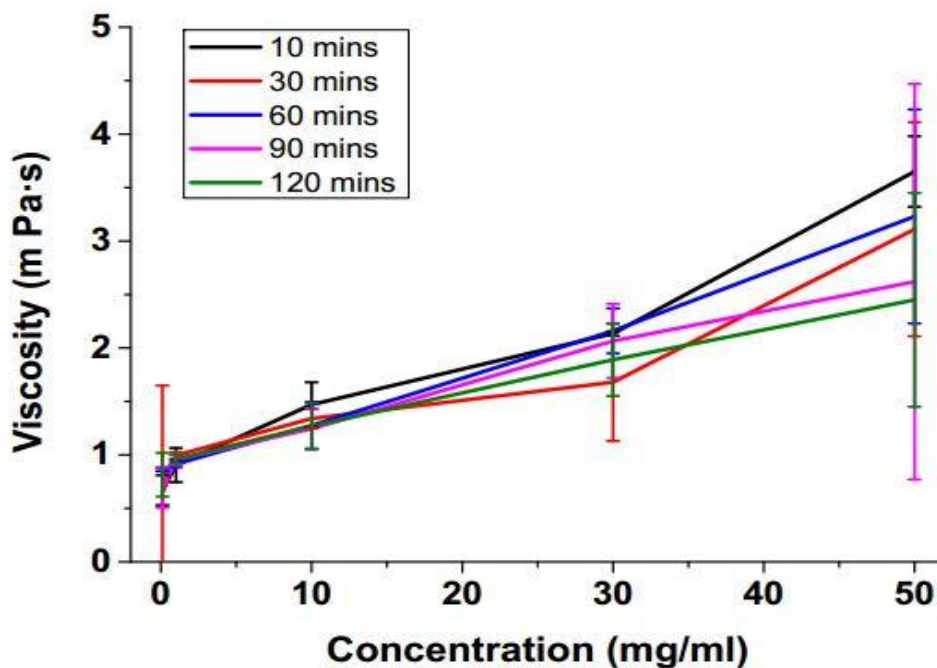
Figure 3-7 Dynamic viscosity (mPa·s) vs concentration of 0.1, 1, 10, 30, and 50 mg/ml for a series of degumming times (10, 30, 60, 90, and 120 mins). RSF solutions was prepared by Ajisawa's reagent.   Each solution repeat twice and was measured in 3 times (N=6), error bars represent standard deviation.
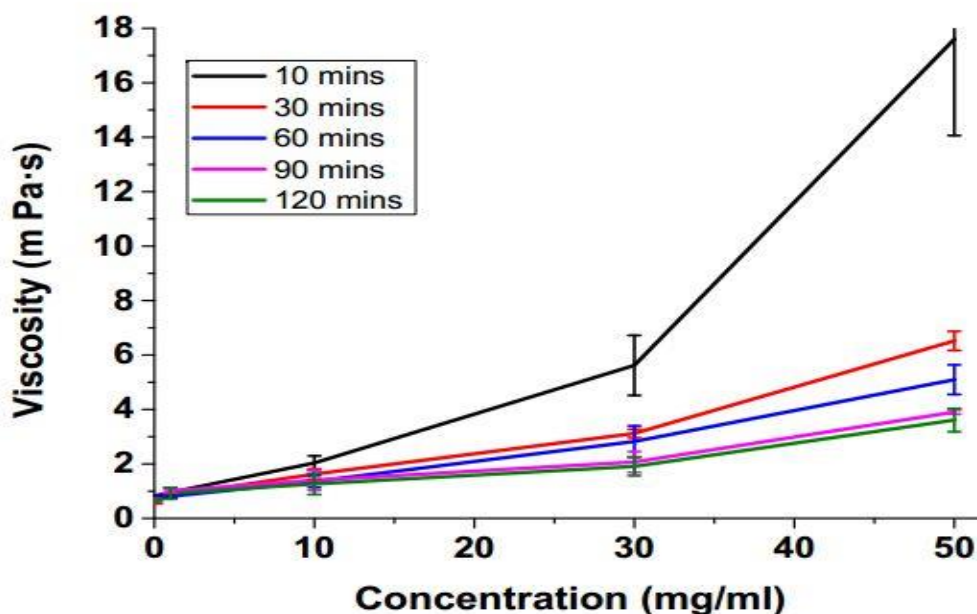
Figure 3-8 Dynamic viscosity (mPa·s) vs concentration of 0.1, 1, 10, 30, and 50 mg/ml for a series of degumming times (10, 30, 60, 90, and 120 mins). RSF solutions was prepared by 9.3 M LiBr reagent. Each solution repeat twice and was measured in 3 times (N=6), error bars represent standard deviation.

In both type of solutions, the viscosity increases with increasing protein concentration and decreased degumming times. Comparing the proportional relationship observed between concentration and viscosity for degumming times from 60 to 120 min in Figure 3-7 and

Figure **3-8**, the viscosity of RSF solutions are quite similar, suggesting these two types of dissolutions do not affect the viscosity of RSF solution under long degumming time (60, 90, and 120 minutes). For 10 and 30 min degumming times, the viscosity values are different suggesting that the 9.3 M LiBr dissolution affect the viscosity more than Ajisawa's reagent on short degumming duration.

3.3.1.6 Effect of Z Value on the formation of RSF droplets

As mentioned in Section 1.4.3, the printability of a new ink was determined by the Z value, theoretically. Table 1-6 listed and show how to calculate the useful constants: the Reynolds (Re), Weber (We) and inverse (Z) Ohnesorge (Oh) numbers. For RSF solutions, section 3.3.1.4 and 3.3.1.5 have showed the surface tensions and viscosities of all possible RSF solutions which can be used for printing. In theory, the Z values of all possible RSF solutions can be calculated. For example, Table 3-1 lists the physical properties of a series of different concentration of 30 min degummed RSF solutions (dissolved in Ajisawa's reagent at 75 °C for 3 hours). The reason for using the Ajisawa's reagent to dissolve fibroin was the $CaCl_2$-RSF solutions having longer store time than LiBr-RSF solutions without changing to gel. The Z values of the 10, 20, 30 and 40 mg/ml SRSF solutions are 40.9, 32.1, 25.3 and 20.3 respectively. It is worth noting that the Z values of all the inks are above 14, which mean that they require extra pressure to form stable single droplets

[155]. These inks were then loaded into the printer vessel. Figure 3-9 shows charge-coupled device (CCD) camera caught droplets ejection images which experimental observation of droplet formation for (a) 10 mg/ml, (b) 20 mg/ml, (c) 30 mg/ml and (d) 40 mg/ml of RSF inks. It can be seen from the images that single droplets were formed, with the higher concentration ink forming better droplets due to the lower *Z* value.

Table 3-1 Physical properties of RSF inks

RSF inks (mg/ml)	0 H₂O	10	20	30	**40**
ρ (Kg/m³)	1000	1010	1020	1030	1040
η (mPa·s)	1.08	1.29	1.63	2.08	2.6
γ (mN/m)	72.9	45.96	44.76	44.65	44.73
Inverse (*Z*) of *Oh*	61.2	40.9	32.1	25.3	20.3

ρ - density; η – viscosity; γ- Surface tension;droplet diameter is 60 μm.
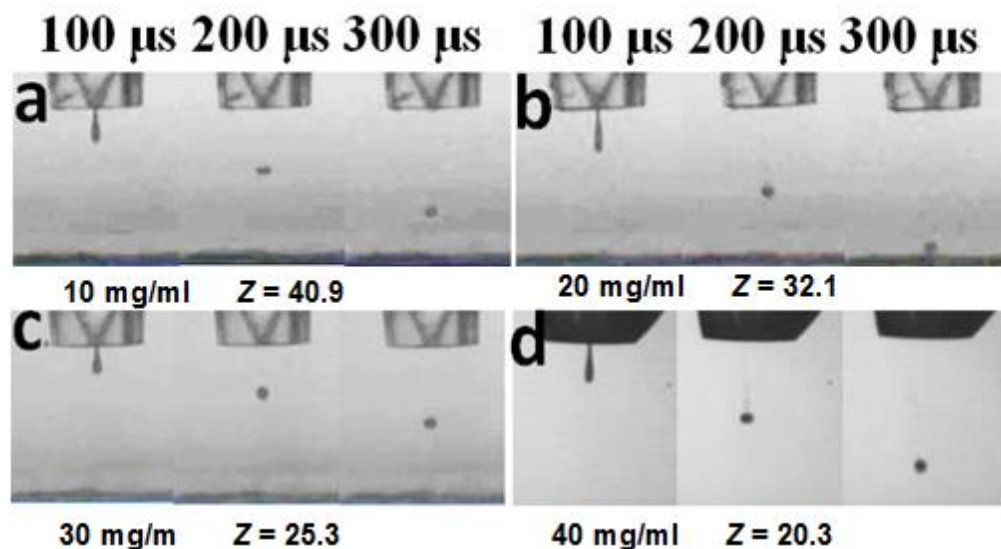
Figure 3-9 These CCD camera microscope images, depicting silk droplets ejected from 60 μm nozzles, shows the formation of a single droplets from different concentration of RSF solutions, (a), 10 mg/ml (Z = 40.9), (b), 20 mg/ml (Z = 32.1), (c), 30 mg/ml (Z = 25.3) and (d), 40 mg/ml (Z = 20.3) respectively.

90

Overall, this section mainly demonstrated the printability of the RSF solution by analyzing their physical properties, theoretically. In fact, a printable ink is judged by weather the ink can form an individual droplet. However, the formation of an individual droplet not only depends on the inks but also relies on the printing settings. The basic printing settings will be introduced in next section.

3.3.2 Analysis of Printed Patterns

Silk swimmers are formed by printing the basic pattern layer-by-layers. The quality of the primary layer is significant and it determines whether the final swimmers can accumulate to the required structures. This section shows how to control the shape of the primary printing pattern by adjusting different substrates, the distances between two adjacent dots and different scripts (including txt scripts and bitmap scripts).

3.3.2.1 Effect of contact angles of substrate on printing patterns

In case of using water as the liquid phase, measuring contact angle helps to determine the hydrophilicity/hydrophobicity of different surfaces. It is considered that the hydrophilicity/hydrophobicity will influence the printed patterns on the surface. Figure 3-10 shows the charge-coupled-device (CCD) camera images of the moment when the Di-water droplet landed on the surfaces and the static contact angles were measured. Here, there are 4 types of substrates were measured: the glass slide, silicon wafer, gold (Au) coated silicon wafer, and C8 modified silicon wafer. The contact angle for them are 4.3 ± 0.5°, 34.9 ± 0.3°, 71.8 ± 1°, and 74.9 ± 0.6°, respectively. The representative images were showed in **Figure 3-10**. The glass slide has the most hydrophilic

surface, then silicon wafer, Au-silicon wafer and C8-slicon wafer. Then, one droplet of RSF ink (40 mg/ml, 30 min degummed duration, Ajisawa's reagent) was printed on those substrates and the representative printed patterns were showed in Figure 3-11. Due to the Coffee-Ring Effect [192, 193], a ring pattern was remained after the ink droplet dry up. **Figure 3-11** shows that different hydrophilicity-hydrophobicity of the surfaces results in the difference of the size and edge of the ring structure. The ring structure on the glass slide has the lumpy edge while the ring structure on the other 3 substrates (silicon wafer, Au-coated silicon wafer, and C8-silicon wafer) have smooth edge. Overall, the diameter of the ring structure for glass silde, silicon wafer, Au-silicon wafer and C8-silicon wafer were 200 ± 20, 150 ± 15, 140 ± 15 and 135 ± 20 µm, respectively. The results also show that the higher hydrophilicity of the surface is, the wider the diameter of the ring pattern will be.

The data presented here suggest that substrate surfaces must be taken into account during printing process for different applications. For silk swimmers, the C8-silicon wafers were selected due to its high hydrophobic surface convenient to take the printed swimmers off the substrate and the cost is less than the Au coated wafer.
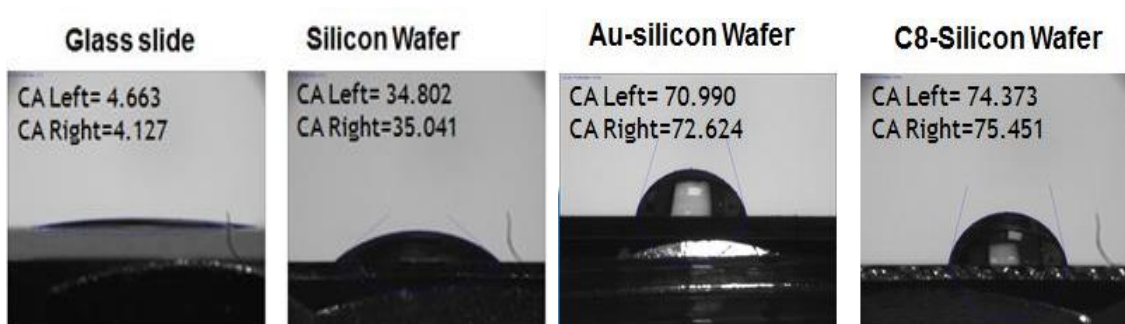
Figure 3-10 These CCD camera images show the contact angles of various substrate (glass slide, silicon wafer, Au-silicon wafer and C8-silicon wafer).
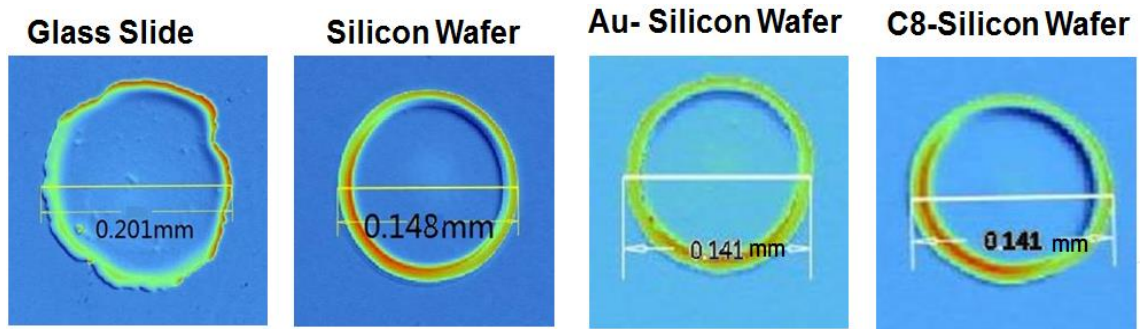
Figure 3-11 These microsocpe images show respective samples of the ring pattern printed on various substrates (glass slide, silicon wafer, Au-silicon wafer and C8-silicon wafer).

3.3.2.2 Effect of humidity on printing patterns

Humidity show the percentage of water vapour present in the air and it is considered as one of the most important printing parameters for drop-on-demand printing. **Figure 3-12** shows the printing RSF patterns on 80%, 65% and 50% humidity environment. It demonstrated that the 80% humidity resulted in the droplets coalescing and a 'pond' pattern instead of the designed '└┐' pattern. On 65% humidity, part of the printed '└┐' pattern can be observed. When the humidity adjusted to 50%, a clear '└┐' pattern was showed in the image. When the humidity is under 50%, no pattern can be seen on the substrate due to the quick evaporation of the small droplet before it landed on the surface (no data can be shown in image). The estimated range of the suitable printing humidity range is between 50% and 65%.
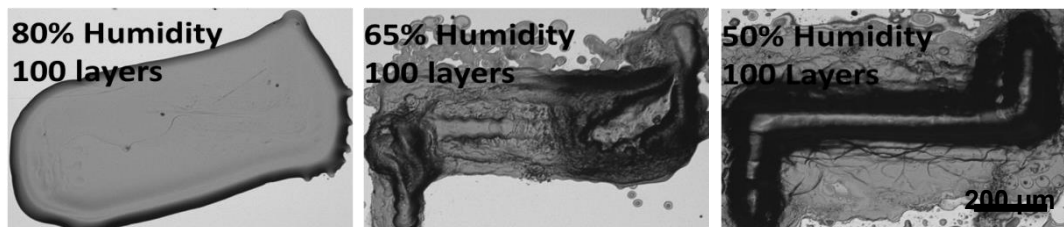
Figure 3-12 These microscope images show respective samples of the printed RSF patterns under different humidity. RSF inks : 40 mg/ml, 30 min degummed duration, Ajisawa's reagent. The tested humidity are 80%. 65% and 50%, respectively.

3.3.2.3 Analysis of Different Printing RSF Patterns

Regenerated silk fibroin (RSF) protein is an FDA approved biomaterial and has been used as a bio-ink to fabricate structures using inkjet printing [33, 38, 91, 161, 190]. The characteristic of RSF, which is the change for water soluble amorphous (Silk I) to water insoluble crystalline conformations (Silk II) made up of beta-sheet structures by addition of an organic solvent (such as methanol, ethanol, and acetone), gives the chance to use the inkjet printer to generate RSF scaffolds in two ways. The two ways are: 1) printed droplets accumulated in vertical direction and the height of the patterns depend on the thickness of each droplets; 2) printed droplets accumulated in horizontal direction and the height of the patterns depend on the distance between the droplets and the amount of the droplets. In this section, RSF inks were used to print various patterns from simple (single dots, line, and film) to complex (bitmap images).

Dots

Images of optical profiler microscope (Contour GT-K, USA) in Figure 3-13 show the morphology of 10, 20, 30 and 40 mg/ml of RSF solution printed dots. The ring structures come from the coffee-ring effect which is a result of a complex balance between outward micro-flow distribution, solution impact and different evaporation rates between the center and the edge of the deposited materials [192, 193]. The ring structures have been observed in **Figure 3-13**A. The thickness (400 $\pm$ 65 nm) of the edge of coffee-ring structure is higher than the thickness (100 $\pm$ 30 nm) of the center area (Figure 3-13). Also, Figure 3-13 shows that the higher concentration of RSF inks form smaller rings than the lower concentration of RSF inks. Therefore, the diameter of the ring pattern

can be controlled by adjusting the concentration of the RSF inks (Figure 3-13e); as concentration increase diameter decrease.
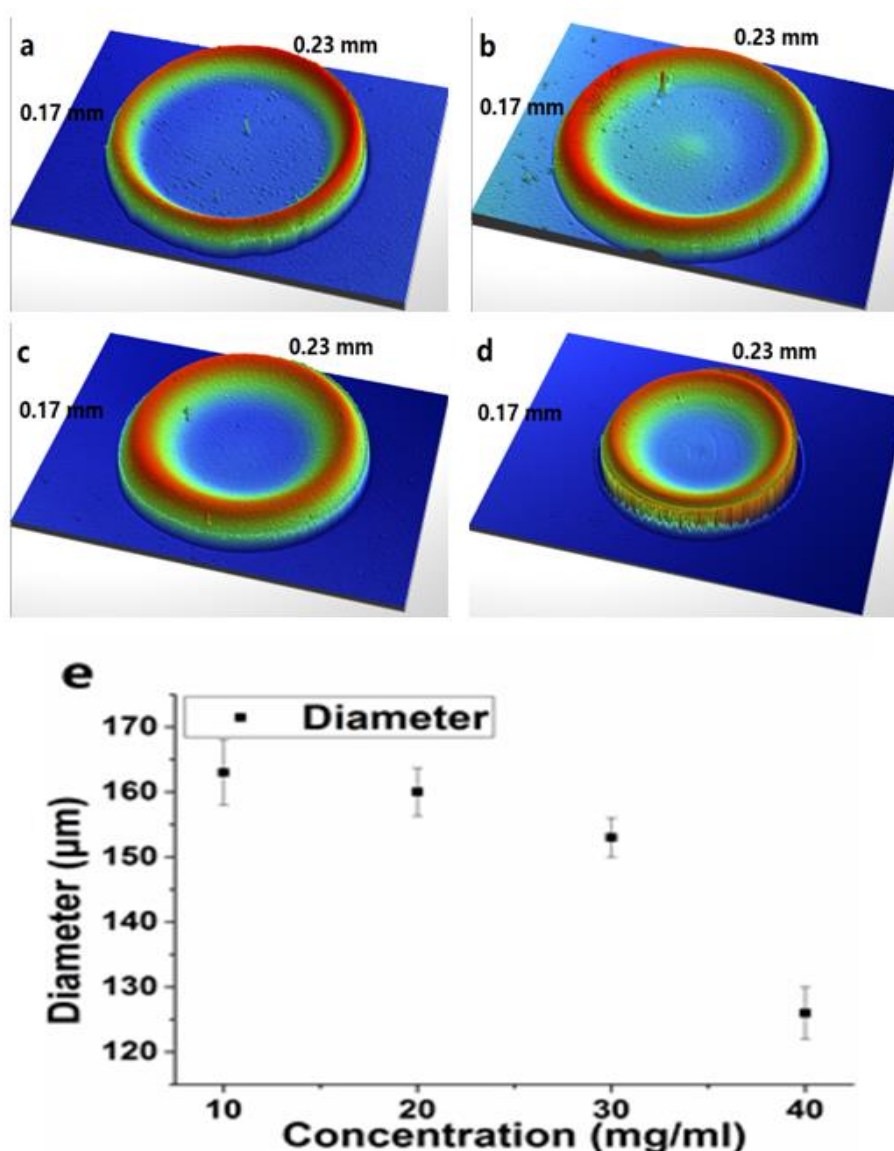
Figure 3-13 Optical profiler microscope images show different concentrations of RSF solution printed dots. The concentrations are (a), 10 mg/ml, (b), 20 mg/ml, (c), 30 mg/ml and (d), 40 mg/ml respectively. e) Graph shows the diameter of the different concentrations of RSF solution printed dots (N = 3), error bars represent standard deviation.

It is possible to generate silk scaffolds by inkjet printing of water soluble RSF inks and then convert it into insoluble *beta*-sheet (Silk II) structure via a second ink containing methanol. Changes in the structure of printed RSF films were determined by Fourier Transform Infrared (FTIR) Spectrophotometer

(IRPrestige-21, Shimadzu, Japan). The infrared (IR) spectral region between 1750 cm^{-1} and 1450 cm^{-1} was classified to absorption by the peptide backbones of amide I (1700-1600 cm^{-1}) and amide II (1600-1500 cm^{-1}), which were mostly used for the analysis of different secondary structures of RSF [194, 195]. As shown in Figure 3-14a, the peaks at 1661-1663 cm^{-1}, 1575-1777 cm^{-1}, and 1525-1522 cm^{-1} were characteristic of silk II secondary structure, whereas the absorptions at 1672-1669 cm^{-1} and 1531- 1529 cm^{-1} were indicative of silk I conformation. After the printing of methanol, the peaks at 1670 cm^{-1} and 1530 cm^{-1} (silk I) decreased, whereas the peaks at 1662 cm^{-1} and 1524 cm^{-1} (silk II) increased. The results indicated that silk films with different amount of crystal structures were achieved by printing layers of methanol.

Height of printed RSF pillar prepared from 10mg/ml RSF solution is illustrated in Figure 3-14b (1-10 layers), Figure 3-14c (20-100 layers), and Figure 3-14d (200-1000 layers). Samples were prepared by printing one layer of RSF solution and followed by another layer of methanol. Evaporation of methanol leaves the silk pillars with *beta*-sheet conformation. The average thickness of each layer within 10 layers was 350 $\pm$50 nm, whereas that within 1000layers was 210 $\pm$60 nm. The difference of each layer height may be cause by the coffee ring effect which results in the height different between the edge and the center of the printed dots pattern. Above all, the more layers are printed, the higher pillars are built up. Methanol helps to form stable RSF structure which allows us to fabricate 3D scaffolds.
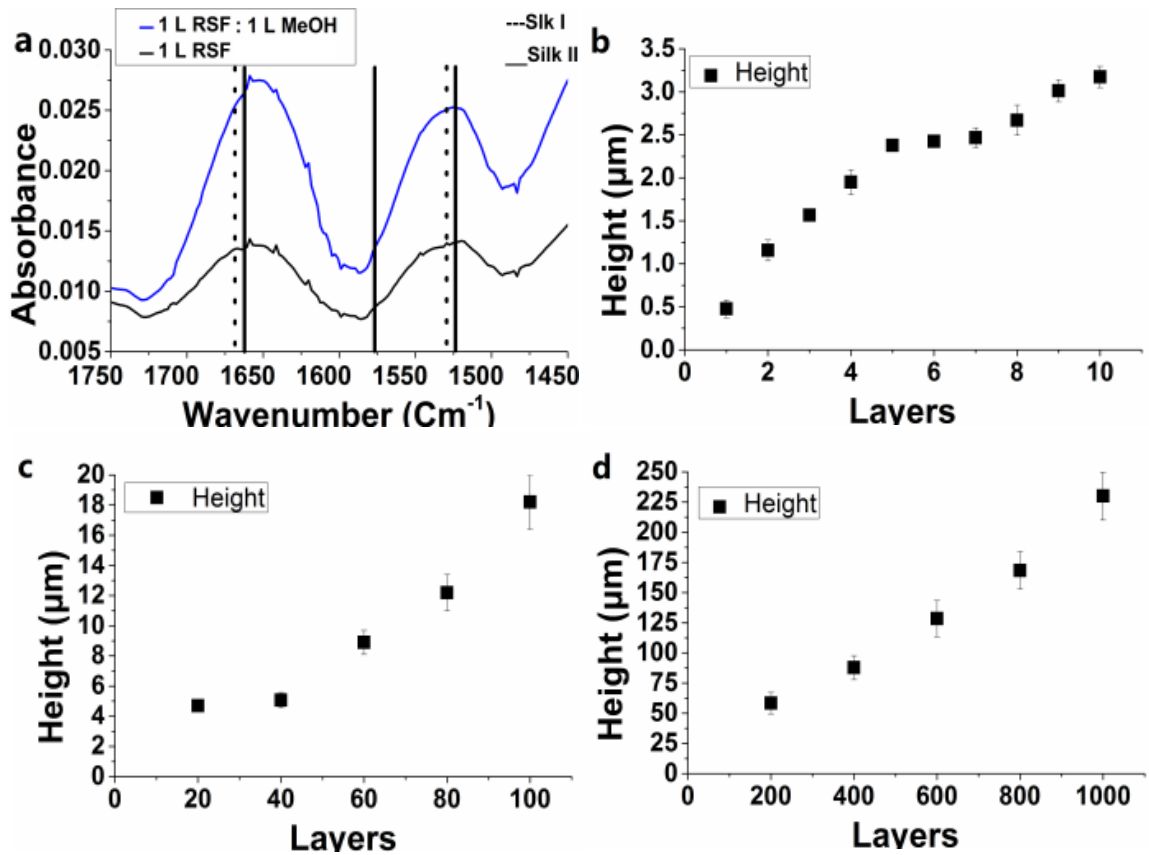
Figure 3-14 (a) FTIR spectra shows silk I converting to silk II of printed RSF films after printing methanol. Thickness at edge of silk column with 10mg/ml RSF solution with different numbers of layers: (b) 1-10 layers, (c) 20-100 layers, (c) 200-1000 layers.

Lines

Figure 3-15 shows a liquid droplet can form a line by controlling the printing distance of two adjacent dots. A few principal behaviors appear when testing printed droplets patterns across a variety of drop spacing, hydrophobicity-hydrophobicity of substrate and temperature. They are labeled as individual dots, a scalloped line, a uniform line and a bulging line [193].

If printed droplets that are too far apart to interact, more than the diameter of the droplet, then individual dots land and dry. Large printing distance (0.2 mm) between each dot makes it hard for droplets to coalesce in this experiment. Then, droplets start to connect with each other by decreasing the distance

(less than dots' diameter). Initial coalescence of liquid droplets forms line with periodic irregularity edge. The distance is between the radius and the diameter of the droplet pattern on the substrate. Further decreasing the drop spacing will eliminate the periodic edge and lead to a smooth, straight line called parallel-side line. Sufficient overlap distance equals to the radius of the droplet pattern on the substrate.

However, if the adjacent droplets are too close to each other, a bulging forms. The distance is less than the radius of the droplet pattern on the substrate. These findings are consistent with poly (3,4-ethylenedioxythiophene) poly (styrene sulfonate) inks reported by Soltman et al [193].

Comparing the lines printed by using various different degumming time RSF solutions in Figure 3-15 has shown that degumming time has no effect on the quality of printed lines. A potential explanation for this observation is that the Z value of tested varied degumming RSF solutions are similar (see work in section 3.3.1, based on the data shown in Figure 3-5 and Figure 3-7，the surface tension and viscosity of the RSF are similar and the concentration of the RSF solutions are same 10 mg/ml.). Thus, when selected the most suitable printing RSF solution, the degumming time is not considered for its effect on the final printed pattern but considered for its effect on the transformation time from protein solution to gel (gelation time, see data shown in section 3.3.1.2). In conclude, by carefully optimizing the droplets pressure wave, spacing, frequency, humidity, temperature and pressure; it is possible to print a smooth line with an even edge (for example, the line in **Figure 3-15** 120 degummed time **e**).
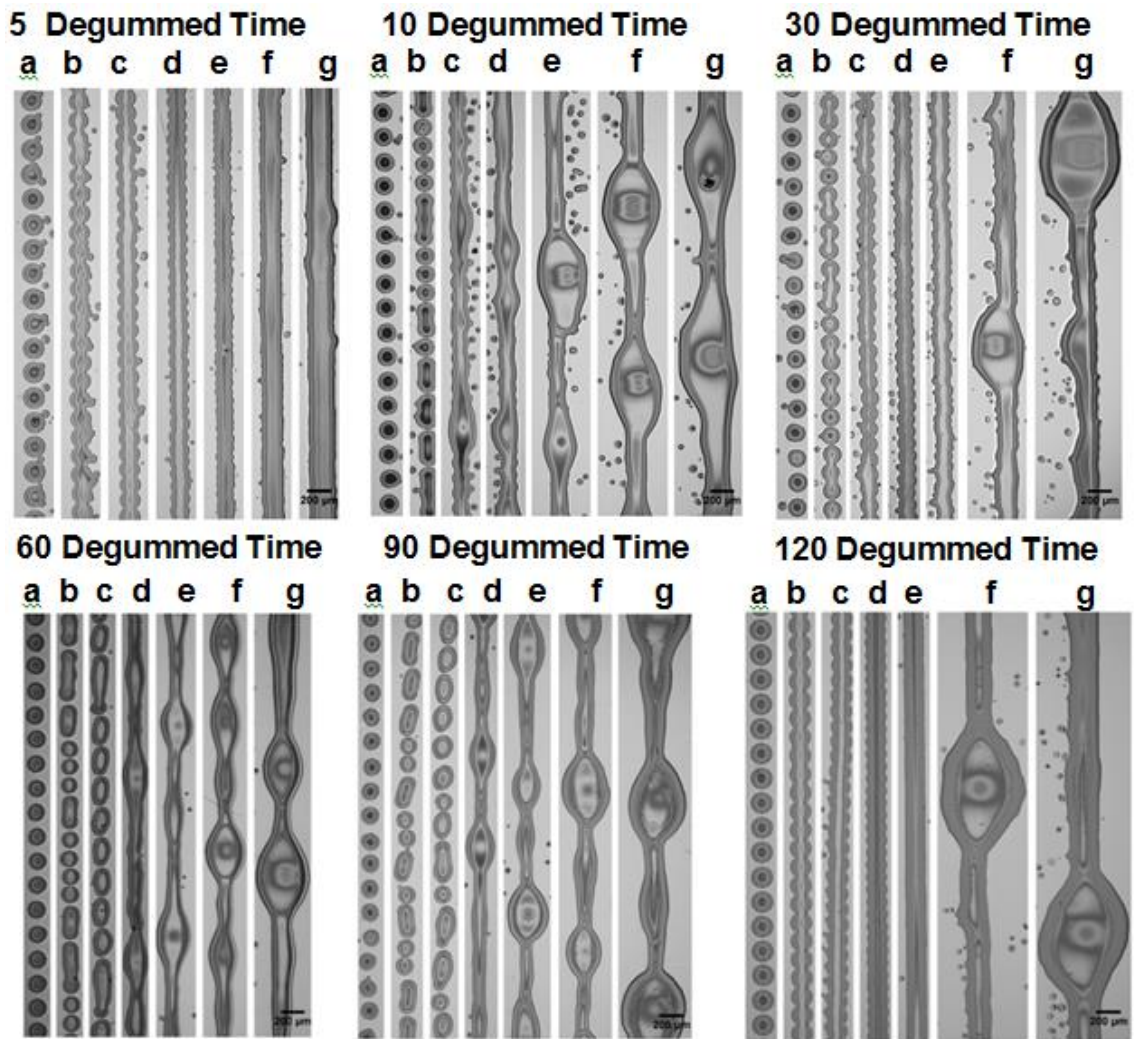
Figure 3-15 Microscope images show inkjet printing lines by adjusting the distance of two adjacent droplets. The distances are a) 0.2 mm, b) 0.15 mm, c) 0.125 mm, d) 0.1 mm, e) 0.075 mm, f) 0.05 mm, and g) 0.025 mm seperately. RSF inks useed the dissolvation of Ajisawa's reagent and the silk fibres were exposed to 5, 10, 30, 60, 90 and 120 minutes degumming time. The concentration of all RSF solutions were 10 mg/ml. 60 µm printhead were used.

Films

Figure 3-16 shows RSF films were produced by printing layers of overlapping

droplets on top of substrates (such as cover glass slips or silicon wafer). Some

typical patterns emerge when examining printed RSF films across of droplet

spacing from x and y direction (setting x = y). I labelled these as individual

dots, partial linked dots, a uniform film and a pond film.

If printing spacing is more than a drop's diameter, individual dots appear on the substrates (in Figure 3-16a). As droplets spacing decreases, the dots start to merge but incompletely which is called partial linked dots (Figure 3-16b) and e)). Further decreasing the dots spacing will eliminate the incomplete linked dots and lead to a smooth, uniform top films. This distance is the optimal distance for the formation of films. However printing drops even closer together than the optimal distance leads to retain RSF inks as a pond, then the superabundant solution dry and form a film. This kind of film is called a pond film which has irregular surface (Figure 3-16c) and f)). In conclusion, ideal films occur by adjusting the droplets spacing to optimal distance.
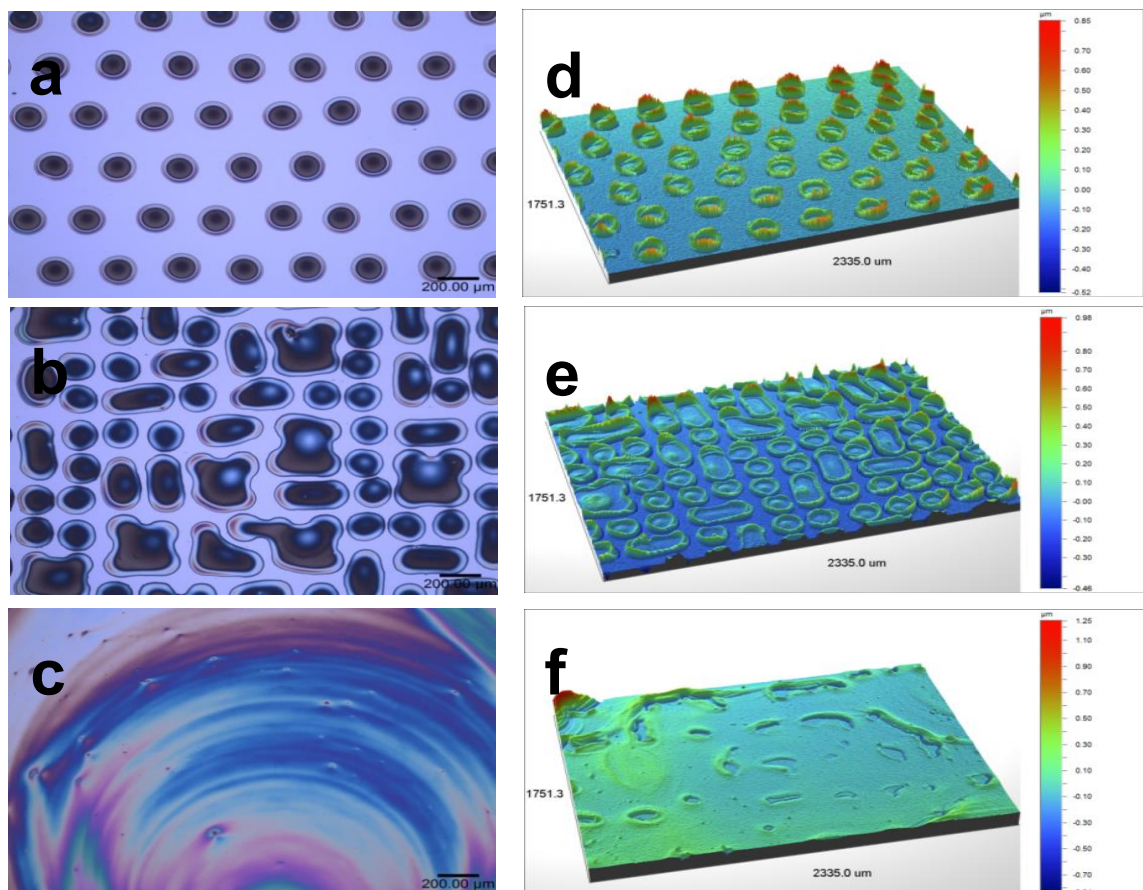
Figure 3-16 Microscope images (a-c) and optical profiler images (d-f) of RSF dot arrays printed on silicon wafer. The concentration of RSF was 10 mg/ml RSF. The distances between two adjacent dots were 0.3 mm (a and d), 0.2 mm (b and e), 0.1 mm (c and f). 60 μm printhead were used.

Cylinders

3D scaffolds are formed by the accumulation of droplet layer-by-layer. Increasing the number of layers and deposited droplets steadily raised the height of the printed pattern. With the help of methanol transferrings the unstable silk I to stable crystalline silk II, a crystal RSF cylinder was formed (Figure 3-17).
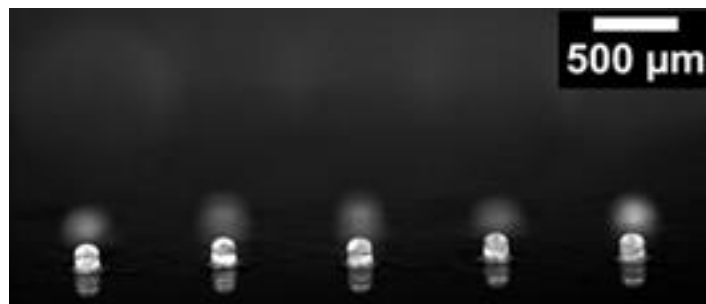
Figure 3-17 Fluoresce microscope image show the printed pillar – "little light ball" shape. Inkjet printing of 3D patterns using functional FITC-RSF inks which RSF crosslinked with FITC. The concentration of RSF is 30 mg/ml. Reactive inkjet printing with 60 μm printhead.

Complex Patterns

Figure 3-18 shows the images of inkjet printing bitmap patterns, a) and c) complex bitmap images printed on paper with blended RSF inks (coomassie blue mix with RSF solutions). b) 'SHEFFIELD ENGINEERING' letters printed on silicon wafer using 40 mg/ml RSF solution.

Figure 3-18 Pattern directly printed using RSF solution, a) and c) complex bitmap images printed on paper with blended RSF inks (coomassie blue mix with RSF solutions); b) 'SHEFFIELD ENGINEERING' letters printed on silicon wafer using 40 mg/ml RSF solution.

3.4 Conclusions

The successfully formation of a single, individual droplet (shown in **Figure 3-9**) proved that RSF solutions are printable by inkjet printer. Both the physical properties of the RSF solution (*Z* value) and the settings of the printing parameters (pressure wave) affect the formation of an individual droplet. Different conditions (degumming times and dissolutions) of the preparation process for the RSF solutions result in the difference on their physical properties. The adjusting of the printing parameters focuses on controlling the pressure wave.

The quality of the printing droplets, the type of the printed substrates, the post-treatment of the methanol, and the setting of the printing process affected the quality of the printed features. In order to get the desired printed scaffolds, the relationships between the number of layers and the total thickness of the printed scaffolds were established. Then, various patterns from simple (such as dot arrays, lines, films, particles) to complex (logos and scaffolds) structures have been printed. To find the optimal distance between the adjacent droplets helped to get best printed features in the end.

Overall, this chapter illustrated that silk fibroin could play an important role as an ink material for inkjet printing technique. RSF based ink can be formulated by adding other components such as growth factors, enzymes, particles, and other functional materials to fabricate various scaffolds that can meet different requirements of the end uses. In this thesis, various self-propelled RSF-swimmers that could be used as drug delivery, bio-mixing and cancer detecting will be introduced in next few chapters.

Chapter 4 Reactive Inkjet Printing of

Catalytic Micro-rockets

4.1   Introduction

The production of small-scale devices that can generate autonomous motion through catalytic reactions within fluidic environments has become an increasingly active field of research [196-201]. These devices have led to some potential applications such as environmental monitoring and remediation [202, 203], lab on a chip diagnostics [204], and *in vivo* drug delivery and repair [17, 85, 86, 205]. However, the current production materials and methods have many limitations. On the one hand, a large proportion of the small devices are based on lithographic approaches in order to control the shape and catalytic distribution. However, these methods have limitations on designing the shape of the devices particularly in respect to further scalability. On the other hand, most of these small-scaled devices are made from platinum and gold which are expensive, require complex chemical processes and are not biocompatible [203, 206, 207]. Thus, it is desirable to find simple production processes and materials which are cheap to make biocompatible small-scale devices.

As described in Chapter 3, it has been demonstrated RSF solutions can be printed via inkjet printing to generate scaffolds. The printed scaffolds have the chance of high designable structural precision and are on the micron scale, which is a potential candidate of small-scale devices. Furthermore, silk fibroin could play an important role as the devices' material because of its own properties including the structure transition flexibility [81, 96], biocompatibility [15, 33, 38] and the simple and water-based reassemble process [53, 208]. RSF based inks can be formulated by adding other components such as growth factors [33], enzymes [189], particles [85], and other functional

materials (e.g. PEG and collagen) [208-210]. It has been shown by Zhang Y.Q. [211] that natural silk fibroin can be used as a support for enzyme immobilization and increased stability. It is an alternative material for expensive metal and avoids complex chemical reaction to combine catalase.

In this chapter, the experiment explored how to make RSF micro-rockets by a RIJ printing approach. RIJ printing is a method where two or more inks are used in order to produce a chemical reaction or cause the morphology of protein to undergo a conformational change. Here, the devices were made of RSF solutions which are mixed with catalase. We show the generation of RSF devices by LBL inkjet printing of water soluble RSF mixture inks and then converting them into insoluble beta-sheet (Silk II) structure via a second ink containing methanol. Furthermore, this Chapter discusses the characterization of RSF micro-rockets, and trajectory analysis of RSF devices in H_2O_2 solutions is discussed. Finally, the optimization of the silk swimmer printing process is mentioned and guilds to fabricate more complex and functional swimmers for further analysis.

.

4.2   Experimental Methods

4.2.1   Materials

The details of the used materials are described in Chapter 2 Section 2.1.1.

4.2.2   Silk Degumming

The silk degumming process is described in Chapter 2 Section 2.1.2.

4.2.3   Preparation of Regenerated Silk Fibroin Solution

The preparation of RSF solution is described in Chapter 2 Section 2.1.3.

4.2.4   Preparation of mix Ink Solution

Two types of ink solutions were prepared in this experiment. Ink-A was Catalase/PEG_{400}/RSF, and Ink-B was PEG_{400}/RSF. Amorphous bovine liver catalase powder (purity 60% Sigma-Aldrich) was dissolved in deionised water at a concentration of 20 mg/ml. The catalase solution samples were inverted several times until fully dissolved and then were filtered with a 0.7 µm glass filter. In order to avoid weighting the highly viscous PEG_{400} liquid, PEG_{400} (Aldrich) was diluted in deionised water at a concentration of 500 mg/ml. Finally, Ink-A was prepared with Catalase and diluted PEG_{400} together with RSF to final concentrations of 30 mg/ml RSF, 10 mg/ml PEG_{400} and 4 mg/ml catalase, and Ink-B to final concentrations of 30 mg/ml RSF and 12 mg/ml PEG_{400}.

4.2.5   Inkjet Printing Process

The basic concept of printing RSF scaffolds has been described in Chapter 2 and Chapter 3. In this Chapter, a drop-on-demand (DOD) inkjet printer (MicroFab IV，MicroFab Inc., USA) was used to fabricate catalytic self-motile particles by using functional inks such as Catalase/RSF/PEG$_{400}$ inks and RSF/PEG$_{400}$ inks. The details of this inkjet printer were described in Chapter 2 Section 2.2.5. An explanatory schematic of the whole process is showed in Figure 4-1.

Two different structures of catalytic RSF micro-rockets were generated by LBL reactive inkjet printing. Fully active micro-rockets and the Janus micro-rockets were printed. Janus means the swimmers being made up of two different half. For example, in this experiment, one half of the swimmers have been encapsulated catalase and the other half has not. For each layer, a 5 x 10 dot arrays script was written and programmed into JetLab (Version 6.3, MicroFab Inc., USA). A total height of 500 layers of RSF columns were printed LBL. Thus, the fully active micro-rockets required two print-heads: one for methanol and the other one for Catalase/RSF/PEG$_{400}$ ink. The Janus micro-rockets are assembled by using four inks, thus four print-heads required: first print-head for methanol ink, second print-head for Catalase/RSF/PEG$_{400}$ ink, third print-head for RSF/PEG$_{400}$ ink and fourth print-head for 1% w/w PMMA/DMF ink. The process is shown in Figure 4-1, where Ink-A (Catalase/RSF/PEG$_{400}$ ink) was printed for 250 layers and Ink-B (RSF/PEG$_{400}$ ink) was printed the other 250 layers of pillar. Each RSF ink layer required one layer of methanol for transforming the RSF silk solution from Silk I to Silk II. An extra 10 layers of PMMA were required as a barrier layer in the case of the Janus micro-rockets.

Figure 4-2 shows the two designed silk micro-rockets: fully active rocket and Janus rocket. Furthermore, the schematic image illustrates the thrust of swimmers created by oxygen bubbles which were generated during peroxide decomposition by the encapsulated catalase. The fast and high-frequency bubble ejection leads to continuous motion of the swimmer.
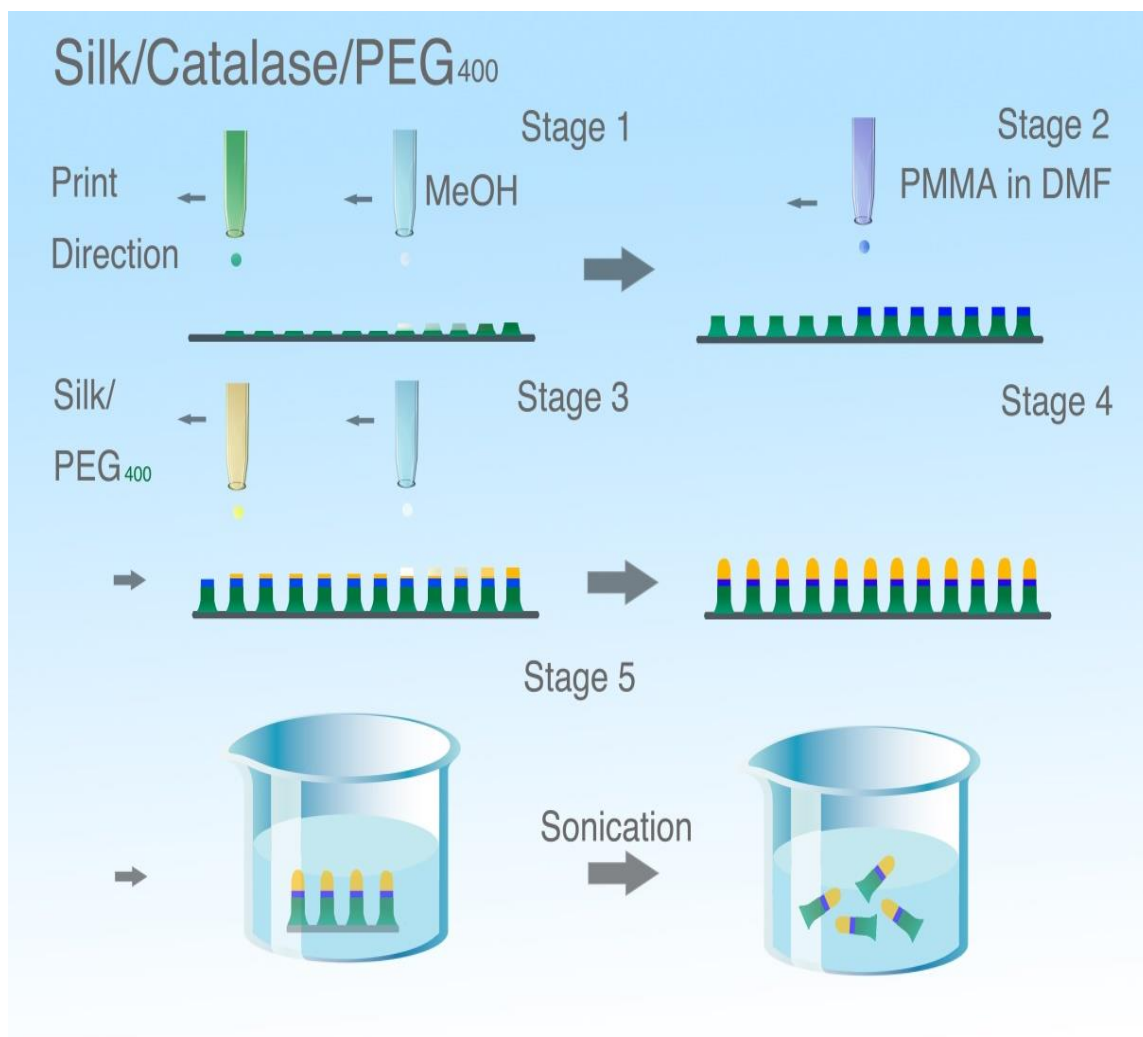
Figure 4-1 Schematic represents the LBL printing process of RSF micro-rockets. Green represents Catalase/RSF/PEG$_{400}$ inks; Yellow represents RSF/PEG$_{400}$ inks; blue represents PMMA barrier when generated Janus RSF micros-rockets.
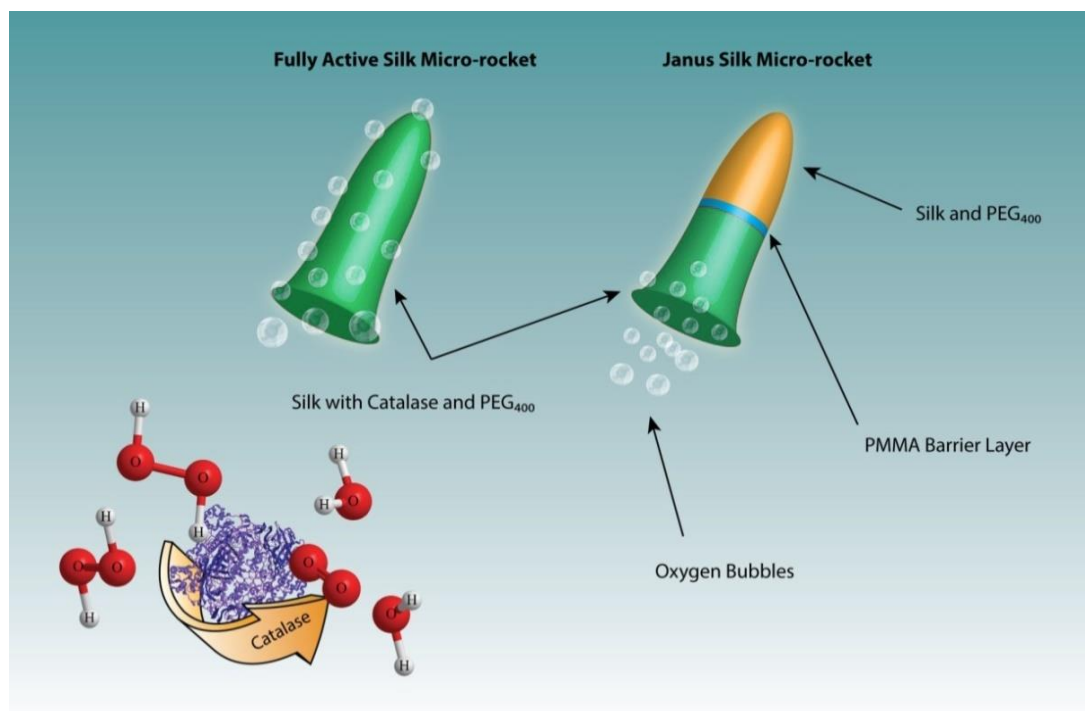
Figure 4-2 The Schematic shows the two designed RSF micro-rockets, left one is the fully active rockets while right one is Janus active rockets. Hydrogen peroxide is decomposided

4.2.6   Particle Preparation of Silk Micro-rockets

RSF micro-rockets were printed on silicon wafers which were plasma cleaned before use. In order to avoid damaging the micro-rockets samples, silicon wafers (with printed rockets on the surface) were immersed in filtered (0.2 μm) deionized water (DI-water) for a while. Then, rockets were removed by using Pasteur pipette with plenty DI-water to wash the surface of silicon wafer. If the rockets remained on the silicon wafer after the previous treatment, the use of a sonicator was needed to help remove the rockets. Silicon wafers were placed into a small beaker and deionised water was poured over the sample just enough to cover it. Then, the small beaker was held in a low power sonicator (37 kHz Ultrasonic Laboratory Cleaner) for few seconds (less than 30) and most of the rockets would become detached from the silicon wafer.

4.2.7   Analysis of Movies

The rockets were transferred into petri dish (8 cm in diameter) containing 6% w/v hydrogen peroxide (H_2O_2). Images were taken under microscope with a connected PixeLink camera, or with extra camera lens for help. Movies were taken at frame rate of 25 frames per second (fps) for 500 to 1000 frames. The analysis of the tracked movies is described in Chapter 2 Section 2.5.

4.3   Results and Discussion

4.3.1   Characterization of silk micro-rockets

This section firstly demonstrates whether Ink-A and Ink-B are printable by inkjet printer, including the analysis of their physical properties and the formation of the single, individual droplets. Secondly, printing process of swimmers will be analysed such as the structure of each printed single droplet and the evaluation of the thickness of the printed samples. Thirdly, all printed micro-rockets were checked under SEM to ensure the structure were reassembled as required.

4.3.1.1 The Formation of Functional RSF droplets

Table 4-1 lists the physical properties of functional RSF ink-A (RSF 30mg/ml, PEG_{400} 10 mg/ml and Catalase 4mg/ml) and Ink-B (RSF 30mg/ml and PEG_{400} 12 mg/ml). Z value (calculation equation is described in Chapter 1，Section1.4.3) of Ink-A is 21.49 and Ink-B is 24.70. The results are reasonable by comparing to previous value that Z value of 30 mg/ml was 25.3 (in Table 3-2 Chapter 3). The difference of Z values was caused by the addition of PEG_{400} and Catalase to RSF solutions and resulted in the increase of surface tension

and viscosity. Figure 4-3 shows CCD camera caught droplets ejection images of Ink-A and Ink-B. Both Ink- A and Ink-B formed single, individual droplets and further proved they are printable by inkjet printer.

Table 4-1 Physical properties of Functional RSF Inks

	Surface Tension (mN/m)	Density (kg m^{-3})	Viscosity (mPa s)	Z
Ink-A	46.12	1044	2.50	21.49
Ink-B	44.69	1042	2.14	24.70

Ink-A – RSF 30 mg/ml, PEG$_{400}$ 10 mg/ml and Catalase 4 mg/ml;

Ink-B – RSF 30 mg/ml, PEG$_{400}$ 12 mg/ml.

L – Characteristic linear dimension (60 μm)
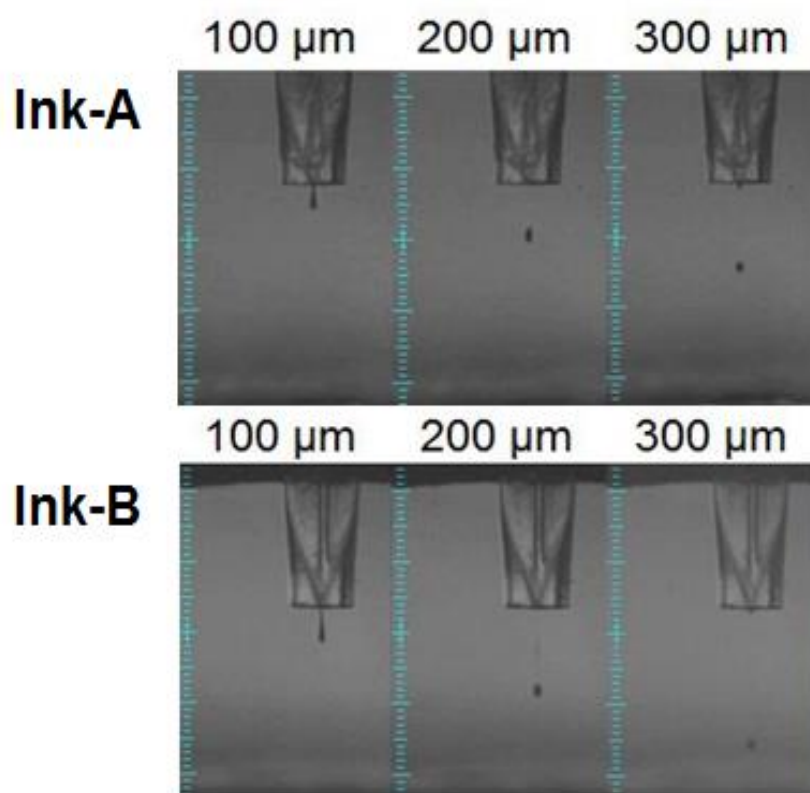
Figure 4-3 These CCD camera microscope images, depicting silk droplets ejected from 60 μm nozzles, shows the formation of a single droplets from (a) Ink-A and (b) Ink-B respectively.

4.3.1.2 Printing Process

The RSF scaffolds were accumulated by printing a drop of mixture RSF inks following a second drop of methanol. This print process was defined as one printing layer. In order to calculate the height of the final micro-rocket and compare how different mixtures of RSF inks affects the printing process, contour GT microscope images were taken of varying printing layers of RSF/PEG$_{400}$ with and without catalase separately. Figure 4-4 shows printed RSF scaffolds by using 30 mg/ml RSF inks with blended-in 12 mg/ml PEG$_{400}$. Figure 4-5 shows printed RSF scaffolds by using 30 mg/ml inks mixed with 10mg/ml PEG$_{400}$ and 4 mg/ml catalase.

Both Figure 4-4 and Figure 4-5 show clearly that for the first few printed layers there was a strong "Coffee Ring" effect present. This effect results in the height of the outer circle higher than the height of centre and forming a "nest" structure. In 2008, Soltman and Subramanian also demonstrated that inkjet printing of a conductive polymer showed this kind of structure [193]. The final structure of multi-layers pillar structure is influenced by how the "nest" structure will be reduced. One possibility is that the following droplets will be filled in the "nest" and "Coffee Ring" effect will diminish after printing enough layers. Another assumption is that the "Coffee Ring" effect results in the inner side of printed columns contain hollow channels which allow O_2 gas to pass through when catalase reacts with H_2O_2. In this situation, when we prepare Janus RSF columns, a barrier layer is required to block the inner channel. The final structure will be characterised in the next section (Section 4.3.1.3).
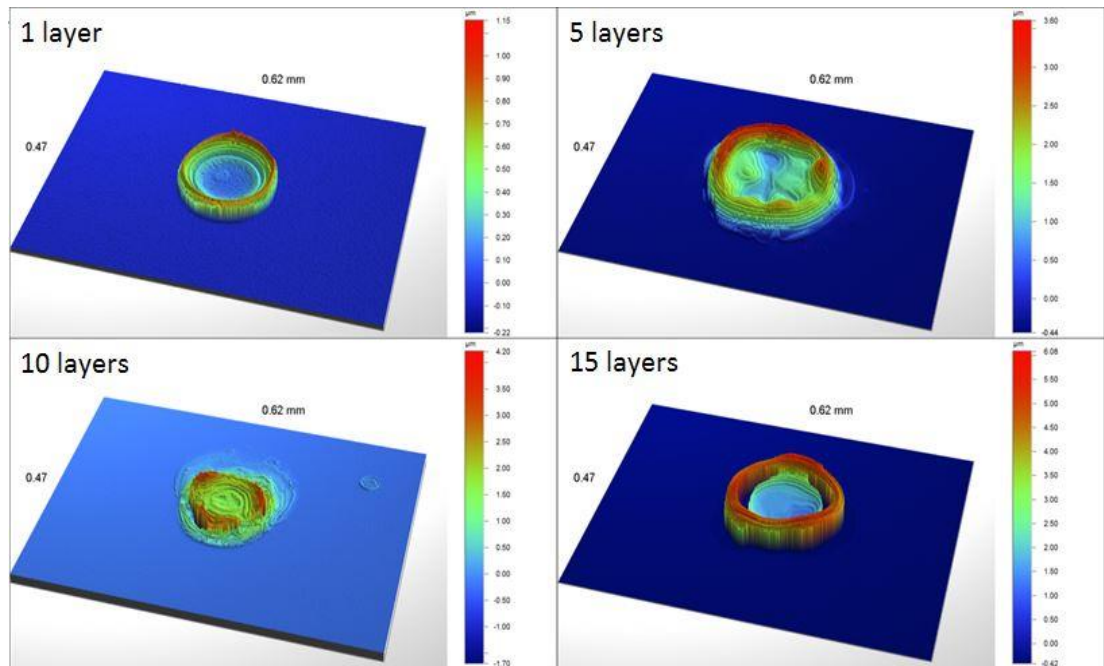
Figure 4-4 Contour GT microscope images of different amounts of Ink-B (30 mg/ml RSF and 12 mg/ml PEG_{400}) printed on Si-wafer substrates showing how the height is affected by the amount of layers printed on top of each other.
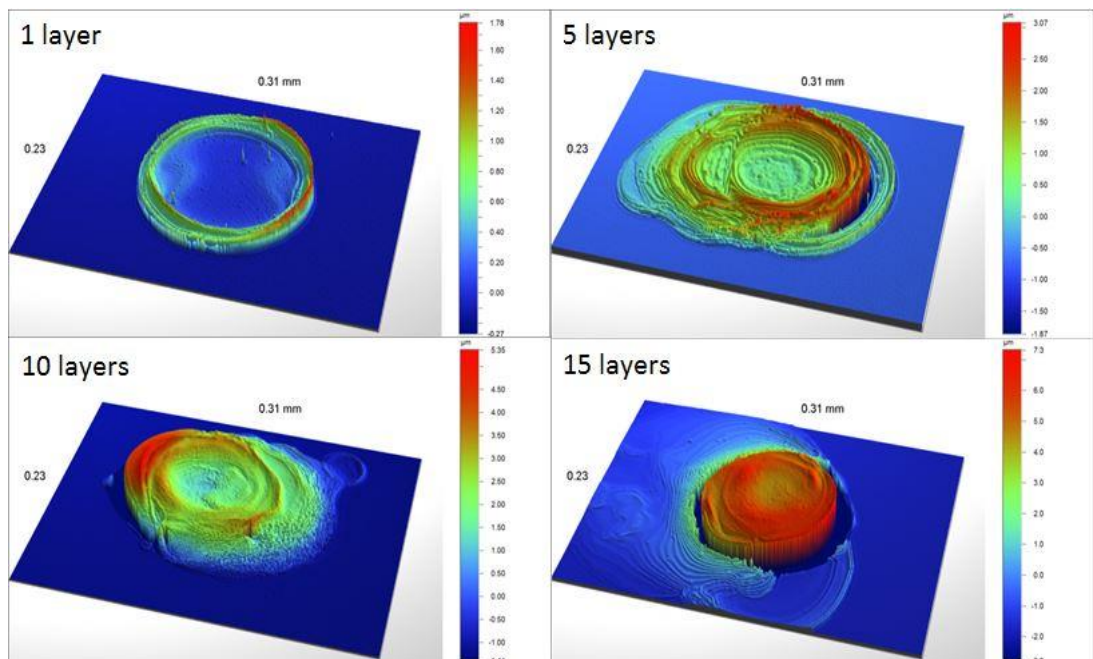
Figure 4-5 Optical profiler microscope (Contour GT) images of different amounts of Ink-A (30 mg/ml RSF, 10 mg/ml PEG_{400} and 4 mg/ml catalase) printed on Si-wafer substrates showing how the height is affected by the amount of layers printed on top of each other.

Figure 4-6 shows the average height of Ink-A printed columns is lower than the

average height of Ink-B printed columns. The thicknesses of each Ink-A and

Ink-B printed layer are about 0.22 μm and 0.20 μm, respectively. Figure 4-5 shows Ink-A printed columns are less defined structures than the column which is printed by Ink-B (in Figure 4-4) which results in the difference in the thickness of each printed layer. There was a clear relationship between height and amount of layers printed in Figure 4-6. The more layers printed, the higher the columns will be. The RSF ink without enzymes seemed to gain height slightly more rapidly than the one containing enzyme. This result is consistent with the observation of the two previous figures and the results published by Suntivich et al. [161]. The differences resulted from the different concentration of the used silk inks. One possible way to avoid the "messy" printing results of Ink-A could be extending drying time before printing next layer.
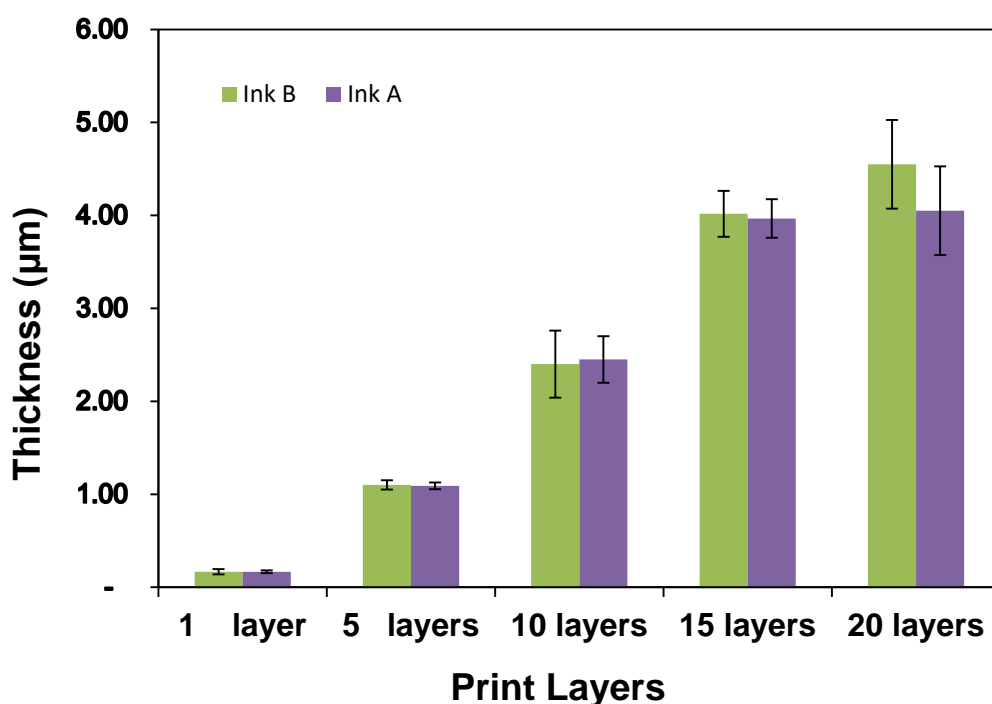
Figure 4-6 Column diagram shows comparison of average height measures of Ink-A (30 mg/ml RSF, 10 mg/ml PEG_{400} and 4 mg/ml catalase enzyme) and Ink-B (30 mg/ml RSF and 12 mg/ml PEG_{400}) , which are as same as the inks used for printing the micro-rockets.

4.3.1.3 Final Structures

The SEM images show the final printed columns structure for both fully active (Figure 4-7a) and Janus active (Figure 4-7b). According to the impact results (Section 4.3.1.2), this structure is characterized by a growth rate at around 0.22 μm/layer and by a diameter of the bottom of each pillar equal to 100 μm. In Figure 4-7, closer comparison of fully active particles and Janus particles shows that the overall size and shape of those particles are similar and the bottom is wider than the top which looks like 'rocket'. The reason for this 'rocket' structure is because during the printing process a little RSF inks flowed over the sides down the column. Furthermore, the overflowing inks smooth the edge surface of the rockets and avoid the rockets disintegrate between each layer when swim in solution. It also can be seen that the top of both fully active and Janus rockets is rounded, which verifies the 'Coffee Ring' structure diminished over printing multiple layers, as was suggested in Section 4.3.1.2. This also clarifies why the Janus rockets require printing first the half containing the enzyme catalyst rather than the half without, as the opposite way the catalase ink would have flow over inactive half and ruin the Janus samples.

In order to show the location of catalase in RSF rockets, catalase was labelled with FITC. In Figure 4-8, fluorescent microscope images verify the fully active rocket contains catalase all over (Figure 4-8A) and the Janus rocket only contain catalase on the bottom half of the particle (Figure 4-8B).
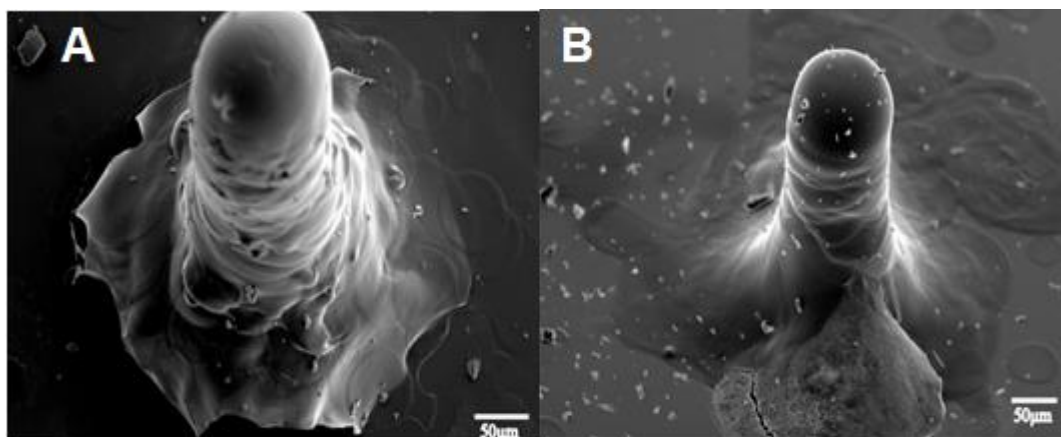
Figure 4-7 Two secondary electron images (at 12 KeV) of fully active silk swimmer particles containing CAT (4 mg/ml), Silk (30 mg/ml) and PEG$_{400}$ (10 mg/ml) and Janus silk swimmer particles containing CAT (4 mg/ml), Silk (30 mg/ml) and PEG$_{400}$ (10 mg/ml) with 10 layers of PMMA barrier and an inactive part containing silk (30 mg/ml) and PEG$_{400}$ (12 mg/ml).
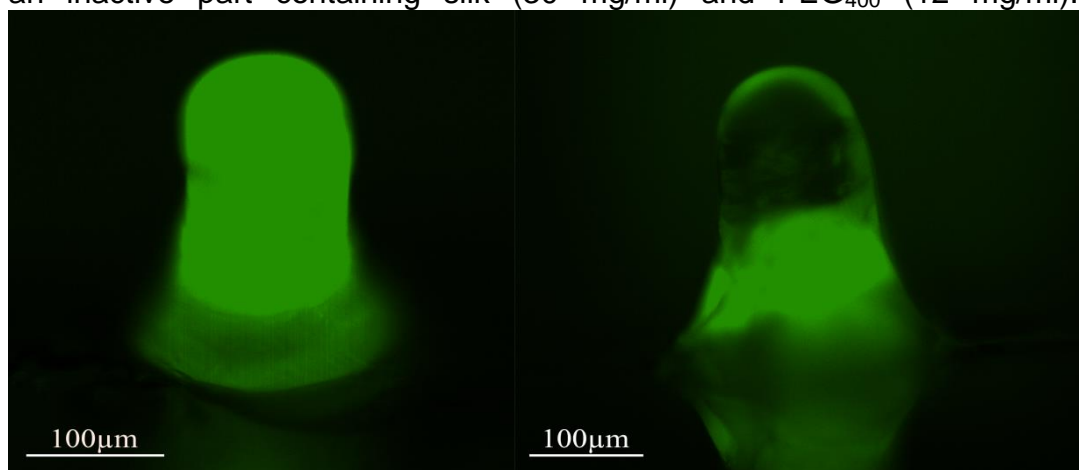
Figure 4-8 Fluorescent microscopy images of FITC labelled catalase in silk rockets, (left) fully active, (right) Janus.

4.3.2   Influence of PEG$_{400}$

Initial experimental data showed that when printed RSF-rockets, with enzyme but without PEG$_{400}$, were put into 5% hydrogen peroxide (H$_2$O$_2$) solution; even though bubbles were readily released form the silk particles, there was a high tendency for one bubbles to build up at the liquid / air interface sticking to the particles but not bursting regularly. An example swimmer is shown in Figure 4-9A that a fully active rocket with no PEG$_{400}$ mixed-in generates a bubble

which can be clearly seen growing over time (10 seconds) but not detaching. The big bubble also locked the swimmer inside it, instead of letting the swimmer move freely on the interface. Compared to CAT-RSF-rockets with PEG$_{400}$ in Figure 4-9B, the "locking" bubble did not appear and rocket moved around freely on the surface interface. In the case of Janus rockets it was observed that if the inactive half mixed no PEG$_{400}$ or contained a lower concentration of PEG$_{400}$ than the catalytic half there was a high probability of "locking" bubbles occurring and hindering the free motion of the rockets. Thus, when Janus rockets were printed with the concentration of PEG$_{400}$ in inactive half was higher than the active half.
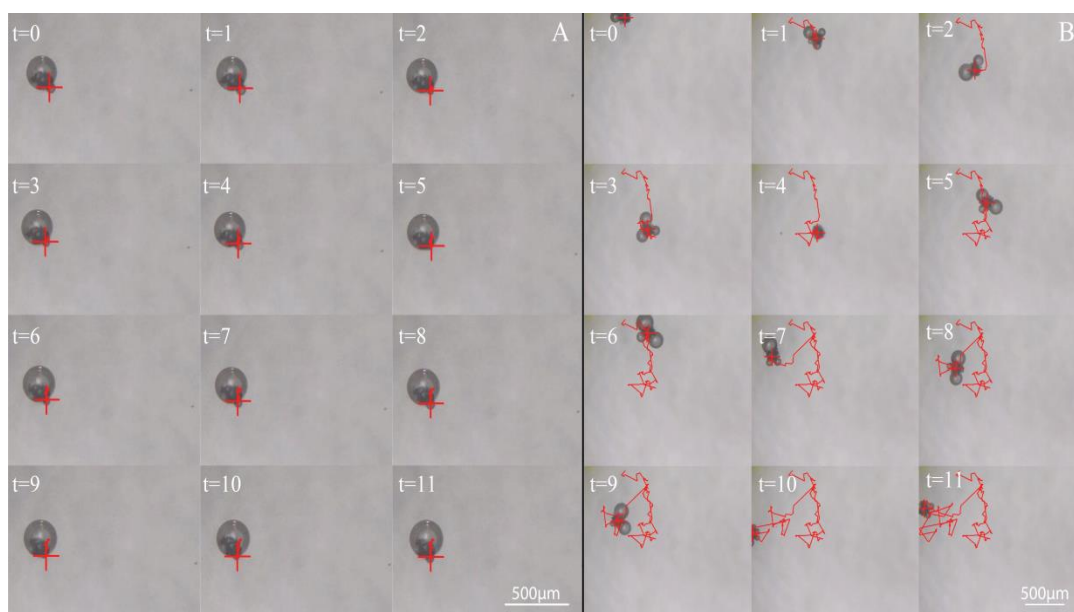
Figure 4-9 Video snapshot images of fully active CAT-RSF rockets (B) with and (A) without PEG$_{400}$ swimming in 5% W/V H$_2$O$_2$. Videos are taken from top-view as rockets swimming on the surface of the fuel solution.

Further analysis of how PEG$_{400}$ influenced the movement of RSF-rockets, the hydrophobicity of the mixture-RSF inks was tested by contact angle measurement. 5 layers of RSF solution with increasing concentration of

PEG_{400} were spun cast onto plasma cleaned silicon wafer substrates. By imitating inkjet printing process of RSF scaffolds, every layer of RSF was followed by spin coating a layer of methanol which helped to generate beta-sheet fibroin structure. The samples were then left to dry over night at room temperature. 2 μl Di-water drops loaded on the substrate, vertically. Each sample was measured 5 different locations and repeated at least 3 times. The contact angle was calculated by the mean value of each sample. Figure 4-10 indicates that the contact angle increased with decreasing the concentration of PEG_{400}. This means that the higher concentration of PEG_{400} blended in RSF ink the more hydrophobic the mixture solution will be.
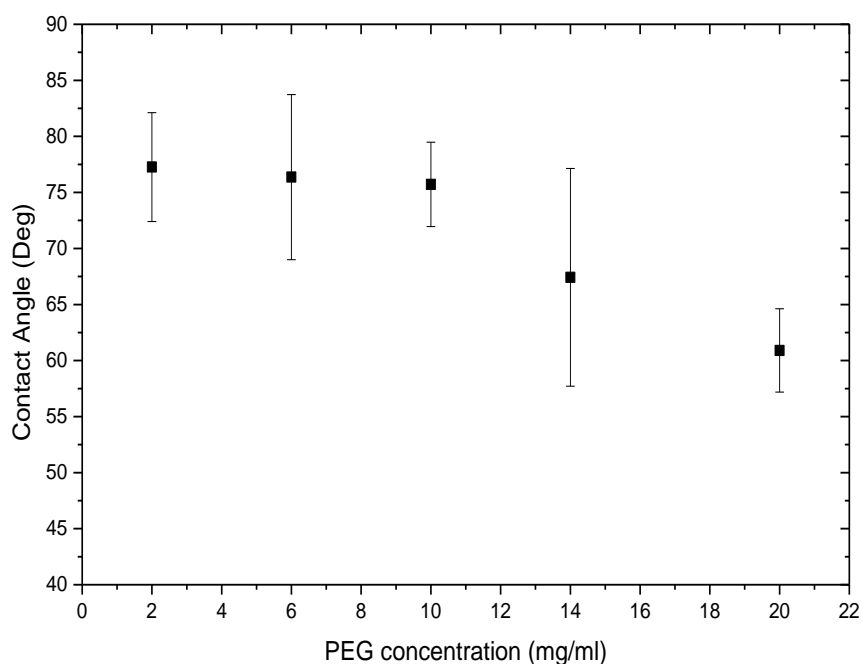
Figure 4-10 Plot showing different contact angle measurements of 5 layers of spin coated RSF (30 mg/ml) films with different concentarions of PEG_{400} mixed-in.

4.3.3   Trajectory Analysis

In this section, the trajectory of fully active rockets and Janus active rockets were analysed. Representative fully active and Janus rockets are showed in Figure 4-11 and Figure 4-12, respectively.

Silk printed swimmers resembled a rocket-like structure, which is characterized in detail through SEM in section 4.3.1.3. Thus, the swimmers were manually tracked on both their extreme points, which is dual point tracking. The dual point tracking allowed determination of the orientation changes and the direction of the self-propelled swimmers during their motion. The schematic image is showed in Chapter 2. Furthermore, it was ensured air moment was minimal during the experiments in order to mitigate any air induced surface flow effects.
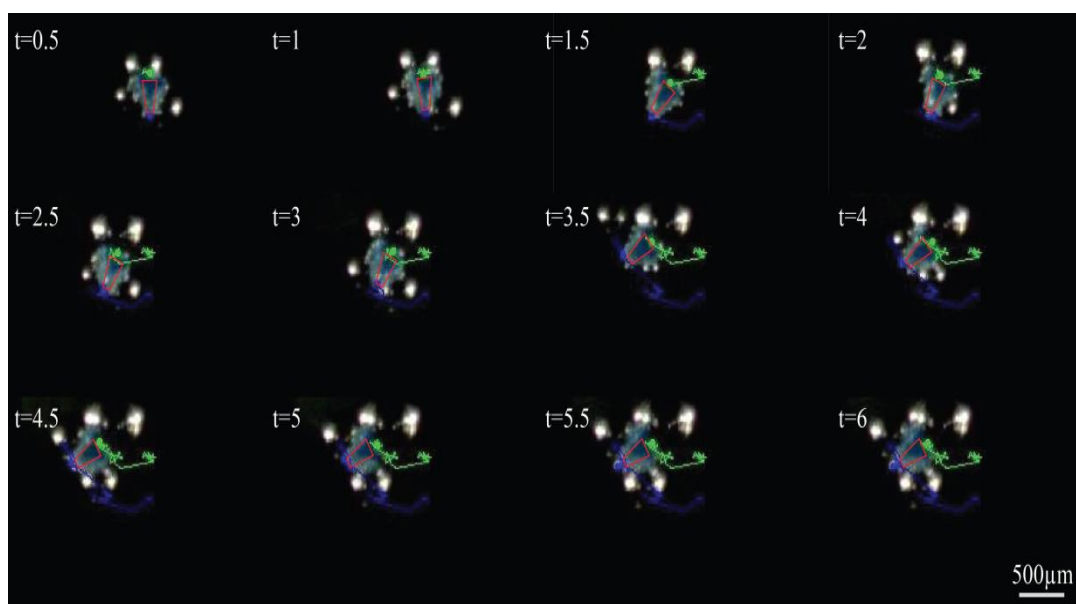
Figure 4-11 Example video snapshot images of a fully active silk rocket swimming in 5% H_2O_2 solution – blue line indicates top and green bottom of the rockets.
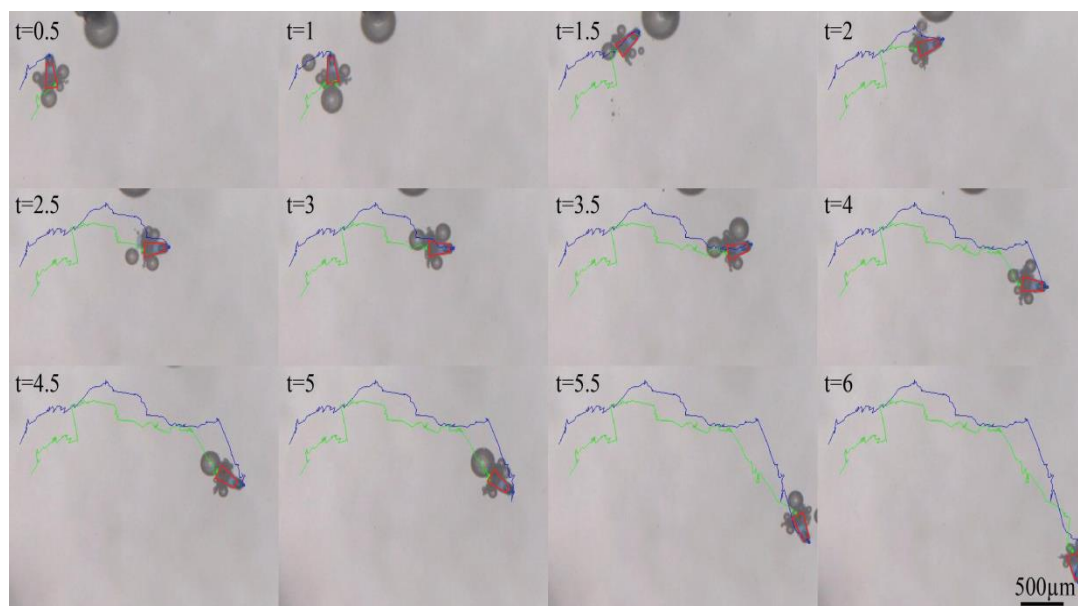
Figure 4-12 Example video snapshot images of a Janus silk rocket swimming in 5% H_2O_2 solution – blue line indicates top and green bottom of the rockets.

4.3.3.1 Directionality Analysis

In Figure 4-13, of the raw trajectories for the fully catalytic active micro-rockets and Janus catalytic active micro-rockets are summarized. Figure 4-13A shows these trajectories had a lot of turns and twists, whereas Figure 4-13B shows those trajectories that are directional resembling straighter lines.
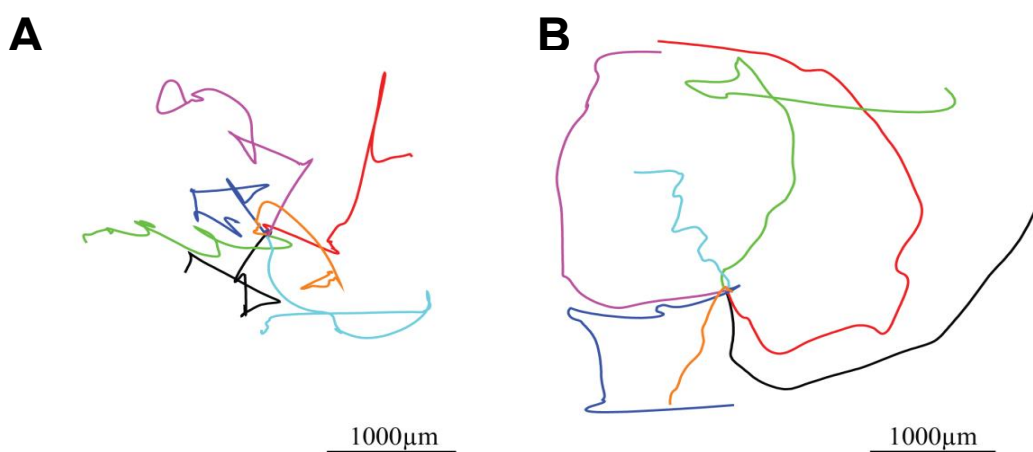
Figure 4-13 Comparison of raw trajectories, A) fully active rockets over a time period about 10 seconds; B) Janus rockets over a time period about 5-10 seconds.

As described in Section 2.5, directionality analysis of micro-rockets investigated the directional angle θ and orientation angle φ of the moving track; fully active and Janus active micro-rockets give strongly different results. As shown in Figure 4-14 and Figure 4-15, there was no noticeable correlation between θ and φ for fully active particles while there was a strong correlation between θ and φ for Janus active particles. The correlation coefficients over the sample set for fully and Janus active micro-rockets were r = = 0.053 ± 0.130 and r = 0.806 ± 0.146, respectively.
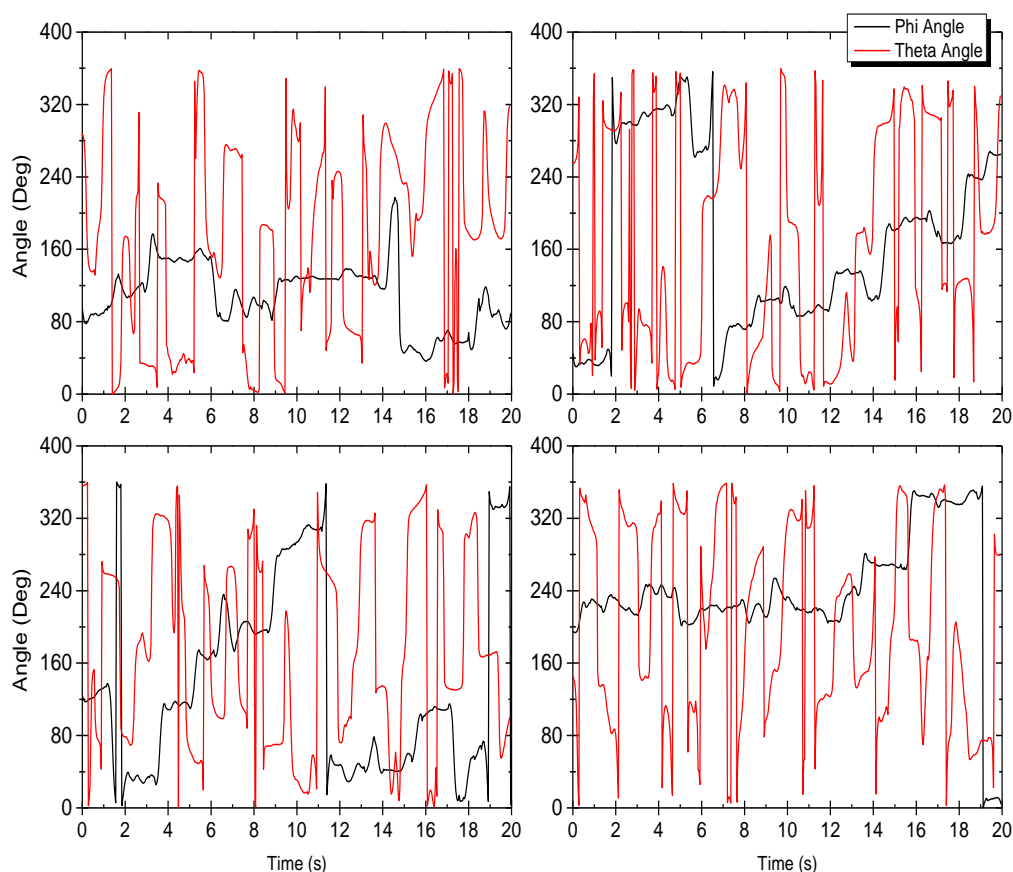
Figure 4-14 Angle Correlation (θ - direction and φ - orientation) of fully active RSF micro-rockets overall correlation for all samples was r = 0.053 ± 0.130.
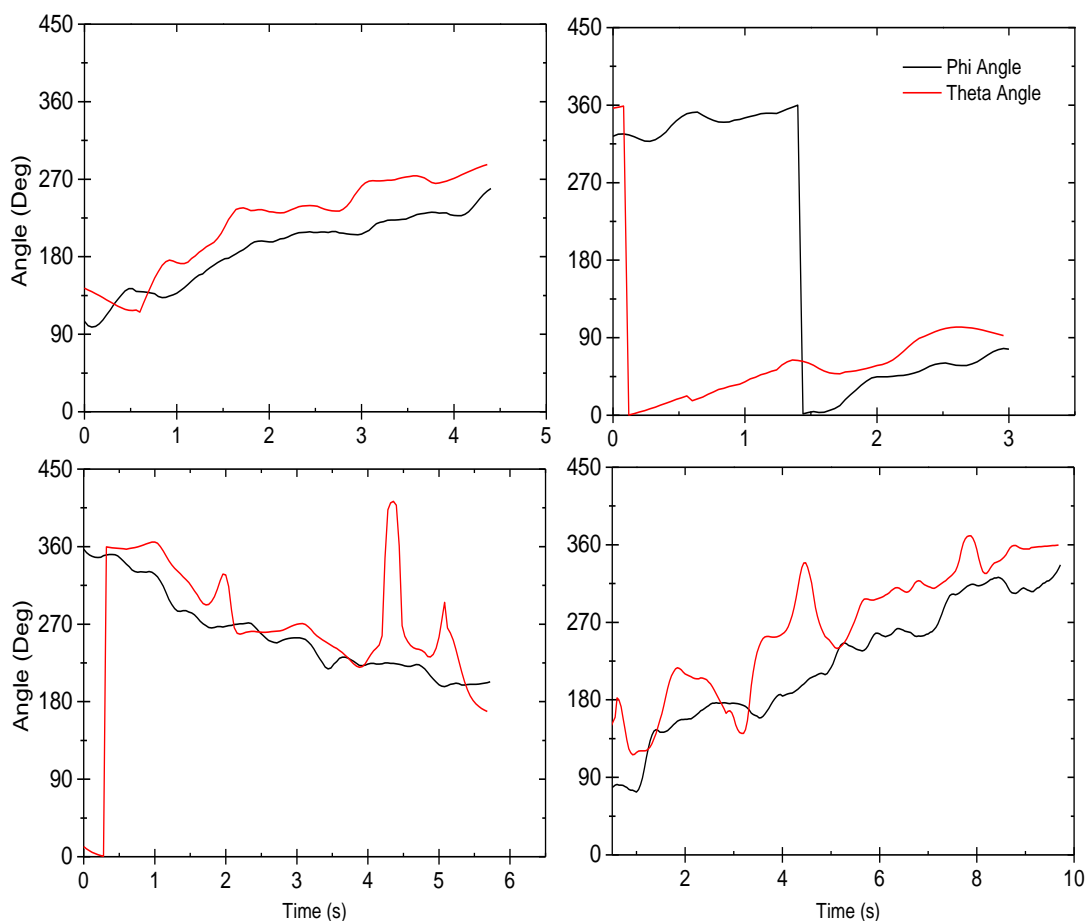
Figure 4-15 Angle Correlation (θ - direction and φ - orientation) of Janus active RSF micro-rockets overall correlation for all samples was r = 0.806 ± 0.146.

Furthermore, it was found that the high correlation of the two angles got disturbed by releasing a large bubble, as the bubbles which were over average size would cause the rockets to move a large distance to opposite direction when those bubbles busted.

It is important to notice that the angles for this analysis were calculated using the tangent function and therefore jumps in the data appeared when the angle changed from 0 ° to 360 °.

4.3.3.2 Velocity and Persistence length

As described in the trajectories analysis (section 4.2.7), each micro-rocket was calculated their man instantaneous velocities and their persistence lengths by analysing the centre of mass trajectory from the dual tracked swimmers. The results are shown in Table 4-2.

Instantaneous velocities were calculated for each frame and averaged over the whole trajectory. It has been showed that the fully active micro-rockets moving less directional than Janus active micro-rockets (in Figure 4-14 and Figure 4-15). However, the average velocity of the Janus micro-rockets was about 1.4 times faster than fully ones. Also, during the experiment, a decrease in velocity of 1/3 over the course of 1 hour was observed which was explained as the catalase denature.

Based on the calculated middle point of mass trajectory from the dual tracked micro-rockets, tracks were analysed for their persistence length. The results also are shown in Table 4-2; the mean persistence length of Janus active RSF rockets was approximated 16 times higher than that of fully active RSF rockets. This result was also consistence with the orientation correlation analysis in section 4.3.2.

Table 4-2 Velocity and persistence length for RSF micro-rockets

Type of Micro-motor	Average velocity [μm/s]	Persistence length [μm]	L_P/L_C [arb. units]
Fully Active rocket	370 ± 30	26 ± 6	0.014 ± 0.002
Janus rocket	510 ± 90	420 ± 180	0.190 ± 0.060

4.3.4   Optimisation of RSF Swimmer Printing Process

As shown in Figure 4-16, the schematic printing process provides another possibility to fabricate RSF swimmers which we defined as horizontal printing. Take generating Janus active RSF micro-rockets as an example, the vertical printing (method used in this chapter) print 250 layers of PEG_{400} / RSF ink droplets on the top of 250 layers of Catalase / PEG_{400} /RSF ink droplets; the horizontal printing print 250layers of PEG_{400} / RSF ink droplets beside 250 layers of Catalase / PEG_{400} /RSF ink droplets. As we described in section 4.3.2.1, the height of the RSF swimmers which were produced in vertical direction related of the total thickness of printed layers. However, the height of the swimmers which were produced in horizontal direction depended on the final length of the printed line on each layer. The width of the swimmers related to the diameter of the droplet in both vertical printing and horizontal printing.
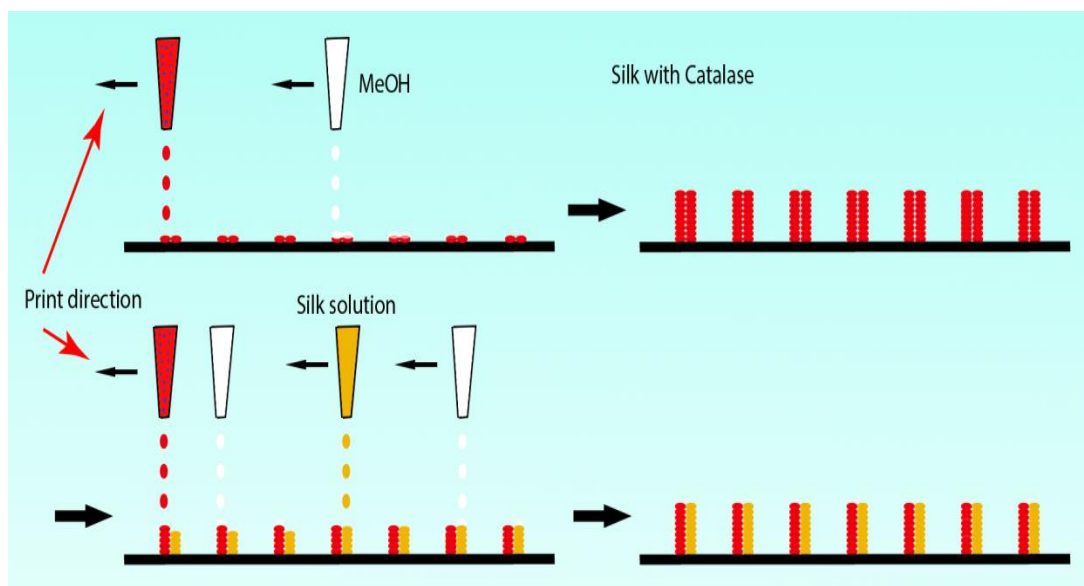
Figure 4-16 Schematic represents the LBL printing proceduce of silk scaffold in horizatial direction (image was designed by David Gregory).

Fluorescence microscope images (in Figure 4-17) show Janus active micro-rockets which are printed in both horizontal and vertical direction. Those images help to prove both ways can produce Janus swimmers. Special shape catalytic active swimmers like ' ⌐ ' and letters are generated and analysed in next two chapters.
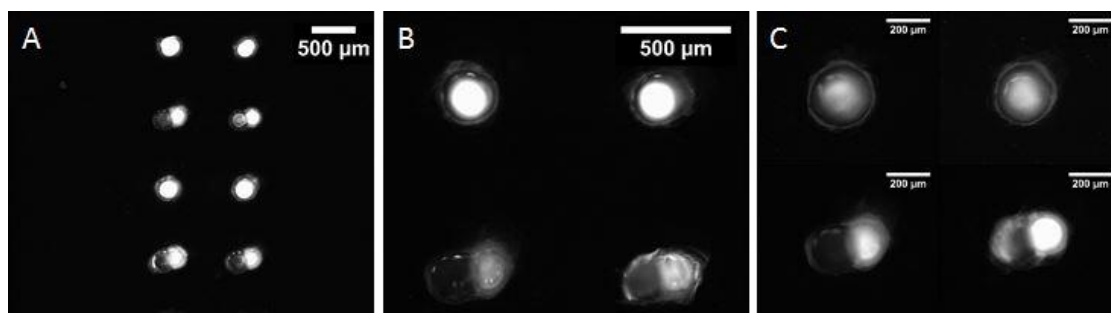
Figure 4-17 Fluorescence Microscope images of comparing printing RSF scaffolds in horizatal direction and vertical direaction.

4.4   Conclusions

In this chapter, it has become clear that the functional RSF inks (Ink-A: catalase/PEG$_{400}$/RSF; Ink-B: PEG$_{400}$/RSF) are printable by RIJ printer. The printed scaffolds which were formed by using the functional inks were well immobilized catalase and keep most of the enzyme activity. These scaffolds were driven by continuous bubbles generated during hydrogen peroxide decomposition at the catalase encapsulated part of scaffolds, demonstrated as new and novel self-propelled particles (swimmers). Furthermore, with the addition of mixed in PEG$_{400}$ in the inks, the bubbles would release more efficiency and the print-heads were not blocked that frequently during the printing time.

In this experiment, there were two types of swimmers: one is fully active micro-rockets, the other one is Janus micro-rockets. Based on comparing their trajectory analysis (including persistence length, oriental changes and direction of the motion), the printed structure and the position of the catalase motor altered the swimmers moving behaviour. For fully active micro-rockets, the trajectories show random diffusive behaviour. For Janus active micro-rockets, the trajectories mainly follow straight lines.

The printed RSF micro-rockets showed excellent swimming capabilities in fuel solutions. Inkjet printing appears to offer a chance to quickly design and fabricate a wide range of swimmers with varying shapes and sizes as well as easily altering the position of the propulsion location; therefore the following Chapters investigate a wide variety of swimmer designs.

Chapter 5 Reactive Inkjet Printing of Silk Stirrers

5.1 Introduction

Micro-mixing is a process in which ingredients rearrange to form a blend in a small volume. In recent years, the technology of micro-mixing has attracted increasing attention due to its applications in analytical chemistry [115, 202, 212], tissue engineering [213-215], and life sciences [216]. A possible way of achieving micro-mixing is by utilizing small self-motile catalytic motors. These motors, in general, are based on catalytic propulsion using hydrogen peroxide or hydrazine as a fuel source, which are not compatible in biological systems [100, 217-219]. Thus, biocompatible micro-motor devices that can stir in a small volume are particularly desired.

Initially, research on the small scale motors used for mimic experiments to proof of some concepts [135]. As more research helps to reveal the motion mechanisms, discovery of new energy input, and the development of procedures for modifying (e.g. chemical reaction and spin coating) these devices, the nano-/micro-motors become more functional and able to use into specific applications (i.e. water pollution detection) [100, 101, 112, 135, 220]. Especially, after the first catalytic centimeter-sized motors (called 'fish' by them) [221], the interest in artificial small-scale motors has had a boost. Nowadays, these small devices have been designed to perform selected mechanical movements (such as delivery, rotation, contraction, and collective behavior) in response to specific stimuli [135]. Stimuli include enzymatic [202, 214, 222, 223] or chemical reactions [100, 217], thermal [108] or concentration gradients [109], electric [114, 115] and/or magnetic fields [110, 113], ultrasonic acoustic waves [119] as well as light [116]. So far, a host of fabrication

methodologies were employed to fabricate multifunctional self-propelling devices, such as sputter coating [108, 116], angled electron beam evaporation [119], templated-assisted deposition [219], photolithography [224] and 3D printing [162, 225].

As described in Chapter 4, regenerated silk fibroin (RSF) micro-rockets were fabricated by inkjet printing of the enzyme-blended RSF based inks and were found to be able to self-propel in aqueous peroxide fuel solution, while catalase differentially decomposed hydrogen peroxide around the swimmers to engender the chemically powered locomotion [162]. These RSF swimmers showed excellent biocompatibility 'swam' well in biological solutions (human serum) without the addition of surfactants. It was also shown, by designing and printing the catalase in different locations, resulting trajectories of fully active micro-rockets and Janus micro-rockets are different. This gives rise to the assumption that it is possible to print differently shaped RSF swimmers that can be used as bio-stirrers for micro-mixing challenges.

In this Chapter, ' └┐ ' shaped swimmers were fabricated and used as bio-stirrers. Reactive inkjet printing allows the fabrication of RSF swimmers with digitally-defined compositions, shapes, and structures. The procedure is convenient without the need for multiple steps to generate complex scaffolds. The ' └┐ ' shape RSF-swimmers were designed by using two types of motion mechanisms: one mechanism is based on the catalytic reaction to decompose hydrogen peroxide to generate continuous bubble $[2\mathrm{H_2O_2}\,(l) \rightarrow 2\,\mathrm{H_2O}\,(l) + \mathrm{O_2}\,(g)]$ to power the swimmers; the other one is based on a surface tension gradient to power the swimmers. For catalytically powered RSF-swimmers, the location of engine is able to be controlled by printing catalase mixed RSF inks

129

to pre-set locations. Thus, single-engine (asymmetrical) and dual-engine (symmetrical) swimmers were fabricated for analyzing the effect of difference locations of engine enzymes on the locomotion of swimmers. Furthermore, different thicknesses (50 layers, 100 layers and 150 layers) were printed to investigate their power and trajectories in various concentrations (1 mg/ml, 10 mg/ml, 20 mg/ml, 30 mg/ml, 60 mg/ml, and 100 mg/ml) of H_2O_2 fuel solutions. For the surface tension gradient powered RSF-swimmers, the spin speed was analysed by comparing the trajectories of various thicknesses (50 printed layers, 100 layers and 150 layers) of the stirrers.

5.2   Experimental Methods

5.2.1   Materials

The details of the used materials were described in Chapter 2 Section 2.1.1.

5.2.2   Silk Degumming Process

The silk degumming process was described in Chapter 2 Section 2.1.2.

5.2.3   Preparation of RSF Solution

The preparation of RSF solution was described in Chapter 2 Section 2.1.3.

5.2.4   Preparation of Mix-RSF Solution

Two types of RSF-based ink solutions were prepared in this experiment. Ink-A consisted of Catalase/PEG_{400}/RSF, Ink-B made up of PEG_{400}/RSF. In order to avoid the inconvenience of weighing a high viscosity liquid, PEG_{400} (Aldrich) was diluted in deionised water at a concentration of 500 mg/ml. Amorphous bovine liver catalase powder (10,000 U/mg purity 60% Sigma-Aldrich) was pre-weighed in the vial. Finally, Ink-A was prepared by mixing diluted PEG_{400} solution with prepared RSF solution in the pre-weighed catalase vial giving final concentrations of 40 mg/ml RSF, 16 mg/ml PEG_{400} and 8 mg/ml catalase. Ink-B was prepared by mixing diluted PEG_{400} with RSF solution giving final concentrations of 40 mg/ml RSF and 20 mg/ml PEG_{400}.

5.2.5   Inkjet printing Process

The basic concept and operation of the DOD inkjet printer has been described in Chapter 2 Section 2.3.3. In this chapter, various ink solutions containing RSF as the scaffold material were used to print RSF stirrers. As described previously, the RSF scaffolds were formed by printing a drop of RSF-based ink followed by a drop of methanol through a second print head and switching between these two inks for every layer, this process is called reactive inkjet printing (RIJ). Methanol triggers the transformation of the conformational structure of the protein (described in Chapter 1 Section 1.3.1. As the conformation change of the SF from silk I to silk II is instant [6], the rapid evaporation time of a printed methanol droplet is enough for the formation of silk II without denaturing the catalase protein any significant amount during the printing process.

Three inks were used during the printing process: ink-A: RSF / Catalase / PEG_{400} mixture, ink-B: RSF / PEG_{400} mixture and ink-C: blue methanol. Ink-A and Ink-B were prepared as described in section 5.2.4. Ink-C was prepared by mixing brilliant blue, $C_{37}H_{34}N_2Na_2O_9S_3$ (FCF), into methanol (98.99%, sigma) to get a final concentration of 1 mg/ml.

The ' └┐ ' shaped stirrers were designed using Paint (version 1607, Microsoft Windows) and saved as a bitmap image. Then the bitmap image was programmed into JetLab (version 6.3, MicroFab Technologies). A schematic of the layer-by-layer (LBL) inkjet printing procedure of RSF stirrers with symmetric swimmers (both ends, **Figure 5-1**) and asymmetrical swimmers (one end, Figure 5-2), containing the catalase enzyme molecules, is shown.

The green colour represents the RSF / Catalase / PEG400 mixture (ink-A); yellow represents the RSF / PEG$_{400}$ mixture (ink-B) and blue the methanol ink (ink-C). The printing temperature was controlled between 18 – 20 °C and a relative humidity range between 50 - 65 %. If the humidity was lower than 50%, the print head would easily block and needed frequent cleaning during the printing procedure. However, for humidity greater than 65 %, the printed droplets need a longer time to dry and the formation of RSF scaffolds is more difficult.
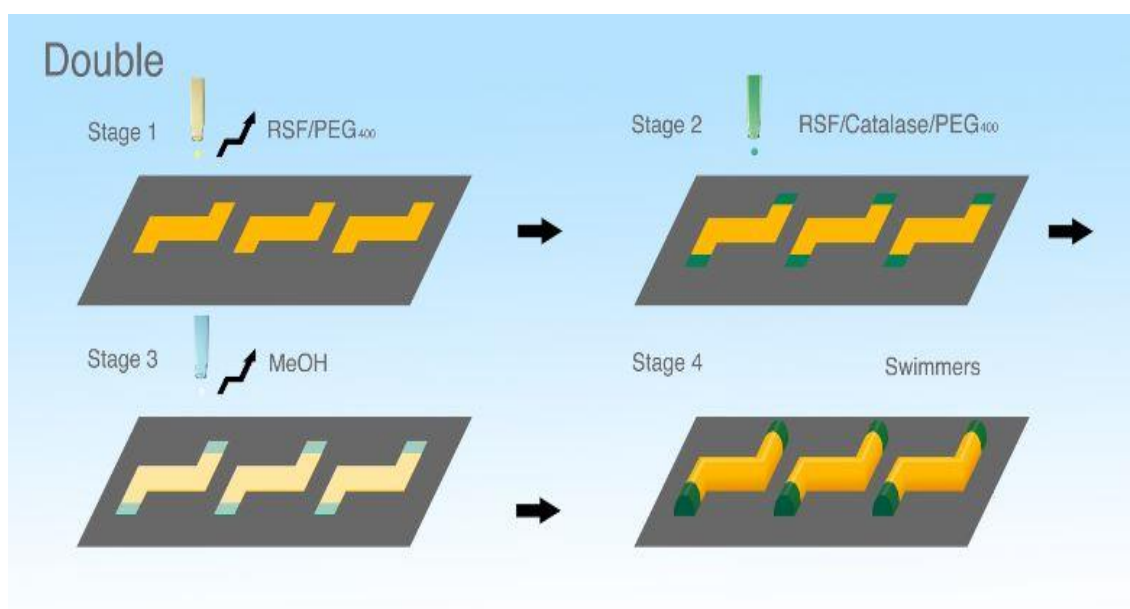
Figure 5-1 Schematic representing the LBL inkjet printing procedure of RSF stirrers with catalase enzyme molecules located at the two ends of the structure, green colour represents the RSF / Catalase / PEG400 mixture (ink-A), yellow colour represents the RSF / PEG400 mixture (ink-B) and sky blue represents methanol ink.

In this chapter, experiments were carried out to establish the relationships between the trajectory/rotation speed and the number of layers and the structure of stirrers. The concentration of H_2O_2 fuel and the location of catalase were investigated to understand the spinning speed and patterns.
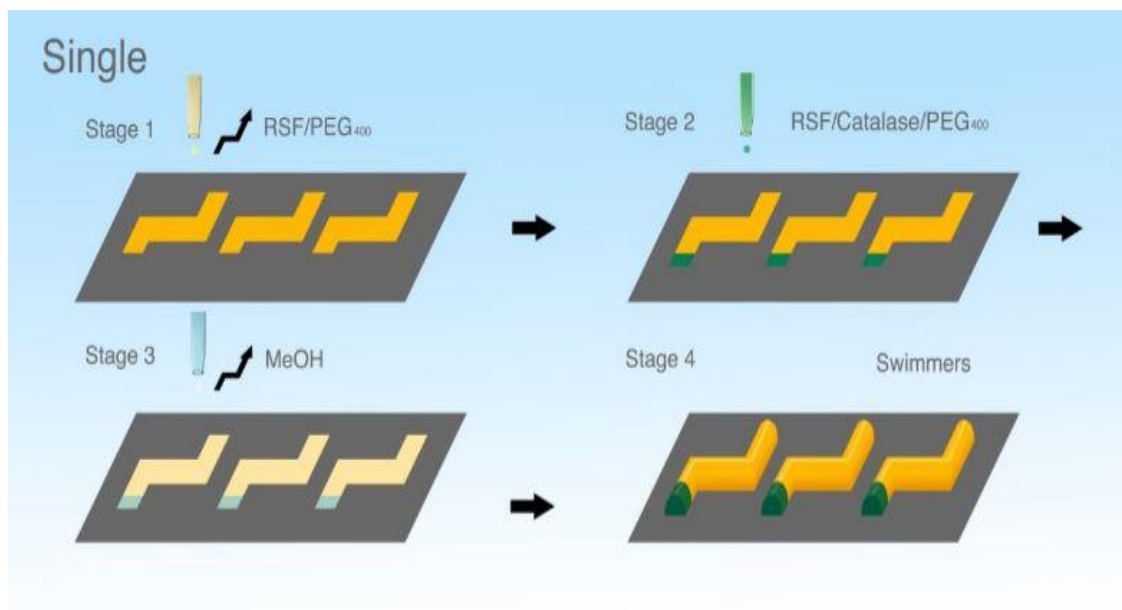
Figure 5-2 A schematic representing the LBL inkjet printing procedure of RSF stirrers with one side with catalase molecules, green colour represents the RSF / Catalase / PEG400 mixture ink, yellow represents the RSF / PEG400 mixture ink and sky blue represents methanol ink.

5.2.6   SEM

The surface and cross section morphologies of the scaffolds and pore distributions, sizes, and interconnectivity were observed with an Inspect[TM] F50 SEM. The specimens were sputter coated with gold and analysed at 5 kV (voltage).

5.2.7   Video analysis

Trajectory videos were taken in an enclosed cabinet in order to avoid external air flow effects influencing the motion of the 'stirrers'. Figure 5-3 shows the setup of the video recording system. An LED light pad was used as an illumination source to avoid side shadows from side-ways illumination. The petri dish (9 cm diameter) was placed on the Light pad surface.
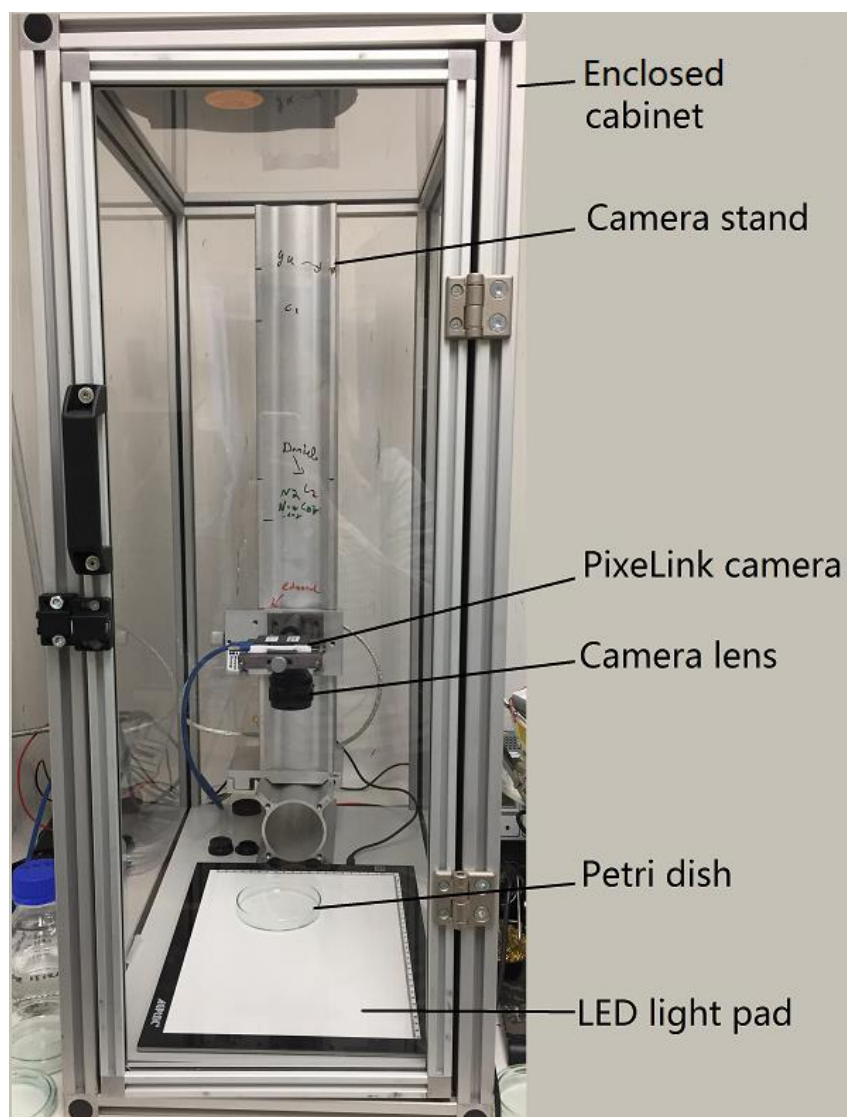
Figure 5-3 The setup of the video system. A custom built LabVIEW program was used to control the PixeLink camera and track the swimmers.

In this chapter, the ' └┐ ' shaped swimmers were driven by two types of propulsion mechanism: one was based on surface tension gradients, which are known as the Marangoni effect and described here as Marangoni (surface tension driven) locomotion, the other mechanism is caused by bubbles being release from the catalytic reaction therefore and is known as bubble propulsion, here referred to as catalytic reaction driven locomotion. For analyzing the catalytic reaction powered mechanism, the ' └┐ ' shape

swimmers needed some pretreatment steps: (1) washing in water to release the "unlocked" PEG_{400}, (2) incubating them in Di-water until they did not show any self-spinning (Marangoni) motion (3) drying for 5-10 minutes. By doing this it was possible to remove any surface tension driven locomotion to influence the bubble propulsion results.

The RSF-stirrers were tracked by a custom-built LabVIEW program (written by Dr David Gregory). The '⌐' shaped RSF-swimmers were manually selected in a rectangular frame and the middle point of the shorter side was the tracking points (dual point tracking). The dual point tracking allowed determination of the direction of motion and orientation changes of the self-propelled RSF-swimmers during their motion and the schematic is shown in **Figure 5-4**. The angle of travelling (Φ) and the angle of orientation (θ) were calculated for every frame of the videos. It was important to smooth the tracking point data through a Savitzky-Golay filter using k = 10 side point because of the start-stop type motion observed for bubble propulsion mechanisms (described in Chapter 2).

Also, in order to calculate instantaneous velocity and persistence length, the centre of mass trajectory point was calculated from the dual tracking and fed into the custom made LabVIEW analysis program. The analysis methods are described in Chapter 2 Section 2.5.
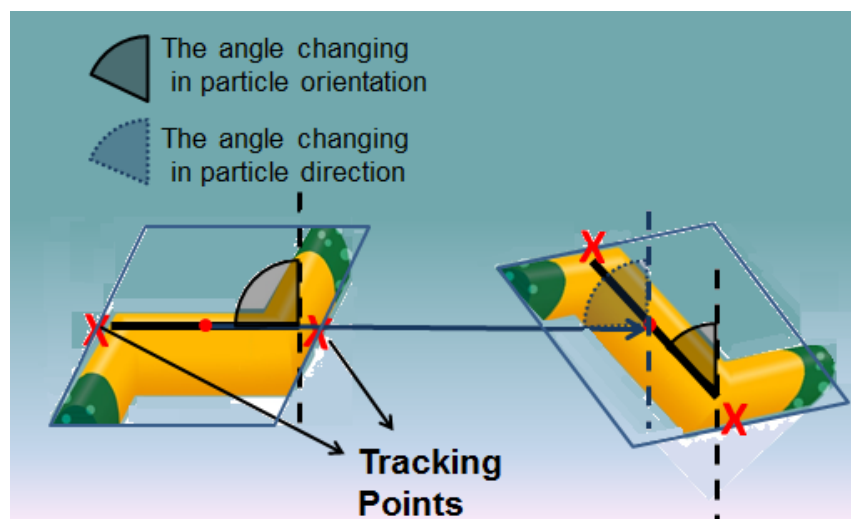
Figure 5-4 A schematic demonstrates the angle of travelling (Φ) and the angle of orientation (θ) of the stirrers.

5.3   Results and Discussion

5.3.1   Selection of silk swimmers

All printed swimmers were checked under an optical microscope in order to select equivalent stirrers. The following SEM images were taken from the printed RSF scaffolds prepared in the same way as those used for the swimming experiments described in Sections 5.3.2-5.3.5.

5.3.1.1 Characterisation of swimmers printed using different ink mixtures

To reveal the surface and inside structures of the swimmers, simple rod-shaped scaffolds were printed for SEM investigations. The SEM images (**Figure 5-5**) below show the different RSF scaffolds prepared by using different RSF-based ink mixtures. Four different mixed inks were used: A) 40 mg/ml RSF, B) 40 mg/ml RSF with 16 mg/ml PEG_{400}, C) 40 mg/ml RSF with 20 mg/ml PEG_{400}, and D) 40 mg/ml RSF, 8 mg/ml catalase and 16 mg/ml PEG_{400}. For each scaffold printed by different inks, the SEM images were taken at 3

different stages: the originally printed scaffolds, the DI-water washed scaffolds and after reacting with H_2O_2, respectively.

Figure 5-5A shows the SEM images of the scaffolds printed using RSF ink. The surface morphology of the original (just after printing) was smooth with no visible pores and was. The smoothest in contrast to scafforlds exposed to H2O2 which showed many pores. The roughness of scaffolds incubated in water was in between, rougher than the original scaffolds while smoother than the scaffolds reacted in H_2O_2.

Three of the four used inks contained PEG_{400} and the printed scaffolds using these inks are shown in **Figure 5-5**B, C and D, respectively. Interestingly, the scaffolds with PEG_{400} show the "skirt" shape structure at the bottom which did not show in the RSF only scaffold (**Figure 5-5**A).The Red rectangle frame marked the "skirt" shape structure in **Figure 5-5**. The "skirt" structure may be caused by the addition of the PEG_{400} in the inks as only scaffolds with PEG_{400} showed these "skirt" shape structure. Comparing **Figure 5-5**B and **Figure 5-5**C, the original scaffolds and the scaffolds in water are similar in both roughness of the surface and shape of the structure. However, the scaffolds reacted in H_2O_2 in **Figure 5-5**C were observed more layered structure than those were showed in **Figure 5-5**B, demonstrating the different concentration of PEG_{400} effect the structure of the scaffolds. Comparing all the images in **Figure 5-5**, the surface morphology of the printed scaffolds changed after they swam in the H_2O_2 fuel. In generally, the original scaffolds had the smoothest surfaces and the surface become rougher after water washing. The scaffolds, which reacted with H_2O_2, have the roughest surface, especially, the scaffolds that contain catalase. The catalase reacted with H_2O_2 and generated oxygen

bubbles which resulted in the porous structure on the printed scaffolds (shown in **Figure 5-5**D). The black spots in some of the images caused by sputter coating the samples before they dried totally.

C 40 mg/ml RSF and 20 mg/ml PEG$_{400}$

Origin

H$_2$O

H$_2$O$_2$

D 40 mg/ml RSF, 8 mg/ml catalase and 16 mg/ml PEG$_{400}$

Origin

H$_2$O

H$_2$O$_2$
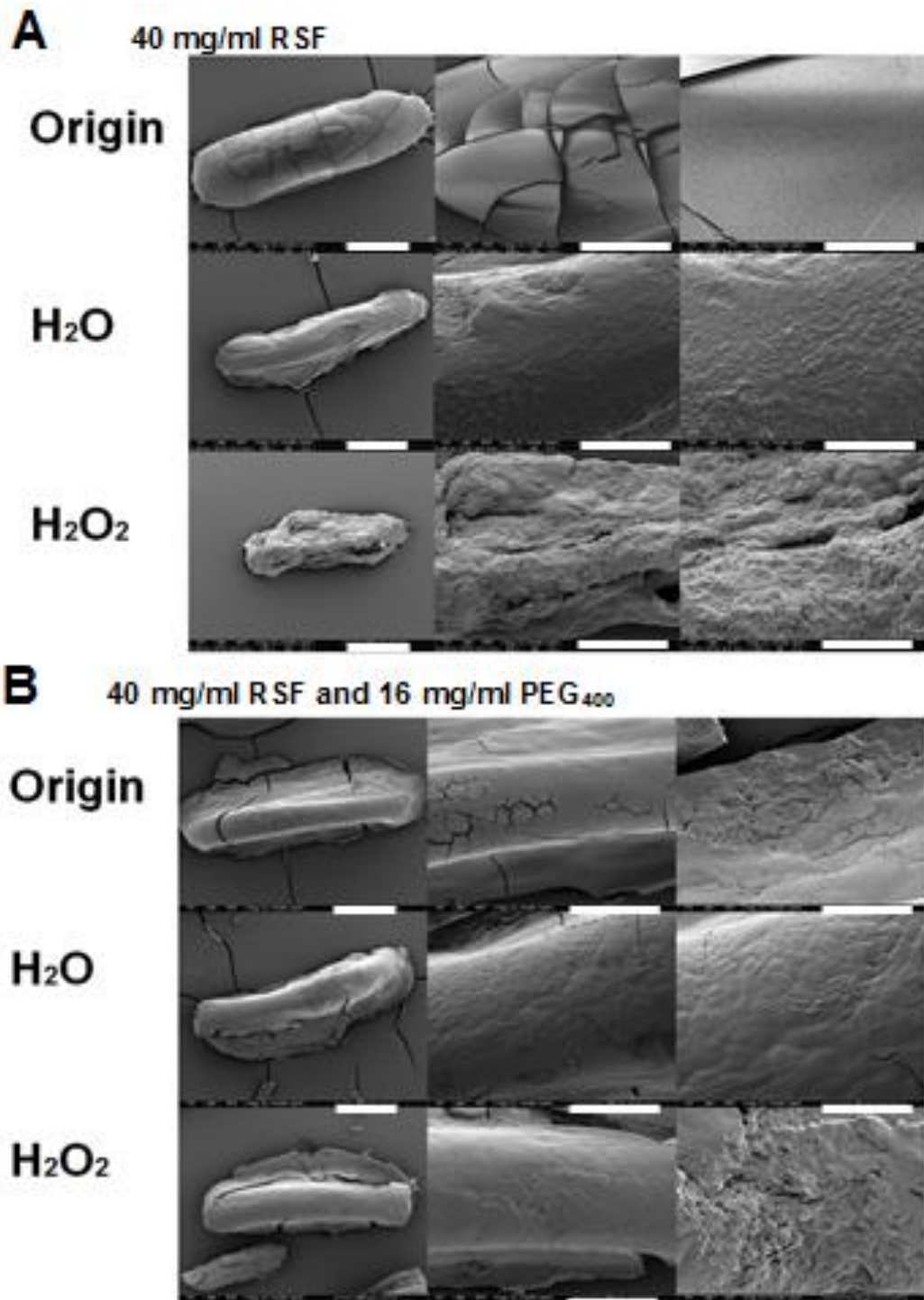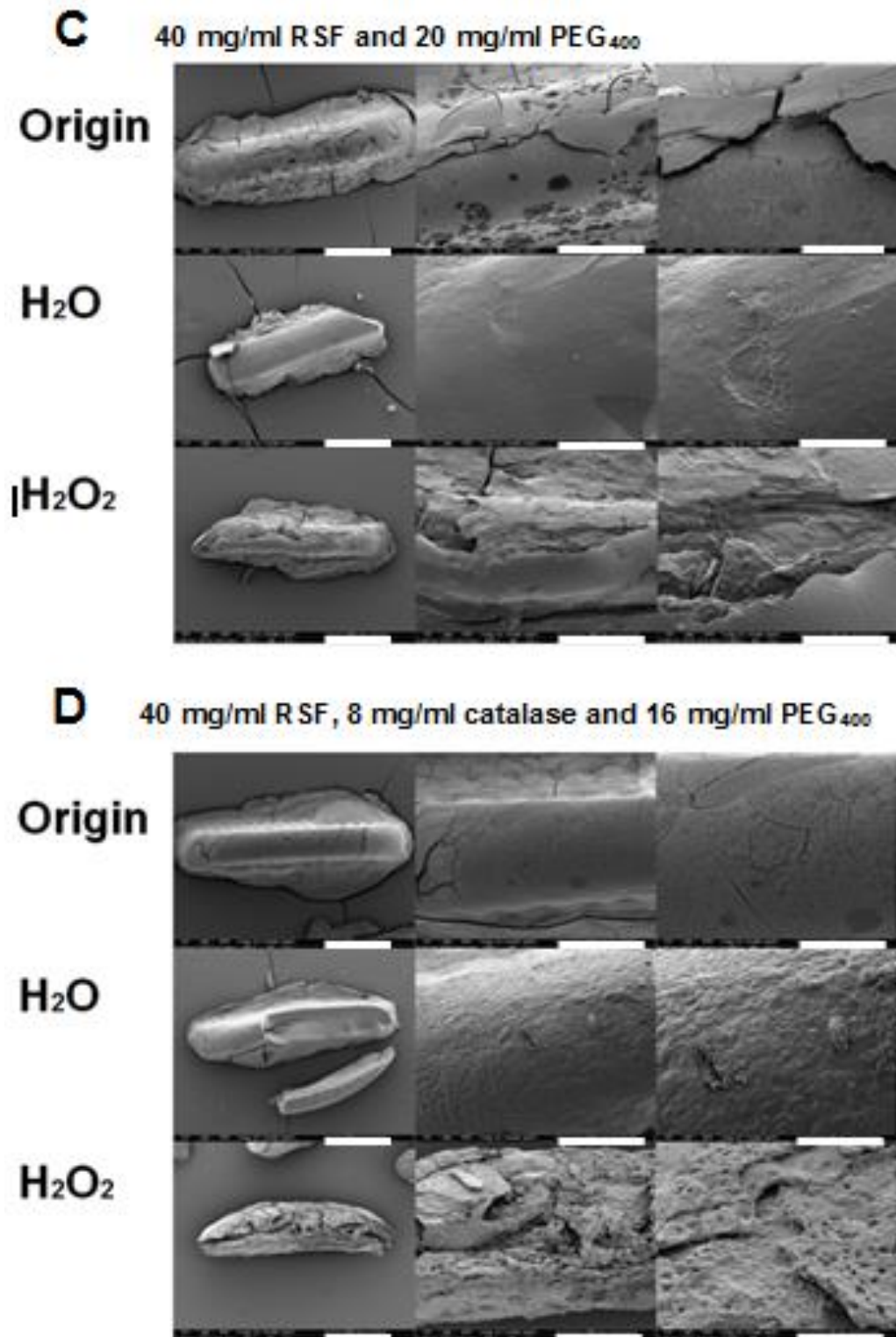
Figure 5-5 Scanning electron microscopy (SEM) images of different scaffolds printed using different ink mixtures. A) 40 mg/ml RSF, B) 40 mg/ml RSF and 16 mg/ml PEG$_{400}$, C) 40 mg/ml RSF and 20 mg/ml PEG$_{400,}$ and D) 40 mg/ml RSF, 8 mg/ml catlase and 16 mg/ml PEG$_{400}$. For each ink, SEM images showed the origin printied scaffolds, DI-water washed scaffolds and the scaffolds after reacted with H$_2$O$_2$.

Apart from investigating the external structure of the RSF scaffolds, it is important to analyse the internal structure of the RSF swimmers. For surface tension driven locomotion, the internal structure affects how the PEG_{400} will be released into the water. For the bubble propelled swimmers, the internal structure reveals how the bubbles migrate through the swimmers' scaffolds and where the bubbles to leave the swimmers.

Figure 5-6 shows the cross-section view of various RSF based scaffolds (RSF, RSF with PEG_{400} and RSF/PEG_{400}/catalase). All these scaffolds were original scaffolds without any treatment such as washing in water or reacting in H_2O_2 fuel solution. There was no clear difference of the cross-section area between those scaffolds. All these scaffolds showed rough surfaces on the cross-section areas. The magnification of the top row of the SEM images was 150 times with 500 µm scale bar. The SEM images in the middle row of **Figure 5-6** showed the hierarchical structure of the scaffolds under 1000 times magnification with 100 µm scale bar. At high magnification (5000 times), the SEM images (the bottom row in **Figure 5-6**) show a porous structure for all four types of scaffolds with 20 µm scale bar.
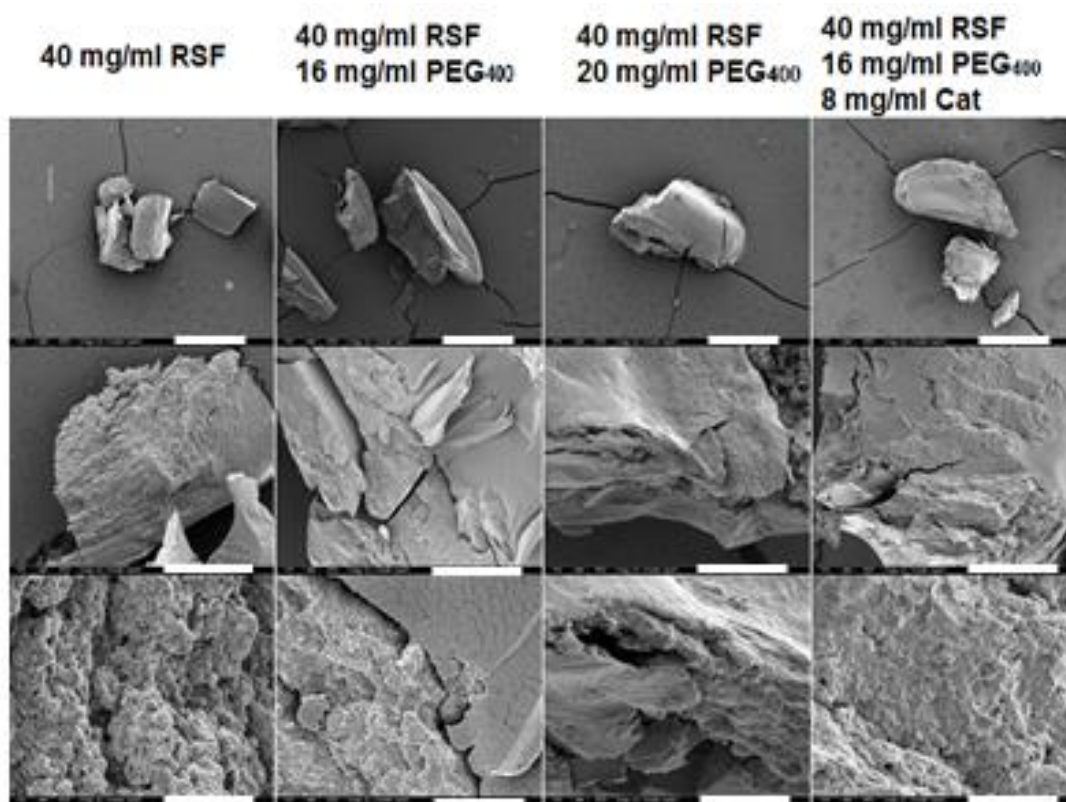
Figure 5-6 Scanning electron microscopy (SEM) images of cross-section view of different scaffolds printed using different RSF ink mixtures, A) 40 mg/ml RSF, B) 40 mg/ml RSF and 16 mg/ml PEG$_{400}$, C) 40 mg/ml RSF and 20 mg/ml PEG$_{400}$, and D) 40 mg/ml RSF, 8 mg/ml catlase and 16 mg/ml PEG$_{400}$. The SEM images were taken at 5 kV and different magnifications: 150 X magnification for top row, 1000 X magnification for middle row and 5000 X magnification for the bottom row, with 500 µm, 100 µm and 20 µm scale bar, repectively.

5.3.1.2 Structures of the swimmers

Figure 5-7 shows scanning electron micrograph (SEM) images of several typical printed RSF stirrer samples in different views. As described in Section 5.2.5, the main body was printed by using RSF/PEG$_{400}$ ink while the RSF/Catalase/PEG$_{400}$ ink was used for the printing of the two "engines" parts. The stirrers which were analysed by SEM were dried and exposed to with/without fuel solutions (60 mg/ml H$_2$O$_2$).

From the top-view (shown in Figure 5-7A-C), the length of the stirrer was about 1800 µm and the width of the main body was approximately 250 µm. In Figure

5-7A1-C1, the stirrers which were not exposed to fuel solution have smooth surface morphology. Figure 5-7A2-C2 shows stirrers which were exposed to H_2O_2 solution for 2 hours. The surface morphology, which was mainly formed by the RSF/Catalase/PEG_{400} ink, is rough and porous, whiles the surface of the main body of stirrers (resembled with RSF/PEG_{400} ink), was flat and smooth. The bulge shapes were caused during the initial formations of bubbles below the silk layers before pored opened up to release the bubbles. The bubble migration within the swimmers then is most likely the result of the porous inner structures as seen previously in **Figure 5-6**. Figure 5-7D-F show the lateral view of the RSF stirrers, a stratified structure can be observed by magnifying the images. A probable explanation of this stratified structure is that it is caused by the LBL printing of alternating mixture RSF and methanol Inks forming accumulating silk II scaffold films.

In order to analyse the interior structure of the stirrers, the stirrers were cut in the middle of the main body and the cross-section was placed facing upwards and attached with Kapton tape. Figure 5-7G shows the sectional view of the stirrers, demonstrating the interior structure of RSF / PEG_{400} mixture ink formed scaffolds. By magnifying the SEM images, the cross section (Figure 5-7I) showed pores with diameters ranging from 0.2 – 1 µm. This means that the interior structure of these stirrers was porous.
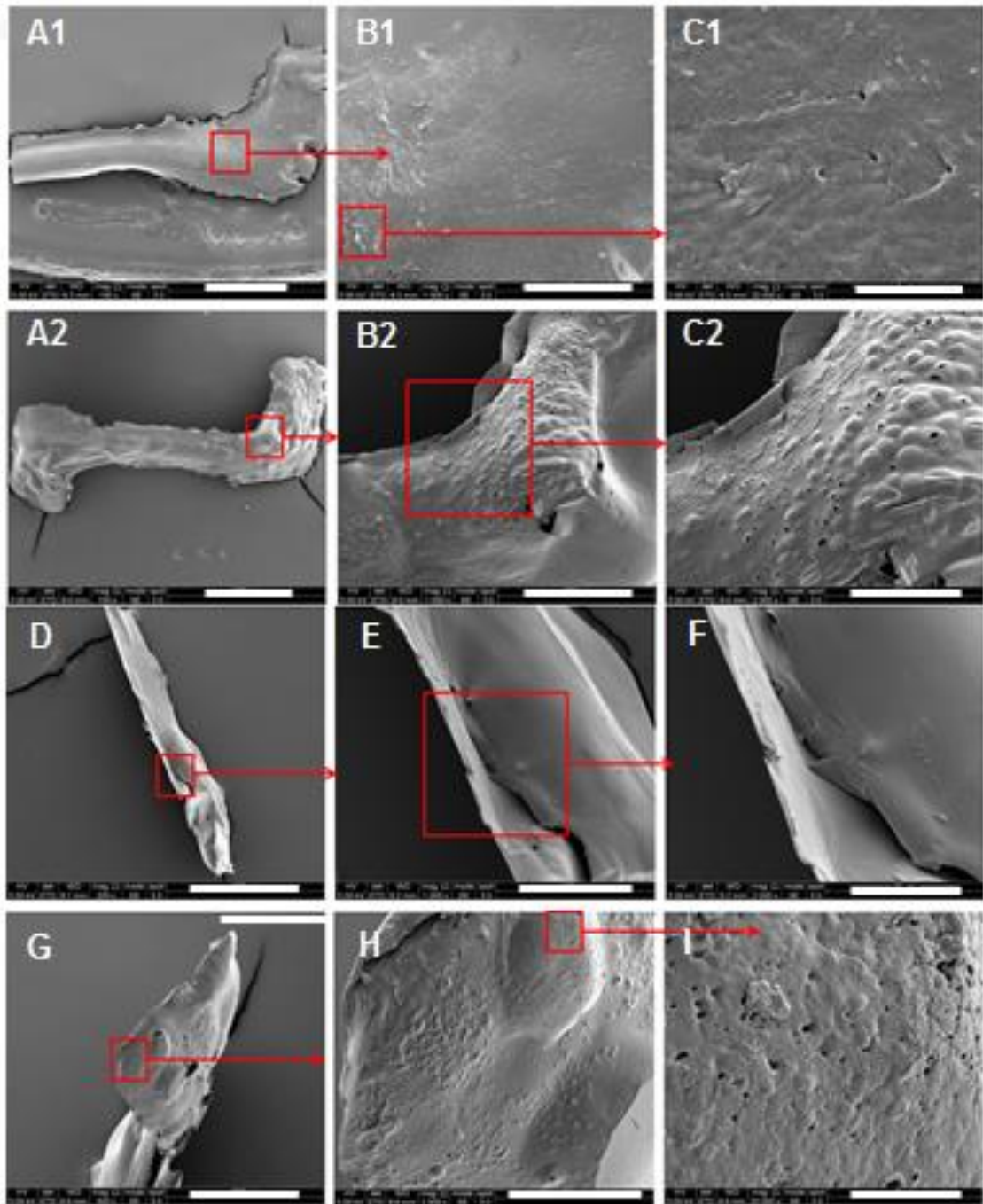
Figure 5-7 Scanning electron microscopy **(**SEM) images of RSF stirrers, showing the top-view (A-C), the lateral view (D-F) and the sectional view (G-I) of them.

5.3.2   Self-motived RSF-Stirrers: surface tension driven locomotion

As described in Chapter 4 Section 4.3.2, adding PEG_{400} in RSF solutions helped bubbles release from the printed RSF-scaffolds surface and also helped to prevent the accumulation of RSF drying at the edge of printer

nozzles. Initially swimmers containing PEG_{400} were prepared. However, during the course of the initial experiments, it was found that PEG_{400} was also able to generate an unexpected rotational propulsion effect. PEG_{400} is known to be able to modify surface tension. In 2004, Nakata et al. reported an asymmetry disk undergoing motion due to surface tension gradients [226]. In addition to this in a recent data, a self-propelling rotator driven by soluto-capillary Marangoni flows [134] has been described. Thus, the most probably cause of motion for RSF swimmers in water containing PEG_{400} would suggest being surface tension driven.

To determine whether the unexpected rotational propulsion effect is caused by PEG_{400} dissolving into water, the swimmers were removed off the silicon wafer by means of a sharp needle ensuring they did not get into contact with water before the experiment. **Figure 5-8** shows representative trajectories of RSF stirrers in water in for the first 10 seconds of the first, fifth and tenth minutes, respectively. It was clear that the RSF swimmer rotated quickly at the beginning and decreased with time. Table 5-1 lists the velocity and rotation speeds of RSF stirrers (n>3 stirrers were tracked) in water during different times. The results showed that the average velocity of the first minute (60000 ± 20000 μm/s) was approximate 15 times that the average velocity of the fifth minute (4000 ± 1000 μm/s) and about 120 times than the average velocity of the tenth minute (500 ± 100 μm/s). As previously described in section 2.5 directionality and orientation of the swimmers can be calculated. From the orientation angle it is possible to count the amount of times the swimmers undergo a full rotation. By counting the time the angle changes form 360 to 0 it

is therefore simple to count the amount of rotation over a given timeframe and calculate the rpm, as shown in

Figure **5-9**. Table 5-1 shows that the rotation speeds of the first minute (96 ± 3 rpm) were approximate 5 times than the rotation speeds of the fifth minute (20 ± 1 rpm) and about 32 times than the rotation speeds of the tenth minute (3 ± 0.5 rpm). The total spinning process lasted approximately 10 to 15 minutes for each swimmer in a volume of 20 ml Di-water and a surface area of about 50 cm^2.
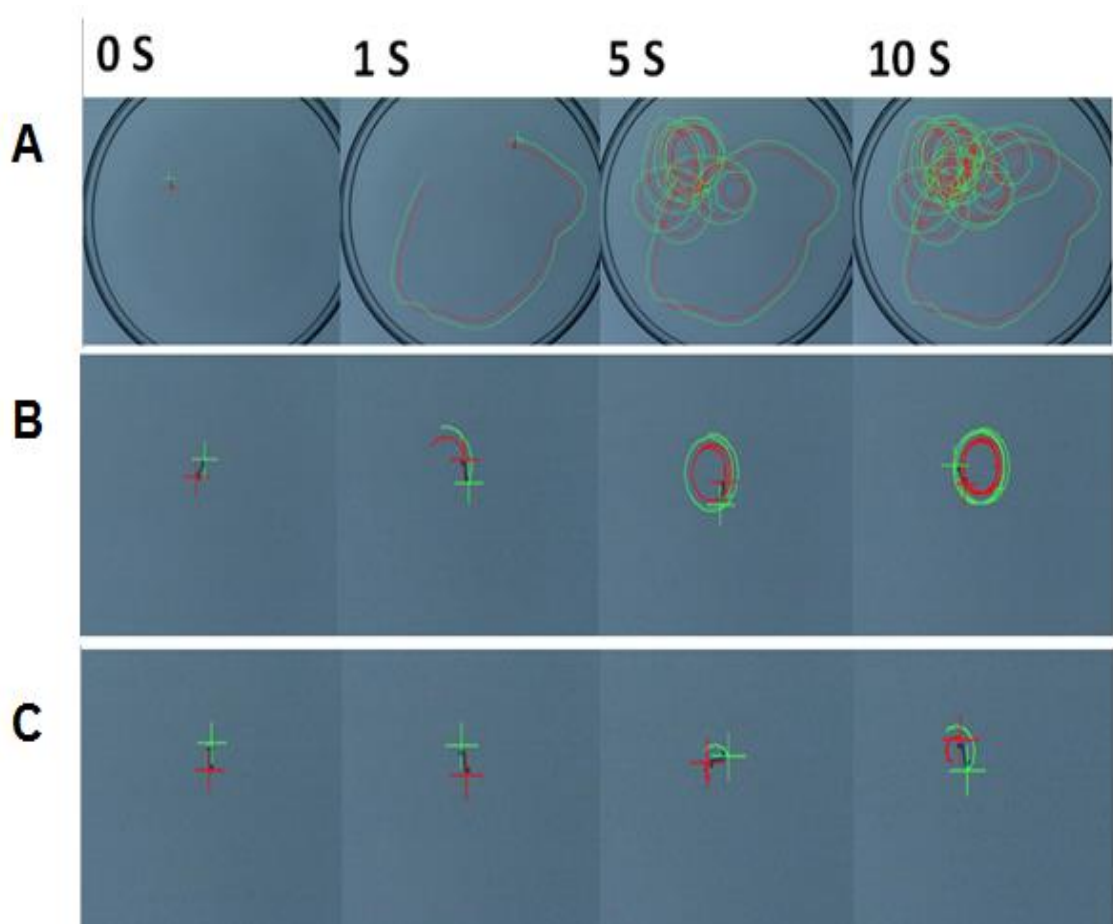
Figure 5-8 Example video snapshot images of RSF stirrer in water from starting spinning to the end. A) initial 10 second of the first minute, B) initial 10 seconds of the fifth minute, and C) initial 10 seconds of the tenth minute.
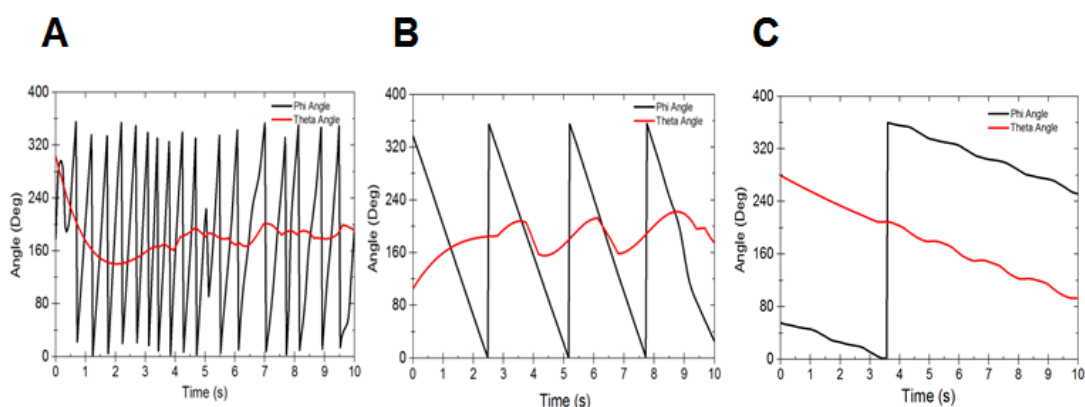
Figure 5-9 Representative samples of angle correlation (θ - Orientation and ψ - direction) of RSF stirrers in water for A) initial 10 second of the first minute, B) initial 10 seconds of the fifth minute, and C) initial 10 seconds of the tenth minute.

Table 5-1 Velocity and Rotation Speed of RSF stirrers in water during different times.

Time	Average Velocity (μm/s)	Vel A/ Vel B (μm/s)	Rotation Speed (rpm)
1st minute	60000 ± 20000	24000 ± 10000 / 50000 ± 20000	96 ± 3
5th minute	4000 ± 1000	2800 ± 400 / 4500 ± 2000	20 ± 1
10th minute	500 ± 100	250 ± 100 / 440 ± 100	3 ± 0.5

The mechanism is able to be explained as the movement of the swimmers was from the released PEG_{400} releasing in the water and resulting in the concentration gradients around the swimmers. The concentration gradients of PEG_{400} around the swimmers further result in the surface tension gradients around the swimmers. This therefore causes the swimmers to undergo self-propulsion at the air liquid interface. **Figure 5-8** shows the swimmers to spin at the surface of water, if pushed into the bulk solution, no motion is observed. This indicates that the stimuli of the movement come from the changing of surface tensions. In order to prove this mechanism, the surface tensions of

different concentration of PEG$_{400}$ were measured and are shown in **Figure 5-10**.

The results revealed that the surface tension of PEG$_{400}$ solutions decreased with the increasing concentration. Therefore, when a swimmer was placed on the surface of Di-water, the PEG$_{400}$ released around the swimmers and resulted in the concentration of PEG$_{400}$ in water around the swimmers sharply increasing. Then, the surface tension of the area where the concentration of PEG$_{400}$ sharply increased was sharply decreased. This is also known as the Marangoni effect. Finally, the changing of surface tension drove the motion of the RSF swimmers with PEG$_{400}$. The results are consistent with the suggested mechanism (Marangoni locomotion).
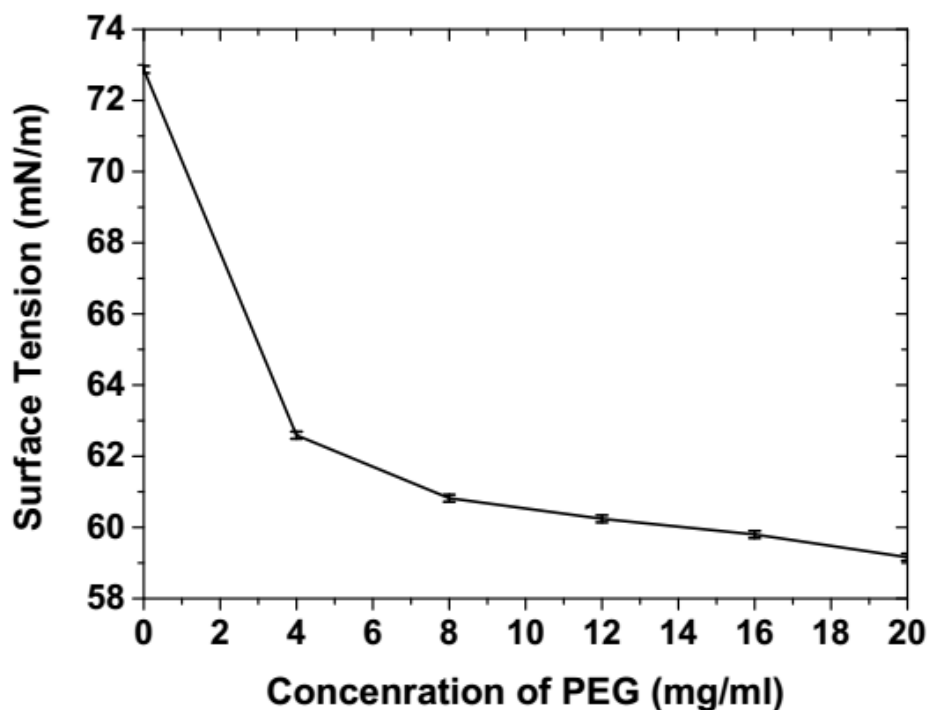
Figure 5-10 Surface tension (mN/m) vs concentration of 4, 8, 12, 16, and 20 mg/ml PEG$_{400}$ in Di-water.

5.3.3 Catalytic powdered RSF-Stirrers – bubble propulsion

In this section, the swimmers were driven by bubble propulsion generated by the decomposition of hydrogen peroxide fuel.

5.3.3.1 RSF stirrers with different locations of catalytic power

Trajectory lines help to do direction analysis, the changing of angles, and velocity of printed swimmers. Representative trajectories of the single-engine and both sides of ' ⌐ ' shape RSF-stirrers are shown in **Figure 5-11** and **Figure 5-12**, respectively. The results illustrate the thrust created by bubbles generated during H_2O_2 decomposition at the one end and two ends of the swimmers in single-engine and dual-engine swimmers, respectively.
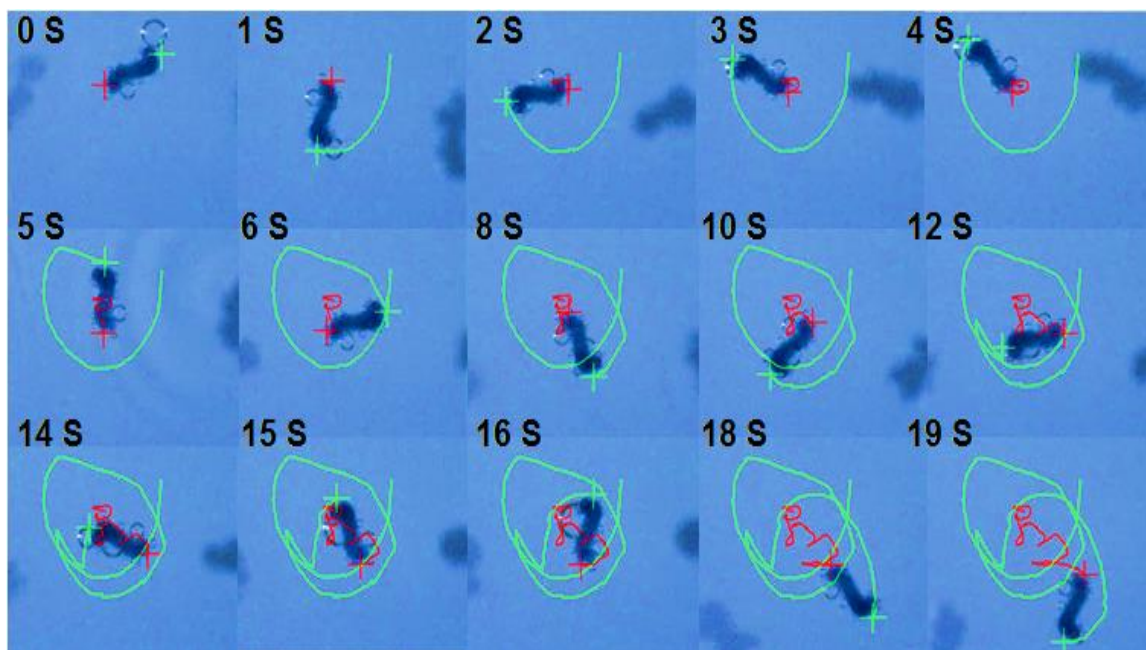
Figure 5-11 Example video snapshot images of single-engine RSF stirrer in 60 mg/ml of H_2O_2 fuel solution.
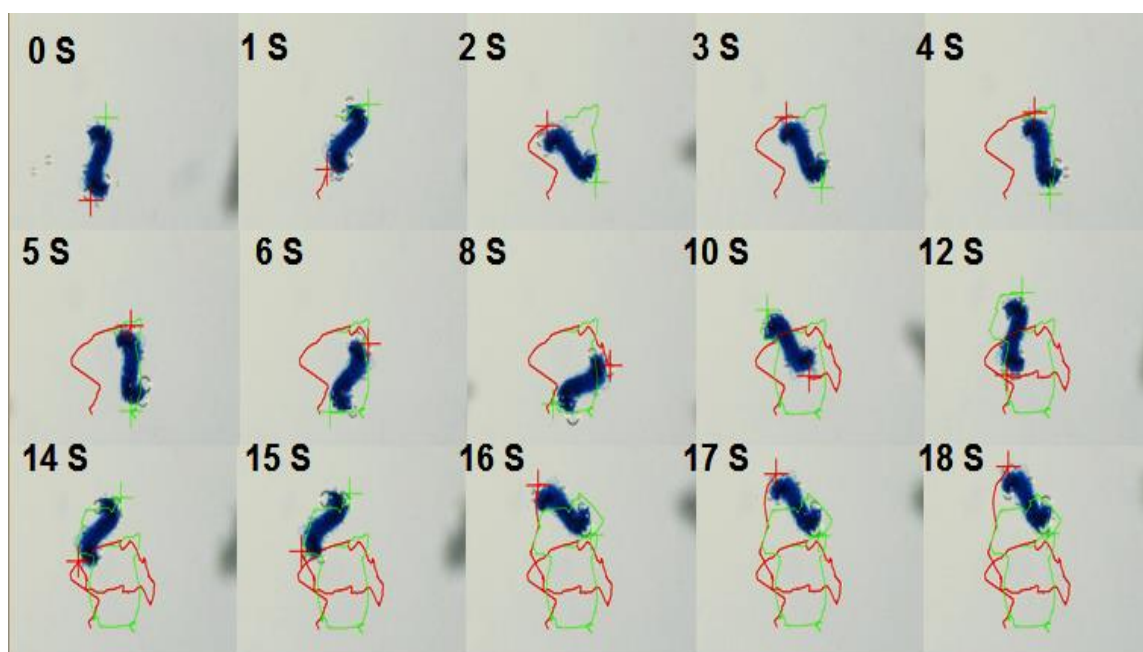
Figure 5-12 Example video snapshot images of dual-engine RSF stirrer in 60 mg/ml of H_2O_2 fuel solution.

Direction Analysis

It was found that the trajectories of the two types of RSF stirrers were circular.

The circular trajectories are shown in the trajectory snapshot images in Figure

5-11 and Figure 5-12. Directionality analysis is described in Section 2.5, where

the angle θ (orientation) and ψ (direction) of the trajectory data of both single-

engine and dual-engine stirrers is investigated. For both types of the RSF-

stirrers, the orientation angle θ was seen to be continuously changing in the

same direction within the range from either going forwards (0°- 360°) or going

backwards (360°- 0°). As shown in Figure 5-13A, for single-engine RSF

stirrers there was a strong correlation between oriental angle θ and directional

angle ψ, where the calculated correlation coefficient over the sample set was

R^2= 240. Also, it can be observed that the direction angle ψ was changing

along with the orientation angle θ as shown in Figure 5-13A. On the other

hand, for dual-engine stirrers the angle ψ did not change together with θ.

There was no noticeable correlation, with the correlation coefficient calculated to be $R^{\wedge 2}$ = 180, as shown in Figure 5-13B.

It is important to note that jumps appeared when the angle θ changed from 0 ° to 360 ° because the angles were calculated using the tangent function.

Figure 5-14 shows schematic images of the trajectories of single-engine stirrers and dual-engine stirrers. The trajectories of the two types of RSF stirrers were circular, but different centre points and radii were observed. The differences can be explained due to the dual-engine stirrers having catalytic power on both sides and therefore propulsion forces from both sides of the stirrers at the same time, so the centre point of the circle trajectory was in the middle of the main stirrer body and the radius of the circle route was half distance of the main stirrer body. However, the single-engine stirrers only had catalytic power in one side and propulsion was asymmetric on one side of the stirrers in the fuel solution, so the centre point of the circle trajectory was at the other side of the stirrer (inactive side) and the radius of the circle route was the length of the main stirrer body (shown in **Figure 5-14**).

Table 5-2 lists the velocity and the rotation speeds of single and dual-engine catalytic RSF stirrers. The average velocities of the middle of the RSF stirrers (n>3 stirrers were tested and more than 25 videos were taken for each stirrers) were 680 ± 240 µm/s and 680 ± 180 µm/s for single and dual-engine stirrers, respectively. The velocities of the two ends for single and dual-engine stirrers were 1300 ± 400 / 550 ± 130 and 970 ± 270 / 1020 ± 220 µm/s, respectively. The difference of the velocities of the two ends for single-engine stirrers was bigger than that for dual-engine stirrers. This result was consistent with the assumption (mentioned in previous paragraph and the schematic (shown

in**Figure 5-14**) that these two stirrers had different spinning trajectories. The rotation speeds of single and both sides' stirrers in 60 mg/ml H_2O_2 were 6.6 and 6 rpm, respectively.
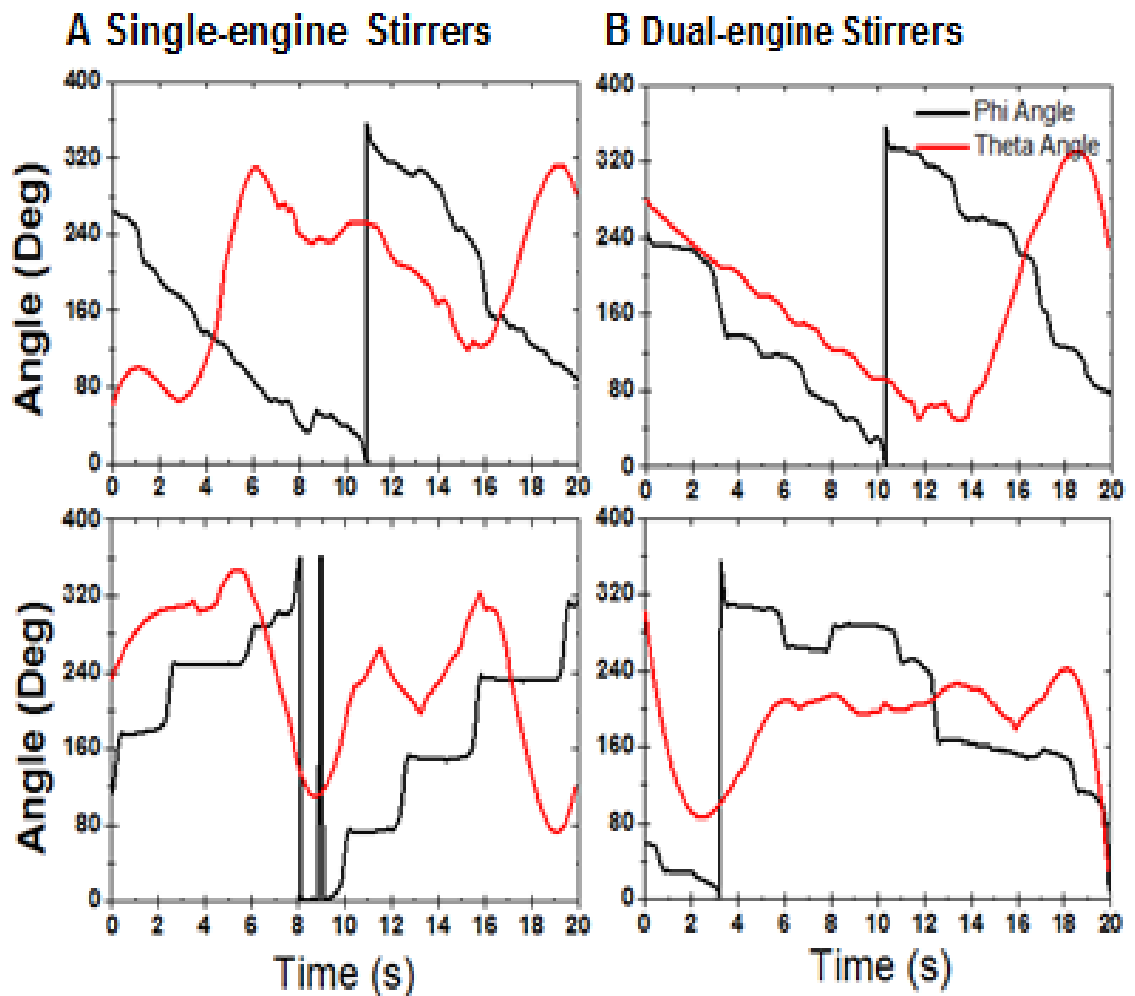
Figure 5-13 Representative samples of angle correlation (θ - Orientation and ψ - direction) of A) single-engine stirrers, and B) dual-engine stirrers in 60 mg/ml of H_2O_2 fuel solutions.
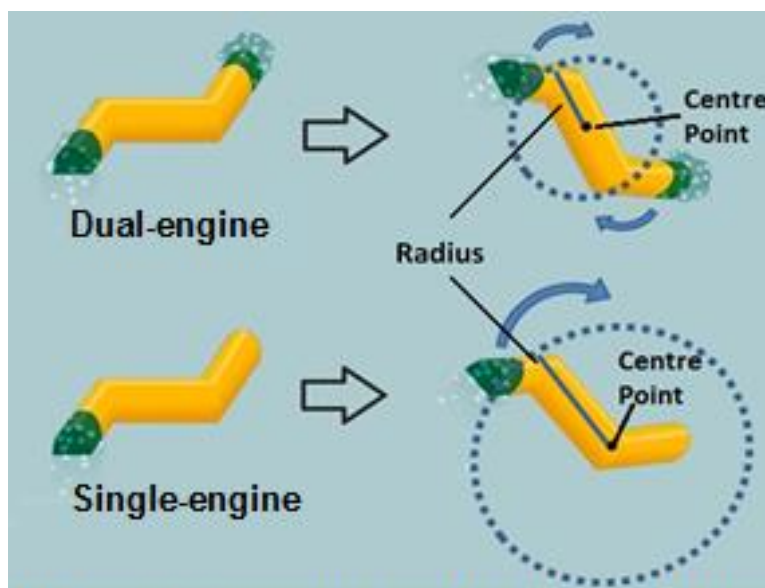
Figure 5-14 Schematic demonstration of the trajectory of dual-engine and single-engine RSF-stirrers.

Table 5-2 Velocity and Rotation Speed of single and both sides catalytic RSF stirrers

Type Of Swimmers	Average Velocity (µm/s)	Vel A/ Vel B (µm/s)	Rotation Speed (rpm)
Single-engine	680 ± 240	1300 ± 400 / 550 ± 130	6.6
Dual-engine	680 ± 180	970 ± 270 / 1020 ± 220	6

So far, two different stimuli driven swimmers have been discussed: one is surface tension driven; the other one is bubble propulsion. Different driven types of swimmers resulted in different speeds under identical fuel concentrations, due to their different operating mechanisms. Here, comparing the surface tension driven (SurfaceT D) swimmers to two different catalytic powered (CAT) swimmers (single-engine and dual-engine CAT swimmers) (shown in **Figure 5-15**), the initial velocity and the rotation speed of SurfaceT D swimmers is about 10 times than those speed of CAT swimmers (60 mg/ml H_2O_2 fuel concentration and 8 mg/ml catalase), respectively. However, the total swimming time of CAT swimmers lasts more than two hours, which is 10 times longer than the swimming time of SurfaceT D swimmers (~10-15 mins). The

above results are based on n = 3 samples for each condition. It is therefore necessary to increase the dataset to gain more accurate results in future. In general, results indicate that SurfaceT D swimmers have higher initial velocity and rotation speed but are short lasting, whereas CAT swimmers achieve prolonged swimming time but have lower initial velocities and rotational speeds.
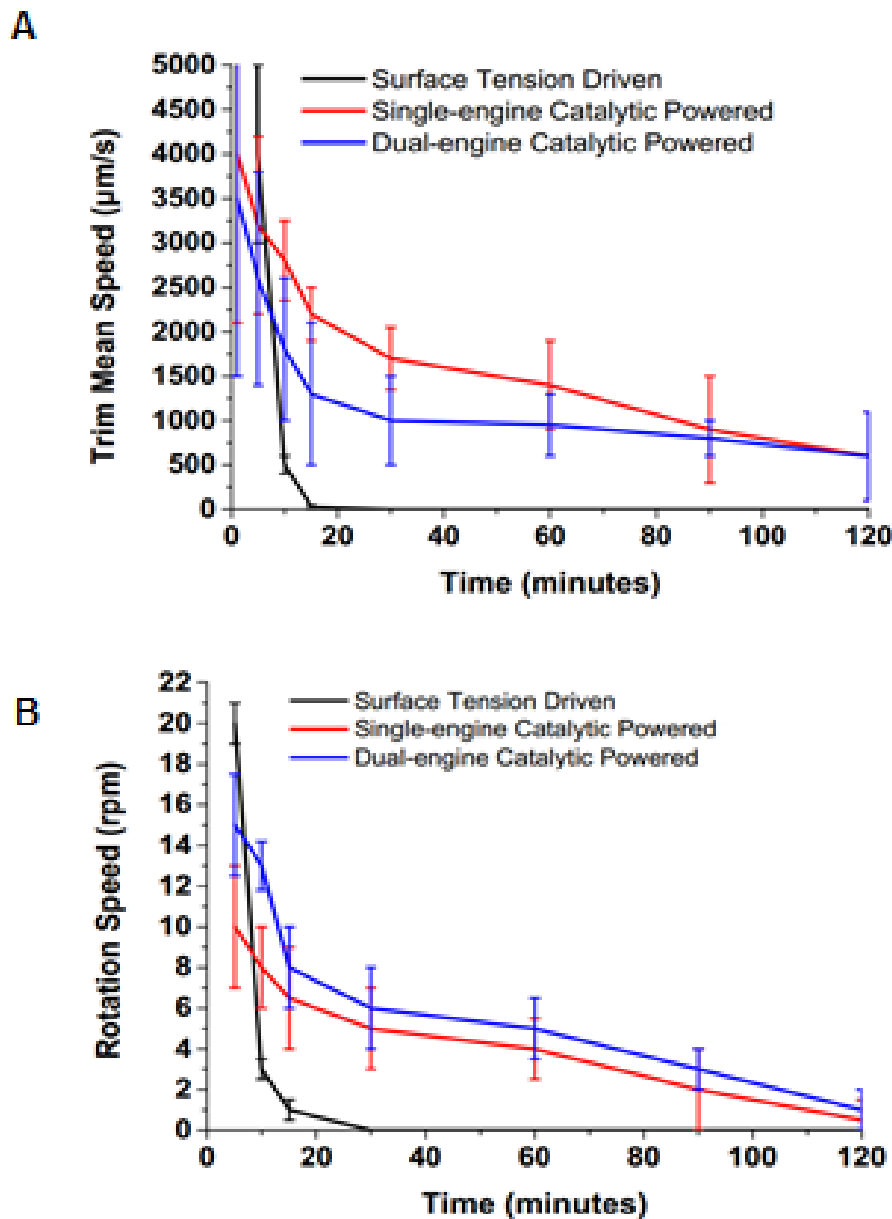
Figure 5-15 Comparison of swimming velocity (A) and rotational speed (B) of differently driven swimmers: surface tension driven, single and dual-engine powered (catalase).

154

It is possible to optimise CP swimmers by controlling fuel concentration and the location as well as the amount of catalytically active enzyme by adjusting the number of printed layers or enzyme concentration. STD swimmers on the other hand can be optimised by controlling the amount of PEG_{400} by adjusting the number of printed layers. These conditions will be analysed in the next few sections.

5.3.3.2 Influence of H_2O_2 Concentration

Catalase encapsulation allows for efficient propulsion of the ' └┐ ' swimmers via Hydrogen peroxide (H_2O_2) decomposition. In this section, the experiments focus on analysing the effect of varying concentrations of H_2O_2 fuel solution on the trajectory of RSF stirrers. ' └┐ ' shape RSF-stirrers were prepared as described in section 5.2.5. These were made up of a total of 150 layers and the dual-engine catalytic powered type stirrers were selected. Trajectory videos were taken in an air controlled cabinet and a 12 cm diameter petri dish as previously described in Section 5.2.7.

Trajectory Analysis of stirrers in different concentrations of H_2O_2 fuel

The track lines of the ' └┐ ' swimmers motion, shown in Figure 5-16 and corresponding to Video-concentration in the supporting information, illustrate the thrust created by bubbles generated during the H_2O_2 decomposition at the two ends of the swimmer. All RSF stirrers containing active catalase enzyme underwent bubble propulsion at the liquid/air interface during the entire experiment. Figure 5-16A-F shows representative trajectories of the RSF stirrers swimming in 1 mg/ml, 10 mg/ml, 20 mg/ml, 30 mg/ml, 60 mg/ml and 100 mg/ml H_2O_2 fuel solutions, respectively.

At 1 mg/ml and 10 mg/ml H_2O_2 fuel concentrations, the RSF-stirrers remained at the air/liquid interface but did not show any signs of motion, as shown in Figure 5-16A and Figure 5-16B. This means that fuel concentrations below 10 mg/ml were not high enough for the catalytic RSF-stirrers to generate adequate bubbles to propel them. Increasing the concentration of H_2O_2 fuel solution to 20 mg/ml, the RSF-stirrer started to move and showed a rotating trajectory as represented in Figure 5-16C. Further increasing of the fuel concentration from 30 mg/ml to 100 mg/ml resulted in the rotation speed of RSF-stirrers increasing (shown in Figure 5-16D-F). The track lines of stirrer motion, shown in Figure **5-16**C-F, and corresponding to Video-concentrations in the supporting information, illustrate the thrust created by bubbles generated during H_2O_2 decomposition at the two ends of the stirrers, demonstrating the efficacy of the site-specific catalase is incorporated loading. The catalytically generated oxygen bubbles released from the two ends drive the stirrers while fast and high frequency bubble ejection leads to continuous rotating of the stirrers. Fundamentally, the propulsion force increases with the rate of the catalytic reaction that results in faster bubble generation [227]. Therefore, increased H_2O_2 concentration and amount of catalase both leads to quicker bubble generation for more efficient propulsion, providing the rate of the molecule diffusion is high enough and also it is below the maximum reaction rate for catalase. In this section, all the stirrers loaded with the same amount of catalase, the increased velocity and rotation speed mainly due to the increased concentration of fuel solution.
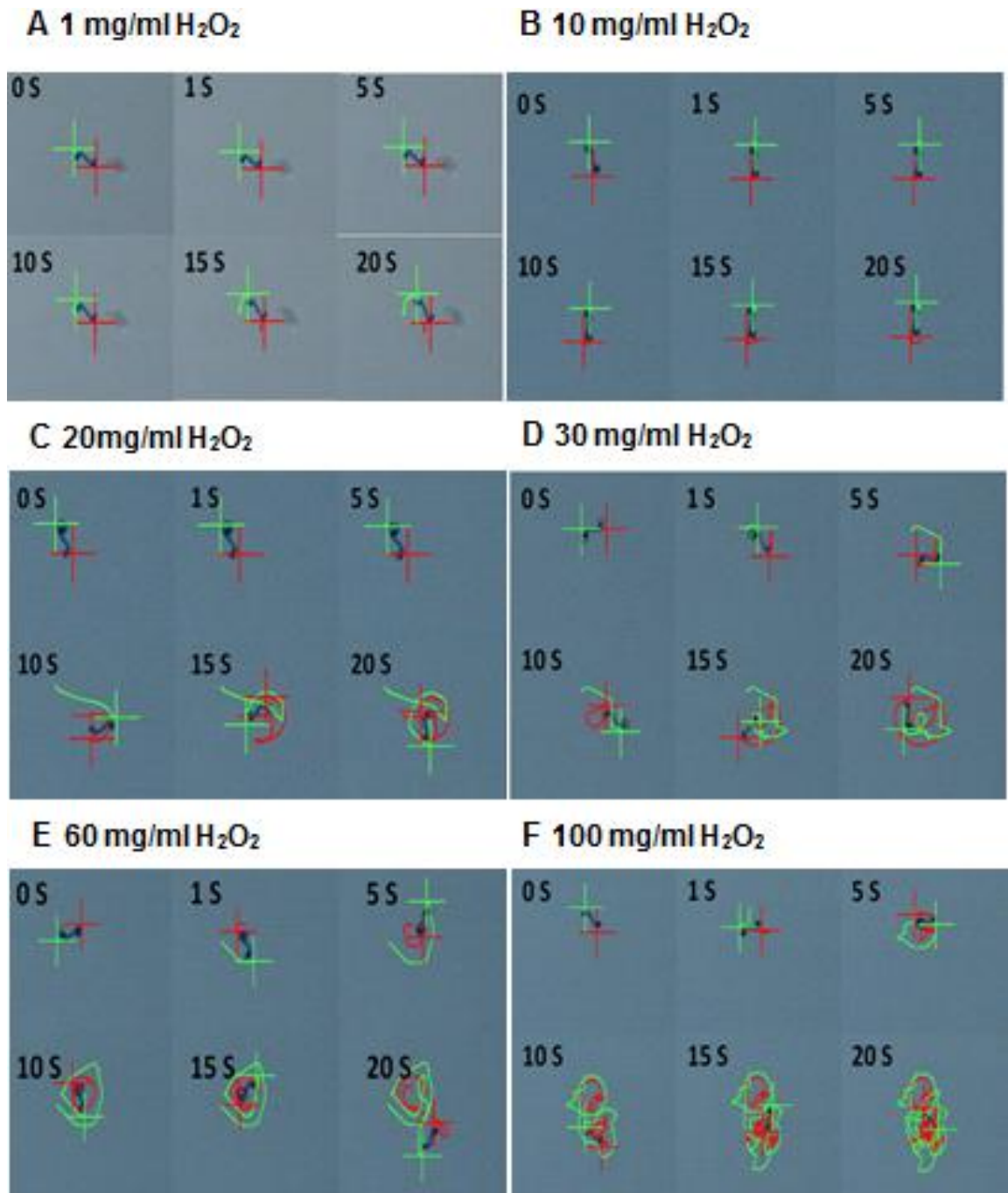
Figure 5-16 Example video snapshot images of catalytic powered RSF-stirrers in A) 1 mg/ml, B) 10 mg/ml, C) 20 mg/ml, D) 30 mg/ml, E) 60 mg/ml and F) 100 mg/ml of H_2O_2 fuel soltuion.

Direction Analysis

In order to get reliable results, more than 3 dual-engine stirrers were used in

each concentration of H_2O_2 fuel solutions and more than 30 videos were taken

for each stirrer. According to the previous trajectories results (shown in Section

5.3.2.1), the ' └┐ ' shape RSF-swimmers preferred to rotate rather than other motion. Therefore, this spinning behaviour is further investigated in the following trajectory analysis. Figure 5-17A-F demonstrates the orientation angle (θ) and the direction angle (Φ) of RSF stirrers in 1 mg/ml, 10 mg/ml, 20 mg/ml, 30 mg/ml, 60 mg/ml and 100 mg/ml of H_2O_2 solutions, respectively. Figure 5-17A and Figure 5-17B show that the orientation angles (θ) do not change during the tracking time which is consistent with the previous results (Figure 5-16A and Figure 5-16B) that RSF-stirrers floating on air/liquid surface of 1 mg/ml and 10 mg/ml H_2O_2 solutions without showing any visible trajectory. Then, **Figure 5-17**C-F shows the regular changing of the orientation angle. If the orientation angle changed from 0 ° to 360 °, it refers to a full rotation. The order for the amount of full rotations among **Figure 5-17**C-F was: **Figure 5-17**C < D < E < F. It means that the same stirrer rotates more circles in higher concentration of fuel solution than in low concentration.

Furthermore, some 'stair' shape curves were observed among the orientation angle vs time diagrams (shown in **Figure 5-17** C-F). As described in Section 5.3.2 and Section 5.3.3.1, the stirrers can be powered in two ways: one is driven by surface tension gradient, the other one is bubble propelled. The 'stair' shape curve only appears on direction analysis diagrams of bubble propelled stirrers. The appearance of the 'stair' shape is reasonable as it reflects the formation of the main athletic bubbles (continuous ejected oxygen bubbles joined together) and the burst of the main bubbles. Whereas, the surface tension driven stirrers based on Marangoni effect rotated coherent. Compared **Figure 5-17** C-F, the 'stair'-shape curves show the difference on their width: **Figure 5-17**C have the widest stair shape, then **Figure 5-17**D,

Figure 5-17E and **Figure 5-17**F. It means that the higher the concentration of

the fuel solution is, the shorter time for formation of the main athletic bubble is

required.
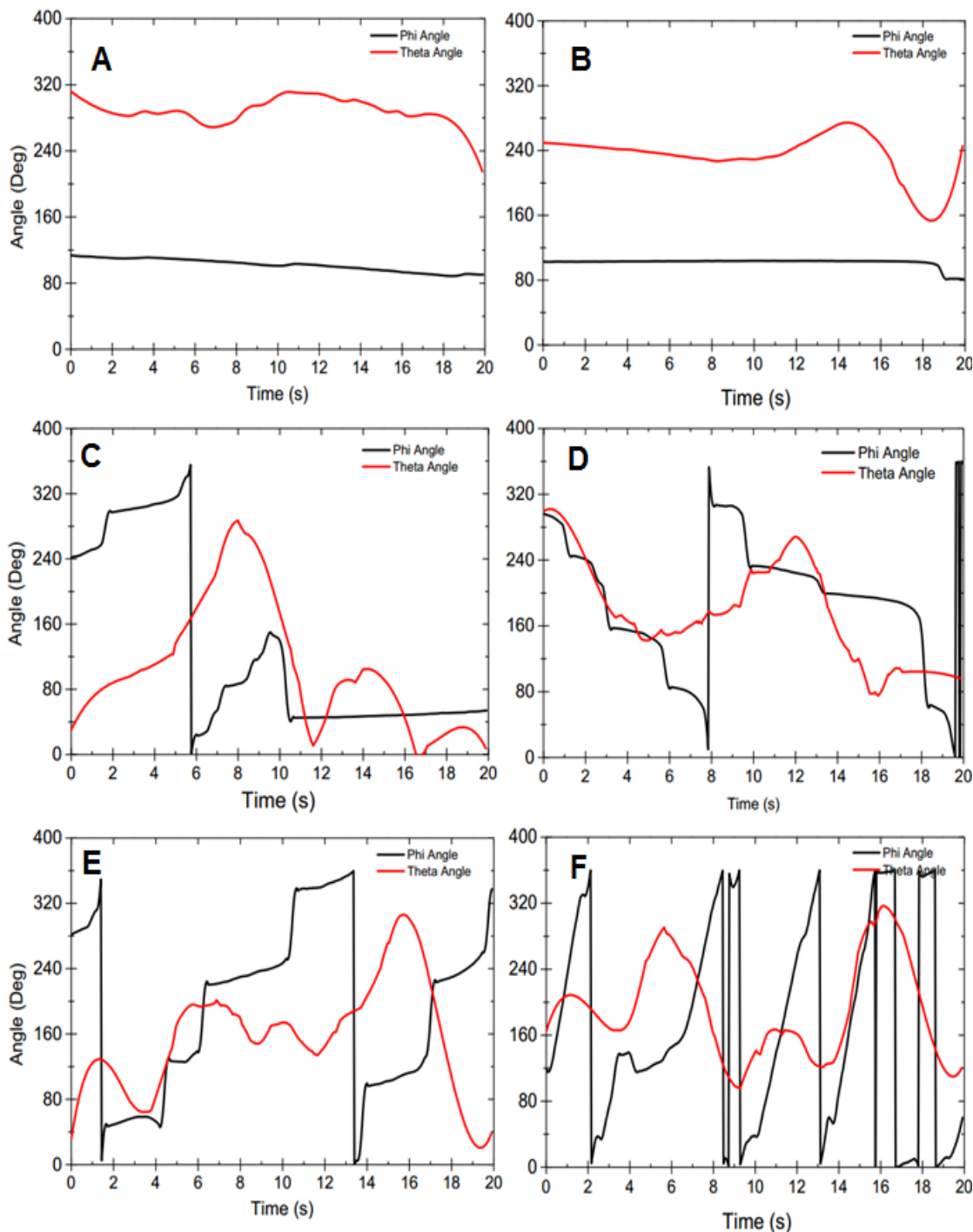
Figure 5-17 Angle correlation (θ - Orientation and ψ - direction) of RSF stirrers in A) 1 mg/ml, B) 10 mg/ml, C) 20 mg/ml, D) 30 mg/ml, E) 60 mg/ml and F) 100 mg/ml of H_2O_2 fuel solutions.

Velocity and Rotation Speed

The trajectories of RSF-stirrers were analysed for their mean instantaneous velocities and rotation speed. The mean instantaneous velocities were based on the calculated centre and two ends of the mass trajectory from the dual tracked RSF stirrers while the rotation speeds were calculated by how many orientation angle jumps (caused by calculating the change form 0 ° to 360 ° using tangent function) occurred per minute. The results are listed in Table 5-3, it can be seen that the mean velocity and rotation speed increased as the concentration of the H_2O_2 fuel solutions increased.

As mentioned before (Section 5.3.3.2 trajectory analysis), the propulsion force increases with the rate of the catalytic reaction that results in faster bubble generating [227]. Based on the experiment results in this section, when certain amount of catalase was loaded in stirrers, the velocity and rotation speed controlled mainly due to the concentration of fuel solution. The minimum concentration of fuel solution which allow the stirrers (150 layers, 8 mg/ml 10,000 units/mg catalase) rotating was 20 mg/ml. The optimized concentration of fuel solution is selected depending on the requirement of the further applications.

Table 5-3 Velocity and Rotation Speed of RSF stirrers in various concentration of H_2O_2

H_2O_2 Concentration	Average Velocity (µm/s)	Vel A/ Vel B (µm/s)	Rotation Speed (rpm)
1 mg/ml	100 ± 6	90 ± 8 / 80 ± 15	0
10 mg/ml	180 ± 20	210 ± 13 / 170 ± 44	0
20 mg/ml	430 ± 90	300 ± 180 / 270 ± 110	3.6
30 mg/ml	720 ± 210	800 ± 300 / 900 ± 400	4.5
60 mg/ml	1500 ± 400	2500 ± 800 / 2500 ± 500	6
100 mg/ml	2040 ± 290	3200 ± 400 / 3600 ± 500	12

5.3.4   Influence of Printing Layers – Trajectory analysis

In this section, I will analyse the effect of the amount of the printing layers on the trajectories of stirrers in certain amount of fuel solution. The amount of the printing layers of stirrers is mainly to control the loaded catalase for bubble propulsion stirrers or the amount of PEG_{400} for surface tension driven stirrers. When the condition of fuel solution is fixed, I can find the limitation of the printing layers of the stirrers based on the experiment results in this section.

5.3.4.1 Catalytic powdered RSF-Stirrers – bubble propulsion

' ⌐ ' shape RSF-stirrers were prepared as described in section 5.2.5. Dual-engine catalytic powered RSF-stirrers were selected and all stirrers were swum in 60 mg/ml of H_2O_2 fuel solution. The following printing layers are analysed: 50, 100 and 150 layers. The analysis starting from the 50 printing layers is due to the stirrers need at least 50 printing layers to form the usable scaffolds. If the printing layers are less than 50 layers, the printed scaffolds will fall apart when taking them from the substrate.

Representative tracks of 50 layers, 100 layers and 150 layers of ' ⌐ ' shape RSF-stirrers swam in 60 mg/ml H_2O_2 fuel solution are shown in Figure 5-18A-C and the direction analysis of them are shown in Figure 5-18D-F. The results show that all three types of RSF-stirrers rotate in the fuel solution. The 'stair' shape curves are observed on the orientation angle vs times curves in **Figure 5-18**D-F. Table 5-4 lists the velocity and rotational speed of 50, 100 and 150 layers of RSF-stirrers. These results showed that stirrers with 150 printing layers have the highest rotation speed, almost 1.3 times higher than the stirrers with 100 printing layers and 5.3 times than the stirrers with 50 printing

161

layers. As mentioned at the beginning of this section, the stirrers with more printing layers contain more amount of catalase enzyme. Thus, the results showed that the more printing layers of the stirrers, the higher the rotation speed it will be.
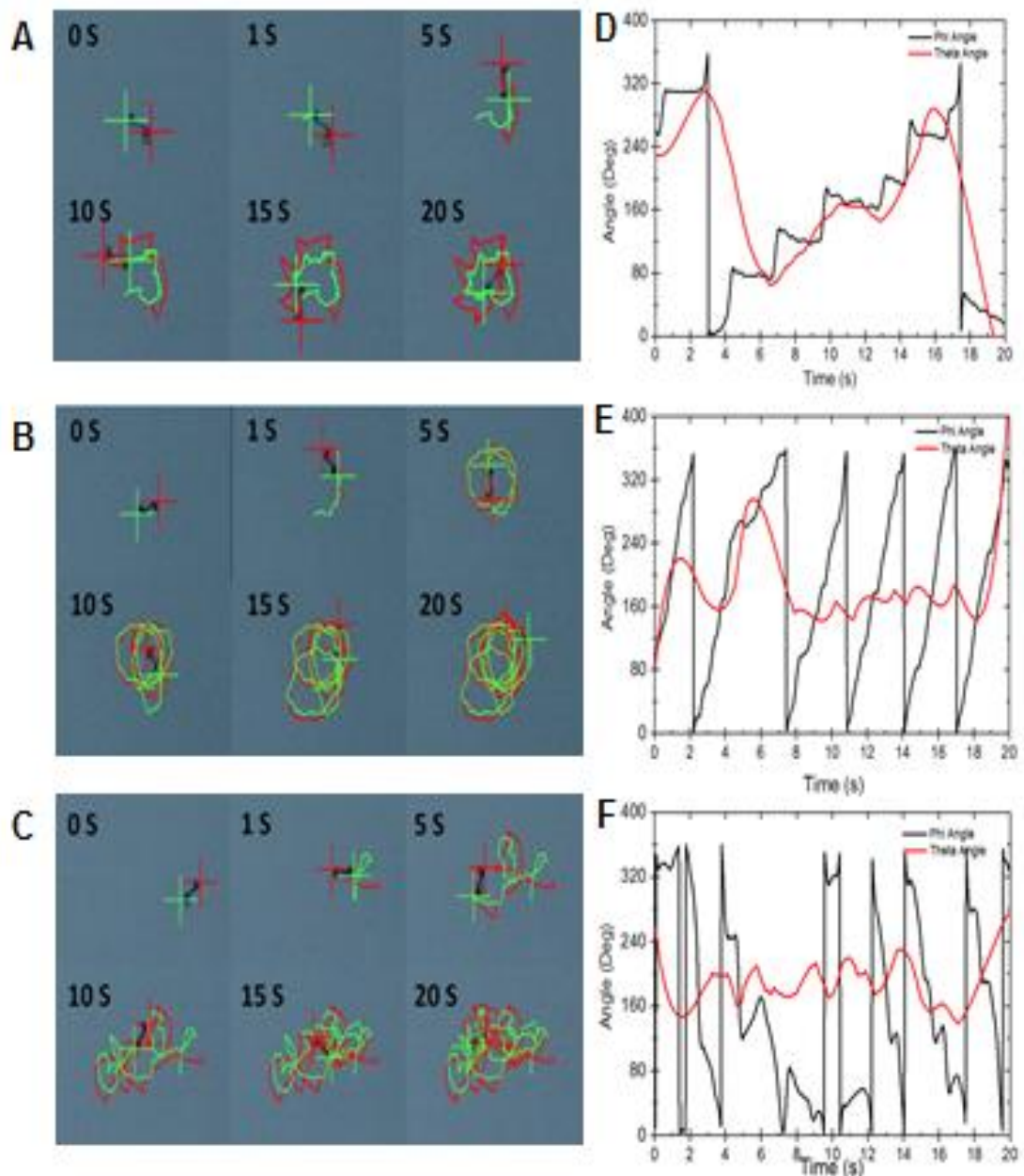
Figure 5-18 Example video snapshot images and angle correlation (θ - Orientation and ψ - direction) of RSF stirrers in 60 mg/ml H_2O_2, A) and D) 50 layers, B) and E) 100 layers, and C) and F) 150 layers.

Table 5-4 Velocity and Rotate Speed of RSF Stirrers with differernt printing layers

Type Of Swimmers	Average Velocity (µm/s)	Vel A/ Vel B	Rotate Speed (rpm)
50 layers	710 ± 180	1000 ± 400 / 1230 ±260	4.5
100 layers	1500 ± 500	2000 ± 600 / 2100 ± 700	18
150 layers	2000 ± 700	2900 ± 800 / 3200 ± 1000	24

5.3.4.2 Self-motived RSF-Stirrers: surface tension driven (Marangoni effect) locomotion

In this section, the experiment analysis the effect of the printing layers of stirrers on the trajectory of surface tension driven stirrer. ' ⌐ ' shape RSF-stirrers were prepared as described in section 5.2.5. The RSF inks contained 16 mg/ml PEG_{400}/40 mg/ml RSF. All the stirrers are analysed in Di-water (20 ml and 50 cm^2 surface areas). The analysed printing layers of stirrers are as same as the bubble propulsion stirrers which are 50, 100 and 150 layers.

Figure 5-19A-C show the representative trajectory of various printing layers (50, 100 and 150 layers) of RSF stirrers and their direction analysis are showed in **Figure 5-19**D-F, respectively. The track line of the stirrers showed that these stirrers also rotated in H_2O solution. In the direction analysis, comparison of bubble prolusion tracks versus surface tension driven swimmers reveal that trajectories are smooth for the latter, see Figure 5-18 and **Figure 5-19**. No 'stair' shape curves were observed on that of surface tension driven stirrers.

Table 5-5 lists the mean velocity of 50, 100 and 150 printing layers of RSF-stirrers with surface tension driven propulsion are 4000 ± 1000, 6100 ± 2400, and 20000 ± 7000 µm/s, respectively. These results proved that the 150 layers' RSF-stirrers spun quickest, almost 1.2 times than the 100 layers' RSF stirrers

and 5 times than the 50 layers' RSF stirrers. The rotation speeds of concentration gradient propulsion of RSF-stirrers for 50, 100 and 150 layers' were 18, 75, and 90 rpm, respectively. Comparison of surface tension driven rotors against bubble driven rotors reveals (shown in Table 5-4) an increase in rotational speed of 3.75 (150 layers), 4.16 (100 layers) and 3.75 (50 layers).
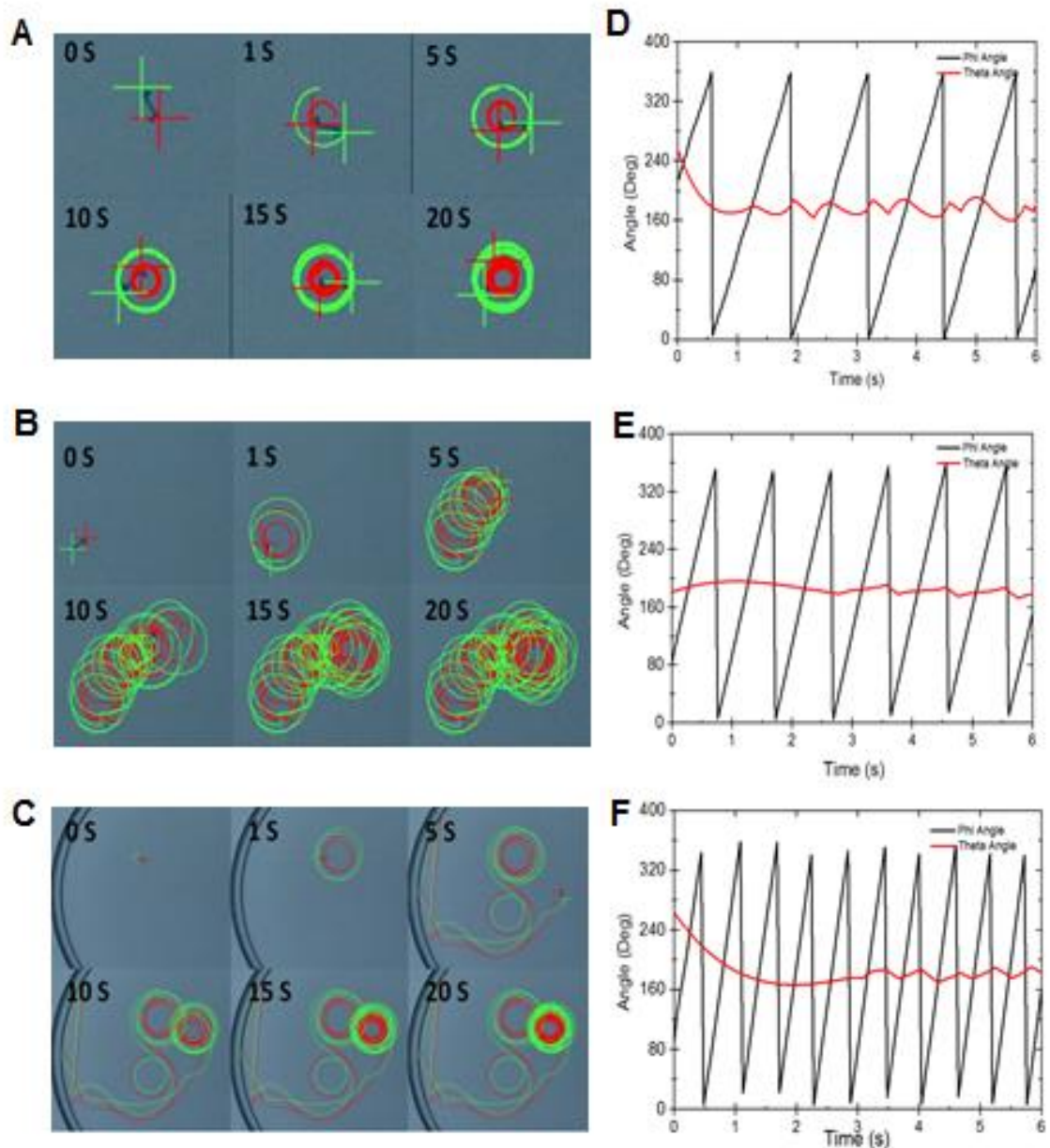
Figure 5-19 Example video snapshot images and angle correlation (θ - Orientation and ψ - direction) of RSF stirrers in H_2O, A) and D) 50 layers, B) and E) 100 layers, and C) and F) 150 layers

Table 5-5 Velocity and rotation Speed of RSF stirrers with different layers in water

Type Of Swimmers	Average Velocity (µm/s)	Vel A/ Vel B (µm/s)	Rotate Speed (rpm)
50 layers	4000 ± 1000	7000 ± 4000 / 11000 ± 6000	18
100 layers	6100 ± 2400	19000 ± 8000 / 20000 ± 8000	75
150 layers	20000 ± 7000	30000 ± 10000 / 35000 ± 17000	90

5.3.5   Application of RSF-Stirrers

As described in Section 5.3.4, there two types of propulsion mechanisms have been observed, catalytic bubble propulsion and surface tension driven locomotion. Surface tension driven motion was shown to result in faster and smoother rotations. Therefore RSF-stirrers were analysed for their mixing quality.

The progress of mixing a solution is shown in **Figure 5-20**. A 90 mm diameter petri-dish was used and analysed the mixing quality between 15 ml H_2O and 1 ml glycerol/blue ink (ratio 1:1, acid ink blue) with and without placing stirrers. The dye diffusion was quicker with the help of the RSF-stirrers, see **Figure 5-20**. Furthermore, **Figure 5-21** shows the changing of diameter of the dye circle during the time. It can be seen that the diameter of the dye circle with the stirrers increases approximately 4.5 times faster than that without stirrers. The bio-mixing quality with/without stirrers shows their difference at the first 10 seconds. However, the mechanism of how the stirrers help the mixing of the solutions still need to be further analysed and more repeat experiments are required in the future.
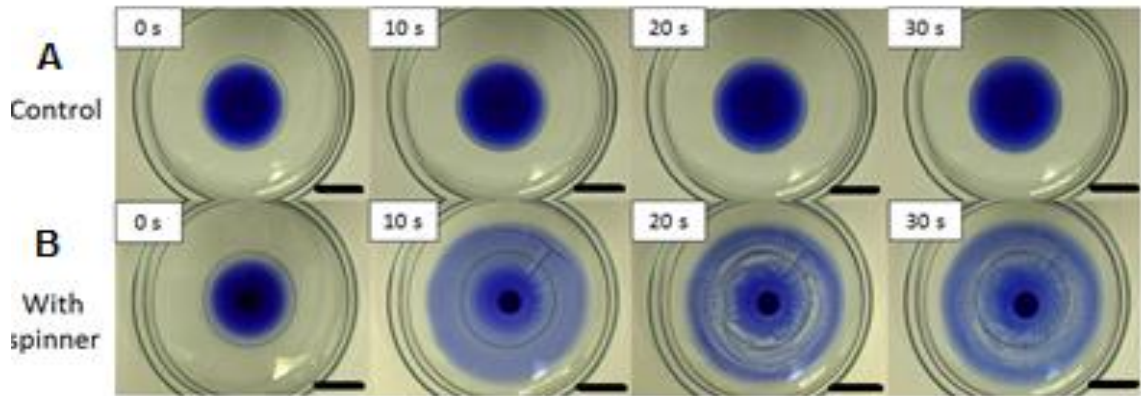
Figure 5-20 Video snapshots images showed the dye diffusion A) with and B) without ' └┐ ' shape RSF-stirrers. Dye is glycerol/blue ink mixture with the ratio of 1:1 and surface tension driven stirrers were used. Scale bar is 20 mm.
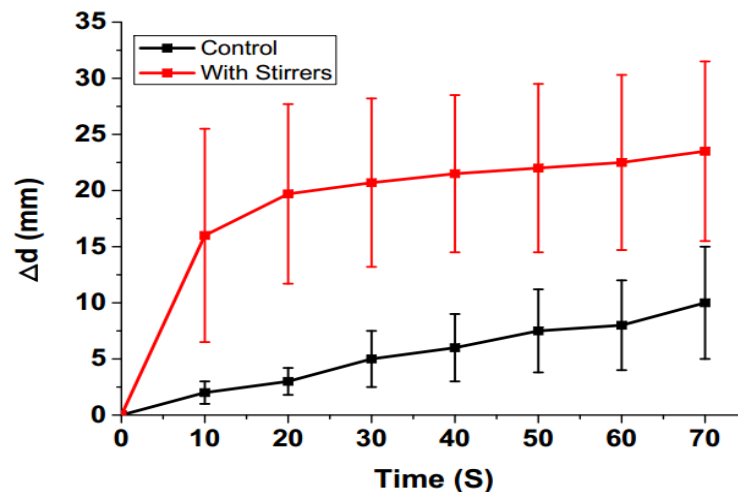
Figure 5-21 The diagram demonstrates the changing of the diameter of the dye circle Vs time, comparing of dye diffusion quality with and without RSF stirrers. N=3, error bars represent standard deviation.

5.4 Conclusions

Two different types of propulsion mechanisms were studied in this chapter, namely catalytically powered bubble propulsion and surface tension gradient powered propulsion. It was shown that catalytic powered ' └┐ ' RSF-swimmers demonstrated circular trajectories. Dependent on the location of the catalytically active engines (single-engine and dual-engines) the

166

rotational trajectories have different center points, namely central for the dual motor spinners and on the inactive far end for the single-engine spinners. Both swimmer thickness (50 layers, 100 layers, and 150 layers) and fuel concentrations (1 mg/ml, 10 mg/ml, 20 mg/ml, 30 mg/ml, 60 mg/ml, and 100 mg/ml) of H_2O_2 solution influenced the velocity and the rotational speeds of the designed stirrers. Increasing number of layers or fuel concentration both resulted in faster propulsion.

For surface tension powered RSF-swimmers, the velocity and the rotation speed were controlled by adjusting the number of layers (50 printed layers, 100 layers and 150 layers). Propulsion was caused by PEG_{400} leaching into the bulk solution causing a concentration gradient and leading to a change in surface tension.

It is therefore clear comparing similar systems the mechanisms of motion rely not only on shape factors but also on the thickness of swimmers and fuel concentrations present. The results reported in this Chapter indicate that multiple propulsion mechanisms may contribute to the motion of swimmers and therefore it is desirable to investigate how these mechanisms operate side by side in order to gain better understanding for each mechanisms contribution. Gaining better understanding for these mechanisms it should be possible to be able to produce highly controlled propulsion systems.

Chapter 6 Reactive Inkjet Printing of Silk Letter Swimmers

6.1 Introduction

A vast majority of deaths worldwide is caused by cancer, mainly due to the inability to effectively diagnose metastatic diseases in the early stages and successfully treat them [228-233]. Generally, cancer metastasis involves the spread of cancer cells, whereby the tumour cells escape from the primary tumour and are transported through the circulation system to healthy organs to form secondary tumours [231, 234, 235]. These cells, which are shed into the bloodstream or lymphatic system, are referred to as circulating tumour cells (CTCs) [236]. The presence of CTCs provides an indicator for the clinical diagnosis and prognosis of various types of cancers [236-239]. However, the amount of CTCs in cancer patients' blood is extremely low and one ml of blood might contain 1-10 CTCs , which increases the difficulty to detect them under the presence of a huge amount of blood cells in blood [236-238]. Specifically, the mechanisms of how the cancer cells invade and transfer at the molecular level is still unclear [237, 238, 240]. These are reasons why current cancer detection methods are still not well established [235].

Current patient cancer diagnosis involve observations via radiological imaging modalities such as computed tomography (CT), traditional radiography (X-ray), positron emission tomography (PET), or magnetic resonance imaging (MRI). These techniques require the visualization of tumour cell colonization, which in turn limit the detection sensitivity and therefore a delay in diagnosis is inevitable and treatments are delayed. In recent years, there has been a rapid growth in the amount of cancer patients, which have generated challenges for the traditional clinical detection approaches due to the vast number of patients

needing screening and therefore new screening methods are needed which can diagnose cancer with specificity, sensitivity, and in also advanced stages of cancer. Hüsemann et al. highlights that CTCs are able to be detected even before a primary tumour is formed [241]. It is possible to enumerate and characterize CTCs by using approaches such as a polymerase chain reaction (PCR) based approach [242-244], immunomagnetic separation with laser scanning cytometry (LSC) [245], flow cytometry [246-248], microchip technology [249, 250] and immunomagnetic techniques [251]. Each of these approaches has advantages and disadvantages.

Recent progress in the field of artificial Nano-/micro- robots have opened the door to new and important biomedical applications ranging from bio-sensing, bio-detection to drug delivery [101, 252], assay enhancement, cargo transport to drug delivery [82, 85, 253]. These man-made motors major advances in the power, motion control and efficiency. In 2011, Balasubramanian et al. reported the catalytic rolled up rockets which are particularly attractive for isolating and transporting cancer cells. However, this approach required complex surface modification and the material of the rockets was not biocompatible [254]. Here, I demonstrate a small bio-swimmer which overcomes previous constraints as a potential method to detect CTCs. These swimmers are made from biocompatible material (natural protein: fibroin) via 3D reactive inkjet printing. It is also easy to control their motion by changing the shape and the position of the catalytic 'engine' of the swimmers during the inkjet printing fabrication process via the printing scripts and layer settings. What's more, by using RIJ it is possible to fabricated different functionalized surfaces of the swimmers (using different inks) to allow for different functions.

6.2 Experimental Methods

6.2.1 Materials

The details of the used materials were described in Chapter 2 Section 2.1.1.

6.2.2 Silk Degumming Process

The silk degumming process was described in Chapter 2 Section 2.1.2.

6.2.3 Preparation of RSF Solution

The preparation of RSF solution was described in Chapter 2 Section 2.1.3.

6.2.4 Preparation of Mix-RSF Solution

The preparation of mix-RSF solution was described in Chapter 5 Section 5.2.4.

6.2.5 Inkjet printing Process

The inkjet printing process was described in Chapter 5 Section 5.2.5. In this Chapter, 26 alphabets (English letters) were drawn on pictures using Paint (Version 1607, Microsoft Windows) and saved as bitmap images. All the letters were drawn in uppercase and designed symmetrically. Then the bitmap images were programmed into JetLab (version 6.3, MicroFab Technologies). **Figure 6-1** shows the schematic of the layer-by-layer (LBL) inkjet printing procedure of RSF letter swimmers: N, A, T, U, R, and E. In the **Figure 6-1**,

yellow represents the RSF / PEG400 mixture inks, green means the RSF / Catalase / PEG400 mixture inks and blue is methanol inks.

All the other printing conditions (such as temperature, humidity) were as same as the conditions which were used in Chapter 5.
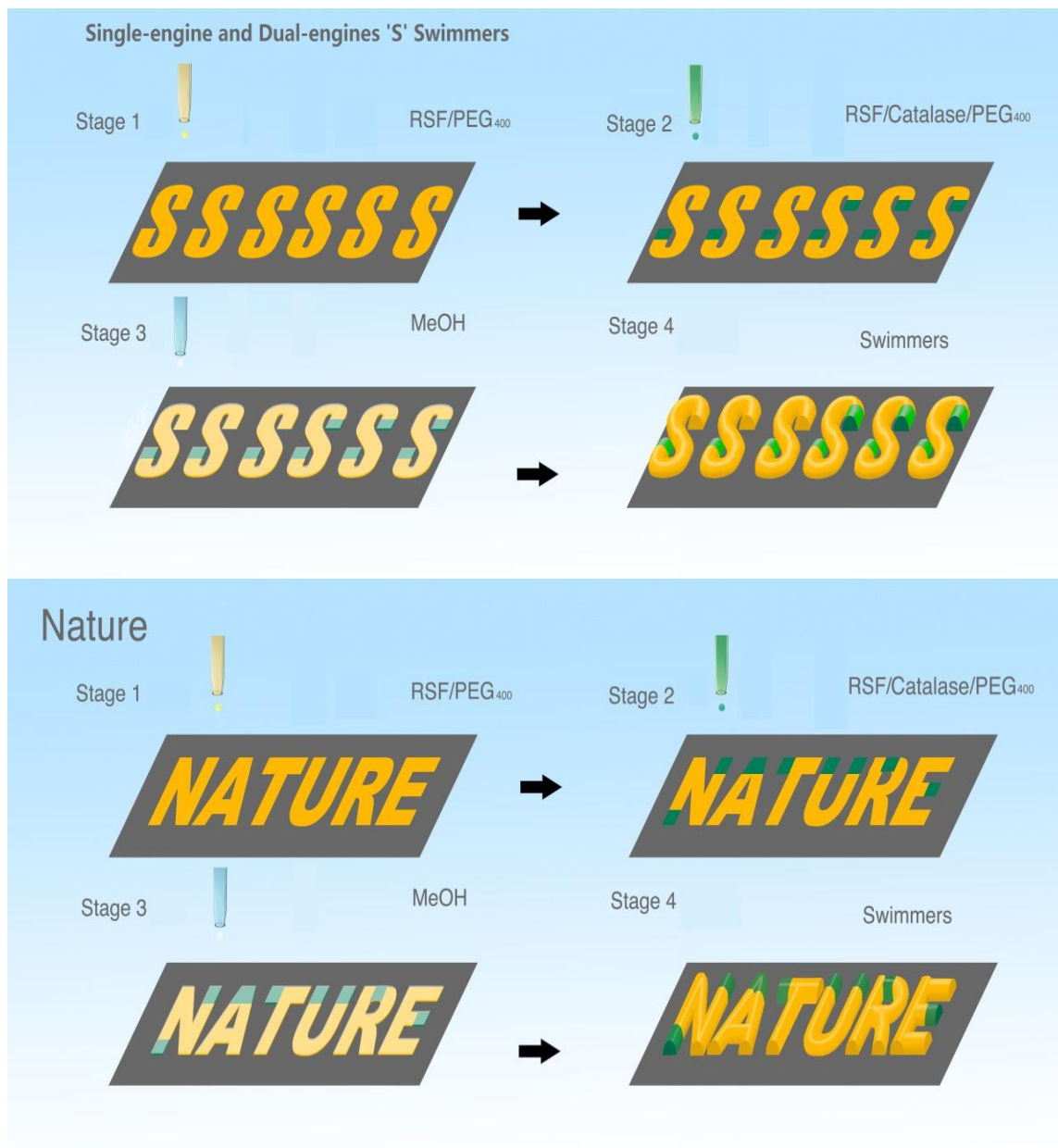
Figure 6-1 Schematic repesenting the LBL inkjet printing procedure of letter swimmers with catalase molecules, green represents the RSF / Catalase / PEG400 mixture ink, yellow represents the RSF / PEG400 mixture ink and sky blue represents methanol ink.

6.2.6 Scanning electron microscope (SEM)

The process was described in Chapter 5 section 5.2.6.

6.2.7 Analysis of movies

The trajectory analysis was described in Chapter 5 section 5.2.7.

6.3 Results and Discussion

In this chapter, 'S' and 'NATURE' swimmers were selected and the details of their trajectories are described as these showed the good repeatability. The remaining letters of the alphabet were also analysed but still need more experiments to prove the repeatability of their trajectories.

The trajectories of the letter swimmers were mainly determined on two conditions: the shapes of the letters and the mechanisms of locomotion. Two mechanisms of locomotion (mentioned in Chapter 5) are analysed. One is the catalytic powered locomotion (bubble propulsion), another one is the surface tension driven locomotion. As previously reported in Chapter 5 it is possible to control the trajectories of swimmers by altering the position of the enzyme 'engine'. Finally, the letter swimmers were used to capture 7.2 µm fluorescent colloids as a preliminary experiment to simulate the capture of cancer cells in blood.

6.3.1 Characterization of Letter Swimmers

All RSF swimmers were pre-checked under an optical microscope to make sure they were assembled as required. In this section, SEM was used to characterise the morphology of RSF letter swimmers. The following SEM images were taken from the printed swimmers and prepared in exactly the same way as those used for the swimming experiments described in Section 2.5.

6.3.1.1 Final Structures of 'S' Letter Swimmers

Figure 6-2 shows the scanning electron micrograph (SEM) images of representative samples of the 'S' letter swimmers. Three types of 'S' swimmers were designed in this experiment, which were:

- single-side catalytic 'S' swimmers (Figure 6-2)
- both-sides' catalytic 'S' letter swimmers (Figure 6-4)
- 'S' swimmers without catalase

The both-sides' catalytic swimmers were selected because they contained all the RSF inks (RSF / PEG400 inks and RSF / Catalase / PEG400 inks) which were used for printing the RSF letter swimmers. RSF / PEG400 inks were used for fabricating the main body of the 's' swimmers without the two ends as the two ends using RSF / Catalase / PEG400 inks.
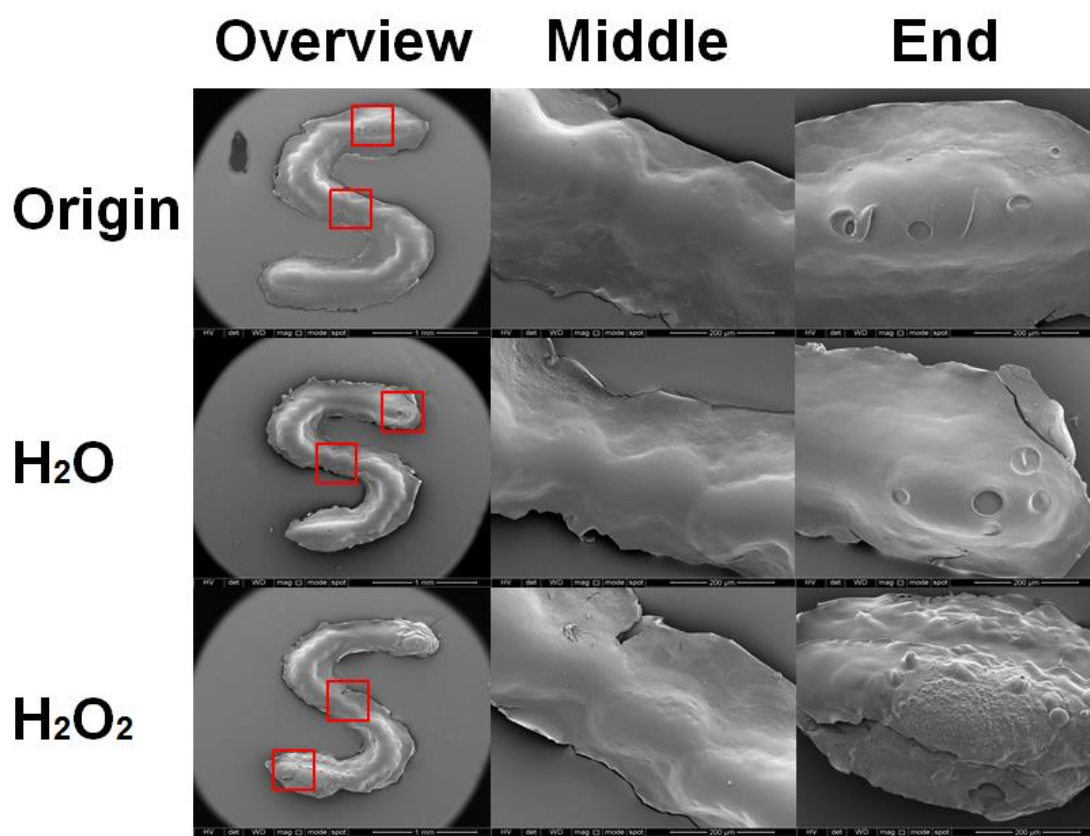
Figure 6-2 Scanning electron microscopy (SEM) images of 'S' Letter Swimmers, first row showing the origin printed swimmers, second row showing the DI water washed swimmers (immersed in water for 30 minutes) and the third row showing the swimmers after reacted with 60 mg/ml H2O2 soltuion (reaction time: 30 minutes). The SEM images at 5 kV of different magnifications: 100 times magnification for first line (overview), 500 times magnification for second line (middle of the letter) and 500 times magnification for the third line (end of the letter), with 1 mm, 200 μm and 200 μm bar for scale, repectively.

From the overview (first column in Figure 6-2) of the "s" letter swimmers, the average size of the swimmers were approximately 1000 μm x 1300 μm (width x length). The images in the first line of Figure 6-2 show the original RSF swimmers prior to being put into water or fuel solutions. The enlarged images show the middle part and the end part of the swimmers. Both parts of the swimmers showed a smooth surface and smooth edges even though the two parts were fabricated from two different inks (middle part without catalase and the end part with catalase). The second line (H_2O) of Figure 6-2 images show

175

the 's' letter swimmers, which were immersed in 20 ml of DI-water for 30 mins. Magnification reveals (middle and last images) the surface of the swimmers is still smooth compared to the overview image in the first line, but the edge of the swimmers is rougher than the same parts of the images in the first line.

The images in the third line of Figure 6-2 show the 's' letter swimmers which were incubated in 20 ml of 60 mg/ml H_2O_2 solution for 30 mins. The magnified image of the middle part shows the roughest surface and edge among the 3 types of the 's' swimmers. Furthermore, Figure 6-3 shows the SEM images of the 's' swimmers at the middle part with extra magnification. Figure 6-3B and C show the edge of the swimmer appears to have some cracks. The surface of the centre of the middle part kept their smooth morphology (shown in Figure 6-3 E and F). However, a lot of microscale 'bumps' were observed at the surface of the two ends of the 's' swimmers, which were quite different compared to the other two types. An explanation of the special morphology was that those bumps caused from oxygen gas trying to escape from the inner scaffolds. The oxygen gas came from the catalase, one solute contained in the ends parts of swimmers, reacted with H_2O_2. In order to better analyse the morphology of the swimmers reacted with H_2O_2, larger magnification was used to observe the samples (shown in Figure 6-4). Figure 6-4 B and C show that if the oxygen successfully escaping from the swimmers, the surface of the swimmers appears microscale pores. What's more interesting, the oxygen bubble generated hierarchical structure at the edge of the end part of the swimmers (shown in Figure 6-4 E and F) instead of bursting the swimmer apart. Those results were consistent with the results I found in Chapter 5 which analysed the scaffolds printed by different types of RSF mixture inks.
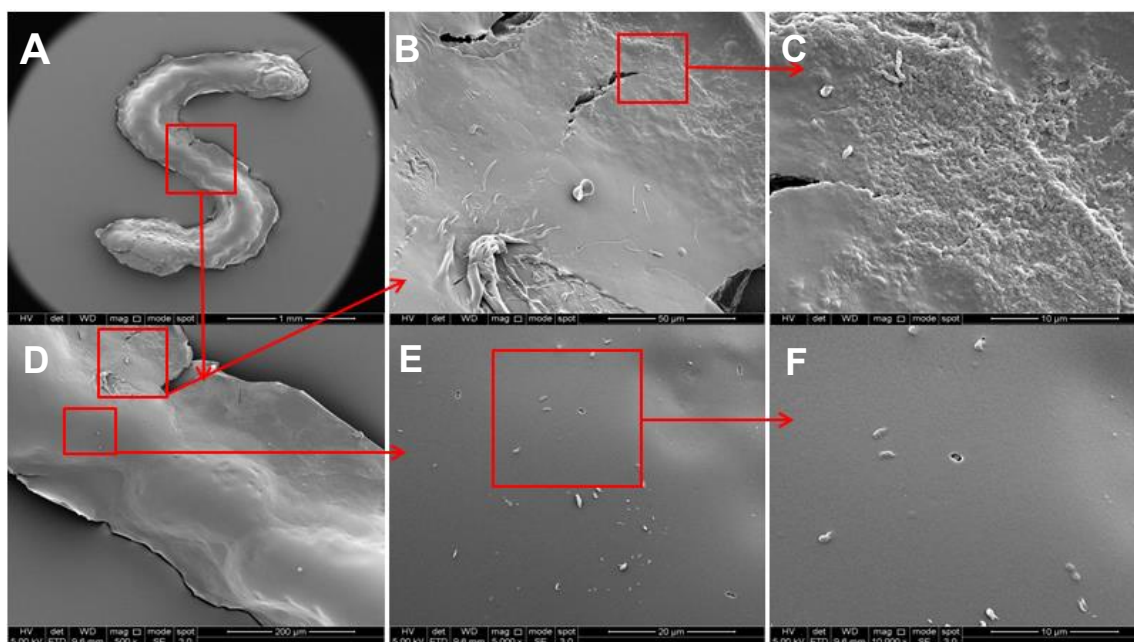
Figure 6-3 Scanning electron microscopy (SEM) images of the middle part of 'S' Letter Swimmers after reacting with 60 mg/ml H_2O_2 soltuions for 30 minutes. The SEM images at 5 kV of different magnifications: (A) 100 times, (B) 2000 times, (C) and (F) 10000 times, (D) 500 times and (E) 5000 times, with 1 mm, 50 µm, 10 µm, 200 µm, and 20 µm bar for scale, repectively.
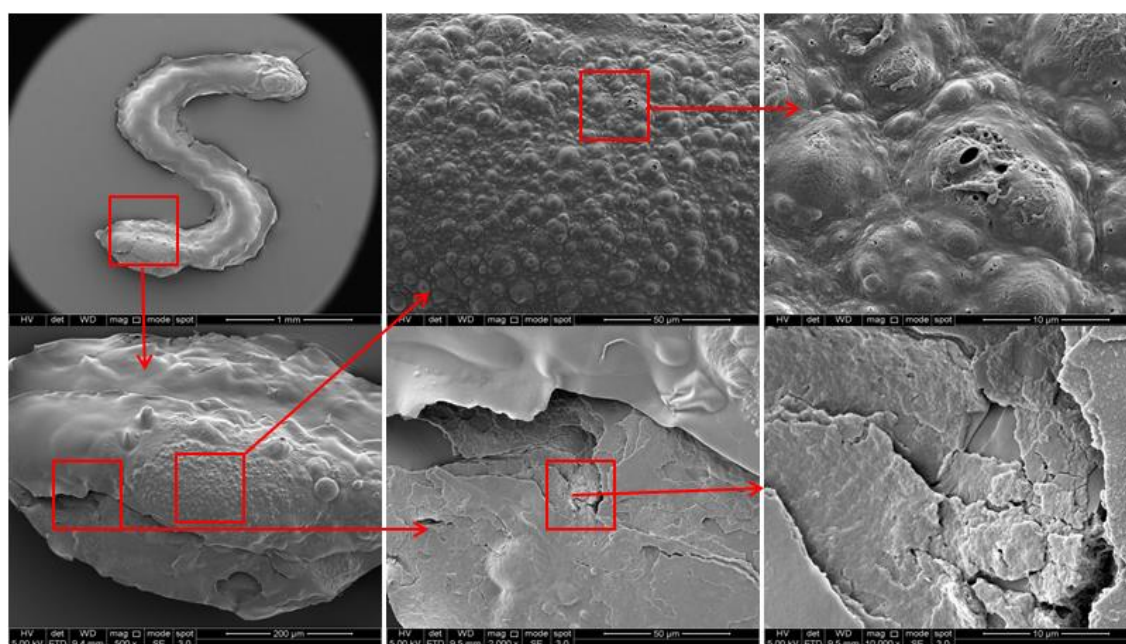
Figure 6-4 Scanning electron microscopy (SEM) images of the middle part of 'S' Letter Swimmers after reacting with 60 mg/ml H_2O_2 soltuions for 30 minutes. The SEM images at 5 kV of different magnifications: (A) 100 times, (B) and (E) 2000 times, (C) and (F) 10000 times, and (D) 500 times with 1 mm, 50 µm, 10 µm, and 200 µm bar for scale, repectively.

6.3.1.2 Final Structures of 'NATURE' Letter Swimmers

Figure 6-5 shows the overview of the RSF 'NATURE' swimmers, the average size of the swimmers are approximate 1200 µm x 1400 µm (width x length). Those swimmers showed the original morphology of the printed letter swimmer samples without any after-treatment. The surfaces of the swimmers were smooth which were consistent with the previous results. Furthermore, the images proved that the swimmers were assembled well. All RSF letters swimmers, shown in Figure 6-5, are exactly as same as those used for the swimming experiments.
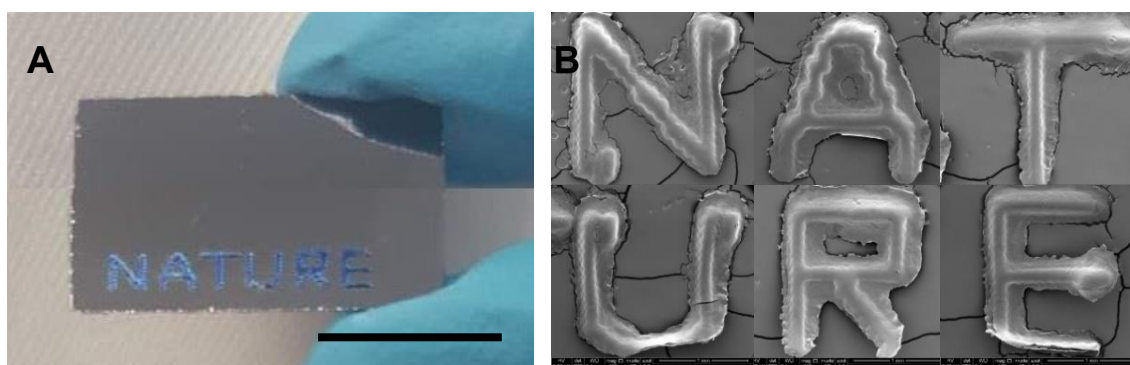
Figure 6-5 Images showing the overview of the RSF 'NATURE' swimmers. (A) was taken by high quality photographic camera. The scale bar was 1 cm. (B) were SEM images taken at 5 kV with the magnificication of 150 times. The scale bar was 1 mm. Those swimmers were original ones without any after-treatment.

6.3.2   Trajectories of 'S' letter swimmers

'S' letter swimmers underwent two types of motion: one was surface tension driven, the other one was catalytic reaction bubble propelled. The mechanisms had been described in Chapter 5 Section 5.3. In this section, Figure 6-6 shows the trajectory analysis of 'S' letter swimmers which is driven by the surface tension gradient. Figure 6-7 and Figure 6-8 show the trajectory analysis of 'S' swimmers undergoing the bubble propulsion.

6.3.2.1 Trajectory of 'S' letter Swimmers in H_2O

For surface tension driven locomotion, the swimmers were printed with 150 layers by using 40 mg/ml RSF / 20 mg/ml PEG_{400} inks. Figure 6-6 shows that the trajectory of the 'S' swimmers in Di-water is circular. It meant that the 'S' letter swimmers were spinning in water. Furthermore, comparing the 'S' letters swimmers with the ' ⌐ ' swimmers which were described in Chapter 5, the shape of them were similar. Both of them had the main body and had two extra parts at the opposite end of the main body. It helped to explained that why the trajectories of 'S' letter swimmers were spinning as the ' ⌐ ' swimmers. As shown in Figure 6-6, the changing of the oriental angle θ from 0° to 360° was smooth and straight. It also can be observed that the direction angle was changing along with the oriental angle. The jump vertical line showed in oriental angle can be used to calculate its rotation speed. The results were listed in Table 6-1.
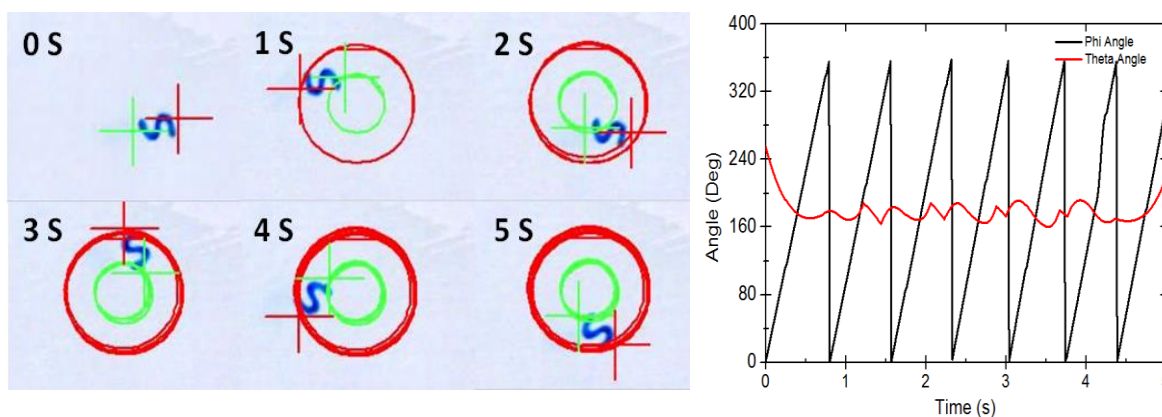
Figure 6-6 Example video snapshot images of surface tension driven 'S' swimmers in Di-water and angle correlation (θ - Orientation and ψ - direction) analysis.

6.3.2.2 Trajectory of catalytic powered 'S' letter Swimmers

For catalytic powered 'S' letter swimmers, the main body of the swimmers were printed by using 40 mg/ml RSF / 20 mg/ml PEG_{400} inks (150 layers) and the bubble 'engine' part of the swimmers were printed by using 40 mg/ml RSF / 20 mg/ml PEG_{400} / 8 mg/ml catalase inks (150 layers). There were two types of catalytic powered 'S' swimmers were prepared. They were classified by the position of their powered 'engine'. One was the single powered 'S' swimmers called single-engine swimmers, the other one was the both-sides powered 'S' swimmers called dual-engine swimmers. In order to make sure all the trajectories ware analysed under the same conditions, 60 mg/ml of H_2O_2 solution was selected as the fuel solution and 20 ml of the fuel solution was used for each swimmer without special mention. All the swimmers were washed with DI-water before they did trajectories analysis in H_2O_2 fuel solution. This pre-treatment avoided disturbing from surface tension driven locomotion.

Figure 6-7 and Figure 6-8 show the trajectory and direction analysis of single-engine and dual-engine 'S' swimmers. It was found that the trajectories of both types of 'S' swimmers were circular, but with different centre point and radiuses. The difference can be explained as the dual-engine swimmers having catalytic power in both side and pushing both sides of the swimmers at the same time, so the centre point of the circle trajectory was in the middle of the main swimmers' body and the radius of the circle route was half distance of the main 'S' swimmers body. However, the single-engine swimmers only had catalytic power in one side and pushing one side of the swimmers in the fuel solution, so the centre point of the circle trajectory was at the other side of the

'S' swimmers (inactive side) and the radius of the circle route was the length of the main 'S' swimmers' body. These results were similar with single-side and both-sides catalytic powered ' ⌐ ' swimmers because the shape of the 'S' swimmers was similar with the ' ⌐ ' swimmers (previously described in section 6.3.2.1). Those results showed that the trajectories of swimmers can be controlled by the shape of the swimmers and position of the power 'engine'. In the next section, different letters with different position of power 'engine' were prepared and analysed in order to better understand how to control the trajectories of the swimmers by their shapes.
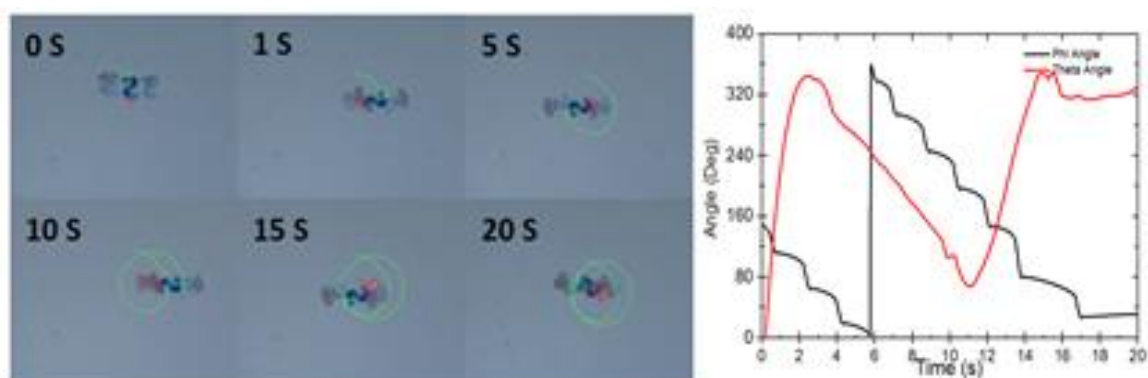
Figure 6-7 Example video snapshot images of the trajectory of single-side powered 'S' swimmers in 60 mg/ml of H_2O_2 fuel solution and angle correlation (θ - Orientation and ψ - direction) analysis.
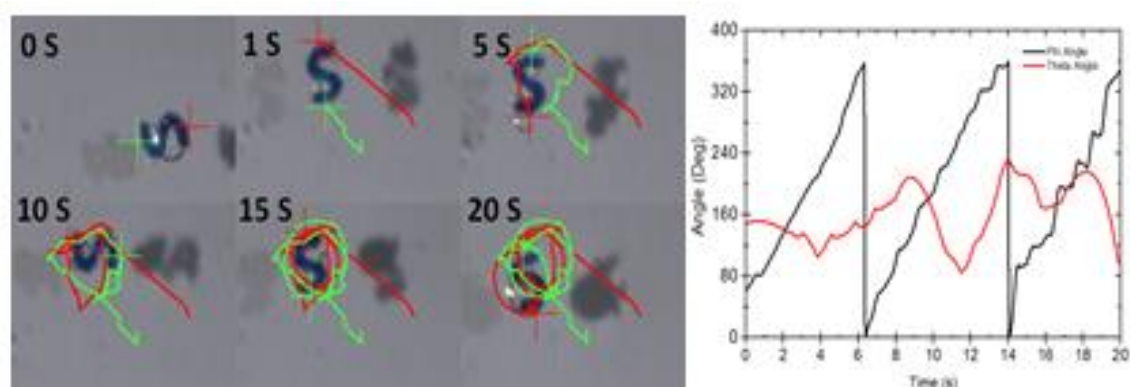
Figure 6-8 Example video snapshot images of Both-sides powered 'S' swimmers in 60 mg/ml of H_2O_2 fuel solution and angle correlation (θ - Orientation and ψ - direction) analysis.

6.3.2.3 Velocity and rotation speed of 'S' shape swimmers

Table 6-1 lists the velocity and rotation speed of the 'S' shaped swimmers with bubble propelled and surface tension driven. The surface tension driven swimmers showed the higher velocity and rotation speed than the bubble propelled swimmers. As I mentioned at the beginning of this section, the structure of 'S' shape swimmers were similar with '⌐' shape swimmers (analysed in Chapter 5). Both of them were centre symmetric structure and same size (about 1.5 mm X 1 mm, 150 printing layers). The trajectory and the speeds of 'S' and '⌐' swimmers also showed the consistent results.

Table 6-1 Velocity and rotation speed of 'S' letter swimmers

Type Of Swimmers	Average Velocity (µm/s)	Vel A/ Vel B (µm/s)	Rotate Speed (rpm)
Catalytic Single-side	500 ± 280	890 ± 500 / 400 ± 160	5 ± 2
Catalytic Both-sides	1580 ± 670	2200 ± 1500 / 2120 ± 850	6 ± 1
Surface Tension driven	11600 ± 8400	13600 ± 9500 / 18600 ± 9500	80 ± 5

6.3.3 Trajectory of 'NATURE' Letter Swimmers

Optimizing the swimming performance of letter swimmers requires control over their shape and the position of the 'engine'. My inkjet printing method is capable of building a wide array of complex shape swimmers, allowing for iteration via various pattern designs. Here, I chose to print letter swimmers to demonstrate the potential for using this approach to systematically refine the letter swimmers design to optimize its swimming track. In order to characterize the morphology of the printed letter swimmers, Figure 6-5A shows the printed 'NATURE' swimmers on silicon wafer substrate and subsequently construct a SEM (Inspect F50) image is used to capture the images of 'NATURE' letter

swimmers from top-view at 5 kV (Figure 6-5B). The length of each letter is approximately 1400 μm and the average width of the swimmers is approximate 1200 μm (described in section 6.3.1.2). These parameters can be readily varied during the fabrication process by changing the modelling bitmap images and script settings in MicroFab software.

Catalase encapsulation allows for efficient propulsion of the letter swimmers and hydrogen peroxide (Sigma-Aldrich) was used as the fuel source. Before analysing the catalytic powered swimmers, I washed all letter swimmers in Di-water at room temperature for 20 min till no visible moving was observed (surface tension driven locomotion). All swimmers were loaded with the same concentration of catalase (8 mg/ml).

The representative track lines of 'NATURE' swimmers' locomotion, shown in Figure 6-9A, Figure 6-10A, Figure 6-11A, Figure 6-12A, Figure 6-13A and Figure 6-14A and corresponding to Video V-NATURE in the supporting information, respectively. Those snipping images illustrate the thrust created by bubbles generated during peroxide decomposition at the two side ends of the 'N' swimmer, at top point of the 'A' swimmer, at the top left part of 'T' swimmer, at the one ends of the 'U' swimmer, at the top centre point of R swimmer and at the middle line of 'E' swimmer, demonstrating the efficacy of the site-specific catalase loading, respectively. The trajectories are highly related to the geometry of the structures. Different letter geometries and position of power engine result in different tracks under identical fuel concentrations (60 mg/ml hydrogen peroxide).

In Figure 6-9A, Figure 6-10A, and Figure 6-12A, 'N', 'A', and 'U' swimmers all rotate in fuel solution but with different rotating centre. For 'N' letter, the

structure is similar to ' └┐ ' (shown in Chapter 5) and 'S' (shown in Section 6.3.2) swimmer, as they are all mirror symmetry. When catalase was loaded at the two opposite ends of the 'N' swimmers, the catalytically generated oxygen bubbles expelled from the two ends and the continuous bubbles actuate the swimmer rotate on its mirror symmetry centre. For 'A' swimmer, the catalytically generated bubbles expelled from the middle line of the 'A' swimmer, and then the fast and high-frequency bubbles merge together and generate a big bubble which locks the 'A' swimmer inside. Thus, the continuous bubbles actuate the 'A' swimmer rotate on the centre of the big bubble circle. However, the continuous merging of small bubbles results in the bubble bursting finally and the burst force push the swimmers to move a big distance in one direction. Then, another big bubble would be generated and repeat the previous steps again and again to form the spiral trajectory finally. The letter 'U' is a structure has reflectional symmetry. Figure 6-12A shows the trajectory of the single-engine 'U' swimmer. 'U' swimmer not only rotates on the cross point of the axial symmetry and the bottom line of 'U' but also slightly moving straight forward every time when the merging bubble burst. Thus, a spiral trajectory was observed from the single side powered 'U' swimmer.

In Figure 6-11A, the top side-way powered 'T' swimmer show a special trajectory which looks like a flower. The catalytically generated small oxygen bubbles expelled from the one top side of 'T' swimmer and the small bubbles merged together to form a big bubble. During the formation of the big bubble, the 'T' swimmer was pulled by the big bubble to rotate following the direction which as same as the expanding direction of the big bubble. Then, the continuous expanded big bubble burst and the burst force suddenly pushed 'T'

swimmer straight back following the bubble burst direction. The expanding and bursting steps repeat and form the 'flower' shape trajectory of 'T' swimmer.

For top-engine 'R' swimmer, a cambered trajectory is observed in Figure 6-13A. The fast and high-frequency bubble ejection leads to continuous motion of 'R' swimmer. Comparing 'R' swimmer to 'A' swimmer, both of them formed big merging bubbles. However, the big bubble generated from 'A' swimmer locking itself inside the bubble while the big bubble generated from 'R' swimmer not locking the swimmer inside the bubble but pushing the swimmer. This difference results in the different of the trajectories between 'R' swimmer and 'A' swimmer.

In Figure 6-14, the middle-engine 'E' swimmer almost move straight forward. The trajectory is reasonable because the 'E' letter is axial symmetry. So, when engine loaded on the axis of symmetry of 'E' letter, the two sides beside the axis of symmetry are balanced and the catalytically generated oxygen bubble ejection leads to continuous motion of the 'E' swimmer moving straight forwards.

In general, my results indicate that the shape of the letter and the position of the 'engine' can be optimized to achieve different trajectory of the swimmers. It can readily convert these letter swimmers into efficient and controllable swimmers for diverse application.
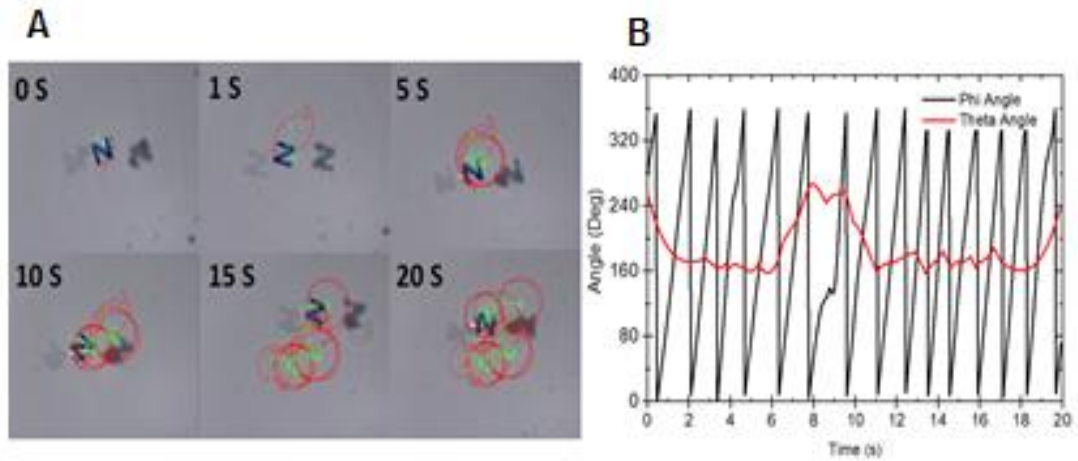
Figure 6-9 Representative track line of motion of of dual-engine 'N' swimmers (A), over 20 s in the presence of 60 mg/ml H_2O_2 fuel solution. B) angle correlation (θ - Orientation and ψ - direction) analysis of 'N' swimmers.
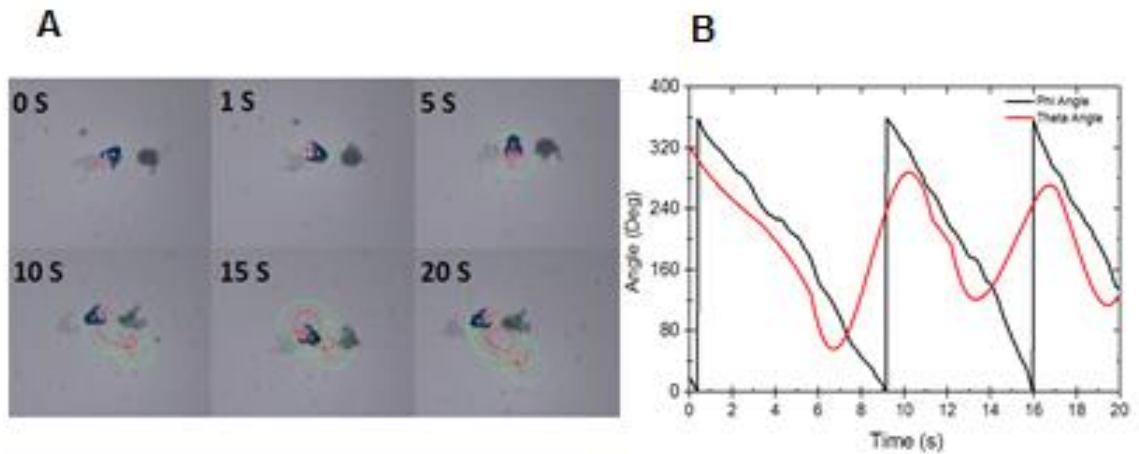
Figure 6-10 Representative track line of motion of middle-line powered 'A' swimmers (A), over 20 s in the presence of 60 mg/ml H_2O_2 fuel solution. B) angle correlation (θ - Orientation and ψ - direction) analysis of 'A' swimmer
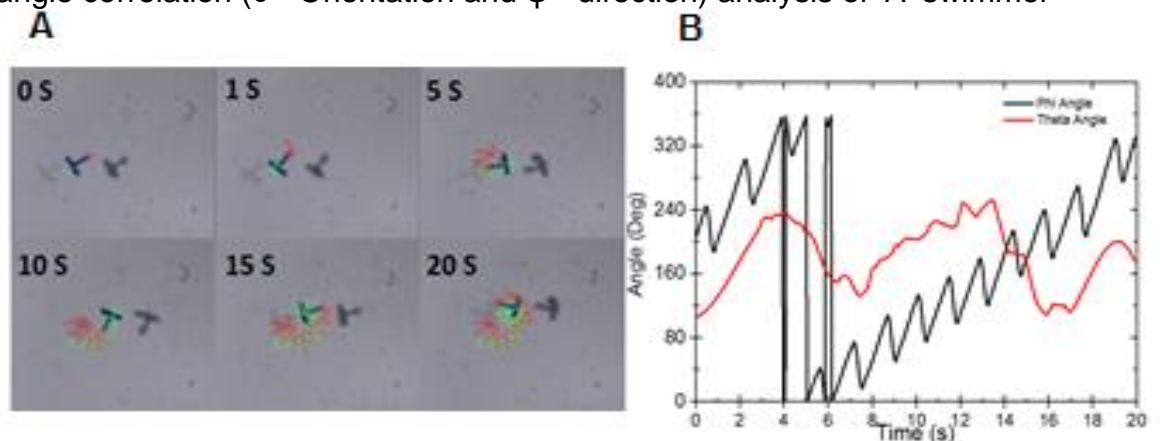
Figure 6-11 Representative track line of motion of a hand-engine 'T' swimmers (A), over 20 s in the presence of 60 mg/ml H_2O_2 fuel solution. B) angle correlation (θ - Orientation and ψ - direction) analysis of 'T' swimmers.
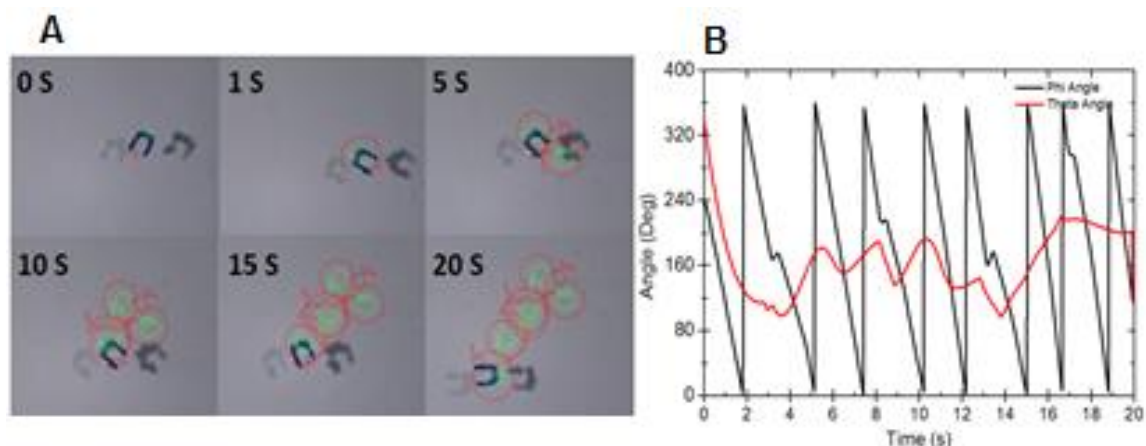
Figure 6-12 Representative track line of motion of a single-engine 'U' swimmers (A), over 20 s in the presence of 60 mg/ml H_2O_2 fuel solution. B) angle correlation (θ - Orientation and ψ - direction) analysis of 'U' swimmers.
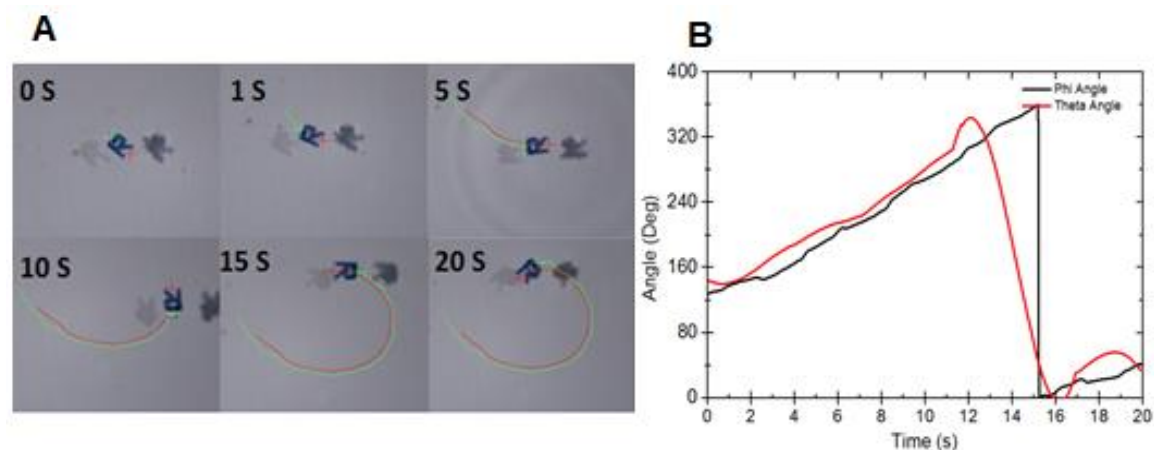
Figure 6-13 Representative track line of motion of a top-engine 'R' swimmers (A), over 20 s in the presence of 60 mg/ml H_2O_2 fuel solution. B) angle correlation (θ - Orientation and ψ - direction) analysis of 'R' swimmers.
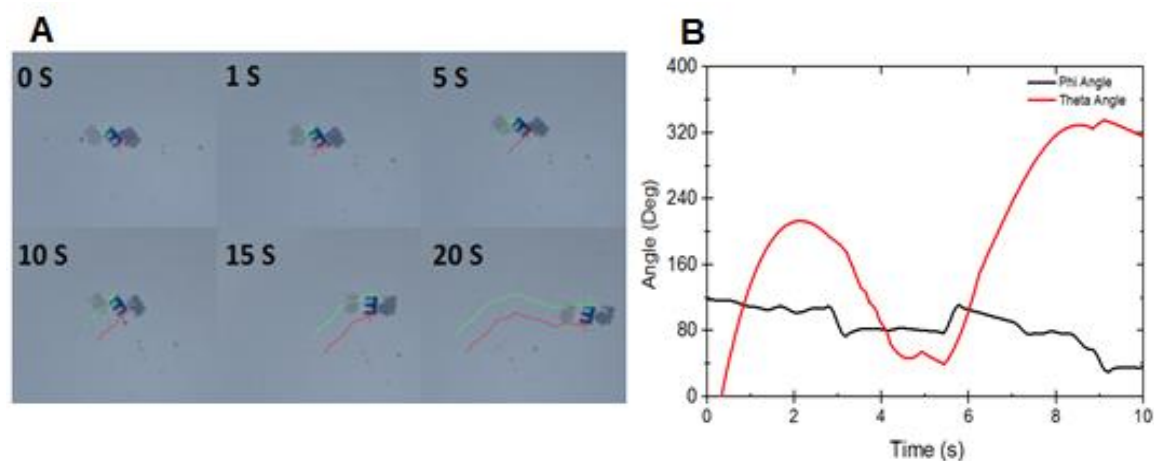
Figure 6-14 Representative track line of motion of a middle-engine 'E' swimmers (A), over 20 s in the presence of 60 mg/ml H_2O_2 fuel solution. B) angle correlation (θ - Orientation and ψ - direction) analysis of 'E' swimmers.

6.3.4   Application - Chemical reaction grab of beads

To explore a potential application of the inkjet-printed letter swimmers, I further incorporated functional NH_3-biotin into the RSF inks which use to fabricate the letter swimmers as a proof-of-concept demonstration of its further use in capturing cancer cells. Specifically, I used EZ-link NHS-Biotin reagents labelled Polyethylenimine (PEI, branched, sigma-aldrich) which is rich contained primary amine macromolecules in solution. Then, the biotin labelled PEI was mixed into RSF inks which were prepared to produce swimmers. Finally, the rich biotin-containing swimmers were fabricated by using the biotin-PEI-mixed RSF inks. It is known that biotin is a naturally occurring vitamin which binds with high affinity to avidin and streptavidin proteins. The fluorescent avidin-polystyrene beads were used to biomimetic cells in order to test whether the letter can capture cells in solution in the early stage experiment.

To evaluate whether the biotin-lined letter swimmers can catch the avidin beads, I designed two test groups (**Figure 6-15**). In the control group, I use the letter swimmers without adding biotins (**Figure 6-15**A). The RSF swimmers were incubated in Di-water containing 0.01 %weight beads at 22 °C for 10 mins, and some visible beads were observed attached on the surface of the swimmers (**Figure 6-15**B). After washing the incubated RSF swimmers, most of the avidin beads detached (**Figure 6-15**C). In the second group, **Figure 6-15**D shows the biotin labelled RSF swimmers. The biotin-RSF swimmers were also incubated in the Di-water containing fluorescent nile red particles (0.1% w/v, 7.24µm, SpheroTech Inc.) at 22 °C for 10 mins. No catalase was loaded into this group, so the swimmers were stationary during the incubation

period. As shown in **Figure 6-15**E, a high intensity of fluorescence was observed. After washing the incubated biotin-RSF swimmers, most of the avidin beads stay on the swimmer (**Figure 6-15**E). Comparing these two groups, I confirmed that the biotin was encapsulated in RSF swimmers' scaffolds, and the interaction between biotin and avidin works.
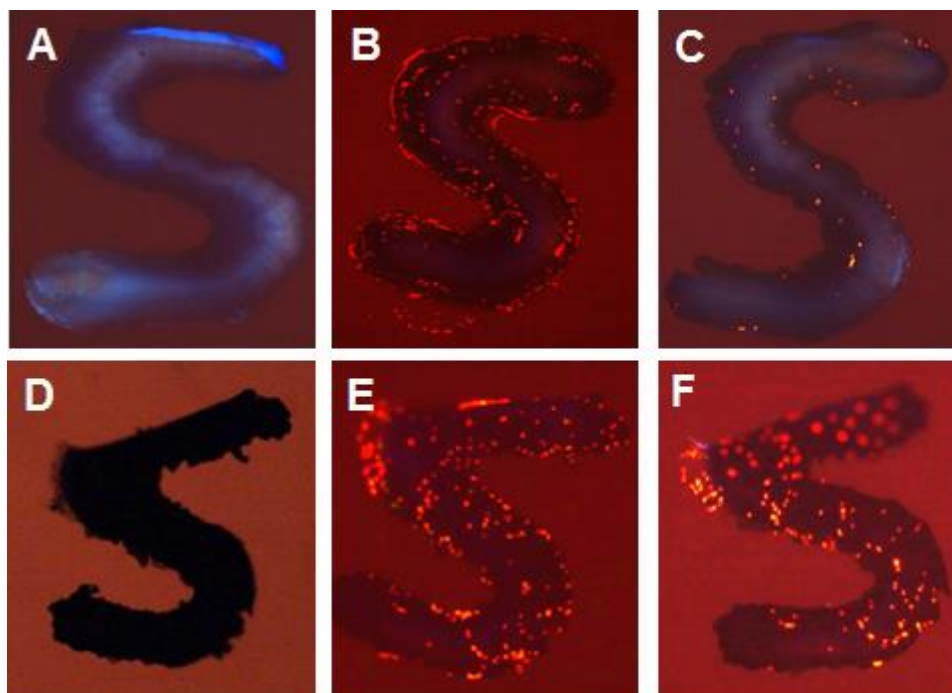
Figure 6-15 Fluorescence microscope images of RSF swimmers (A-C) and biotin mixed RSF swimmers (D-F). A) and D) before putting into avidin-beads, B) and E) reacting with avidin-beads, and C) and F) washing after biotin-avidin linked swimmers.

6.4   Conclusions and future work

Two mechanisms of locomotion (mentioned in Chapter 5) for printed swimmers were found: the first is the catalytic powered locomotion (bubble propulsion), the second is surface tension driven locomotion. In this chapter, studies showed that the trajectories of swimmers could be pre-designed by adjusting swimmer shapes and positions of their 'engine', the latter which only was tested for catalytically powered swimmers.

For the bubble propelled swimmers: Based on analysing the 'S' and 'NATURE' shape swimmers and adjusting the position of catalase, four types of motion have been found, namely: rotation, arc，delivery, and advance and return movement. 1. Rotation: was observed for swimmers which had a central symmetric shape (e.g. 'S', 'N'). IN addition to this 'A' shaped swimmers with the middle-engine also underwent rotation. 2. Arc movement: 'R' shape swimmers with top-engine. 3. Delivery: 'E' shape swimmers with middle-engine. 4. Advance and return movement: 'T' shape swimmers with hand-engine. Furthermore, other letter swimmers were analysed and show some special movements, but still need some more experiments to prove the repeatability of their trajectories. The surface tension driven swimmers were not systematically analysed in regards to the relationship between their structure and trajectory due to the limited time. However, it will be an interesting project to be continued in the future.

The 'S' shape swimmers, which were modified with biotin, caught Nile Red particles. The successfully functional modified swimmers together with the trajectory pre-designed swimmers are potential cancer cell detection devices in the future.

Chapter 7 Conclusions and Future Work

7.1 Conclusions

Different aspects of using inkjet printing to fabricate RSF scaffolds are discussed in this thesis. In the first experimental chapter, chapter 3, I the dissolution process of *Bombyx mori* silk fibroin in suitable solvents in order to generate RSF solutions is described. The resulting RSF silk inks are shown to be inkjet printable bio-inks. Different patterns and substrates were used to confirm the feasibility of using inkjet printing to deposit designed patterns onto target substrates with controllable pattern dimensions. Based on the optical microscopy results, the optimized substrate for printing RSF inks was silicon wafer. Pattern dimensions can be modified / optimized according to the distance of adjacent printed droplets, the amount of layers printed and the printing speed. These results have been published in *Journal of Materials Science [38]* and *Printing for Fabrication (conference paper) [185]*.

In the following Chapters 4 – 6, I investigated the feasibility of reactive inkjet printing of self-propelled swimmers (micro-rockets, stirrers, and letter swimmers) using RSF and analysed the trajectories of the printed RSF swimmers. Chapter 4 focuses on enzyme- (catalase) powered bubble-propelled micro-rockets, these were printed via a layer-by-layer, RIJ printing process. Both fully active micro-rockets and Janus active micro-rockets were printed, and their trajectories compared. This was the first time to use this method and material to fabricate self-propelled micro-rockets and this work has been published in *Small [162]* and *Printing for Fabrication (conference paper) [255]*.

Then, I printed ' └┐ ' RSF swimmers in Chapter 5 and letter swimmers in Chapter 6. Two different types of propulsion mechanisms for swimmers were studied in these chapters: Catalytically powered bubble propulsion and surface tension gradient powered. The different propulsion mechanisms give rise to different ways to control their trajectories. This is described as follows:

❖ In the case of bubble propelled swimmers the trajectories were influenced by the position of the catalase 'engine', the shape of the swimmers, and the rate of catalytic reaction. Higher concentrated fuel solution as well as greater amount of immobilized catalase resulted in quicker rotation speeds and average centre velocities.

❖ In order to influence the trajectories of surface tension driven swimmers the shape of the swimmers and the amount of the encapsulated PEG_{400} was altered. A higher concentration of PEG_{400} resulted in higher initial speeds, both rotational speed and average centre velocities.

After having the ability to control trajectories of the previously described swimmers they were used to investigate the use in different future applications:

In Chapter 5, the ' └┐ ' shape swimmers were used as stirrers for bio-mixing solutions. For this application, the surface tension driven swimmers were selected due to their quicker rotational speeds and smoother trajectories, compared to the bubble propelled swimmers, which have a start - stopping motion due to bubble release. It was shown that the RSF-stirrer were able to mix blue dye dropped into a water solution quicker than without.

In the last experimental Chapter 6, letter swimmers were used as targeted capture devices via modified functional ingredient on the surface of the

swimmers. In this study PEI was functionalised with biotin and immobilised onto the silk swimmers ('S') via entanglement and adsorption. These were then able to capture fluorescent streptavidin functionalized polystyrene colloids in an attempt to mimic the capture of cancer cells, which is the target of future work.

This thesis introduced a novel method to fabricating self-propelled micro-swimmers via RIJ and was able to swim via two different mechanisms: bubble propulsion and surface tension driven.

Due to the nature of RIJ as a fabrication process it is possible to easily alter the structures of printed swimmers along with their functional moieties such as enzymes and antibodies. The inks used also give rise to their biocompatibility which extends their capable application areas from previous polystyrene/ Platinum and similar based systems. Furthermore, the work described here has resulted in a new type of swimmer which shows great potential for future studies.

7.2 Future Work

The work conducted in this thesis has identified that inkjet printing can be used to print RSF scaffolds. It is important to establish a database of trajectories for different types of swimmers. Future work includes a deeper analysis of functional swimmers, which are able to be designed as different structures and adding more functional ingredients e.g. peptide I_3K , antibody.

There are some ideas that I would have liked to try during the fabrication of the micro-rockets in chapter 4. Figure 7-1 shows the schematic images of how to design the different micro-rockets with different percentages of 'catalase motor' parts (catalase gradient) and further to help better control the trajectories of micro-rockets.
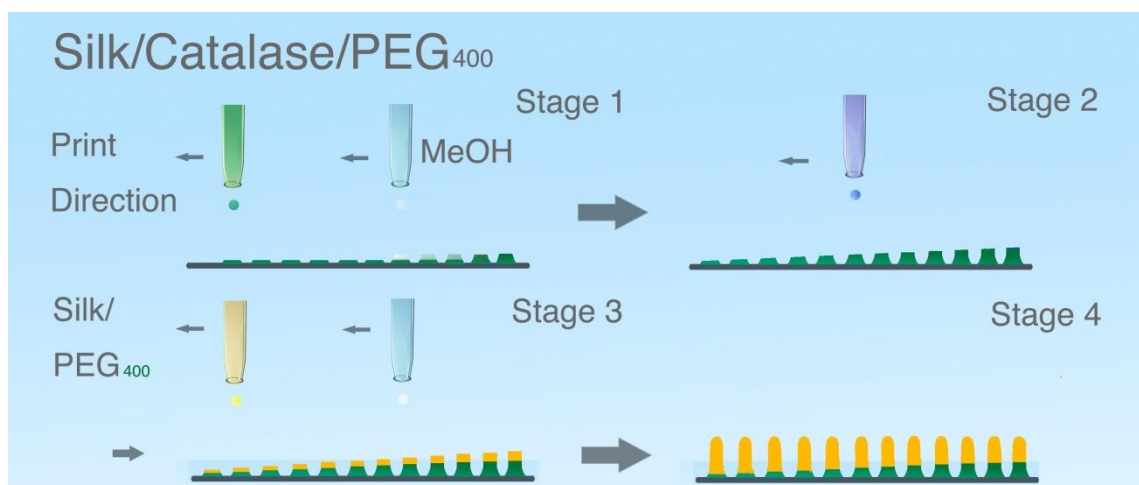
Figure 7-1 Schematic represents the LBL printing process of RSF micro-rockets with differnet percentages of catalase part. Green represents Catalase/RSF/PEG400 inks and yellow represents RSF/PEG400 inks when generated Janus RSF micros-rockets.

Furthermore, in the case of surface tension driven swimmers, it would be interesting to analyse how different structures (e.g. 'L', 'M', etc.) will affect the trajectories of these.

Finally To explore more applications the swimmers can be used in is the most

important part of future work. Here, greater analysis into the beads capture experiment described in Chapter 6 is a good starting point. The analysing of how the reaction happened between the streptavidin loaded swimmers with the biotin binding beads is a pre-experiment for future cancer cell capture experiment. The PS-beads is used in the experiment are supposed to mimic the capture of cancer cells, where streptavidin loaded swimmers can have bio-ethylated antibodies easily attached to the surfaces of the swimmers which could prove a simple method of creating cancer cells specific swimmers as a method to detect certain types of cancer.

8. Reference

[1]   D. L. M. Kaplan, SM. ; Arcidiacono,s. ; Fossey, S. ; semeca,KWM., *Protein based materials*. Boston: Birkhauser, 1998.

[2]   G. H. Altman, F. Diaz, C. Jakuba, T. Calabro, R. L. Horan, J. Chen*, et al.*, "Silk-based biomaterials," *biomaterials,* vol. 24, pp. 401-416, 2003.

[3]   C. Vepari and D. L. Kaplan, "Silk as a Biomaterial," *Prog Polym Sci,* vol. 32, pp. 991-1007, 2007.

[4]   J. G. Hardy and T. R. Scheibel, "Composite materials based on silk proteins," *Progress in Polymer Science,* vol. 35, pp. 1093-1115, 2010.

[5]   F. Wang, C. Yang, and X. Hu, "Advanced Protein Composite Materials," vol. 1175, pp. 177-208, 2014.

[6]   F. D. Gregory H. Altman, Caroline Jakuba,Tara Calabro,Rebecca L. Horan,Jingsong Chen,Helen Lu,John Richmond,David L. Kaplan, "Silk-based biomaterials," *biomaterials,* vol. 24, pp. 401-416, 2003.

[7]   Y. Zhang, "Applications of natural silk protein sericin in biomaterials," *Biotechnology Advances,* vol. 20, pp. 91-100, 2002.

[8]   H. S. G. Sung-Won Ha, Alan E. Tonelli, Samuel M. Hudson, "Structural Study of Irregular Amino Acid Sequences in the heavy chain of Bombyx mori silk fibroin," *Biomacromolecules,* vol. 6, pp. 2563-2569, 2005.

[9]   *Mysterious Natural Protein-Silk.*

[10]   S. P. G. Regina Valluzzi, "The Crystal Structure of Bombyx mori Silk Fibroin at the Air-water Interface," *Biopolymers,* vol. 42, pp. 705-717, 1997.

[11]   R. Rajkhowa, B. Levin, S. L. Redmond, L. H. Li, L. Wang, J. R. Kanwar*, et al.*, "Structure and properties of biomedical films prepared from aqueous and acidic silk fibroin solutions," *J Biomed Mater Res A,* Feb 9 2011.

[12]   H.-J. a. D. L. Kaplan, "Mechanism of silk processing in insects and spiders," *NATURE,* vol. 424, pp. 1057-1061, 2003.

[13]   S. J. H. R.Valluzzi, S.P.Gido, David Kaplan, "Bombyx morisilk fibroin liquid crystallinity and crystallization at aqueous fibroin-organic solvent interfaces," *Biological Macromolecules,* vol. 24, pp. 277-236, 1999.

[14]   X. Dong, Q. Zhao, L. Xiao, Q. Lu, and D. L. Kaplan, "Amorphous Silk Nanofiber Solutions for Fabricating Silk-Based Functional Materials," *Biomacromolecules,* vol. 17, pp. 3000-3006, 2016/09/12 2016.

[15]   T. Yucel, M. L. Lovett, and D. L. Kaplan, "Silk-based biomaterials for sustained drug delivery," *J Control Release,* vol. 190C, pp. 381-397, Sep 28 2014.

[16]   T. Wongpinyochit, B. F. Johnston, and F. P. Seib, "Manufacture and Drug Delivery Applications of Silk Nanoparticles," *J Vis Exp,* Oct 08 2016.

[17]   E. Wenk, H. P. Merkle, and L. Meinel, "Silk fibroin as a vehicle for drug delivery applications," *J Control Release,* vol. 150, pp. 128-41, Mar 10 2011.

197

[18]   N. K. a. U. Bora, "Silk Fibroin in Tissue Engineering," *Advanced Healthcare Materials,* vol. 1, pp. 393-412, 2012.

[19]   F. G. Omenetto and D. L. Kaplan, "New Opportunities for an Ancient Material," *Science,* vol. 329, pp. 528-531, 2010.

[20]   B. Kundu, R. Rajkhowa, S. C. Kundu, and X. Wang, "Silk fibroin biomaterials for tissue regenerations," *Adv Drug Deliv Rev,* vol. 65, pp. 457-70, Apr 2013.

[21]   H. O. Sadayuki Kurosaki, Mayumi Kunitomo, Mamoru Koyama, Ruby Pawankar and Koshi Matumoto, "Fibroin allergy IgE mediated hypersensitivity to silk suture materials," vol. 66, pp. 41-44, 1999.

[22]   K. R. k. H. Kaz Soong, "Adverse Reactions to Virgin Silk sutures in Cataract Surgery," *Ophthalmology,* vol. 91, pp. 479-483, 1984.

[23]   M. K. Kim, H. W. Kwak, H. H. Kim, T. R. Kwon, S. Y. Kim, B. J. Kim*, et al.*, "Surface modification of silk fibroin nanofibrous mat with dextran for wound dressing," *Fibers and Polymers,* vol. 15, pp. 1137-1145, 2014.

[24]   B. L. Xiaomeng Li, Jun Ma, Xiaoyu Wang and Shengming Zhang, "Development of a silk fibroin_HTCC_PVA sponge for chronic wound dressing," *Journal of Bioactive and Compatible Polymers,* vol. 29, pp. 398 – 411, 2014.

[25]   L. P. Stefania Elena Navone, Marta Dossena, Anna Ferri, Gloria Invernici, Francesco Acerbi,Silvia Cristini, Gloria Bedini, Valentina Tosetti, Valentina Ceserani, Arianna Bonomi, Augusto Pessina,Giuliano Freddi, Antonio Alessandrino, Piero Ceccarelli, Rolando Campanella, Giovanni Marfia,Giulio Alessandri and Eugenio Agostino Parati, "Decellularized silk fibroin scaffold primed with adipose mesenchymal stromal cells improves wound healing in diabetic mice," *Navoneet al. Stem Cell Research & Therapy,* vol. 5, p. 15, 2014.

[26]   U. R. R. Jesada Chutipakdeevong, Pitt Supaphol, "process optimization of electrospun silk fibroin fiber mat for accelerated wound healing," *Journal of Applied Polymer Science,* vol. 130, pp. 3634-3644, 2013.

[27]   A. M. Altman, Y. Yan, N. Matthias, X. Bai, C. Rios, A. B. Mathur*, et al.*, "IFATS Collection: Human Adipose-Derived Stem Cells Seeded on a Silk Fibroin-Chitosan Scaffold Enhance Wound Repair in a Murine Soft Tissue Injury Model," *STEM CELLS,* vol. 27, pp. 250-258, 2009.

[28]   R. Okabayashi, M. Nakamura, T. Okabayashi, Y. Tanaka, A. Nagai, and K. Yamashita, "Efficacy of polarized hydroxyapatite and silk fibroin composite dressing gel on epidermal recovery from full-thickness skin wounds," *Journal of Biomedical Materials Research Part B: Applied Biomaterials,* vol. 90B, pp. 641-646, 2009.

[29]   S. K. Sugihara A, Morita H, Ninagawa T, Tubouchi K, Tobe R, Izumiya M, Horio T, Abraham NG, Ikehara S., "Promotive effects of a silk film on epidermal recovery from full-thickness skin wounds.," *Proc Soc Exp Biol Med,* vol. 225, pp. 58-64, 2000.

[30]   H. O. Sadayuki Kurosaki, Mayumi Kunitomo, Mamoru Koyama, Ruby Pawankar and Koshi Matumoto, "Fibroin allergy: IgE mediated

hypersensitivity to silk suture materials," *Journal of Nippon Medical School,* vol. 66, pp. 41-44, 1999.

[31]   M. Santin, A. Motta, G. Freddi, and M. Cannas, "In vitro evaluation of the inflammatory potential of the silk fibroin," *Journal of Biomedical Materials Research,* vol. 46, pp. 382-389, 1999.

[32]   L. Meinel, S. Hofmann, V. Karageorgiou, C. Kirker-Head, J. McCool, G. Gronowicz*, et al.*, "The inflammatory responses to silk films in vitro and in vivo," *Biomaterials,* vol. 26, pp. 147-155, 2005/01/01/ 2005.

[33]   Y. Shen, S. L. Redmond, J. M. Papadimitriou, B. M. Teh, S. Yan, Y. Wang*, et al.*, "The biocompatibility of silk fibroin and acellular collagen scaffolds for tissue engineering in the ear," *Biomed Mater,* vol. 9, p. 015015, Feb 2014.

[34]   M. Vert, Y. Doi, K.-H. Hellwich, M. Hess, P. Hodge, P. Kubisa*, et al.*, "Terminology for biorelated polymers and applications (IUPAC Recommendations 2012)," *Pure and Applied Chemistry,* vol. 84, 2012.

[35]   J. N. Wang, Z. W. Liu, Y. X. Yang, and H. Y. Huang, "Enzymatic degradation behavior of silk fibroin fiber treated by -ray irradiation," *Textile Research Journal,* vol. 82, pp. 1799-1805, 2012.

[36]   Y. Wang, D. D. Rudymb, A. Walsh, L. Abrahamsend, H.-J. Kimc, H. S. Kime*, et al.*, "In vivo degradation of three-dimensional silk fibroin scaffolds," *Biomaterials,* vol. 29, pp. 3415-28, Aug-Sep 2008.

[37]   Y. Hu, Q. Zhang, R. You, L. Wang, and M. Li, "The Relationship between Secondary Structure and Biodegradation Behavior of Silk Fibroin Scaffolds," *Advances in Materials Science and Engineering,* vol. 2012, pp. 1-5, 2012.

[38]   P. Rider, Y. Zhang, C. Tse, Y. Zhang, D. Jayawardane, J. Stringer*, et al.*, "Biocompatible silk fibroin scaffold prepared by reactive inkjet printing," *Journal of Materials Science,* 2016.

[39]   K. Numata, P. Cebe, and D. L. Kaplan, "Mechanism of enzymatic degradation of beta-sheet crystals," *Biomaterials,* vol. 31, pp. 2926-33, Apr 2010.

[40]   E. M. Pritchard, T. Valentin, D. Boison, and D. L. Kaplan, "Incorporation of proteinase inhibitors into silk-based delivery devices for enhanced control of degradation and drug release," *Biomaterials,* vol. 32, pp. 909-18, Jan 2011.

[41]   J. Qian, A. Suo, X. Jin, W. Xu, and M. Xu, "Preparation and in vitro characterization of biomorphic silk fibroin scaffolds for bone tissue engineering," *J Biomed Mater Res A,* vol. 102, pp. 2961-71, Sep 2014.

[42]   M. D. M. D. Pierschbacher, "Cell attachment activity of fibronectin can be duplicated by small synthetic fragments of the molecule," *Nature* vol. 309(5963), pp. 30-33, 1984.

[43]   F. Galeotti, A. Andicsova, F. Bertini, and C. Botta, "A versatile click-grafting approach to surface modification of silk fibroin films," *Journal of Materials Science,* vol. 48, pp. 7004-7010, 2013.

[44]   V. Dhyani and N. Singh, "Controlling the cell adhesion property of silk films by graft polymerization," *ACS Appl Mater Interfaces,* vol. 6, pp. 5005-11, Apr 9 2014.

[45] K. Boonla and S. Saikrasun, "Influence of silk surface modification via plasma treatments on adsorption kinetics of lac dyeing on silk," *Textile Research Journal,* vol. 83, pp. 288-297, 2012.

[46] M. Liang, J. Yao, X. Chen, L. Huang, and Z. Shao, "Silk fibroin immobilization on poly(ethylene terephthalate) films: comparison of two surface modification methods and their effect on mesenchymal stem cells culture," *Mater Sci Eng C Mater Biol Appl,* vol. 33, pp. 1409-16, Apr 1 2013.

[47] A. H. Teuschl, L. Neutsch, X. Monforte, D. Runzler, M. van Griensven, F. Gabor*, et al.*, "Enhanced cell adhesion on silk fibroin via lectin surface modification," *Acta Biomater,* vol. 10, pp. 2506-17, Jun 2014.

[48] Susan Sofia, Mary Beth McCarthy, Gloria Gronowicz, and D. L. Kaplan, "Functionalized silk-based biomaterials for bone formation," *Journal of Biomedical Materials Research,* vol. 54, pp. 139-148, 2001.

[49] S. Hofmann, K. S. Stok, T. Kohler, A. J. Meinel, and R. Muller, "Effect of sterilization on structural and material properties of 3-D silk fibroin scaffolds," *Acta Biomater,* vol. 10, pp. 308-17, Jan 2014.

[50] M. A. de Moraes, R. F. Weska, and M. M. Beppu, "Effects of sterilization methods on the physical, chemical, and biological properties of silk fibroin membranes," *J Biomed Mater Res B Appl Biomater,* vol. 102, pp. 869-76, May 2014.

[51] A. C. Rodas, R. Polak, P. H. Hara, E. I. Lee, R. N. Pitombo, and O. Z. Higa, "Cytotoxicity and endothelial cell adhesion of lyophilized and irradiated bovine pericardium modified with silk fibroin and chitosan," *Artif Organs,* vol. 35, pp. 502-7, May 2011.

[52] M. T. Yohko Gotoh, Norihiko Minoura and Yohji Irnai, "Synthesis of poly(ethylene glycol)-silk fibroin conjugates and surface interaction between L-929 cells and the conjugates," *Biomaterials,* vol. 18, pp. 267-271, 1997.

[53] D. N. Rockwood, R. C. Preda, T. Yucel, X. Wang, M. L. Lovett, and D. L. Kaplan, "Materials fabrication from Bombyx mori silk fibroin," *Nat Protoc,* vol. 6, pp. 1612-31, Oct 2011.

[54] J. P. U.J. Kim, C. Li, H.-J. Jin, R. Valluzzi, D.L. Kaplan, "Structure and Properties of Silk Hydrogels," *Biomacromolecules,* vol. 5, pp. 786–792, 2004.

[55] X. Wang, J. A. Kluge, G. G. Leisk, and D. L. Kaplan, "Sonication-induced gelation of silk fibroin for cell encapsulation," *Biomaterials,* vol. 29, pp. 1054-64, Mar 2008.

[56] T. Yucel, P. Cebe, and D. L. Kaplan, "Vortex-induced injectable silk fibroin hydrogels," *Biophys J,* vol. 97, pp. 2044-50, Oct 7 2009.

[57] G. G. Leisk, T. J. Lo, T. Yucel, Q. Lu, and D. L. Kaplan, "Electrogelation for protein adhesives," *Adv Mater,* vol. 22, pp. 711-5, Feb 9 2010.

[58] A. Motta, C. Migliaresi, F. Faccioni, P. Torricelli, M. Fini, and R. Giardino, "Fibroin hydrogels for biomedical applications: preparation, characterization and in vitro cell culture studies," *Journal of Biomaterials Science, Polymer Edition,* vol. 15, pp. 851-864, 2004.

[59] N. Guziewicz, A. Best, B. Perez-Ramirez, and D. L. Kaplan, "Lyophilized silk fibroin hydrogels for the sustained local delivery of therapeutic monoclonal antibodies," *Biomaterials,* vol. 32, pp. 2642-50, Apr 2011.

[60] P. H. Chao, S. Yodmuang, X. Wang, L. Sun, D. L. Kaplan, and G. Vunjak-Novakovic, "Silk hydrogel for cartilage tissue engineering," *J Biomed Mater Res B Appl Biomater,* vol. 95, pp. 84-90, Oct 2010.

[61] B. D. Lawrence, S. Wharram, J. A. Kluge, G. G. Leisk, F. G. Omenetto, M. I. Rosenblatt*, et al.*, "Effect of hydration on silk film material properties," *Macromol Biosci,* vol. 10, pp. 393-403, Apr 8 2010.

[62] S. K. K. Maneesh K. Gupta, David M. Phillips,Laura A. Sowards,Lawrence F. Drummy,Madhavi P. Kadakia, and Rajesh R. Naik, "Patterned silk films cast from Ionic Liquid solubilized fibroin as scaffolds for cell growth," *Langmuir,* vol. 23, pp. 1315-1319, 2007.

[63] M. Y. Akon Higuchi, Takeshi Ohno, Tetsuo Asakura & Mariko Hara, "Production of interferon-beta in a culture of fibroblast cells on some polymeric films.pdf>," *Cytotechnology,* vol. 34, pp. 165–173, 2000.

[64] X. Zhang, M. R. Reagan, and D. L. Kaplan, "Electrospun silk biomaterial scaffolds for regenerative medicine," *Adv Drug Deliv Rev,* vol. 61, pp. 988-1006, Oct 5 2009.

[65] S. V. F. Hyoung-Joon Jin, Gregory C. Rutledge, and David L. Kaplan, "Electrospinning Bombyx mori silk with poly(ethylene oxide)," *Biomacromolecules,* vol. 3, pp. 1233-1239, 2002.

[66] H. Cao, X. Chen, J. Yao, and Z. Shao, "Fabrication of an alternative regenerated silk fibroin nanofiber and carbonated hydroxyapatite multilayered composite via layer-by-layer," *Journal of Materials Science,* vol. 48, pp. 150-155, 2012.

[67] C. Meechaisue, P. Wutticharoenmongkol, R. Waraput, T. Huangjing, N. Ketbumrung, P. Pavasant*, et al.*, "Preparation of electrospun silk fibroin fiber mats as bone scaffolds: a preliminary study," *Biomed Mater,* vol. 2, pp. 181-8, Sep 2007.

[68] A. S. Badami, M. R. Kreke, M. S. Thompson, J. S. Riffle, and A. S. Goldstein, "Effect of fiber diameter on spreading, proliferation, and differentiation of osteoblastic cells on electrospun poly(lactic acid) substrates," *Biomaterials,* vol. 27, pp. 596-606, Feb 2006.

[69] M. E. Kinahan, E. Filippidi, S. Koster, X. Hu, H. M. Evans, T. Pfohl*, et al.*, "Tunable silk: using microfluidics to fabricate silk fibers with controllable properties," *Biomacromolecules,* vol. 12, pp. 1504-11, May 9 2011.

[70] A. E. T. Sung-Won Ha, and Samuel M. Hudson, "Structural studies of Bombyx mori silk fibroin during regeneration from solutions and wet fiber spinning," *biomacromolecules,* vol. 6, pp. 1722-1731, 2005.

[71] N. Ashammakhi, A. Ndreu, Y. Yang, H. Ylikauppila, and L. Nikkola, "Nanofiber-based scaffolds for tissue engineering," *European Journal of Plastic Surgery,* vol. 35, pp. 135-149, 2008.

[72]   X. Zhang, X. Wang, V. Keshav, J. T. Johanas, G. G. Leisk, and D. L. Kaplan, "Dynamic culture conditions to generate silk-based tissue-engineered vascular grafts," *Biomaterials,* vol. 30, pp. 3213-23, Jul 2009.

[73]   M. Lovett, C. Cannizzaro, L. Daheron, B. Messmer, G. Vunjak-Novakovic, and D. L. Kaplan, "Silk fibroin microtubes for blood vessel engineering," *Biomaterials,* vol. 28, pp. 5271-9, Dec 2007.

[74]   M. L. Lovett, C. M. Cannizzaro, G. Vunjak-Novakovic, and D. L. Kaplan, "Gel spinning of silk tubes for tissue engineering," *Biomaterials,* vol. 29, pp. 4650-7, Dec 2008.

[75]   T. Hino, M. Tanimoto, and S. Shimabayashi, "Change in secondary structure of silk fibroin during preparation of its microspheres by spray-drying and exposure to humid atmosphere," *Journal of Colloid and Interface Science,* vol. 266, pp. 68-73, 2003.

[76]   H. Onishi, T. Oosegi, Y. Machida, and J. W. McGinity, "Preparation and in vitro evaluation of chitosan microspheres containing prednisolone: comparison of simple and conjugate microspheres," *Drug Dev Ind Pharm,* vol. 31, pp. 597-605, Aug 2005.

[77]   Z. Cao, X. Chen, J. Yao, L. Huang, and Z. Shao, "The preparation of regenerated silk fibroin microspheres," *Soft Matter,* vol. 3, p. 910, 2007.

[78]   X. Wang, E. Wenk, A. Matsumoto, L. Meinel, C. Li, and D. L. Kaplan, "Silk microspheres for encapsulation and controlled release," *J Control Release,* vol. 117, pp. 360-70, Feb 26 2007.

[79]   E. Wenk, A. J. Wandrey, H. P. Merkle, and L. Meinel, "Silk fibroin spheres as a platform for controlled drug delivery," *J Control Release,* vol. 132, pp. 26-34, Nov 24 2008.

[80]   R. Rajkhowa, L. Wang, J. Kanwar, and X. Wang, "Fabrication of ultrafine powder from eri silk through attritor and jet milling," *Powder Technology,* vol. 191, pp. 155-163, 2009.

[81]   R. Rajkhowa, X. Hu, T. Tsuzuki, D. L. Kaplan, and X. Wang, "Structure and biodegradation mechanism of milled Bombyx mori silk particles," *Biomacromolecules,* vol. 13, pp. 2503-12, Aug 13 2012.

[82]   A. S. Lammel, X. Hu, S. H. Park, D. L. Kaplan, and T. R. Scheibel, "Controlling silk fibroin particle features for drug delivery," *Biomaterials,* vol. 31, pp. 4583-91, Jun 2010.

[83]   L. Zhu, R. P. Hu, H. Y. Wang, Y. J. Wang, and Y. Q. Zhang, "Bioconjugation of neutral protease on silk fibroin nanoparticles and application in the controllable hydrolysis of sericin," *J Agric Food Chem,* vol. 59, pp. 10298-302, Sep 28 2011.

[84]   X. Wen, X. Peng, H. Fu, Y. Dong, K. Han, J. Su*, et al.*, "Preparation and in vitro evaluation of silk fibroin microspheres produced by a novel ultra-fine particle processing system," *Int J Pharm,* vol. 416, pp. 195-201, Sep 15 2011.

[85]   B. Subia and S. C. Kundu, "Drug loading and release on tumor cells using silk fibroin-albumin nanoparticles as carriers," *Nanotechnology,* vol. 24, p. 035103, Jan 25 2013.

[86] X. Wang, T. Yucel, Q. Lu, X. Hu, and D. L. Kaplan, "Silk nanospheres and microspheres from silk/pva blend films for drug delivery," *Biomaterials,* vol. 31, pp. 1025-35, Feb 2010.

[87] M. Kazemimostaghim, R. Rajkhowa, T. Tsuzuki, and X. Wang, "Production of submicron silk particles by milling," *Powder Technology,* vol. 241, pp. 230-235, 2013.

[88] M. Kazemimostaghim, R. Rajkhowa, K. Patil, T. Tsuzuki, and X. Wang, "Structure and characteristics of milled silk particles," *Powder Technology,* vol. 254, pp. 488-493, 2014.

[89] W. Song, M. Muthana, J. Mukherjee, R. J. Falconer, C. A. Biggs, and X. Zhao, "Magnetic-Silk Core–Shell Nanoparticles as Potential Carriers for Targeted Delivery of Curcumin into Human Breast Cancer Cells," *ACS Biomaterials Science & Engineering,* vol. 3, pp. 1027-1038, 2017.

[90] H.-J. J. Rina Nazarov, and David L. Kaplan, "Porous 3-D Scaffolds from Regenerated Silk Fibroin," *Biomacromolecules,* vol. 5, pp. 718-726, 2004.

[91] A. L. Oliveira, L. Sun, H. J. Kim, X. Hu, W. Rice, J. Kluge*, et al.*, "Aligned silk-based 3-D architectures for contact guidance in tissue engineering," *Acta Biomater,* vol. 8, pp. 1530-42, Apr 2012.

[92] U. J. Kim, J. Park, H. J. Kim, M. Wada, and D. L. Kaplan, "Three-dimensional aqueous-derived biomaterial scaffolds from silk fibroin," *Biomaterials,* vol. 26, pp. 2775-85, May 2005.

[93] P. Wongpanit, N. Sanchavanakit, P. Pavasant, T. Bunaprasert, Y. Tabata, and R. Rujiravanit, "Preparation and characterization of chitin whisker-reinforced silk fibroin nanocomposite sponges," *European Polymer Journal,* vol. 43, pp. 4123-4135, 2007.

[94] S. Talukdar, Q. T. Nguyen, A. C. Chen, R. L. Sah, and S. C. Kundu, "Effect of initial cell seeding density on 3D-engineered silk fibroin scaffolds for articular cartilage tissue engineering," *Biomaterials,* vol. 32, pp. 8927-37, Dec 2011.

[95] H. J. Kim, U. J. Kim, G. G. Leisk, C. Bayan, I. Georgakoudi, and D. L. Kaplan, "Bone regeneration on macroporous aqueous-derived silk 3-D scaffolds," *Macromol Biosci,* vol. 7, pp. 643-55, May 10 2007.

[96] Q. Lu, B. Zhang, M. Li, B. Zuo, D. L. Kaplan, Y. Huang*, et al.*, "Degradation mechanism and control of silk fibroin," *Biomacromolecules,* vol. 12, pp. 1080-6, Apr 11 2011.

[97] A. Leal-Egaña and T. Scheibel, "Silk-based materials for biomedical applications," *Biotechnology and Applied Biochemistry,* vol. 55, pp. 155-167, 2010.

[98] Y. Wang, H. J. Kim, G. Vunjak-Novakovic, and D. L. Kaplan, "Stem cell-based tissue engineering with silk biomaterials," *Biomaterials,* vol. 27, pp. 6064-82, Dec 2006.

[99] T. Li, Y. L. Wang, F. F. Guo, and D. L. Shi, "Synthesis and Biomedical Applications of Magnetic Nanocomposites with Complex Morphologies," *Progress in Chemistry,* vol. 25, pp. 2053-2067, Dec 24 2013.

[100] S. Sánchez, L. Soler, and J. Katuri, "Chemically Powered Micro- and Nanomotors," *Angewandte Chemie International Edition,* vol. 54, pp. 1414-1444, 2015.

[101] J. Wang, "Self-propelled affinity biosensors: Moving the receptor around the sample," *Biosensors and Bioelectronics,* vol. 76, pp. 234-242, 2016/02/15/ 2016.

[102] V. Magdanz, S. Sanchez, and O. G. Schmidt, "Development of a Sperm-Flagella Driven Micro-Bio-Robot," *Advanced Materials,* vol. 25, pp. 6581-6588, 2013.

[103] H. Yin, M. D. Wang, K. Svoboda, R. Landick, S. M. Block, and J. Gelles, "Transcription Against an Applied Force," *Science,* vol. 270, pp. 1653-1657, 1995.

[104] X. L. Yuan, W. Wei, X. P. Chen, X. Z. Wang, J. Ren, and Y. H. Sun, "Effect of Sm2O3 promoter on catalytic performance of Cu/Mn/Zr/Ni catalyst for alcohol synthesis," *Chinese Journal of Catalysis,* vol. 22, pp. 541-544, Nov 2001.

[105] W. F. Paxton, A. Sen, and T. E. Mallouk, "Motility of Catalytic Nanoparticles through Self-Generated Forces," *Chemistry – A European Journal,* vol. 11, pp. 6462-6470, 2005.

[106] K. Y. Han, H. R. Zuo, Z. W. Zhu, G. P. Cao, C. Lu, and Y. H. Wang, "High Performance of Palladium Nanoparticles Supported on Carbon Nanotubes for the Hydrogenation of Commercial Polystyrene," *Industrial & Engineering Chemistry Research,* vol. 52, pp. 17750-17759, Dec 18 2013.

[107] R. Maria-Hormigos, B. Jurado-Sanchez, and A. Escarpa, "Labs-on-a-chip meet self-propelled micromotors," *Lab on a Chip,* vol. 16, pp. 2397-2407, 2016.

[108] L. Baraban, R. Streubel, D. Makarov, L. Han, D. Karnaushenko, O. G. Schmidt*, et al.*, "Fuel-Free Locomotion of Janus Motors: Magnetically Induced Thermophoresis," *ACS Nano,* vol. 7, pp. 1360-1367, 2013/02/26 2013.

[109] D. Velegol, A. Garg, R. Guha, A. Kar, and M. Kumar, "Origins of concentration gradients for diffusiophoresis," *Soft Matter,* vol. 12, pp. 4686-4703, 2016.

[110] T. Bhuyan, A. K. Singh, D. Dutta, A. Unal, S. S. Ghosh, and D. Bandyopadhyay, "Magnetic Field Guided Chemotaxis of iMushbots for Targeted Anticancer Therapeutics," *ACS Biomaterials Science & Engineering,* 2017/03/22 2017.

[111] A. K. Singh, T. K. Mandal, and D. Bandyopadhyay, "Magnetically guided chemical locomotion of self-propelling paperbots," *RSC Advances,* vol. 5, pp. 64444-64449, 2015.

[112] A. K. Singh, K. K. Dey, A. Chattopadhyay, T. K. Mandal, and D. Bandyopadhyay, "Multimodal chemo-magnetic control of self-propelling microbots," *Nanoscale,* vol. 6, pp. 1398-1405, 2014.

[113] K. E. Peyer, L. Zhang, and B. J. Nelson, "Bio-inspired magnetic swimming microrobots for biomedical applications," *Nanoscale,* vol. 5, pp. 1259-1272, 2013.

[114]   L. Bouffier, V. Ravaine, N. Sojic, and A. Kuhn, "Electric fields for generating unconventional motion of small objects," *Current Opinion in Colloid & Interface Science,* vol. 21, pp. 57-64, 2016/02/01/ 2016.

[115]   J. Orozco, L. A. Mercante, R. Pol, and A. Merkoci, "Graphene-based Janus micromotors for the dynamic removal of pollutants," *Journal of Materials Chemistry A,* vol. 4, pp. 3371-3378, 2016.

[116]   R. Dong, Q. Zhang, W. Gao, A. Pei, and B. Ren, "Highly Efficient Light-Driven TiO2–Au Janus Micromotors," *ACS Nano,* vol. 10, pp. 839-844, 2016/01/26 2016.

[117]   Y. Hong, M. Diaz, U. M. Córdova-Figueroa, and A. Sen, "Light-Driven Titanium-Dioxide-Based Reversible Microfireworks and Micromotor/Micropump Systems," *Advanced Functional Materials,* vol. 20, pp. 1568-1576, 2010.

[118]   M. Ibele, T. E. Mallouk, and A. Sen, "Schooling Behavior of Light-Powered Autonomous Micromotors in Water," *Angewandte Chemie International Edition,* vol. 48, pp. 3308-3312, 2009.

[119]   W. Wang, L. A. Castro, M. Hoyos, and T. E. Mallouk, "Autonomous Motion of Metallic Microrods Propelled by Ultrasound," *ACS Nano,* vol. 6, pp. 6122-6132, 2012/07/24 2012.

[120]   V. Garcia-Gradilla, J. Orozco, S. Sattayasamitsathit, F. Soto, F. Kuralay, A. Pourazary*, et al.*, "Functionalized Ultrasound-Propelled Magnetically Guided Nanomotors: Toward Practical Biomedical Applications," *ACS Nano,* vol. 7, pp. 9232-9240, 2013/10/22 2013.

[121]   S. Oberti, D. Möller, A. Neild, J. Dual, F. Beyeler, B. J. Nelson*, et al.*, "Strategies for single particle manipulation using acoustic and flow fields," *Ultrasonics,* vol. 50, pp. 247-257, 2010/02/01/ 2010.

[122]   A. L. Dounce, "A proposed mechanism for the catalatic ation of catalase," *Journal of Theoretical Biology,* vol. 105, pp. 553-567, 1983/12/21/ 1983.

[123]   M. Alfonso-Prieto, X. Biarnés, P. Vidossich, and C. Rovira, "The Molecular Mechanism of the Catalase Reaction," *Journal of the American Chemical Society,* vol. 131, pp. 11751-11761, 2009/08/26 2009.

[124]   D. Pantarotto, W. R. Browne, and B. L. Feringa, "Autonomous propulsion of carbon nanotubes powered by a multienzyme ensemble," *Chemical Communications,* pp. 1533-1535, 2008.

[125]   S. Sanchez, A. A. Solovev, Y. Mei, and O. G. Schmidt, "Dynamics of Biocatalytic Microengines Mediated by Variable Friction Control," *Journal of the American Chemical Society,* vol. 132, pp. 13144-13145, 2010/09/29 2010.

[126]   J. Orozco, V. García-Gradilla, M. D'Agostino, W. Gao, A. Cortés, and J. Wang, "Artificial Enzyme-Powered Microfish for Water-Quality Testing," *ACS Nano,* vol. 7, pp. 818-824, 2013/01/22 2013.

[127]   B. V. Derjaguin, G. Sidorenkov, E. Zubashchenko, and E. Kiseleva, "Kinetic Phenomena in the boundary layers of liquids 1. the capillary osmosis," *Progress in Surface Science,* vol. 43, pp. 138-152, 1993/05/01/ 1993.

[128] J. J. McDermott, A. Kar, M. Daher, S. Klara, G. Wang, A. Sen*, et al.*, "Self-Generated Diffusioosmotic Flows from Calcium Carbonate Micropumps," *Langmuir,* vol. 28, pp. 15491-15497, 2012/11/06 2012.

[129] G. P. S. B. V. Derjaguin, E. A. Zubashchenko and E. V. Kiseleva, "Kinetic Phenomena in Boundary Films of Liquids,," *Kolloid. Zh.,* vol. 9, pp. 335-347, 1947.

[130] J. L. Anderson, M. E. Lowell, and D. C. Prieve, "Motion of a particle generated by chemical gradients Part 1. Non-electrolytes," *Journal of Fluid Mechanics,* vol. 117, pp. 107-121, 2006.

[131] D. C. Prieve, J. L. Anderson, J. P. Ebel, and M. E. Lowell, "Motion of a particle generated by chemical gradients. Part 2. Electrolytes," *Journal of Fluid Mechanics,* vol. 148, pp. 247-269, 2006.

[132] H. Hu and R. G. Larson, "Marangoni Effect Reverses Coffee-Ring Depositions," *The Journal of Physical Chemistry B,* vol. 110, pp. 7090-7094, 2006/04/01 2006.

[133] "The Marangoni Effect," *https://www.comsol.com/multiphysics/marangoni-effect COMSOL inc. all right reserved,* 2017

[134] M. Frenkel, G. Whyman, E. Shulzinger, A. Starostin, and E. Bormashenko, "Self-propelling rotator driven by soluto-capillary marangoni flows," *Applied Physics Letters,* vol. 110, p. 131604, 2017.

[135] M. Guix, C. C. Mayorga-Martinez, and A. Merkoçi, "Nano/Micromotors in (Bio)chemical Science Applications," *Chemical Reviews,* vol. 114, pp. 6285-6322, 2014/06/25 2014.

[136] W. Zhu, J. Li, Y. J. Leong, I. Rozen, X. Qu, R. Dong*, et al.*, "3D-Printed Artificial Microfish," *Advanced Materials,* vol. 27, pp. 4411-4417, 2015.

[137] Y. L. Sung, J. Jeang, C. H. Lee, and W. C. Shih, "Fabricating optical lenses by inkjet printing and heat-assisted in situ curing of polydimethylsiloxane for smartphone microscopy," *Journal of Biomedical Optics,* vol. 20, Apr 2015.

[138] J. Li, F. Rossignolb, and J. Macdonald, "Inkjet printing for biosensor fabrication: combining chemistry and technology for advanced manufacturing," *Lab on a Chip,* vol. 15, pp. 2538-2558, 2015.

[139] K. Christensen, C. X. Xu, W. X. Chai, Z. Y. Zhang, J. Z. Fu, and Y. Huang, "Freeform Inkjet Printing of Cellular Structures with Bifurcations," *Biotechnology and Bioengineering,* vol. 112, pp. 1047-1055, May 2015.

[140] B. Derby, "Bioprinting: inkjet printing proteins and hybrid cell-containing materials and structures," *Journal of Materials Chemistry,* vol. 18, pp. 5717-5721, 2008.

[141] H. P. Le, "Progress and trends in ink-jet printing technology," *Journal of Imaging Science and Technology,* vol. 42, pp. 49-62, 1998.

[142] B.-J. de Gans and U. S. Schubert, "Inkjet Printing of Polymer Micro-Arrays and Libraries: Instrumentation, Requirements, and Perspectives," *Macromolecular Rapid Communications,* vol. 24, pp. 659-666, 2003.

[143] Y. Zhang, C. Tse, D. Rouholamin, and P. Smith, "Scaffolds for tissue engineering produced by inkjet printing," in *Open Engineering* vol. 2, ed, 2012, p. 325.

[144] B. Derby, "Additive Manufacture of Ceramics Components by Inkjet Printing," *Engineering,* vol. 1, pp. 113-123, 2015.

[145] E. L. Kyser and S. B. Sears, "Method and apparatus for recording with writing fluids and drop projection means therefor," ed: Google Patents, 1976.

[146] Z. Yin, Y. Huang, N. Bu, X. Wang, and Y. Xiong, "Inkjet printing for flexible electronics: Materials, processes and equipments," *Chinese Science Bulletin,* vol. 55, pp. 3383-3407, 2010.

[147] J. P. Lombardi, R. S. Aga, E. M. Heckman, and C. M. Bartsch, "Characterisation of DNA biopolymer-based UV photodetector fabricated by inkjet printing," *Electronics Letters,* vol. 51, pp. 778-779, May 14 2015.

[148] S. Shukla, K. Domican, K. Karan, S. Bhattacharjee, and M. Secanell, "Analysis of Low Platinum Loading Thin Polymer Electrolyte Fuel Cell Electrodes Prepared by Inkjet Printing," *Electrochimica Acta,* vol. 156, pp. 289-300, Feb 20 2015.

[149] C. Zanelli, G. L. Gungor, A. Kara, M. Blosi, D. Gardini, G. Guarini*, et al.*, "Micronizing ceramic pigments for inkjet printing: Part II. Effect on phase composition and color," *Ceramics International,* vol. 41, pp. 6507-6517, Jun 2015.

[150] P. Gingter, A. M. Watjen, M. Kramer, and R. Telle, "Functionally Graded Ceramic Structures by Direct Thermal Inkjet Printing," *Journal of Ceramic Science and Technology,* vol. 6, pp. 119-124, Jun 2015.

[151] V. Bergeron, D. Bonn, J. Y. Martin, and L. Vovelle, "Controlling droplet deposition with polymer additives," *NATURE* vol. 405 (6788), p. 772, 2000.

[152] B. Derby and N. Reis, "Inkjet printing of highly loaded particulate suspensions," *Mrs bulletin,* vol. November, pp. 815-818, 2003.

[153] H. Tao, B. Marelli, M. Yang, B. An, M. S. Onses, J. A. Rogers*, et al.*, "Inkjet Printing of Regenerated Silk Fibroin: From Printable Forms to Printable Functions," *Advanced Materials,* vol. 27, pp. 4273-4279, 2015.

[154] D. Jang, D. Kim, and J. Moon, "Influence of Fluid Physical Properties on Ink-Jet Printability," *Langmuir,* vol. 25, pp. 2629-2635, 2009.

[155] Y. Liu, M. Tsai, Y. Pai, and W. Hwang, "Control of droplet formation by operating waveform for inks with various viscosities in piezoelectric inkjet printing," *Applied Physics a-Materials Science & Processing,* vol. 111(2), pp. 509-516, 2013.

[156] M. N. Dmitriev and N. M. Dmitriev, "On Determining the Percolation Reynolds Number and the Characteristic Linear Dimension for Ideal and Fictitious Porous Media," *Fluid Dynamics,* vol. 40, pp. 585-592, July 01 2005.

[157] B. Derby, "Inkjet Printing of Functional and Structural Materials: Fluid Property Requirements, Feature Stability, and Resolution," *Annual Review of Materials Research,* vol. 40, pp. 395-414, 2010.

[158] J. E. Fromm, "Numerical-calculation of the fluid-dynamics of dropon-demand jets.," *IBM J. Res. Dev.,* vol. 28, pp. 322-333, 1984.

[159] Y. Wang, D. D. Rudym, A. Walsh, L. Abrahamsen, H. J. Kim, H. S. Kim*, et al.*, "In vivo degradation of three-dimensional silk fibroin scaffolds," *Biomaterials,* vol. 29, pp. 3415-28, Aug-Sep 2008.

[160] G. H. McKinley and M. Renardy, "Wolfgang von Ohnesorge," *Physics of Fluids,* vol. 23, p. 127101, 2011.

[161] R. Suntivich, I. Drachuk, R. Calabrese, D. L. Kaplan, and V. V. Tsukruk, "Inkjet Printing of Silk Nest Arrays for Cell Hosting," *Biomacromolecules,* vol. 15, pp. 1428-1435, 2014/04/14 2014.

[162] D. A. Gregory, Y. Zhang, P. J. Smith, X. Zhao, and S. J. Ebbens, "Reactive Inkjet Printing of Biocompatible Enzyme Powered Silk Micro-Rockets," *Small,* vol. 12, pp. 4048-4055, 2016.

[163] W. Shi, M. Sun, X. Hu, B. Ren, J. Cheng, C. Li*, et al.*, "Structurally and Functionally Optimized Silk-Fibroin–Gelatin Scaffold Using 3D Printing to Repair Cartilage Injury In Vitro and In Vivo," *Advanced Materials,* vol. 29, pp. 1701089-n/a, 2017.

[164] E. M. Pritchard, X. Hu, V. Finley, C. K. Kuo, and D. L. Kaplan, "Effect of silk protein processing on drug delivery from silk films," *Macromol Biosci,* vol. 13, pp. 311-20, Mar 2013.

[165] H.-Y. W. a. Y.-Q. Zhang, "Effect of regeneration of liquid silk fibroin on its structure and characterization," *Soft Matter,* vol. 9, pp. 138-145, 2013.

[166] S. Ling, C. Li, K. Jin, D. L. Kaplan, and M. J. Buehler, "Liquid Exfoliated Natural Silk Nanofibrils: Applications in Optical and Electrical Devices," *Advanced Materials,* vol. 28, pp. 7783-7790, 2016.

[167] A. Ajisawa, "Dissolution of silk fibroin wieh CaCl2 ethanol H2O," *J.Seric.Sci.Jpn.,* vol. 67, pp. 91-94, 1998.

[168] G. J. Gittens, "Variation of surface tension of water with temperature," *Journal of Colloid and Interface Science,* vol. 30, pp. 406-412, 1969/07/01/ 1969.

[169] LinkedIn. (2016, 08 March). *PHYSICS FREE NOTES: Surface Tension (Theory).BY ATC*.

[170] B. Samuel, H. Zhao, and K.-Y. Law, "Study of Wetting and Adhesion Interactions between Water and Various Polymer and Superhydrophobic Surfaces," *The Journal of Physical Chemistry C,* vol. 115, pp. 14852-14861, 2011/08/04 2011.

[171] L. B. a. E. Lauga, "A smooth future?," *Nature Mater.,* pp. 334-337., 2011.

[172] D. Hansen, N. Bomholt, J. C. Jeppesen, and A. C. Simonsen, "Contact angle goniometry on single micron-scale fibers for composites," *Applied Surface Science,* vol. 392, pp. 181-188, 2017.

[173] R. J. Hamers, "Scanned Probe Microscopies in Chemistry," *The Journal of Physical Chemistry,* vol. 100, pp. 13103-13120, 1996/01/01 1996.

[174] W. F. Heinz and J. H. Hoh, "Getting Physical with Your Chemistry: Mechanically Investigating Local Structure and Properties of Surfaces with the

Atomic Force Microscope," *Journal of Chemical Education,* vol. 82, p. 695, 2005/05/01 2005.

[175] F. Paquet-Mercier, T. Lefèvre, M. Auger, and M. Pézolet, "Evidence by infrared spectroscopy of the presence of two types of β-sheets in major ampullate spider silk and silkworm silk," *Soft Matter,* vol. 9, pp. 208-215, 2013.

[176] A. Einstein, "Zur Theorie der Brownschen Bewegung," *Annalen der Physik,* vol. 324, pp. 371-381, 1906.

[177] A. Banerjee and K. D. Kihm, "Experimental verification of near-wall hindered diffusion for the Brownian motion of nanoparticles using evanescent wave microscopy," *Physical Review E,* vol. 72, Oct 2005.

[178] A. J. Goldman, R. G. Cox, and H. Brenner, "Slow viscous motion of a sphere parallel to a plane wall—I Motion through a quiescent fluid," *Chemical Engineering Science,* vol. 22, pp. 637-651, 1967.

[179] F. Cordelieres, "Manual Tracking Plugin For ImageJ, http://rsb.info.nih.gov/ij/plugins/track/track.html, accessed: 11, 2015.."

[180] G. Dunderdale, S. Ebbens, P. Fairclough, and J. Howse, "Importance of Particle Tracking and Calculating the Mean-Squared Displacement in Distinguishing Nanopropulsion from Other Processes," *Langmuir,* vol. 28, pp. 10997-11006, Jul 2012.

[181] D. A. Gregory, A. I. Campbell, and S. J. Ebbens, "Effect of Catalyst Distribution on Spherical Bubble Swimmer Trajectories," *The Journal of Physical Chemistry C,* vol. 119, pp. 15339-15348, Oct 6, 2015.

[182] D. Li, S. Banon, and S. L. Biswal, "Bending dynamics of DNA-linked colloidal particle chains," *Soft Matter,* vol. 6, pp. 4197-4204, 2010.

[183] M. G. L. van den Heuvel, S. Bolhuis, and C. Dekker, "Persistence Length Measurements from Stochastic Single-Microtubule Trajectories," *Nano Letters,* vol. 7, pp. 3138-3144, Oct 1, 2007.

[184] R. Pritchard, Y. Yan Shery Huang, and E. Terentjev, *Mechanics of biological networks: From the cell cytoskeleton to connective tissue* vol. 10, 2014.

[185] Y. Zhang, D. A. Gregory, X. Zhao, and P. J. Smith, "Regenerated silk fibroin as an inkjet printable biomaterial," presented at the Printing for fabrication Manchester, 2016.

[186] H. Cheung , K. Lau, T. Lu, and D. Hui, "A critical review on polymer-based bio-engineered materials for scaffold development," *Composites: Part B,* vol. 38, pp. 291-300, 2006.

[187] D. L. M. Kaplan, SM. ; Arcidiacono,s. ; Fossey, S. ; semeca,KWM., *Protein based materials*. Boston: Birkhauser, 1998.

[188] F. S. LUCAS, JTB; SMITH, (SMITH, SG), "The silk fibroins," *Advanced in protein chemistry,* pp. 107-242, 1958.

[189] S. K. Samal, M. Dash, H. A. Declercq, T. Gheysens, J. Dendooven, P. Van Der Voort*, et al.*, "Enzymatic mineralization of silk scaffolds," *Macromol Biosci,* vol. 14, pp. 991-1003, Jul 2014.

[190] L. S. Wray, X. Hu, J. Gallego, I. Georgakoudi, F. G. Omenetto, D. Schmidt*, et al.*, "Effect of processing on silk-based biomaterials: reproducibility and biocompatibility," *J Biomed Mater Res B Appl Biomater,* vol. 99, pp. 89-101, Oct 2011.

[191] M. Yang, Y. Shuai, W. He, S. Min, and L. Zhu, "Preparation of porous scaffolds from silk fibroin extracted from the silk gland of Bombyx mori (B. mori)," *Int J Mol Sci,* vol. 13, pp. 7762-75, 2012.

[192] O. B. Robert D. Deegan, Todd F. Dupont, Greb Huber, Sidney R. Nagel and Thomas A. Witten, "Capillary flow as the cause of ring stains from dried liquid drops," *Nature,* vol. 389 (6653), p. 827, 1997.

[193] D. Soltman and V. Subramanian, "Inkjet-Printed Line Morphologies and Temperature Control of the Coffee Ring Effect," *Langmuir,* vol. 25 (5), pp. 2224-2231, 2008.

[194] O. Shchepelina, I. Drachuk, M. K. Gupta, J. Lin, and V. V. Tsukruk, "Silk-on-silk layer-by-layer microcapsules," *Adv Mater,* vol. 23, pp. 4655-60, Oct 25 2011.

[195] E. Kharlampieva, J. M. Slocik, S. Singamaneni, N. Poulsen, N. Kröger, R. R. Naik*, et al.*, "Protein-Enabled Synthesis of Monodisperse Titania Nanoparticles On and Within Polyelectrolyte Matrices," *Advanced Functional Materials,* vol. 19, pp. 2303-2311, 2009.

[196] Y. G. Yulin Wang, Yin Yang, Peng Yu, Yaqin Huang, "Enhancing the Stability of Immobilized Catalase on Activated Carbon with Gelatin Encapsulation.pdf>," *Journal of Applied Polymer Science,* 2013.

[197] J. Zhang, X. H. Zhou, D. Wang, Y. L. Wang, X. Zhou, H. H. Wang*, et al.*, "Studies on the co-immobilized GOD/CAT on cross-linked chitosan microsphere modified by lysine," *Journal of Molecular Catalysis B-Enzymatic,* vol. 97, pp. 80-86, Dec 15 2013.

[198] Y. L. Wang, Y. P. Guan, Y. Yang, P. Yu, and Y. Q. Huang, "Enhancing the stability of immobilized catalase on activated carbon with gelatin encapsulation," *Journal of Applied Polymer Science,* vol. 130, pp. 1498-1502, Nov 5 2013.

[199] G. Bayramoglu and M. Y. Arica, "Reversible immobilization of catalase on fibrous polymer grafted and metal chelated chitosan membrane," *Journal of Molecular Catalysis B-Enzymatic,* vol. 62, pp. 297-304, Mar 2010.

[200] L. S. Wan, B. B. Ke, J. Wu, and Z. K. Xu, "Catalase immobilization on electrospun nanoribers: Effects of porphyrin pendants and carbon nanotubes," *Journal of Physical Chemistry C,* vol. 111, pp. 14091-14097, Sep 27 2007.

[201] D. L. Jurgen-Lohmann and R. L. Legge, "Immobilization of bovine catalase in sol-gels," *Enzyme and Microbial Technology,* vol. 39, pp. 626-633, Aug 2 2006.

[202] L. Soler and S. Sanchez, "Catalytic nanomotors for environmental monitoring and water remediation," *Nanoscale,* vol. 6, pp. 7175-7182, 2014.

[203] W. Gao, X. Feng, A. Pei, Y. Gu, J. Li, and J. Wang, "Seawater-driven magnesium based Janus micromotors for environmental remediation," *Nanoscale,* vol. 5, pp. 4696-4700, 2013.

[204] L. Baraban, D. Makarov, R. Streubel, I. Mönch, D. Grimm, S. Sanchez*, et al.*, "Catalytic Janus Motors on Microfluidic Chip: Deterministic Motion for Targeted Cargo Delivery," *ACS Nano,* vol. 6, pp. 3383-3389, 2012/04/24 2012.

[205] K. Zhao, W. Li, T. T. Huang, X. M. Luo, G. Chen, Y. Zhang*, et al.*, "Preparation and Efficacy of Newcastle Disease Virus DNA Vaccine Encapsulated in PLGA Nanoparticles," *Plos One,* vol. 8, Dec 26 2013.

[206] S. Ebbens, D. A. Gregory, G. Dunderdale, J. R. Howse, Y. Ibrahim, T. B. Liverpool*, et al.*, "Electrokinetic effects in catalytic platinum-insulator Janus swimmers," *EPL (Europhysics Letters),* vol. 106, p. 58003, 2014.

[207] S. Ebbens, M.-H. Tu, J. R. Howse, and R. Golestanian, "Size dependence of the propulsion velocity for catalytic Janus-sphere swimmers," *Physical Review E,* vol. 85, p. 020401, 02/15/ 2012.

[208] A. Teimouri, L. Ghorbanian, A. Najafi Chermahini, and R. Emadi, "Fabrication and characterization of silk/forsterite composites for tissue engineering applications," *Ceramics International,* vol. 40, pp. 6405-6411, 2014.

[209] M. Rahimi, H. Mohseni-Kouchesfehani, A. H. Zarnani, S. Mobini, S. Nikoo, and S. Kazemnejad, "Evaluation of menstrual blood stem cells seeded in biocompatible Bombyx mori silk fibroin scaffold for cardiac tissue engineering," *J Biomater Appl,* vol. 29, pp. 199-208, Jan 19 2014.

[210] S. Suganya, J. Venugopal, S. Ramakrishna, B. S. Lakshmi, and V. R. Dev, "Naturally derived biofunctional nanofibrous scaffold for skin tissue regeneration," *Int J Biol Macromol,* vol. 68, pp. 135-43, Jul 2014.

[211] Y.-Q. Zhang, "Natural silk fibroin as a support for enzyme immobilization," *Biotechnology Advances,* vol. 16, pp. 961-971, 1998/09/01/ 1998.

[212] L. Soler, V. Magdanz, V. M. Fomin, S. Sanchez, and O. G. Schmidt, "Self-Propelled Micromotors for Cleaning Polluted Water," *ACS Nano,* vol. 7, pp. 9611-9620, 2013/11/26 2013.

[213] H. Wang, J. G. S. Moo, and M. Pumera, "Tissue cell assisted fabrication of tubular catalytic platinum microengines," *Nanoscale,* vol. 6, pp. 11359-11363, 2014.

[214] Y. Gu, S. Sattayasamitsathit, K. Kaufmann, R. Vazquez-Duhalt, W. Gao, C. Wang*, et al.*, "Self-propelled chemically-powered plant-tissue biomotors," *Chemical Communications,* vol. 49, pp. 7307-7309, 2013.

[215] M. L. You, J. J. Zhong, Y. Hong, Z. F. Duan, M. Lin, and F. Xu, "Inkjet printing of upconversion nanoparticles for anti-counterfeit applications," *Nanoscale,* vol. 7, pp. 4423-4431, Mar 14 2015.

[216] M. Caffrey, "Membrane protein crystallization," *Journal of Structural Biology,* vol. 142, pp. 108-132, 2003/04/01/ 2003.

[217] J. G. S. Moo and M. Pumera, "Chemical Energy Powered Nano/Micro/Macromotors and the Environment," *Chemistry – A European Journal,* vol. 21, pp. 58-72, 2015.

[218] K. K. Dey, X. Zhao, B. M. Tansi, W. J. Méndez-Ortiz, U. M. Córdova-Figueroa, R. Golestanian*, et al.*, "Micromotors Powered by Enzyme Catalysis," *Nano Letters,* vol. 15, pp. 8311-8315, 2015/12/09 2015.

[219] M. Safdar, O. M. Wani, and J. Jänis, "Manganese Oxide-Based Chemically Powered Micromotors," *ACS Applied Materials & Interfaces,* vol. 7, pp. 25580-25585, 2015/11/25 2015.

[220] L. K. E. A. Abdelmohsen, F. Peng, Y. Tu, and D. A. Wilson, "Micro- and nano-motors for biomedical applications," *Journal of Materials Chemistry B,* vol. 2, pp. 2395-2408, 2014.

[221] R. F. Ismagilov, A. Schwartz, N. Bowden, and G. M. Whitesides, "Autonomous Movement and Self-Assembly," *Angewandte Chemie International Edition,* vol. 41, pp. 652-654, 2002.

[222] R. J. Archer, A. I. Campbell, and S. J. Ebbens, "Glancing angle metal evaporation synthesis of catalytic swimming Janus colloids with well defined angular velocity," *Soft Matter,* vol. 11, pp. 6872-6880, 2015.

[223] R. A. Pavlick, K. K. Dey, A. Sirjoosingh, A. Benesi, and A. Sen, "A catalytically driven organometallic molecular motor," *Nanoscale,* vol. 5, pp. 1301-1304, 2013.

[224] S. Tottori, L. Zhang, F. Qiu, K. K. Krawczyk, A. Franco-Obregón, and B. J. Nelson, "Magnetic Helical Micromachines: Fabrication, Controlled Swimming, and Cargo Transport," *Advanced Materials,* vol. 24, pp. 811-816, 2012.

[225] M. M. Stanton, C. Trichet-Paredes, and S. Sanchez, "Applications of three-dimensional (3D) printing for microswimmers and bio-hybrid robotics," *Lab on a Chip,* vol. 15, pp. 1634-1637, 2015.

[226] H. Kitahata, S.-i. Hiromatsu, Y. Doi, S. Nakata, and M. Rafiqul Islam, "Self-motion of a camphor disk coupled with convection," *Physical Chemistry Chemical Physics,* vol. 6, pp. 2409-2414, 2004.

[227] J. Li, G. Huang, M. Ye, M. Li, R. Liu, and Y. Mei, "Dynamics of catalytic tubular microjet engines: Dependence on geometry and chemical environment," *Nanoscale,* vol. 3, pp. 5083-5089, 2011.

[228] R. L. Siegel, K. D. Miller, and A. Jemal, "Cancer statistics, 2017," *CA: A Cancer Journal for Clinicians,* vol. 67, pp. 7-30, 2017.

[229] R. L. Siegel, K. D. Miller, and A. Jemal, "Cancer statistics, 2016," *CA: A Cancer Journal for Clinicians,* vol. 66, pp. 7-30, 2016.

[230] R. L. Siegel, K. D. Miller, and A. Jemal, "Cancer statistics, 2015," *CA: A Cancer Journal for Clinicians,* vol. 65, pp. 5-29, 2015.

[231] A. F. Chambers, A. C. Groom, and I. C. MacDonald, "Metastasis: Dissemination and growth of cancer cells in metastatic sites," *Nat Rev Cancer,* vol. 2, pp. 563-572, 08//print 2002.

[232] A. L. Allan and M. Keeney, "Circulating Tumor Cell Analysis: Technical and Statistical Considerations for Application to the Clinic," *Journal of Oncology,* vol. 2010, p. 426218, 12/13 2010.

[233] L. A. Torre, F. Bray, R. L. Siegel, J. Ferlay, J. Lortet-Tieulent, and A. Jemal, "Global cancer statistics, 2012," *CA: A Cancer Journal for Clinicians,* vol. 65, pp. 87-108, 2015.

[234] K. Pantel and R. H. Brakenhoff, "Dissecting the metastatic cascade," *Nat Rev Cancer,* vol. 4, pp. 448-456, 06//print 2004.

[235] W. S. Low and W. A. B. Wan Abas, "Benchtop Technologies for Circulating Tumor Cells Separation Based on Biophysical Properties," *BioMed Research International,* vol. 2015, p. 22, 2015.

[236] S. C. P. Williams, "Circulating tumor cells," *Proceedings of the National Academy of Sciences,* vol. 110, p. 4861, March 26, 2013 2013.

[237] M. Tellez-Gabriel, H. K. Brown, R. Young, M. F. Heymann, and D. Heymann, "The Challenges of Detecting Circulating Tumor Cells in Sarcoma," 2016.

[238] C. L. Sawyers, "The cancer biomarker problem," *Nature,* vol. 452, pp. 548-552, 04/03/print 2008.

[239] S. K. Arya, B. Lim, and A. R. A. Rahman, "Enrichment, detection and clinical significance of circulating tumor cells," *Lab on a Chip,* vol. 13, pp. 1995-2027, 2013.

[240] G. Christofori, "New signals from the invasive front," *Nature,* vol. 441, pp. 444-450, 05/25/print 2006.

[241] Y. Hüsemann, J. B. Geigl, F. Schubert, P. Musiani, M. Meyer, E. Burghart*, et al.*, "Systemic Spread Is an Early Step in Breast Cancer," *Cancer Cell,* vol. 13, pp. 58-68, 2007.

[242] W. Harb, A. Fan, T. Tran, D. C. Danila, D. Keys, M. Schwartz*, et al.*, "Mutational Analysis of Circulating Tumor Cells Using a Novel Microfluidic Collection Device and qPCR Assay," *Translational Oncology,* vol. 6, pp. 528-IN1, 2013/10/01/ 2013.

[243] V. V. Iakovlev, R. S. Goswami, J. Vecchiarelli, N. C. R. Arneson, and S. J. Done, "Quantitative detection of circulating epithelial cells by Q-RT-PCR," *Breast Cancer Research and Treatment,* vol. 107, pp. 145-154, January 01 2008.

[244] P. Bossolasco, C. Ricci, G. Farina, D. Soligo, D. Pedretti, A. Scanni*, et al.*, "Detection of micrometastatic cells in breast cancer by RT-PCR for the mammaglobin gene," *Cancer Detection and Prevention,* vol. 26, pp. 60-63, 2002/03/01/ 2002.

[245] A. E. Ring, L. Zabaglo, M. G. Ormerod, I. E. Smith, and M. Dowsett, "Detection of circulating epithelial cells in the blood of patients with breast cancer: comparison of three techniques," *Br J Cancer,* vol. 92, pp. 906-912, 02/15/online 2005.

[246] I. Cruz, J. Ciudad, J. J. Cruz, M. Ramos, A. Gómez-Alonso, J. C. Adansa*, et al.*, "Evaluation of Multiparameter Flow Cytometry for the Detection of Breast Cancer Tumor Cells in Blood Samples," *American Journal of Clinical Pathology,* vol. 123, pp. 66-74, 2005.

[247] Y. Hu, L. Fan, J. e. Zheng, R. Cui, W. Liu, Y. He*, et al.*, "Detection of circulating tumor cells in breast cancer patients utilizing multiparameter flow cytometry and assessment of the prognosis of patients in different CTCs levels," *Cytometry Part A,* vol. 77A, pp. 213-219, 2010.

[248] N. Wang, L. Shi, H. Li, Y. Hu, W. Du, W. Liu*, et al.*, "Detection of circulating tumor cells and tumor stem cells in patients with breast cancer by using flow cytometry," *Tumor Biology,* vol. 33, pp. 561-569, April 01 2012.

[249] S. Nagrath, L. V. Sequist, S. Maheswaran, D. W. Bell, D. Irimia, L. Ulkus*, et al.*, "Isolation of rare circulating tumour cells in cancer patients by microchip technology," *Nature,* vol. 450, pp. 1235-1239, 12/20/print 2007.

[250] A. A. Adams, P. I. Okagbare, J. Feng, M. L. Hupert, D. Patterson, J. Göttert*, et al.*, "Highly Efficient Circulating Tumor Cell Isolation from Whole Blood and Label-Free Enumeration Using Polymer-Based Microfluidics with an Integrated Conductivity Sensor," *Journal of the American Chemical Society,* vol. 130, pp. 8633-8641, 2008/07/01 2008.

[251] F. Breton, B. Bennetau, R. Lidereau, L. Thomas, G. Regnier, J.-C. Ehrhart*, et al.*, "A mesofluidic multiplex immunosensor for detection of circulating cytokeratin-positive cells in the blood of breast cancer patients," *Biomedical Microdevices,* vol. 13, pp. 1-9, 2011/02/01 2011.

[252] E. W. A. Visser, L. J. van Ijzendoorn, and M. W. J. Prins, "Particle Motion Analysis Reveals Nanoscale Bond Characteristics and Enhances Dynamic Range for Biosensing," *ACS Nano,* vol. 10, pp. 3093-3101, 2016/03/22 2016.

[253] Y. C. Wang, Y. Zheng, L. Zhang, Q. W. Wang, and D. R. Zhang, "Stability of nanosuspensions in drug delivery," *Journal of Controlled Release,* vol. 172, pp. 1126-1141, Dec 28 2013.

[254] S. Balasubramanian, D. Kagan, C.-M. Jack Hu, S. Campuzano, M. J. Lobo-Castañon, N. Lim*, et al.*, "Micromachine-Enabled Capture and Isolation of Cancer Cells in Complex Media," *Angewandte Chemie International Edition,* vol. 50, pp. 4161-4164, 2011.

[255] D. A. Gregory, Y. Zhang, P. J. Smith, and a. S. J. E. X. Zhao, "Altering the Bubble Release of Reactive Inkjet Printed Silk Micro-rockets," presented at the Printing For Fabrication (NIP), Manchester 2016.